이학박사학위논문

Carbon Dioxide Capture by Metal-Organic Frameworks with Flexible Building Units

유연한 건축단위가 포함된 금속-유기 골격체를 이용한 이산화탄소 포집에 관한 연구

2014년 2월

서울대학교 대학원

화학부 무기화학 전공

홍 대 호

이학박사학위논문

Carbon Dioxide Capture by Metal-Organic Frameworks with Flexible Building Units

유연한 건축단위가 포함된 금속-유기 골격체를 이용한 이산화탄소 포집에 관한 연구

지도교수 백 명 현

이 논문을 이학박사학위논문으로 제출함

2014년 2월

서울대학교 대학원

화학부 부기화학 전공

홍 대 호

홍대호의 박사학위 논문을 인준함

2014년 2월

위 원 장 _____ (인)

부위원장 _____ (인)

위 원 _____ (인)

위 원 _____ (인)

위 원 _____ (인)

Carbon Dioxide Capture by Metal-Organic Frameworks with Flexible Building Units

By

Dae Ho Hong

Supervisor: Prof. Myunghyun Paik Suh

A Thesis for the Ph.D.

in Inorganic Chemistry

Department of Chemistry

Graduate School

Seoul National University

February, 2014

Abstract

PART I. SELECTIVE ADSORPTION OF CARBON DIOXIDE USING A POROUS METAL-ORGANIC FRAMEWORK CONSTRUCTED WITH A FLEXIBLE LINEAR LIGAND

We have synthesized a porous metal-organic framework $\{[Zn_2(mpm\text{-}PBODB)_2bpy]\cdot 3DMF\}_n$ (**SNU-110**) by using an organic ligand containing flexible joints. **SNU-110** has a 3D pillared-layer structure generating 1D channels with window size of 4.4 × 3.7 $Å^2$. The solvent accessible volume is 30% of the whole structure. On activating **SNU-110** with supercritical CO_2 fluid, desolvated solid $[Zn_2(mpm\text{-}PBODB)_2bpy]_n$ (**SNU-110'**) resulted, which has a unit cell volume reduced by 8.8%. **SNU-110'** hardly adsorbs N_2 and H_2 gases at 77 K, indicating its smaller window size than the kinetic diameter (2.89 Å) of H_2. However, it uptakes 97 $cm^3\ g^{-1}$ of CO_2 at 195 K despite that CO_2 has much larger kinetic diameter than H_2, indicating that CO_2 can open up the gate of the flexible MOF due to its much higher polarizability and quadrupole moment than N_2 and H_2. **SNU-110'** shows a two-step CO_2 adsorption curve related with structural transformation on CO_2 adsorption, together with a big desorption-hysteresis. Expansion of the framework by CO_2 adsorption is evidenced by powder X-ray diffraction data measured under CO_2 stream at 248 K. The selectivities for CO_2 adsorption over N_2, H_2, and CH_4 at 195 K are 35:1, 61:1, and 15:1, respectively.

Keywords: metal–organic frameworks • carbon dioxide capture • stepwise adsorption • flexible networks • hysteresis

PART II. ENHANCED CARBON DIOXIDE CAPTURE BY POST-SYNTHETIC MODIFICATION OF METAL-ORGAIC FRAMEWORKS WITH FLEXIBLE ALKANEDIOIC ACIDS

A series of porous metal-organic frameworks having flexible carboxylic acid pendants in their pores (UiO-66-AD*n*: *n* = 4, 6, 8, and 10, where *n* de notes the number of carbons in a pendant) have been synthesized by the post-synthetic ligand exchange of terephthalate in UiO-66 with a series of alkanedioic acids ($HO_2C(CH_2)_{n-2}CO_2H$). The NMR, IR, PXRD, TEM, and Mass spectral data suggested that a terephthalate linker in UiO-66 was substituted with two alkanedioates to result in free carboxyl pendants in the pores. When post-synthetically modified UiO-66 was partially digested by adjusting the amount of added HF/sample, the NMR spectra indicated that the ratio of alkanedioic acid/terephthalic acid was increased with the lesser amount of acid, implying that the ligand substitution proceeded from the outer layer of the particle. Gas sorption studies indicated that the surface area and the pore volume of all UiO-66-AD*n*s were decreased compared to those of UiO-66 while the CO_2 adsorption capacities of UiO-66-AD*n* (*n* = 4, 8) were similar to that of UiO-66. In case of UiO-66-AD6, the CO_2 uptake capacity was greater by 34% at 298 K and by 58% at 323 K compared to those of UiO-66. It was elucidated by the thermodynamic calculations that the introduction of the flexible carboxyl pendants with appropriate length has two effects: 1) Increasing interaction enthalpy between the host framework and CO_2 molecules. 2) Mitigating the entropy loss upon CO_2 adsorption due to the formation of multiple configurations for the interactions between carboxyl groups and the CO_2 molecules. The IAST selectivity of CO_2

adsorption over CH_4 was enhanced for all UiO-66-AD*n*s compared to that of UiO-66 at 298 K. In particular, UiO-66-AD6 showed the most highly enhanced CO_2 uptake capacities and significantly increased selectivities of CO_2 adsorption over CH_4 at ambient temperature, suggesting that it is a promising CO_2 separation material from landfill gas.

Keywords: metal-organic frameworks • carbon dioxide separation • carboxyl pendants • post-synthetic modification • ligand substitution • thermodynamics

Table of contents

Abstract i

PART I. SELECTIVE ADSORPTION OF CARBON DIOXIDE USING A POROUS METAL-ORGANIC FRAMEWORK CONSTRUCTED WITH A FLEXIBLE LINEAR LIGAND 1

I.1. Introduction 2

I.1.1. Global warming 2

I.1.1.1. Facts and countermeasures 2

I.1.1.2. Carbon capture and storage (CCS)[9] 6

I.1.1.2.1. Conditions for CCS materials 10

I.1.1.2.2. CO_2 capture materials for CCS 14

I.1.2. Metal-organic frameworks (MOFs) 18

I.1.2.1. Properties and analytic methods 19

I.1.2.2. Synthetic strategies for MOFs 24

I.1.2.3. Flexibility of MOFs 27

I.1.2.3.1. Analysis of flexible MOFs 28

I.1.2.3.2. Types of flexible MOFs 31

I.2. Experimental Section 45

I.3. Results and Discussion 49

I.3.1. Design of a ligand 49

I.3.2. Synthesis and structure analysis of **SNU-110** and **SNU-110'** 52

I.3.3. Gas sorption properties of SNU-110' 59

I.4. Conclusions 66

PART II. ENHANCED CARBON DIOXIDE CAPTURE BY POST-SYNTHETIC MODIFICATION OF METAL-ORGAIC FRAMEWORKS WITH FLEXIBLE ALKANEDIOIC ACIDS 67

II.1. Introduction 68

II.1.1. Post-synthetic modifications of MOFs 68

II.1.1.1. Coordinated guest exchange grafting 69

II.1.1.2. Ligand insertion/removal/exchange and metal exchange 70

II.1.2. Energetic aspects of adsorption and desorption functions 77

II.2. Experimental Section 82

II.3. Results and Discussion 85

II.3.1. Preparation of UiO-66-AD*n*s by post synthetic modification of UiO-66 85

II.3.2. Distribution of substituted adipic acid in post-synthetically modified UiO-66 96

II.3.3. Gas sorption properties and thermodynamic analyses of UiO-66 and UiO-66-AD*n*s 99

II.3.4. Selectivity estimated by ideal adsorption solution theory (IAST) 111

II.4. Conclusions 115

References 116

Publications 131

국문 초록 158

감사의 말 162

PART I. SELECTIVE ADSORPTION OF CARBON DIOXIDE USING A POROUS METAL-ORGANIC FRAMEWORK CONSTRUCTED WITH A FLEXIBLE LINEAR LIGAND

I.1. Introduction

I.1.1. Global warming

I.1.1.1. Facts and countermeasures

Highly developed technologies have been changing the environment and circumstances as well as the life of human being. After 200 years from the Industrial Revolution, humans' demand and consumption of energy have been sharply increased ever (Figure 1). Global warming is considered as a one of direct consequences of this human activity. Massive use of carbon based fossil fuel resulted in increased concentrations of anthropogenic greenhouse gases (GHG) in atmosphere, which are regarded as a primary cause of the rise of atmospheric temperature (Figure 2).[1] The major component of anthropogenic GHG is carbon dioxide (CO_2), which account for more than 90% of total GHG, and the rest are methane (CH_4) and nitrous oxide (N_2O).[2] Unlike N_2 and O_2, which are prevailing in atmosphere and not absorbing earth radiation, GHG gases are able to absorb infrared radiation from Earth (Figure 3) and increase the surface temperature of Earth. The problems of increasing temperature are increased occurrences of extreme weather events, extinctions of poorly adapted species, rise of sea level with partial deglaciation of ice sheets.[1] However, we are still relying on fossil fuel as a major energy source, and the level of CO_2 is expected to be raised further. The speed of the increasing concentrations of GHG already exceeds the tolerance of nature. Current global emission amount of CO_2 was 30 gigaton in 2010 and the concentration of atmospheric CO_2 was 394 ppm in 2013,[3,4] and the total emission amount of CO_2 is projected to be 60 gigaton in 2050.[5,6]

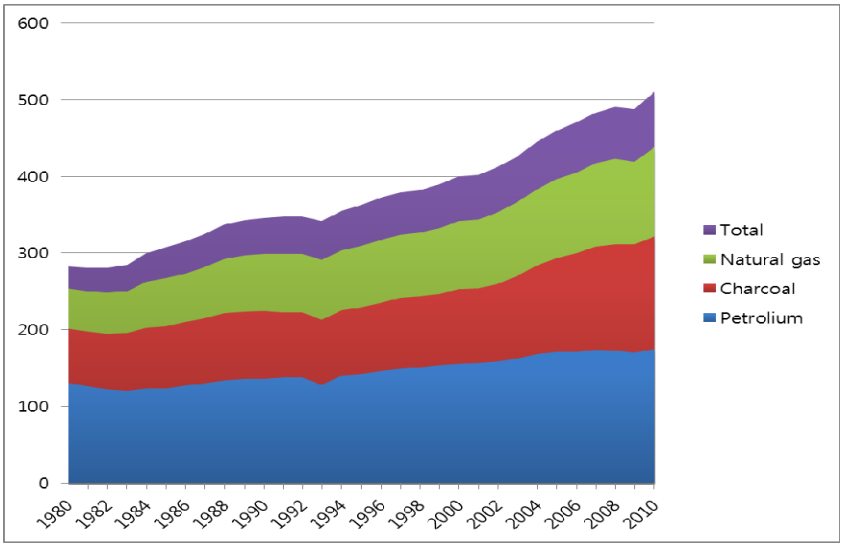

Figure 1 International primary energy consumption in Quadrillion Btu (1 Btu = 1055 J). Data was taken from U.S. Energy Information Administration (http://www.eia.gov).

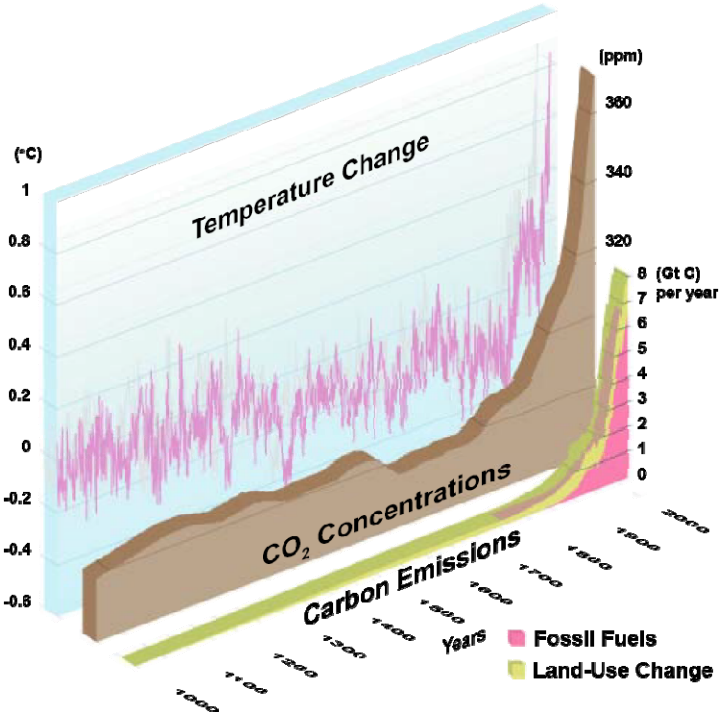

Figure 2 1000 years of changes in carbon emissions, CO_2 concentrations and temperature.[1]

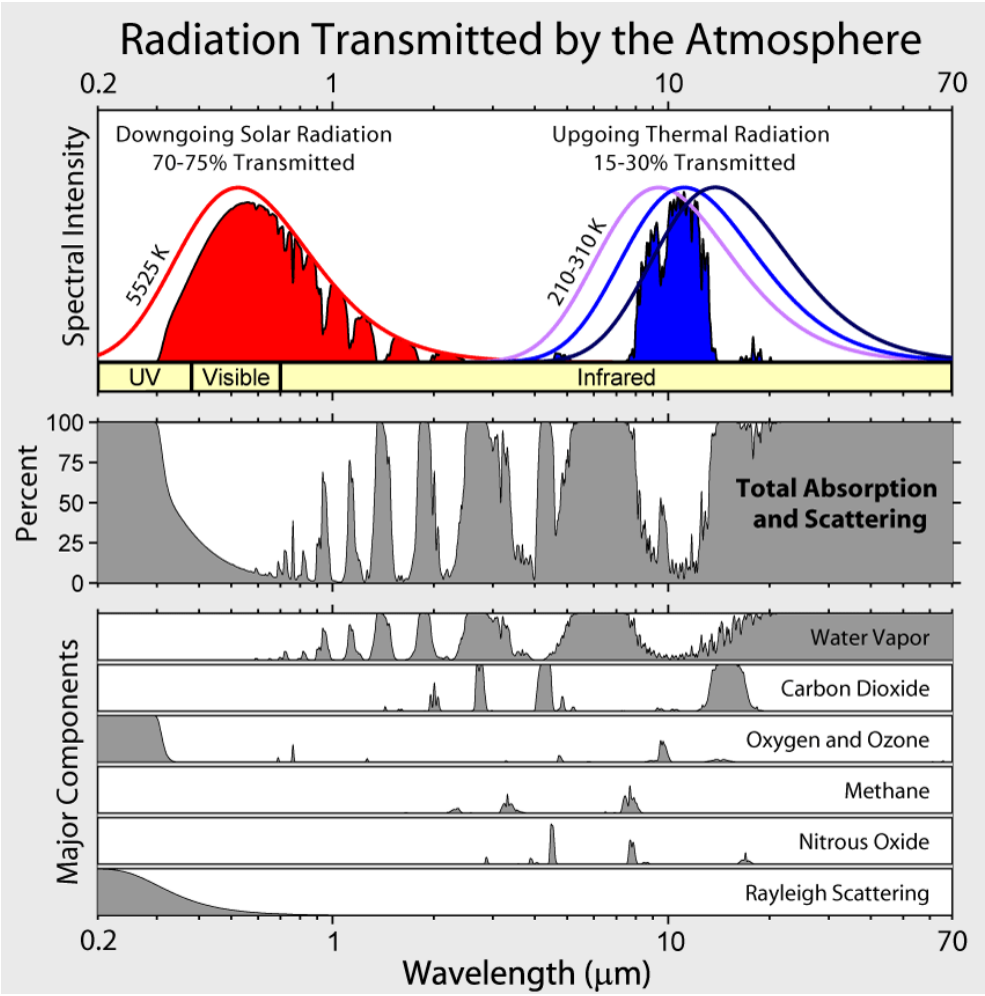

Figure 3 Atmospheric transmission.[7] Radiation from the sun and Earth are illustrated in red and blue color, respectively. Adsorption and scattering effect of gas components are described in bottom.

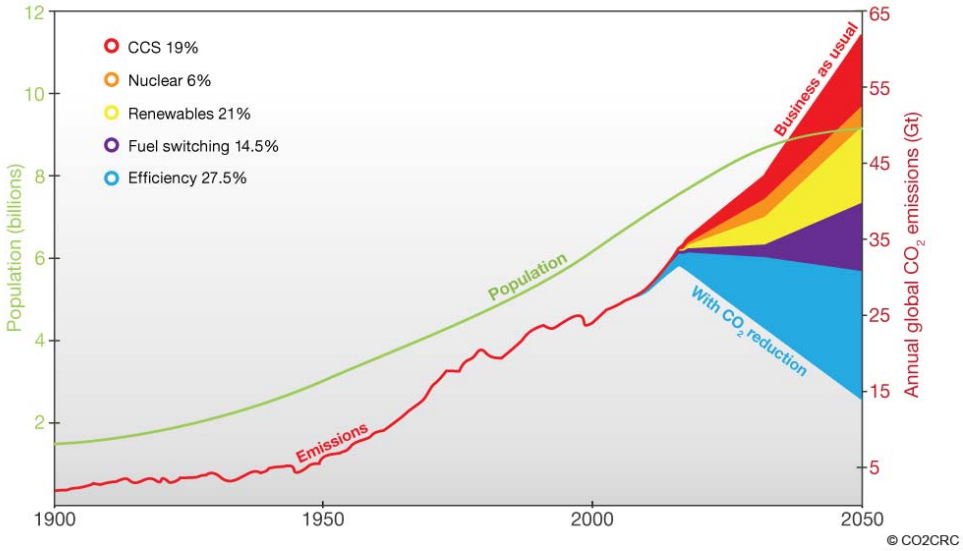

Figure 4 Projection of global CO_2 emissions. The total amount of CO_2 emission is expected to be raised to about 60 gigaton per year in 2050. Increase of energy efficiency, switching to a carbon-free fuel, utilization of renewable energy, enhanced use of nuclear energy, and carbon capture and storage (CCS) are suggested as solutions and the effects of them are illustrated:.[6]

To reduce the emission of CO_2, several strategies have been suggested, and five technologies out of them are regarded as main solutions to mitigate the situation: They are to increase energy efficiency, to switch to a carbon-free fuel such as hydrogen, to utilize renewable energy, to increase an energy dependency to nuclear energy, and to capture and sequestrate the CO_2 (Figure 4).[5,8] As drawn in the Figure 4, to lessen the momentum of increasing CO_2 concentration in the atmosphere, five strategies should take effect concurrently. In this thesis, researches related with the carbon capture and storage (CCS) will be covered.

I.1.1.2. Carbon capture and storage (CCS)[9]

The target of carbon capture and storage (CCS) is to collect CO_2 from atmosphere and to store it in lithosphere (Figure 5). The CCS process is composed of three major steps: CO_2 capture from emission spots, transport via pipeline, and underground injection with pressurized state. Among these steps, CO_2 capture process requires most of energy and cost among all CCS process,[9] therefore the development of new technologies for capturing CO_2 is very important. The major CO_2 emission spots are plants and factories where capture process should be applied. According to the statistical data, these spots accounts for 40% of total worldwide CO_2 emission.

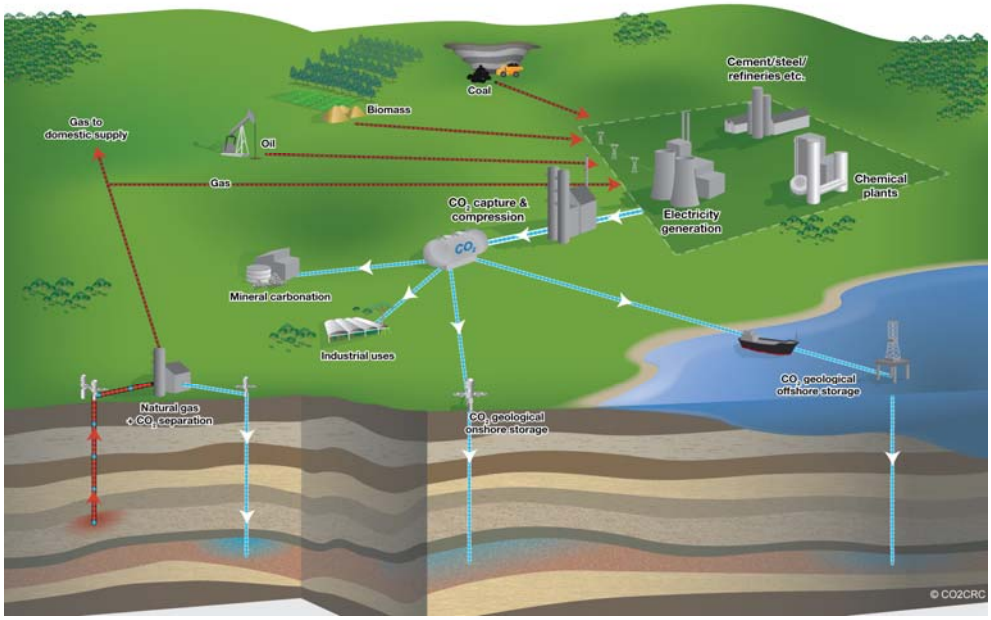

Figure 5 Suggested CCS system including emission sources, capture system, and storage sites.[10]

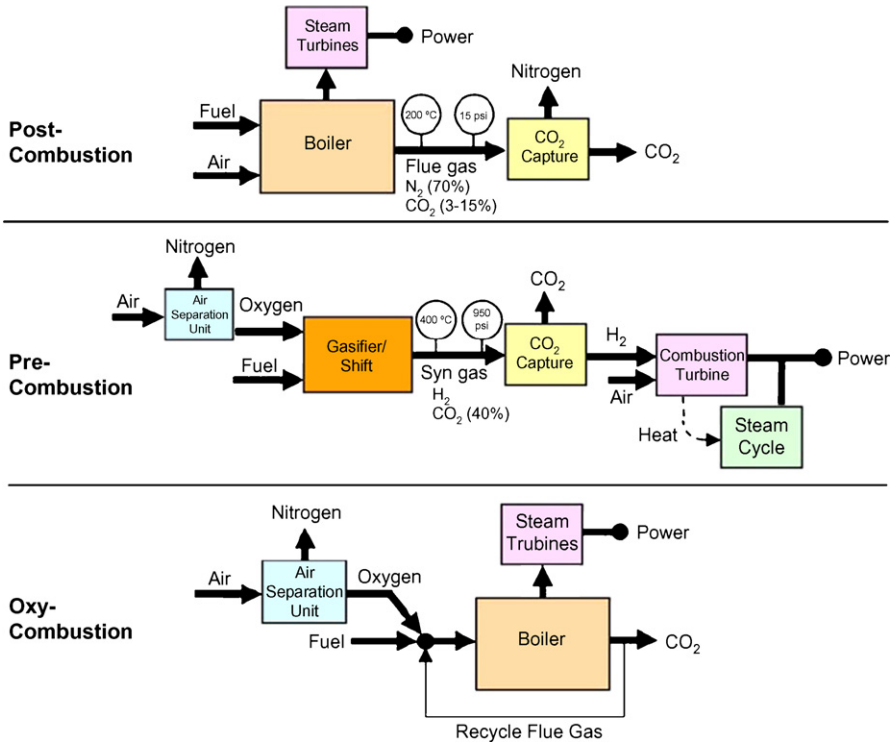

Figure 6 Three methods of capturing CO_2 from a plant.[11]

There are three methods for capturing CO_2 from a plant: Post-combustion, pre-combustion, and oxy-fuel combustion (Figure 6).[12] In addition to this, CO_2 can be captured from low-grade nature gas or land fill gas, containing CH_4 as a major component. The species, compositions and partial pressures of the gas to be separated are different depending on the method (Table 1). Post-combustion method is the most general method which captures CO_2 from the flue gas, containing less than 15% of CO_2 and the most of rest is N_2. The major advantage of this method is that the most of current facilities can be retrofitted by this method without extensive alterations of devices. However, due to the low concentration of CO_2 in the flue gas, the thermodynamic driving force for capturing CO_2 is low. In pre-combustion method, a

mixture of H_2 and CO_2 gas is produced through steam reforming reaction of synthesis gas. The advantages of this method are the easy separation between CO_2 and H_2, and high thermodynamic driving force from pressurized CO_2 gas mixture. But the disadvantage of this method is requirement of H_2 combustion turbine. Finally, in oxy-fuel combustion reaction, the inlet air has to be separated. N_2 component of inlet air is separated to result in O_2-rich gas which is combusted to produce a mixture of CO_2 and H_2O. Because the boiler can be overheated by the combustion of pure O_2, resulting CO_2 and H_2O are recycled and mixed with O_2 gas before combustion to moderate the temperature.

Once CO_2 is captured, the captured gas are pressurized and transported to the sequestration spot. In this spot, pressurized supercritical CO_2 gas is injected. Various spots for storage have been evaluated by their storage time and scale (Figure 7).[13] Among the whole options, injection into the deep earth is the easiest option to apply, however, this option has a potential problem of leaking. A more safer and permanent method is to store CO_2 with water in alkaline mineral strata. Resulting carbonic acid will be neutralized to carbonate or bicarbonate form which is free from leaking. Carbonation of rocks rich in magnesium silicates is also considerable option to store CO_2 in a specific site on the ground. Injection into the deep sea is not recommended due to the potential hazard of acidic ocean water to the biosphere.

Table 1 compositions of gases. The major species to be separated are marked as b old font. The minor species ratio of which is less than 1% are listed as traces.

	flue gas[14]	syngas[15]	air	natural gas[9]	landfill gas[16]
CH_4		0-15		**75-99**	**45-60**
CO		35-40			
CO_2	**15-16**	**25-35**	0.04	**0-10**	**40-60**
H_2		**20-40**			
N_2	**73-77**	2-5	**78**	0-15	2-5
O_2	3-4		**21**		0.1-1
He				0-5	
H_2O	5-7				
H_2S				0-30	
hydrocarbons				2-29	
traces	CO, HCl, hydrocarbon, SO_x, NO_x,		Ar		H_2, CO, SO_x, NH_3

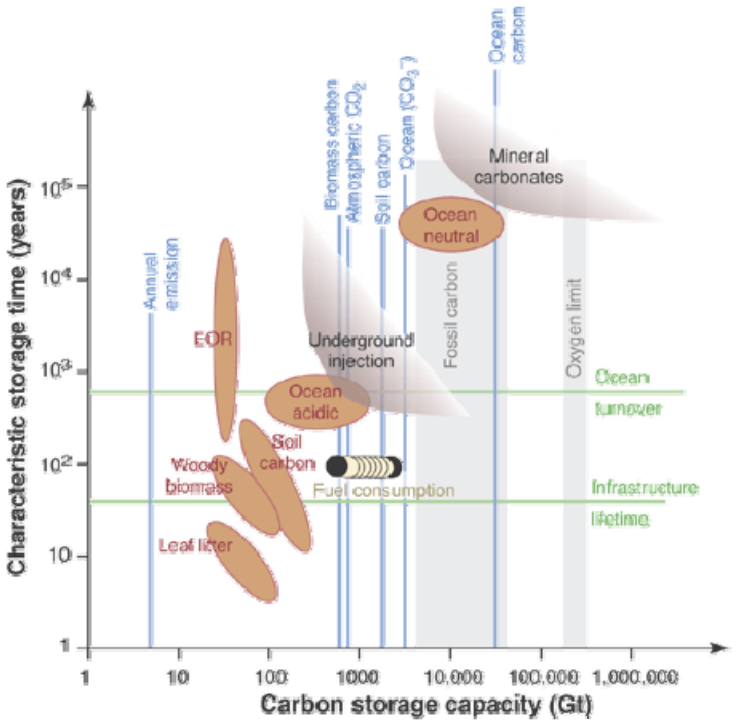

Figure 7 various options for storing CO_2.

I.1.1.2.1. Conditions for CCS materials

Capturing CO_2 can be achieved in four ways. Firstly, using liquid phase CO_2 scrubber adsorb CO_2 from liquid-gas interface, circulate using pump, and regenerate scrubber under desorption condition. This method is applied to the currently used liquid based technology such as amine solution. Secondly, for the solid based porous materials, swing method can be used. To apply swing method, more than two columns packed with solid sorbents should be prepared. At the initial stage, a column is exposed to the flue gas, and after it reached to saturation, a flow of purge gas is applied under desorption condition while the flue gas passes through the other column. Depending on the adsorption/desorption condition, swing method can be categorized as pressure swing, vacuum swing, and temperature swing. In pressure swing, adsorption process

processed with pressurized gas while atmospheric pressure is applied for desorption process. Contrarily, atmospheric and evacuated conditions are applied to adsorption and desorption processes, respectively, in vacuum swing. Thirdly, membrane-based technology uses permeable film to separate the gas flows. Finally, cryogenic condition can be used to liquefy the specific species.[9]

This research deals with solid based sorbent, therefore, properties of materials will be evaluated based on swing type method. Followings should be considered for efficient capture of CO_2 from flue gas in swing type method.

1) **Capacity (N^{ads}), working capacity (ΔN), and regenerability (R)**:[17] Capacity is the ability of capturing CO_2 per unit dimension in given conditions. Weight based capacity is generally used because it is more convenient to measure, however, volume based capacity is more reasonable for fixed volume of packing column. Working capacity is effective capacity for swing method, which is difference of the adsorption capacities between adsorption conditions and desorption conditions (Equation 1). Even the material showing high capacity can have small working capacity depending on the swing condition.[18] The ratio of working capacity to capacity is regenerability of the adsorbent (Equation 2). The higher regenerability means the large portion of adsorption sites are available to adsorb adsorbate reversibly.

Equation 1 $\Delta N = N^{ads} - N^{des}$

Equation 2 $R = \Delta N / N^{ads} \times 100\%$

2) **Adsorption selectivity**:[14,17] Adsorption selectivity is a degree of preference of an adsorbent to a specific component in a gas mixture. As a rule, this value should be measured with a mixture gas. However, this value is normally estimated from the adsorption isotherms measured with a single component gas. A simple estimation of adsorption selectivity is the ratio of adsorption amount of two different gases at the same adsorption condition or the ratio of adsorption amounts of each gas divided by the ratio of the pressure of each gas at adsorption conditions (Equation 3).

Equation 3 $$\alpha_{12} = \frac{N_1^{ads} / N_2^{ads}}{P_1^{ads} / P_2^{ads}}$$

Other calculation method is also available. Henry constant of each gas can be derived from its adsorption isotherm. This value represents the initial interaction strength between adsorbent and adsorbate, therefore the ratio of henry constant can be applied to a calculation of adsorption selectivity (Equation 4).[19] The limitation of this calculation is that the adsorption selectivity may not valid for saturation condition.

Equation 4 $$\alpha_{12} = \frac{K_1}{K_2}$$ where K_1 and K_2 are Henry constants

The most recently suggested method is the calculation using the idealized adsorption solution theory (IAST). In this theory, virtual thermodynamic term, spreading pressure (π, Equation 5), is introduced and used for calculation. Spreading pressure is the pressure that applied to adsorbed phase, and this value is assumed to

be identical for every species that adsorbed on the surface of an adsorbent (Equation 6).

Equation 5 $$\pi = RT\int_0^P \frac{n}{P}dP = RT\int_0^P nd\ln P$$

Equation 6 $$\alpha_{1,2} = \frac{P_2^{\circ}(\pi)}{P_1^{\circ}(\pi)}$$

Where R is gas constant, n is adsorption isotherm, and $P^{\circ}(\pi)$ is pressure of single-component gas under given spreading pressure. The calculation based on this theory is generally accepted as reasonable method to simulate adsorption isotherm of multi-component gas using isotherm data of single-component gas. Detailed explanation of calculation and limitations of this method will be discussed later.

3) **Kinetics of adsorption**: The speed of adsorption/desorption for the swing process is also important. If the kinetic property of the adsorbent is bad for an adsorbent that adsorbing large amount of gas, the efficiency of total process can be lowered. To have a good kinetic property, the interaction energy between adsorbent and adsorbate has to be in proper range. Otherwise, temperature control should be applied to increase the speed of adsorption/desorption.

4) **Stability**:[9,20] An adsorbent can be subjected to various environments such as high temperature, humid air, acidic vapors, or mechanical stress in the swing process. Thermal, moisture, chemical, and mechanical stability have to be tested to assure

long period operation of the material. Degradation of adsorbent can reduce the performance of separation while increase the cost of maintenance. However, additional steps of capturing moisture or acidic gas in the separation process can compensate for the weak stabilities of the adsorbent.

5) **Cost**: Cost of synthesizing the adsorbent has to be considered. High capital cost of preparing a material is an obstacle for commercialization. Scale-up synthesis, reduction of synthesis steps, and introduction of low-cost base materials can help reduce the cost of synthesis.

6) **Operation condition**: Optimum conditions for the adsorbent are different case by case. Working temperature or pressure deviated far from ambient condition requires lots of energy just for maintaining temperature. Therefore, an adsorbent optimized near at ambient temperature and pressure is more favorable.

I.1.1.2.2. CO_2 capture materials for CCS

Currently, there are several commercialized technologies for capturing CO_2. Those technologies are categorized as solvents, membranes, solid sorbents, or cryogenic technologies.[9] Chemical solvents, physical solvents, polymeric membranes, zeolites, and activated carbons are used for practical applications. The widely used technique for CO_2 capture is alkanolamine solution. The solution generally contains monoethanolamine (MEA), diethanolamine (DEA), methyldiethanolamine (MDEA), triethanolamine (TEA) and diglycolamine. When it exposed to CO_2 gas, two primary or secondary amine groups react with a CO_2 molecule to form carbamide and

ammonium, or single tertiary amine group reacts with a CO_2 and water molecule to form bicarbonate and ammonium ion (Figure 8). The capture of CO_2 is based on strong chemical interaction between amine group and CO_2, therefore it could adsorb 20-40 wt% of CO_2 of low concentration from flue gas.[21] However, wide implementation of the technology is hindered by the costs for installation and utilization, energy loss from the capture process, and corrosive nature of amine solution. As a solid sorbent material, zeolite 13X uptakes 3.5 mmol g^{-1} (~15 wt%) of CO_2 at 0.15 bar.[22] However, the adsorption of CO_2 is hindered by H_2O adsorption and it requires high regeneration temperature of 135 °C. New technologies which are able to overcome the problems of cost, maintenance, and efficiency have to be developed.

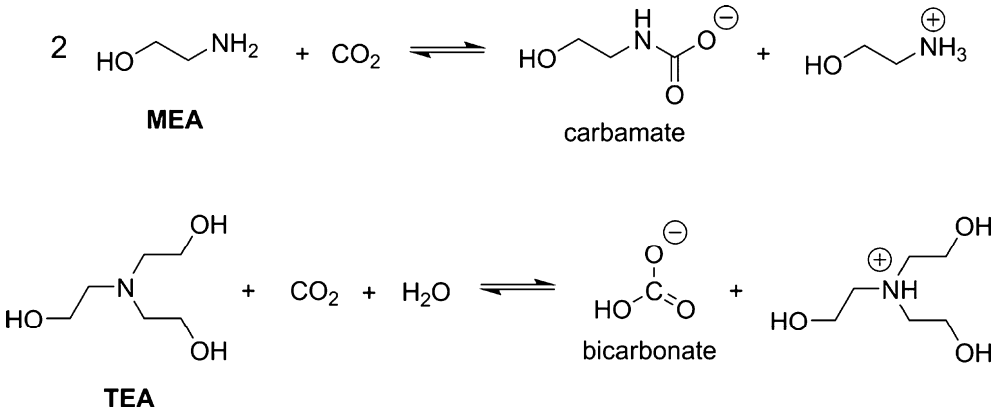

Figure 8 Reaction of monoethanolamine (MEA) and triethanolamine (TEA) with CO_2.[14]

Needs for more energy and cost effective processes forced the development of various technologies of gas separation materials (Figure 9).[12] Ionic liquids, enzymatic membranes, chemical looping, metal-organic frameworks, ceramic

autothermal recovery, oxygen transport membranes and ion transport membranes are such materials designed to separate gas mixtures of CO_2/CH_4, CO_2/H_2, CO_2/N_2, or O_2/N_2.

Metal-organic frameworks, abbreviated to MOFs, are the highly adaptable materials to satisfy the criteria for solid based adsorbents, because the organic ligand in the structure can be modified by highly developed technologies of organic synthesis. For example, extension and functionalization of an organic building block can result in a new MOF with increased pore size and functional groups on the surface. Therefore, capacity and adsorption selectivity can be finely adjusted by 1) making a prototype networks with simple building blocks, 2) preparing a newly modified organic ligand according to a purpose, and 3) synthesizing a new MOF having the same connectivity with the prototype network using the ligand. Stability of the MOF is depends on the strength of the metal-ligand coordination bond and the stability of the organic ligand itself. Kinetics of adsorption using the MOF is normally fast because the adsorption is based on physical adsorption. The major obstacles for the MOF are the high cost for synthesis and the weak stability. Although there are several problems to overcome, the MOF is the most viable option for capture CO_2 using a solid sorbent system.

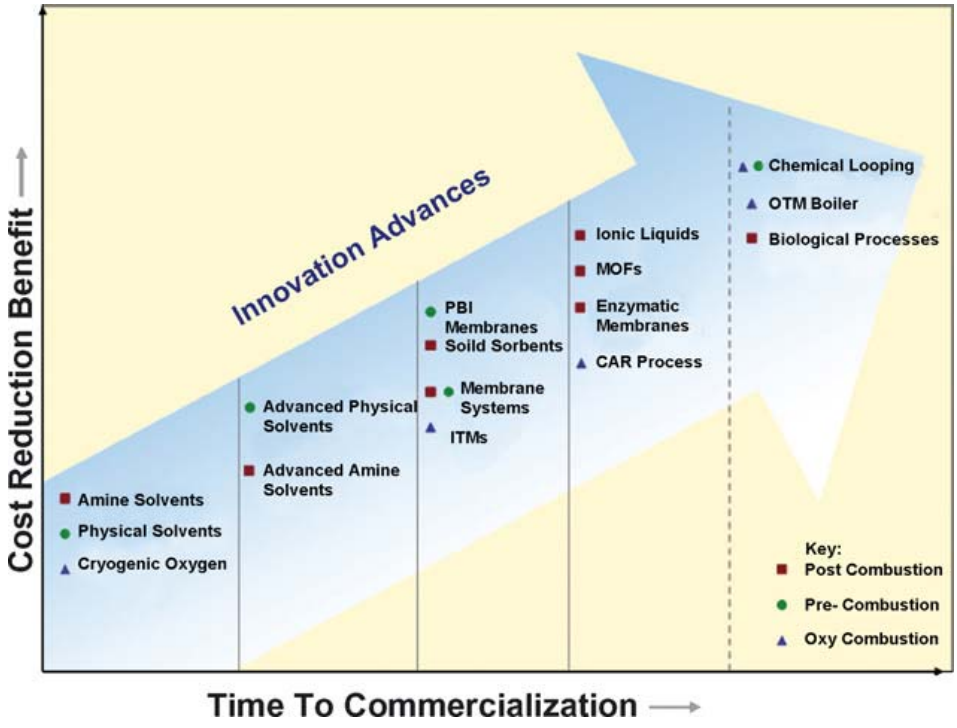

Figure 9 Schematic diagram of a blueprint of CO_2 capture technologies. (PBI = polybenzimidiazole; ITM = ion transport membrane; MOF = metal-organic framework; CAR = ceramic autothermal recovery; OTM = oxygen transport membrane).[12]

I.1.2. Metal-organic frameworks (MOFs)

A MOF is a coordination compound extending in 1, 2 or 3 dimensions with organic ligands containing potential voids (Figure 10).[23] Various combinations of metal species and organic ligands can result in numerous kinds of new MOFs, enabling us to examine various chemistries in them. A MOF are synthesized by self-assembly. A conventional procedure of synthesizing a MOF is to heat up the solution containing a metal salt and a neutral organic ligand for several hours to days. There are a numerous ways of synthesizing a MOF. The morphology and size of a MOF can be controlled by adding mineralizer, precursor, or applying different ways of applying energy such as microwave, ultrasound, ball-milled physical energy, electronic energy.[24] Due to the MOF has high surface area, well defined pore size, and chemically tunable pore surface, it could be applied as a material for gas storage/separation/purification,[14,25–27] as a sensor,[28] or as a heterogeneous catalyst.[29]

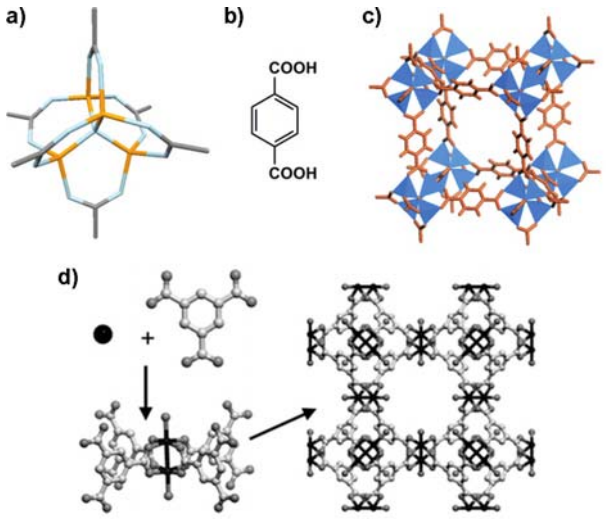

Figure 10 6-directional tetrahedral Zn_4O Metal cluster (a), terephthalate ligand (bdc, b), and assembled structure (MOF-5, c). Formation of Cu-paddlewheel cluster from Cu and btc ligand, and resulting HKUST-1 (d).[26,30,31]

I.1.2.1. Properties and analytic methods

A MOF is a crystalline compound having a high porosity filled with guest molecules. A number of techniques are used to analyze the properties of this kind of compounds.

1) **Structure:** A structure of a MOF is determined by solving an X-ray diffraction pattern. A crystal size of which is bigger than 0.1 mm is suitable for single crystal X-ray diffraction. After determining the structure of a single crystal, a powder X-ray diffraction (PXRD) pattern of bulk sample is compared with a simulated PXRD pattern from the X-ray structure to check the homogeneity of the sample. PXRD patterns of the sample in different conditions are also measured to confirm the maintenance of the phase of the sample. In the case of the size of crystals are too small, PXRD patterns can be used to obtain the X-ray structure.[32–34] Full structure solving from PXRD pattern have been successful only for the MOFs constructed from rigid building blocks. For a low resolution data, computer simulation can assist the positioning of organic ligands in the structure of the single-crystal diffraction pattern of a ligand extended structure.[35]

2) **Morphology:** Shapes, sizes, and colors of MOFs are visualized by a microscope. Color of a MOF is determined by its components, metal and ligand. For submicron size MOFs an electron microscope such as transmission electron microscope (TEM) and scanning electron microscope (SEM) is used to see the morphology of crystals.

3) **Guest assignment and chemical formula**: A MOF with narrow size channels, the positions and shapes of guest molecules in the structure can be assigned by X-ray

diffraction data. For a highly porous MOF, however, the guest molecules are randomly disordered. In this case, the species of guest molecules are determined by Fourier transform infrared spectroscopy (FTIR), and the amount of them are determined by elemental analyzer (EA) and thermogravimetric analysis (TGA). After the determination of the guest molecules, a complete chemical formula of a MOF can be provided.

4) **Porosity**: Surface area and pore volume of a MOF can be obtained by two ways using adsorption isotherm or crystallographic data. In the case of using adsorption isotherm, the isotherm data taken below the critical temperature can be used for calculation of surface area and pore volume. There are two models frequently used for calculation of surface area using N_2 adsorption isotherm at 77 K. One is Langmuir model, in which gas molecules adsorb on the adsorbent forming a monolayer on the surface, and the other one is Brunauer-Emmett-Teller (BET) model, which allows multilayer adsorption of gas molecules on the adsorbent surface. Both models are applicable to calculate surface area of a MOF, however, a MOF has big pores large enough to support multilayer, which means BET model is more favorable. The standard range for BET analysis is $0.05 < P/P_0 < 0.3$. Generally, saturation pressure range for microporous MOFs is well below the standard range. There are two criteria for calculation of BET model (1) the y-intercept of BET plot should has positive value. (2) The saturation range should be taken where $n_{ads}(1-P/P_0)$ is increasing as P/P_0 increases. The surface area of a MOF can also be calculated with crystallographic data. In a given structure, we can calculate a surface accessible to a probe molecule. The surface is called accessible surface. Accessible surface area is

proven to have similar value with the BET surface area if the structure is properly activated.[36] Pore volume is calculated by applying Saito-Foley (SF) method, Hovath-Kawazoe (HK) method, or density functional theory (DFT) and Monte Carlo method to adsorption isotherm depending on the sample. When a MOF doesn't adsorb N_2 at 77 K, Dubinin-Radushkevich (DR) method are used to calculate the surface area and pore volume using CO_2 adsorption isotherm at 195 K.

5) **Gas sorption properties**: Uptake capacities of single component gas are measured with adsorption isotherm instrument. There are two types of measurement: Gravimetric and volumetric. Gravimetric method directly measures weight of sample and adsorbed gas. A sensitive balance is required and buoyancy effect has to be considered. In volumetric method, pressure difference in confined volume of manifold is counted and converted to uptake amount. The uptake amount measured with the instrument is denoted as surface excess amount (N^{ex}), obtained from the excess density near the surface.[37] Therefore, total amount of adsorption is estimated by adding bulk gas stored in pore volume to excess amount (Equation 7). The bulk gas stored in pore should be considered for high pressure measurements and when a surface excess amount is very small.

Equation 7 $$N^{ads} = N^{ex} + \rho_{bulk} V_{pore}$$

To examine a MOF as a packing material for swing adsorption procedure, breakthrough experiment has to be done.[38–43] In this experiment, mixed gas passes through the column packed with a MOF and the eluent is analyzed by GC or mass

spectrum (Figure 11). The stronger the interaction between the MOF and gas species, the longer the retention time of the gas species. The retention time can be prolonged by the capacity of the MOF. Thermogravimetric analysis runs with alternating two gas types can also be used for this test.[44–47] This test is called gas-cycling experiment. 15% CO_2 in N_2 gas at ambient temperature is used for adsorption condition, and pure CO_2 gas under increased temperature is used for desorption condition. Pure CO_2 gas should be used for desorption condition to obtain pure CO_2 gas as a separation product.[47]

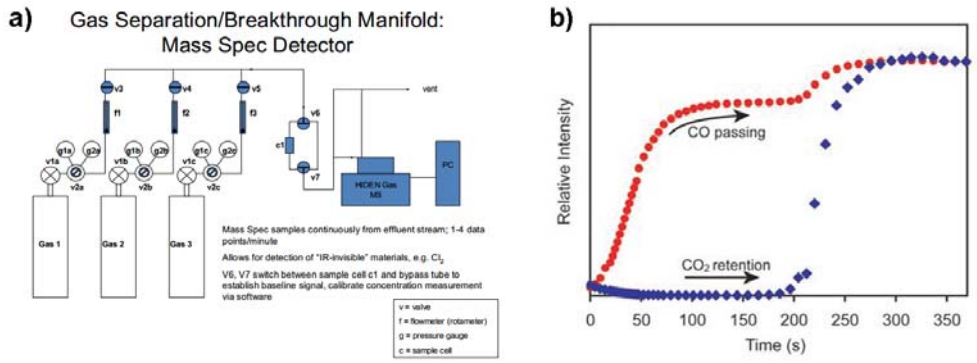

Figure 11 Instrument for break through experiment (a) and experimental data (b). Strongly interacting species have more long retention time.[48]

6) **Isosteric heat of adsorption**: Isosteric heat of adsorption (Q_{st}) is an important measure for determination of interaction strength between a MOF and adsorbed gas molecules. In the case of a MOF has low Q_{st} value, the adsorbate is hardly saturated at low partial pressure, while high Q_{st} value requires high temperature for reactivate the MOF. The value is calculated with multiple gas sorption isotherms, or it is directly measured with microcalorimeter attached to sorption instrument.[49,50] In case

of using gas sorption data, Clausious-Clapeyron equation (Equation 8) or virial equation (Equation 9 and Equation 10) is used.[14]

Equation 8 $$Q_{st} = -R\frac{\partial \ln P}{\partial (1/T)}\bigg|_n$$

Equation 9 $$\ln P = \ln N + \frac{1}{P}\sum_{i=0}^{m} a_i N^i + \sum_{j=0}^{m} b_j N^j$$ where a_i and b_i are virial coefficient

Equation 10 $$Q_{st} = -R\sum_{i=0}^{m} a_i N^i$$

7) **Stability**: Various stabilities including thermal stability, water stability, and chemical stability can be tested. Thermal stability is measured by Thermogravimetric analysis. Water and chemical stability is measured by immersing the MOF in the water or chemicals or by exposing the MOF to the water or chemical vapor, followed by PXRD measurement.

8) **Heterogeneity**: In some cases, a MOF contains multiple metal species and ligands.[46,51–54] Multiple metal species can be assigned by inductively charged plasma-atomic emission spectrometry (ICP-AES) of digested sample, and multiple ligand species can be assigned by ^{1}H NMR of digested sample or by ^{13}C CP MAS solid NMR. Homogeneity of the sample particles has to be checked by microscope image or PXRD pattern before analysis.

I.1.2.2. Synthetic strategies for MOFs

The synthesis of a new MOF is done by assembling the building blocks prepared with some specific strategies. The things to be considered when we synthesize a MOF are 1) surface area/pore size, 2) surface polarity/specific functional group, and 3) stability, and we can determine which metal or ligand to use according to them. Previously, researches have targeted a limitless increase of surface area and Q_{st} values. However, there are optimal values of surface area, pore size, and Q_{st} values depending on the running conditions.[18]

A synthesis of a new MOF is tried when we want to find a new way of network connectivity by introducing a new metal ion or a new ligand or when we want to see a new property of MOF originated from a new functional group. In the latter case, previously reported network connectivity can be referred.

1) **Selection of metal ions and donors:** Stability and crystallinity of a resulting MOF are affected by the choice of metal species and donor ligand which occasionally form metal clusters. Tetrahedral Zn_4O cluster and Cu-paddlewheel cluster are widely used in a number of researches due to their fine crystallinity.[26,30,55] The high charge of cations (Al^{III}, Cr^{III}, and Zr^{IV}) is known to form a highly stable metal cluster with carboxyl donor groups, but the crystallinity is bad to be analyzed by single crystal X-ray diffraction.[33,56–58] In addition, the coordination bonding between Zn and N in imidazole is known to be stable.[38,48,59]

2) **Selection of network**: Even though we don't know the structure of a resulting MOF before synthesis, we can predict it when we choose building blocks according

to a known network connectivity. For example, Zn and linear linker may result in MOF-5 like structures while Cu and triangular linker may result in HKUST-1 like structures (Figure 10).

3) **Ligand modifications**: There are two strategies of modifying the ligand: 1) extension of ligand to increase the porosity (Figure 12 and Table 2); and 2) attachment of a functional group to enhance the polarity of the surface or to introduce a specific property (Figure 13).

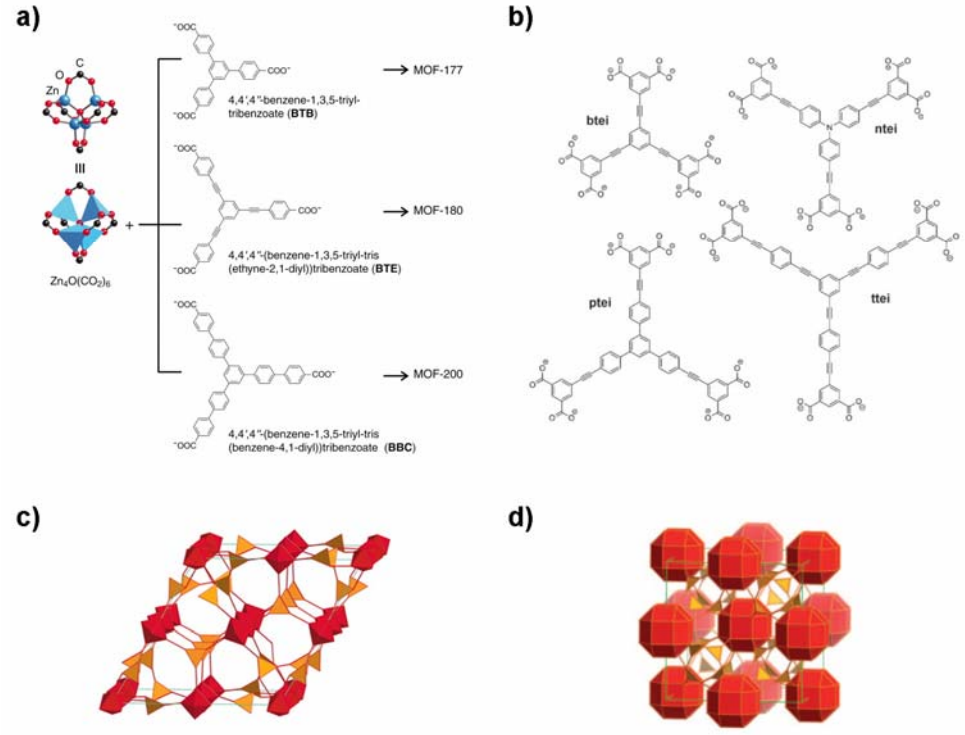

Figure 12 Elongation of ligands (a, b) and corresponding network types (c, d).[35,60]

Table 2 The surface area and pore volume of MOFs by ligand extension.

Network type	Ligand	MOF	Surface area [m^2 g^{-1}] (BET/Langmuir/Calc.)	Pore volume [cm^3 g^{-1}]	Ref.
qom	BTB	MOF-177	4500/5340/4740	1.89	35
qom	BTE	MOF-180	NA/NA/6080	NA	35
qom	BBC	MOF-200	4530/10400/6400	3.59	35
ntt	btei	PCN-61	3000/3500/3455	1.36	61
ntt	ntei	PCN-66	4000/4600/3746	1.63	61
ntt	ptei	PCN-68	5109/6033/3871	2.13	61
ntt	ttei	PCN-610 /NU-100	6143/NA/6515	2.82	61,62

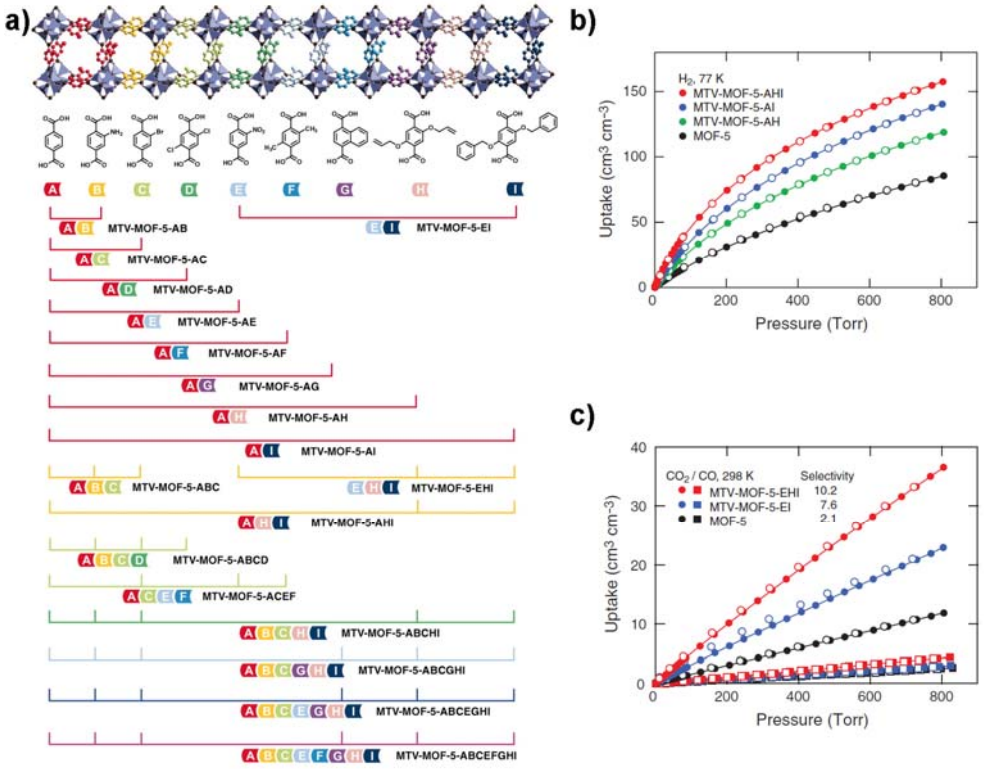

Figure 13 Variations of ligands and combinations of them in the same network structure (a). Differentiated H_2 (b), CO_2, and CH_4 (c) sorption properties by ligand variations.[63]

4) **Reaction conditions**: The controllable variables of a reaction are solvent, temperature, concentrations, ratio of metal/ligand, proton density of the solution, and heating method.

5) **Activation methods**: Heating-evacuation method is conventional way of removing guest molecules in a MOF. However, if the structure of a MOF is not maintained during the activation, freeze-drying[64] or supercritical CO_2 drying methods[65] are used. The MOF having exceptionally high surface area is known to be successfully activated only by the supercritical CO_2 drying.[35,61,66]

I.1.2.3. Flexibility of MOFs

The flexible nature of MOFs accompanied with guest removal and inclusion has been discovered since Suh and co-workers reported a 2D-bilayered structure that the distance between layers was dramatically changed by the guest exchange while maintaining its single crystallinity in 2002 (Figure 14).[67] The application of a flexible metal-organic framework as a CO_2 capture material has been extensively researched after the Férey group reported a breathing coordination polymer whose breathing effect was triggered by water vapor adsorption/desorption.[68] The strategy of capturing CO_2 by using flexible MOFs is based on the strong interaction between CO_2 gas and a framework, resulting in the transformation of a structure. Therefore, they show superior selectivity of CO_2 over non-polar gases like H_2, N_2, O_2, and CH_4, which are the major component of gases to be separated. However, polar gases like NO_x, SO_x, and water vapor are the potential inhibitor of reducing their performance.

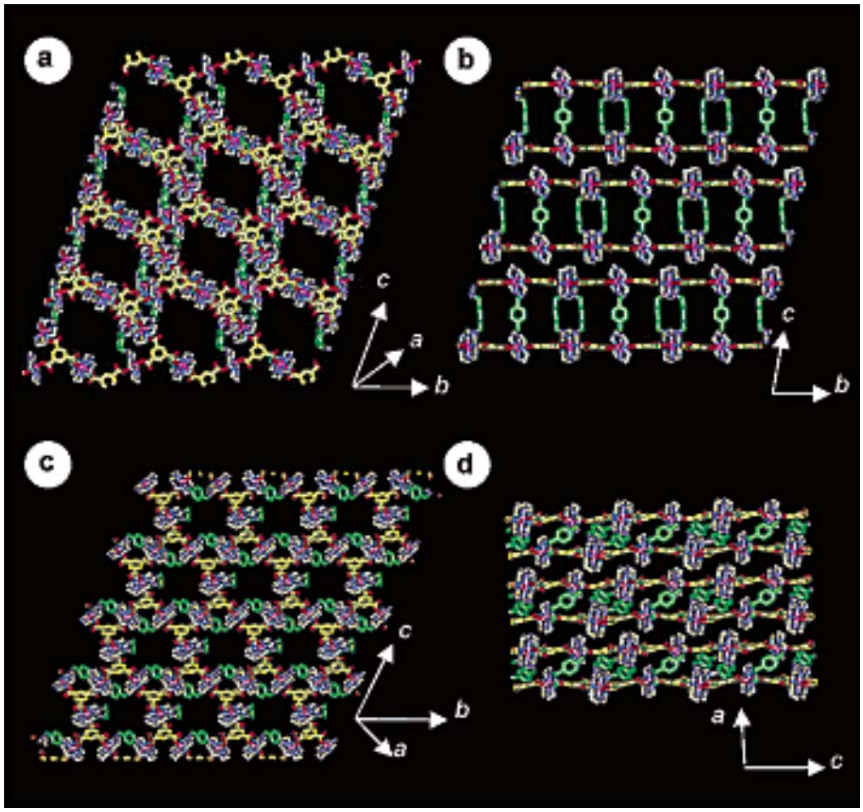

Figure 14 X-ray structures of BOF-1. Thickness of bilayer in as synthesized (11.91(1) Å in (a), (b)) structure is 1.7 times larger than that of desolvated (6.82(2) Å in (c), (d)) structure.

I.1.2.3.1. Analysis of flexible MOFs

The flexible nature of MOFs can be evidenced by X-ray diffraction. The most undoubted method is single-crystal-to-single-crystal transformation (SCSC). In this method, a single crystal is picked, and the x-ray diffraction patterns before and after a procedure are obtained from the single crystal.[45,69–72] In other cases, two different single crystals can be picked before and after a procedure and subjected to x-ray crystallography.[73] SCSC only indicates the former case under the strict definition;

however, the latter case is also accepted as SCSC. If the single crystallinity is not maintained during an experimental procedure or obtaining a single crystal of starting material itself is not available, powder x-ray diffraction is used for solving x-ray structures (Figure 15).[58]

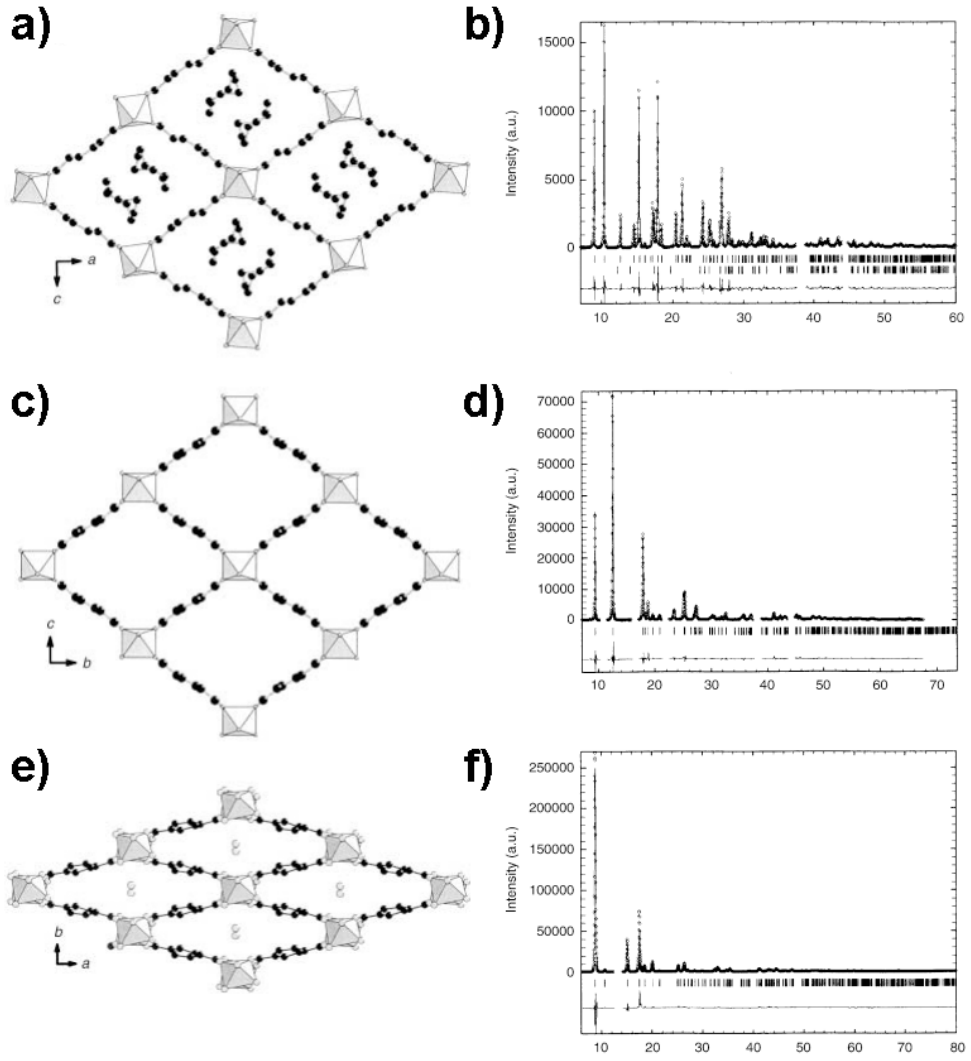

Figure 15 (a) Structure of MIL-53*as* and (b) its PXRD pattern. (c) Structure of MIL-53*ht* and (d) its PXRD pattern. (e) Structure of MIL-53*lt* and (f) its PXRD pattern.

A sorption isotherm provides an indirect evidence of flexibility of a MOF. A gate opening,[74,75] abrupt adsorption of guest molecules at specific pressure, or a stepwise gas sorption isotherm[68,76–78] suggests a presence of phase transition of an adsorbent (Figure 16). In case of structural change is undetectable by X-ray diffraction, sorption data can be suggested to rationalize the flexibility of the structure.[79,80] If the mobile part is the pendants in the rigid framework, the positions of pendants are obtained with high disorder.[81] For the MOF porosity of which is controlled by light source, a lamp attached sorption instrument has been used to record the effect of light during adsorption.

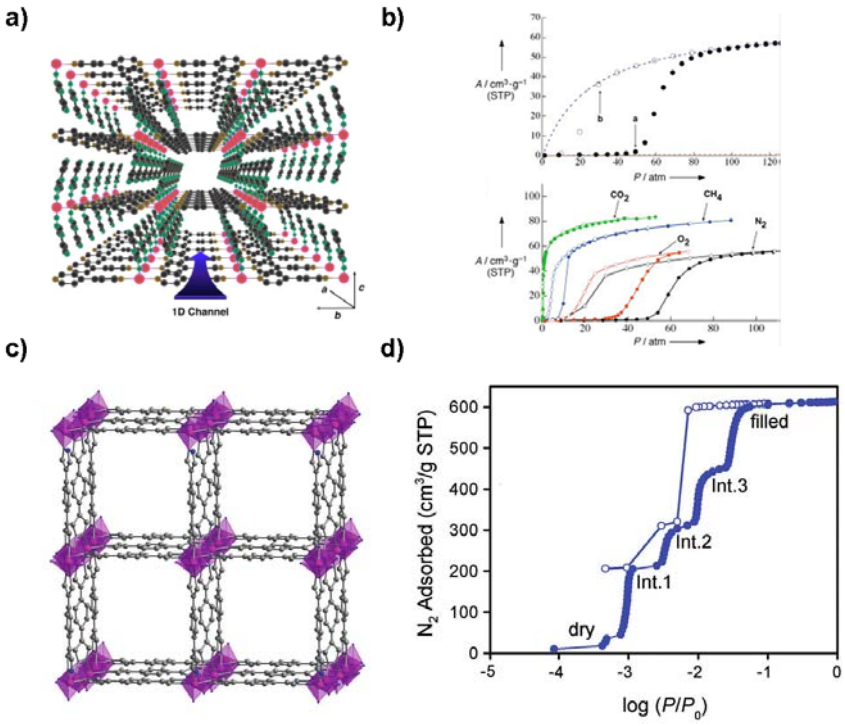

Figure 16 (a) Structure of interdigitated $[Cu(dhbc)_2(4,4'\text{-bpy})]\cdot H_2O$ and (b) its sorption properties showing gate openings. (c) Structure of flexible Co(1,4-benzenedipyrazolate) and (b) its sorption properties showing stepwise sorption.

I.1.2.3.2. Types of flexible MOFs

The flexibility of MOFs can be categorized by three types (Figure 17): One is the flexibility originated from metal cluster or ligand (Figure 17a); another is interpenetrated or interdigitated framework (Figure 17b); and the other is the framework with flexible arms (Figure 17c).

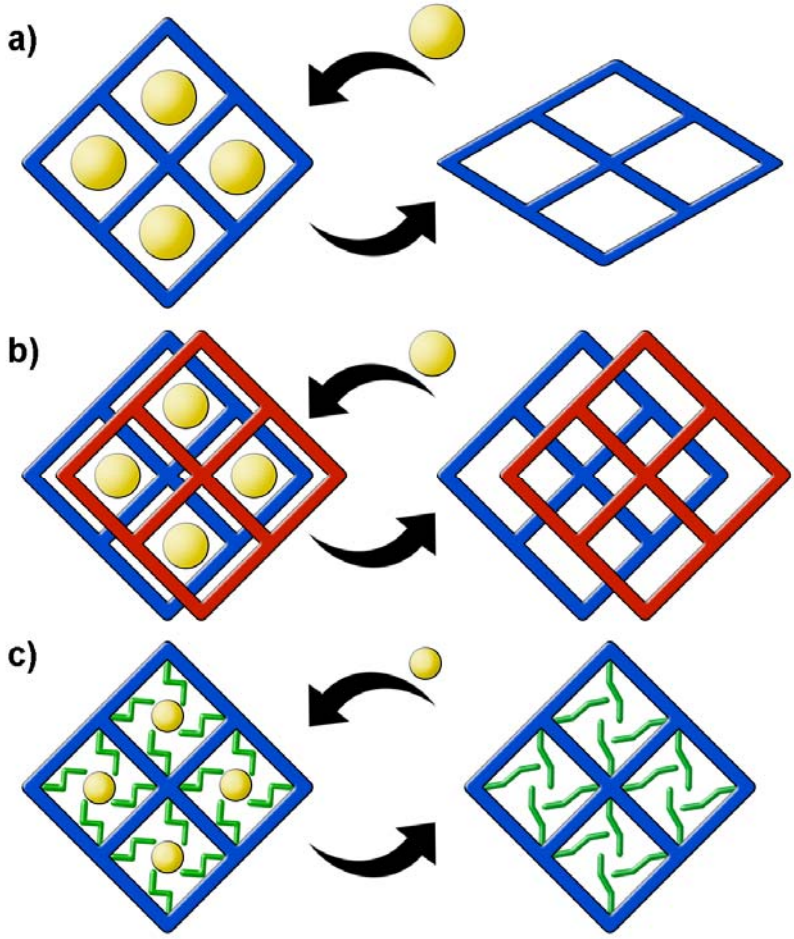

Figure 17 Schematic diagram of flexible networks. Color scheme: framework, blue and red; pendant, green; guest, yellow.

1) **Entire flexibility from building blocks**: The idea of using a flexible building block for making porous materials seems contradictory. Because rigid building blocks are often used for construction of MOFs to impose metastable porous structures in which the interaction between building blocks is minimized. In fact, there has been no paper reporting a porous MOF which is assembled from totally flexible building blocks. At least, a rigid phenyl ring is included in an organic ligand. Fine adjustment between rigidity and flexibility of a structure is necessary to build a flexible MOF with porosity. Flexible property of MOF can be originated from metal clusters or flexible organic ligands.

There are several MOFs such as MIL-53 (M = Cr, Al),[58,68,78,82,83] MIL-88,[84] M(BDC)dabco (M=Cu or Zn),[85–87] and Co(1,4-benzenedipyrazolate)[88,89] that showing their flexibility originated by metal cluster. In order to be a flexible metal cluster, it should possess a mirror plane with the ligand in symmetrical position towards it (Figure 18).[90] 1D-metal chain in MIL-53 and Co(1,4-benzenedipyrazolate), M^{II}_2-paddlewheel cluster in M(BDC)dabco, and M^{III}_3O cluster in MIL-88 all are satisfying this condition. Zn_4O cluster which is octahedral cluster as M^{III}_3O cluster doesn't have such mirror plane, and therefore it's not flexible.

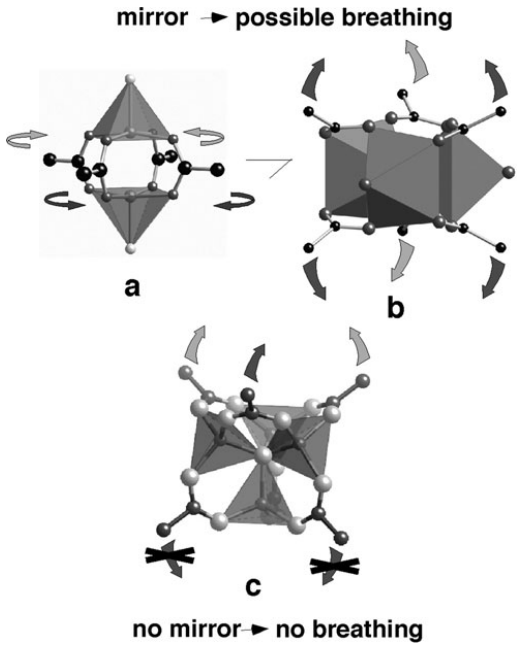

Figure 18 A condition for metal cluster to have flexible property.[91]

MIL-53, whose flexible nature is extensively studied, possess a linear metal cluster (Cr or Al) connected by terephthalate to form rhombic channels (Figure 19).[78] It exhibits two-stepwise CO_2 adsorption while typical single step adsorption was obtained from CH_4. The samples undergo a "breathing type" mechanism by the hydroxyl group in the metal cluster interacts with CO_2 to cause a shrinkage of the structure below 6 bar (narrow pore, NP), followed by the reopening of the structure under high pressure up to a maximum filling (~10 mmol/g) of the tunnel (large pore, LP) at 298 K.[92] CO_2/CH_4 mixture gas system has also been tested.[83] In CH_4-rich mixture (CO_2:CH_4 = 1:3), LP form is always maintained as pure CH_4 case. The transform of LP form to NP form was observed from equimolar mixture and CO_2-rich mixture (CO_2:CH_4 = 3:1). The transition of the structure was totally controlled by the partial pressure of CO_2 while that of CH_4 affected the extent of the transition.

Experimental data suggest that CH_4 is not adsorbed in NP structure filled with CO_2 in accordance with molecular simulations.

Effect of organic linker on phase transition of MIL-53 type MOFs has been studied.[93,94] Amino-MIL-53(Al) has polar amine functional group attached on aromatic ring.[95] This amine group interacts with CO_2 strongly in NP form to require higher pressure for structural transformation to LP form. Another aspect given by amine group is reduced apolar adsorption sites for CH_4, which is essentially non-adsorbed at pressure below 2 bar. A series of flexible solids of the MIL-53(Fe) type modified by introducing amine, carboxylate, halide, and methyl groups has been investigated for the effect on CO_2 adsorption.[96] The solids bearing functional groups which could potentially lead to strong interactions with CO_2 ($-CO_2H$, $-NH_2$) were found to remain in their nonporous CP (closed pore) forms under the investigated conditions, because of strong intra-framework interactions favoring the pore closure. In contrast, the MIL-53(Fe)–X (X = -Cl, -Br, $-CH_3$) solids adsorb a significant amount of CO_2 with a flexible character (CP/NP and NP/LP transitions). These functional groups do not directly interact with the CO_2 molecules, but allow modulation of the interactions between the guest molecules and the inorganic μ_2-OH groups.

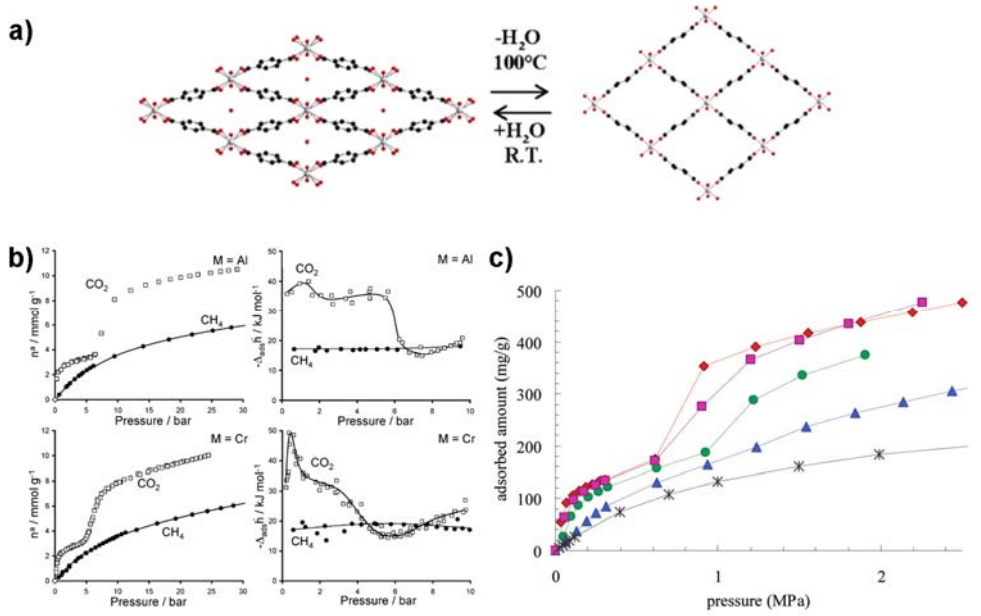

Figure 19 Structure and breathing phenomenon of MIL-53 (a). CO_2 and CH_4 gas adsorption isotherms of MIL-53 (Cr or Al) and isosteric heat of adsorption (b). CO_2/CH_4 mixture gas adsorption isotherms of MIL-53 (Cr) (c). The ratio of CO_2:CH_4 are 100:0 (◆), 75:25 (■), 50:50 (●), 25:75 (▲), and 0:100(Ж).[78,83]

A coordination bond formed between a single metal and a ligand also has flexible nature. [Zn(pydc)(DMA)] (pydc = 3,5-pyridinedicarboxylate), a MOF assembled from a single Zn unit and a rigid ligand form a non-interpenetrating (10,3)-a topology possess narrow one-dimensional channels, which is flexible enough to show guest-dependent breakthrough-like adsorption.[97] $[Cu(Hoxonic)(bpy)_{0.5}]_n \cdot 1.5nH_2O$ (2⊃H_2O) (H_3oxonic: 4,6-dihydroxy-1,3,5-triazine-2-carboxylic acid; bpy: 4,4'-bipyridine) is based on 2D layers of octahedral copper(II) ions bridged by Hoxonic ligands, further pillared by bpy spacers.[98] The resulting 3D network possesses small hydrated cavities. In spite of the lack of a

porous structure, this material is able to readily and selectively incorporate guest molecules. The guest uptake is facilitated by increasing the thermal energy of both the guest and the framework. Thus, both N_2 at 77 K and CO_2 at 195 K are not incorporated, and CH_4 is only minimally adsorbed at 273 K and 25 bar. By contrast, CO_2 is readily incorporated up to 2.5 mmol g^{-1} at 273 K and 25 bar. $[Zn_2(bpdc)_2(bpee)]$ (bpee = 1,2-bis(4-pyridyl)-ethene) exhibits 3D network by connecting 2D layers, assembled with Zn^{II} and $bpdc^{2-}$ ligand, with bpee pillars (Figure 20).[99] With a gas mixture of 20% CO_2 and 80% air, the CO_2/N_2 separation ratio reaches to 84 at 50 °C. Compared to $[Zn_2(bpdc)_2(bpee)]$, $[Zn_2(bpdc)_2(bpe)]$ was constructed using bpe (bpe = 1,2-bis(4-pyridyl)-ethane) as a pillar rather than bpee.[100] In this case, effect on flexible nature of the MOF from flexible organic pillar reflected to gas-adsorption property. Due to the similar structures, the total uptake amounts of CO_2 at 298 K and 1 bar are similar each other, but one more step around 0.7 bar is observed for $[Zn_2(bpdc)_2(bpe)]$.

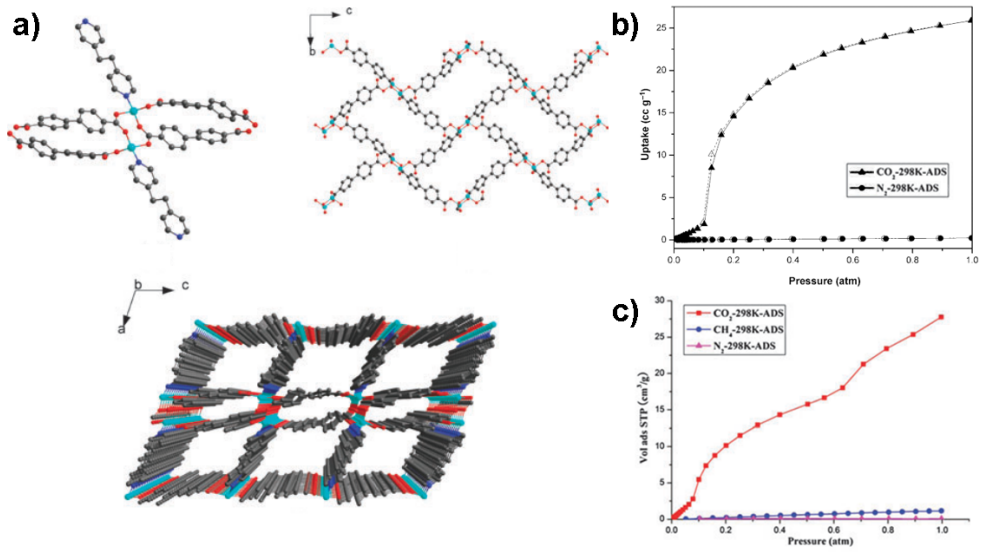

Figure 20 X-ray Structure of $[Zn_2(bpdc)_2(bpe)]$ (a), and CO_2, CH_4, and N_2 adsorption isotherms of $[Zn_2(bpdc)_2(bpee)]$ (b) and $[Zn_2(bpdc)_2(bpe)]$ (c) at 298 K. The structure of $[Zn_2(bpdc)_2(bpee)]$ is isostructural as $[Zn_2(bpdc)_2(bpe)]$.[101,102]

If an organic ligand has a bent part, that part may cause a transformation of a structure by rotational motion. Ethylene ($-CH_2-$), secondary amine (-NH-) and ether (-O-) are representative examples of a bent part. Many organic ligands known as flexible ligands include this kind of connections and they are shown in Table 3. To design a ligand for a MOF having both porosity and flexibility, it is critical to adjust the ratio of bent part in the ligand. For common porous MOFs, donor groups of their ligand are separated by straight spacers such as para-substituted benzene or acetylene functional group to make an empty space between metal ions or metal clusters. As bent parts introduce into a ligand, the void space inside the resulting structure is minimized by the ligand folding. Then, the structure is able to have a flexible character at the expense of losing its porosity. As an extreme example, alkanedioic

acid is a ligand that has two donor groups connected by bent methylene groups. This ligand is too flexible to construct a porous structure. Therefore, a ligand for a flexible and porous MOF should be mainly composed of straight parts with a sparse distribution of bent parts.

Table 3 Ligands with flexible joints

type	ligand	ref
-CH_2-	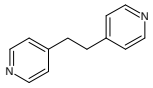 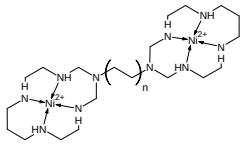 n = 1,2	102,103
-CH_2-, -NH-	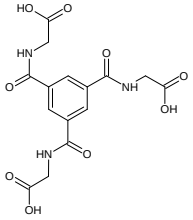	104
-CH_2-, -O-	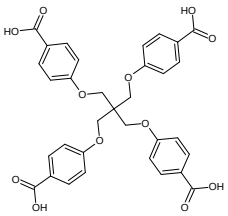	105
-NH-	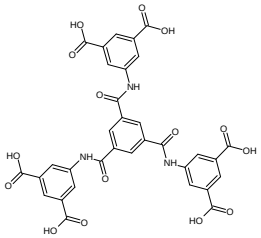 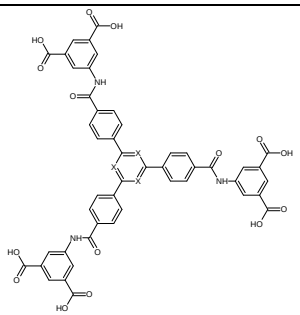 X = C or N	106,107
-O-	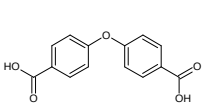 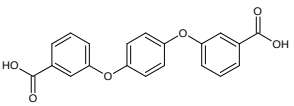	108,109

Two coordination polymer networks, SNU-M10 and SNU-M11 published by Suh and co-worker provide an effect of the length of flexible part on gate opening effect.[103] The extension of flexible alkyl pillar from ethyl to butyl in SNU-M10 and SNU-M11, respectively, does not provide an extended surface area. The CO_2 adsorption isotherms of both networks show gate-opening phenomena and large hysteretic desorption. The gate-opening pressure for SNU-M10 is lower than that for SNU-M11 at the same temperature, indicating the higher flexibility of the ethyl pillars than the butyl pillars.

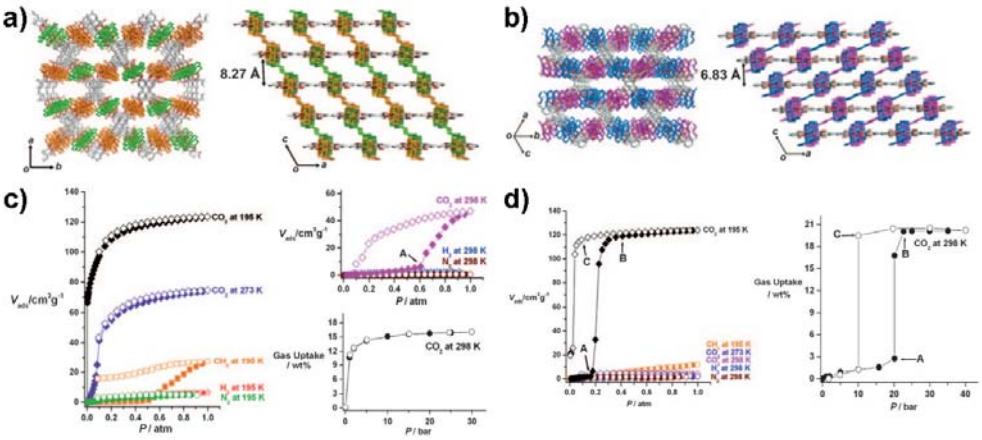

Figure 21 Structure of SNU-M10 (a) and SNU-M11 (b). 2D layers constructed with Ni-macrocycle and BPTC ligand are connected by alkyl pillars connecting two Ni-macrocycles. Gas sorption data of SNU-M10 (c) and SNU-M11 (d).[103]

2) **Interpenetrated/interdigitated structure**: Interpenetrated/interdigitated structures show flexible nature by changing distance between sub-structures upon the introduction or removal of guest molecule. An interdigitated structure, $[Cu(dhbc)_2(4,4'\text{-bpy})]\ H_2O$, possess microporous 1D channels along the *a* axis with a

cross section of 3.6 × 4.2 Å.[110] These channels are closed by activation, but opened by various guest molecules. The gate-opening pressures for N_2, O_2, and CO_2 are 50, 35, and 0.4 atm, and the gate-closing pressures are 30, 25, and 0.2 atm, respectively.

The distance between cationic interpenetrated networks can be changed by exchanging anion (Figure 22).[111] A microporous two-fold network $[[Ni(bpe)_2(N(CN)_2)](N(CN)_2)(5H_2O)]_n$ has $N(CN)_2^-$ anions in the structure some of them are used as building block while the other present as free anion. The N_3^--exchanged framework leads to a dislocation of the mutual positions of the two interpenetrating frameworks, resulting in an increase in the effective pore size in one of the counterparts of the channels and a higher accommodation of adsorbate than in the as-synthesized framework. It is interesting to note that CO_2 adsorption was carried out by the N_3^- exchanged framework, which shows that about 10 ml g^{-1} more CO_2 is adsorbed compared with the as-synthesized $N(CN)_2^-$ anion compound, corroborating the increase in the effective pore size or the framework's permanent porosity.

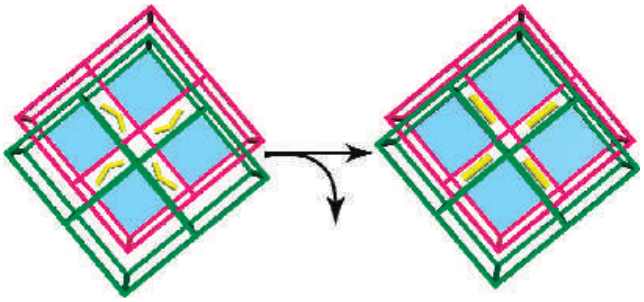

Figure 22 Distance adjustment between interpenetrated frameworks can be adjusted by anion exchange.[112]

3) **Flexible pendants**: Attaching flexible pendant onto the structure is also valid strategy for increasing selectivity of the CO_2 over non-polar gases regardless of the rigidity of the framework. Fischer group published series of papers about the control of the gate opening of the framework by addition of flexible pendants (Figure 23).[113–115] By using Zn-paddlewheel connected by BDC-derivative ligand and dabco pillar, the resulting structure $[Zn_2(fu\text{-}bdc)_2(dabco)]_n$ can transform from large pore (lp) form to narrow pore (np) form or reversely. This "breathing" behavior can be triggered in response to polar guest molecules (DMF, CO_2) while nonpolar guest such as N_2 are barely adsorbed and do not trigger the structural transitions. The substitution pattern of the linker and also the bulkiness and chemical nature of the substituents affect the structure of the narrow pore phase and thus the responsive behavior of the framework. If the linker is substituted in position 2 and 3 the structural flexibility of the respective pillared-layered MOF is drastically reduced, when compared to the corresponding 2,5-disubstituted derivatives. Substituents that are sterically less demanding and/or possess functionalities with a stronger interaction potential provoke a more drastic contraction of the framework.

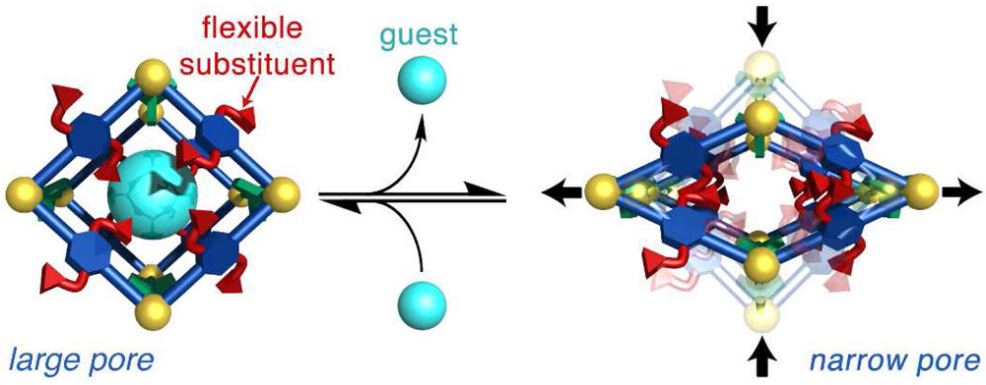

Figure 23 Phase transition of flexible MOF is adjusted by flexible pendants.[116]

3D pillared-layer coordination polymer $[[Cd_2(pzdc)_2L(H_2O)_2]\cdot 5(H_2O)\cdot(CH_3CH_2OH)]_n$ (H_2pzdc: 2,3-pyrazinedicarboxylic acid; L: 2,5-bis(2-hydroxyethoxy)-1,4-bis(4-pyridyl)benzene) with a specifically designed pillar ligand (L) exhibits three specific properties (Figure 24).[117] First, the ligand in response to guest inclusion plays the role of a molecular gate with locking/unlocking interactions. Second, the framework flexibility allows for the slippage of the layers, and finally, the removal of the water ligand provides an unsaturated metal site accessible by guest molecules. The framework clearly shows reversible single-crystal-to-single-crystal transformations in response to removal and rebinding of guest molecules, involving mainly rotation of pillars and slippage of the layers. The structure of dried form, $[Cd_2(pzdc)_2L]_n$, has no void volume and no water ligands. Interestingly, the adsorption isotherm of water for dried structure at 298 K exhibits three distinct steps coinciding with the framework functions. $[Cd_2(pzdc)_2L]_n$ favors the uptake of CO_2 (195 K) over N_2 (77 K) and O_2 (77 K).

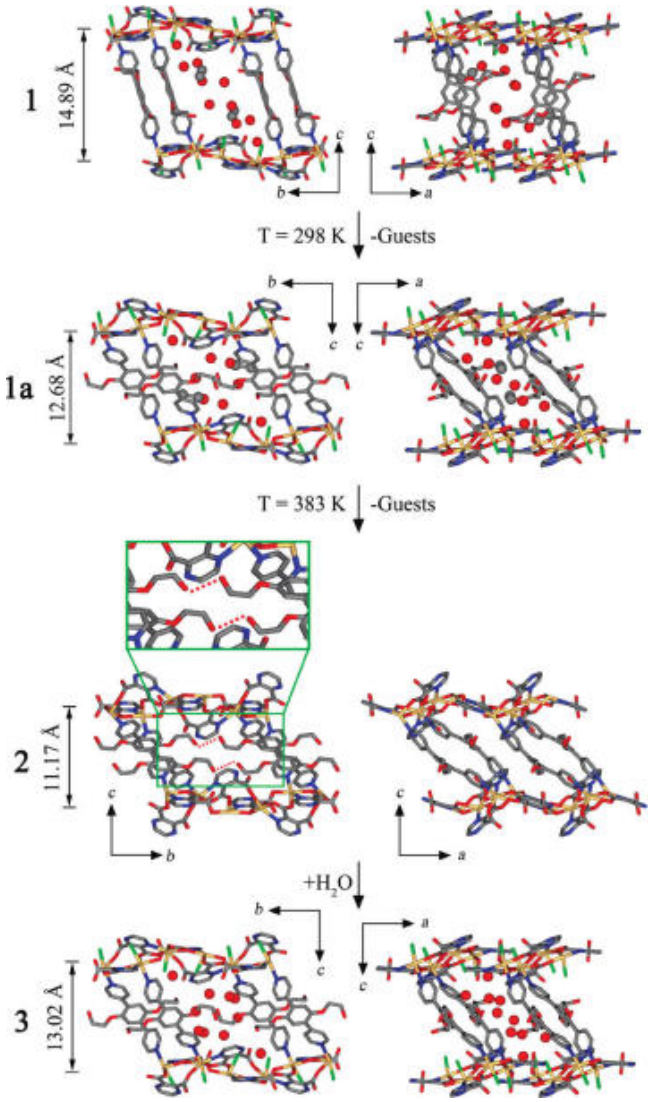

Figure 24 In the desolvated structure (2), hydroxyl pendants acts as interlocked gates. As guest molecules introduces, hydrogen bonding between pendants are broken and further introduction of guest molecules induces the expansion of layer distances. [117]

A MOF, PCN-123, for reversible alteration of CO_2 upon photochemical or thermal treatment has been discovered (Figure 25).[81] An azobenzene functional group, which can switch its conformation upon light irradiation or heat treatment, has been

introduced to the organic linker of a MOF. The resulting MOF adsorbs different amount of CO_2 after UV or heat treatment. The freshly made PCN-123 adsorbs a significant amount of CO_2 but a negligible amount of N_2. Upon light irradiation, the total uptake of CO_2 decreased readily due to the change of conformation of the azobenzene groups inside the pores of the MOF. The adsorbent returns to its original state when allowed to stay at ambient conditions for a prolonged period of time or with gentle heating.

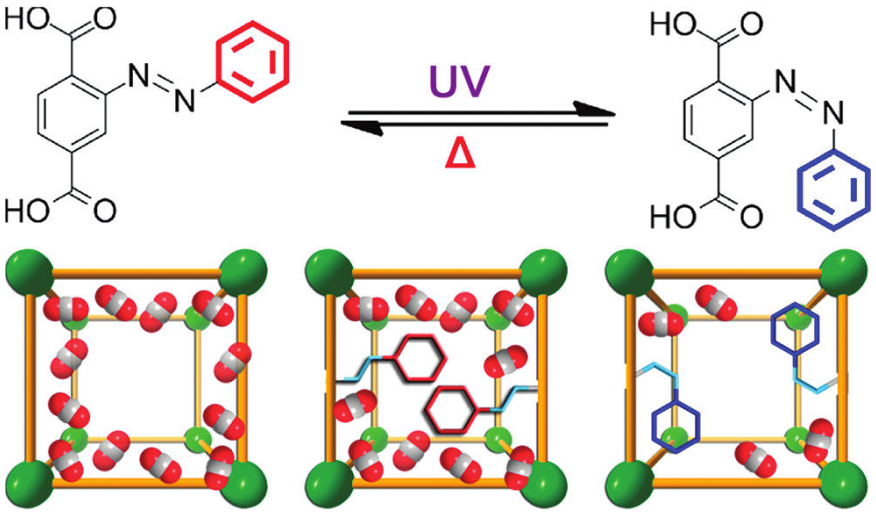

Figure 25 Control of azobenzene pendants in the pore stimulated by light and heat.[81]

I.2. Experimental Section

General Method. All chemicals and solvents used in the synthesis were of reagent grade and used without further purification. Infrared spectra were recorded with a PerkinElmer Spectrum One FT-IR spectrophotometer. Elemental analyses were performed with a PerkinElmer 2400 Series II CHN Analyzer. NMR spectra were measured on a Bruker Advance DPX-300. Thermogravimetric analyses (TGA) and differential scanning calorimetry (DSC) were performed under N_2 (g) at a scan rate of 5 °C min^{-1}, using a TGA Q50 and a DSC Q10 of TA Instruments, respectively. Powder X-ray diffraction data were recorded on a Bruker New D8 Advance diffractometer at 40 kV and 40 mA for Cu Kα (λ = 1.54050 Å), with a scan speed of 0.5s per step and a step size of 0.02º in 2 θ.

Preparation of 1,1'-[benzene-1,4-diylbis(oxy)]bis(3-methylbenzene).[118] To a mixture of m-cresol (24 mL, 0.23 mol) and KOH (12 g, 0.21 mol) heated at 200 °C for 10 min, were added 1,4-dibromobenzene (12 g, 0.05 mol) and copper powder (2.0 g, 0.03 mol). The reaction mixture was heated at reflux for 12 h to afford black oil, which was dissolved in ether (300 mL), washed with brine (200 mL × 3), dried over anhydrous $MgSO_4$, and concentrated under reduced pressure. Resulting yellow oil was purified by column chromatography (EA : hexane = 1 : 4.25), and the eluate was dried *in vacuo* to obtain white powder (5.7 g, 40%). δ_H (300 MHz; CD_2Cl_2) 2.37 (6 H, *s*, Me), 6.84 (2 H, *d*, Ph), 6.88 (2 H, *s*, Ph), 6.96 (2 H, *d*, Ph), 7.03 (4 H, *s*, Ph), 7.26 ppm (2 H, *t*, Ph).

Preparation of 3,3'-(1,4-phenylenebis(oxy))dibenzoic acid (H_2*mpm*-PBODB). Hot aqueous solution (50 mL) of $KMnO_4$ (12 g, 76 mmol) was slowly added to the pyridine solution (50 mL) of 1,4-bis(m-tolyloxy)benzene (3.0 g, 10 mmol). The reaction mixture was heated at 80 °C for 16 h. Brown MnO_2 was removed by filtration while hot, washed with hot water (50 mL), and the filtrate was completely evaporated under reduced pressure. Resulting white solid was dissolved

in water (100 mL), and conc. HCl was added to the solution until the pH became 1. White precipitate was collected by filtration, washed thoroughly with water (20 mL × 3), and dried under vacuum to yield white powder (1.8 g, 53%). FTIR (KBr pellet) ν_{max}/cm^{-1} 1686, 1611 (COOH); δ_H (300 MHz; d_6-DMSO) 7.13 (4 H, *s*, Ph), 7.31 (2 H, *d*, Ph), 7.47 (2 H, *s*, Ph), 7.51 (2 H, *t*, Ph), 7.71 (2 H, *d*, Ph), 13.14 ppm (2 H, *s*, COOH).

Synthesis of $\{[Zn_2(mpm\text{-PBODB})_2bpy]\cdot 3DMF\}_n$ (SNU-110). $Zn(NO_3)_2\cdot 6H_2O$ (150 mg, 0.50 mmol) and H_2*mpm*-PBODB (176 mg, 0.50 mmol) were dissolved in DMF (10 mL), and the solution was heated at 90 °C for 12 h. After the solution was cooled to room temperature, 4,4'-bpy (39 mg, 0.25 mmol) was added and then heated again at 90 °C for 48 h. The crystals formed were filtered off, washed with DMF, and dried briefly in air (160 mg, 53%). FTIR (Nujol mull) ν_{max}/cm^{-1} 1584, 1607 (Ph–O–Ph), 1644 (O–C=O), 1669 (C=O(DMF)); elemental analysis found: C 58.76, H 4.20, N 5.91, calc. for $C_{59}H_{53}N_5O_{15}Zn_2$: C 58.91, H 4.44, N 5.82%.

Preparation of $[Zn_2(mpm\text{-PBODB})_2bpy]_n$ (SNU-110') by the supercritical drying method. Prior to drying, the mother liquor of as-synthesized **SNU-110**, was decanted and the crystals were washed briefly with DMF (15 mL × 3). The crystals were placed inside the supercritical dryer together with the solvent and the drying chamber was sealed. The temperature and pressure of the chamber were raised to 40 °C and 200 bar with CO_2, above the critical point (31 °C, 73 atm) of CO_2. The chamber was vented at a rate of 5 mL min^{-1} and then filled with CO_2 again. The cycles of refilling with CO_2, pressurizing, and venting were repeated for 4 h. After drying, the closed container with the dried crystals (**SNU-110'**) was transferred to a glove bag filled with Ar gas to prevent exposure of the crystals to air. The gas sorption isotherms were measured without further activation. FTIR (Nujol mull) ν_{max}/cm^{-1} 1570, 1610 (Ph–O–Ph), 1632 (O–C=O); elemental analysis found: C 60.64,

H 3.19 N 3.10. calc. for $C_{59}H_{53}N_5O_{15}Zn_2$: C 61.06, H 3.28, N 2.85.

Low-Pressure Gas Sorption Measurements. The gas adsorption-desorption data were measured by an automated micropore gas analyzer Autosorb-1 or Autosorb-3B (Quantachrome Instruments). All gases used were of 99.9999% purity. Sample was activated by supercritical CO_2 as described above and transferred to a gas sorption cell in a glove bag filled with Ar gas to prevent exposure to air. The N_2 gas isotherms were measured at 77 K, 195 K, and 298 K. The O_2 gas isotherms were measured at 77 K. The H_2 gas isotherms were measured at 77 K and 195 K, and the CO_2 and CH_4 gas sorption isotherms were monitored at 195, 231, 273, and 298 K at each equilibrium pressure by the static volumetric method. After gas sorption measurement, the weight of sample was measured again precisely. Surface area and pore volume were calculated from CO_2 adsorption/desorption data measured at 195 K using DR method, by taking the data in the range of P = 0.001 – 0.006 atm and P = 0.008 – 0.05 atm, respectively.

X-ray Crystallographic Analysis. A crystal of **SNU-110** was coated with paratone-N oil and the diffraction data were measured at 95 K with synchrotron radiation (λ = 0.65000 Å) on an ADSC Quantum-210 detector at 2D SMC with a silicon (111) double crystal monochromator (DCM) at the Pohang Accelerator Laboratory, Korea. The ADSC Q210 ADX program[119] was used for data collection (detector distance, 62 mm; omega scan; $\Delta\omega$ = 1º, exposure time, 3.0 sec per frame), and HKL3000sm (Ver. 703r)[120] was used for cell refinement, reduction, and absorption correction. The crystal structure of **SNU-110** was solved by direct methods[121] and refined by full-matrix least-square refinement using SHELXL-97 program.[122] The hydrogen atoms were positioned geometrically by using a riding model. CCDC-885397 contains the supplementary crystallographic data for this paper. This data can be obtained free of charge from the Cambridge Crystallographic Data Centre via www.ccdc.cam.ac.uk/data_request/cif/.

Measurement of Powder X-ray Diffraction Data for [Zn_2(*mpm*-PBODB)$_2$bpy]$_n$ (SNU-110'). A sample was prepared in borosilicate glass capillary (diameter: 0.7 mm, wall thickness: 0.01 mm) and mounted on capillary station with rotation speed of 30 rpm. Powder X-ray diffraction data were recorded on a Bruker D8 Advance diffractometer with a Goebel mirror, selecting the Cu Kα (λ = 1.5418 Å; weighed average of Cu $K\alpha_1$ and Cu $K\alpha_2$ radiation), with a scan speed of 2 s per step and a step size of 0.02° in 2θ at 298 K.

Measurement of Powder X-ray Diffraction Data for [Zn_2(*mpm*-PBODB)$_2$bpy]$_n$ (SNU-110') under CO_2 pressure. Cold CO_2 gas stream was generated from dry ice and provided over the sample. Dry ice was placed beneath the sample holder to keep the temperature of the sample at 248 K. X-ray diffraction data were recorded on a Bruker New D8 Advance diffractometer at 40 kV and 40 mA for Cu Kα (λ = 1.54050 Å), with a scan speed of 0.5s per step and a step size of 0.02º in 2θ.

I.3. Results and Discussion

I.3.1. Design of a ligand

To change the distance between two donors in a linear ligand without breaking a parallel relationship of the two donors, there should be at least four bent parts (Figure 26). In this research, a *para*-substituted benzene group is used as spacer, and ether group and *meta*-substituted benzene group are used as bent part of a ligand (Figure 27). In the ligand, three benzene rings are connected in order of *meta*-, *para*-, and *meta*- (*mpm*-) substitutions. If we compare this ligand with an another ligand composed of same groups but in a different combination of *para*-, *para*-, and *para*- (*ppp*) substitutions, the distance of two carboxyl groups can change by 30% for a *mpm*-substituted ligand while there is negligible difference for a *ppp*-substituted ligand.

To test a porosity, a cavity structure is simulated by connecting 4 ligands and 4 Cu-paddlewheels to make square shaped pore, and rest Cu-paddlewheel sites are capped by 8 benzoates (Figure 28). The structure was simulated by Spartan software, and the rotational isomerization was done by manual rotation, followed by MM2 force field. In the case of four ligands were fully stretched, the size of the pore was 19.4 × 19.2 $Å^2$. When two opposite ligands were folded, the pore size was shrunken to 19.4 × 14.9 $Å^2$, and the size became 15.2 × 13.9 $Å^2$ as the whole four ligands were fully folded.

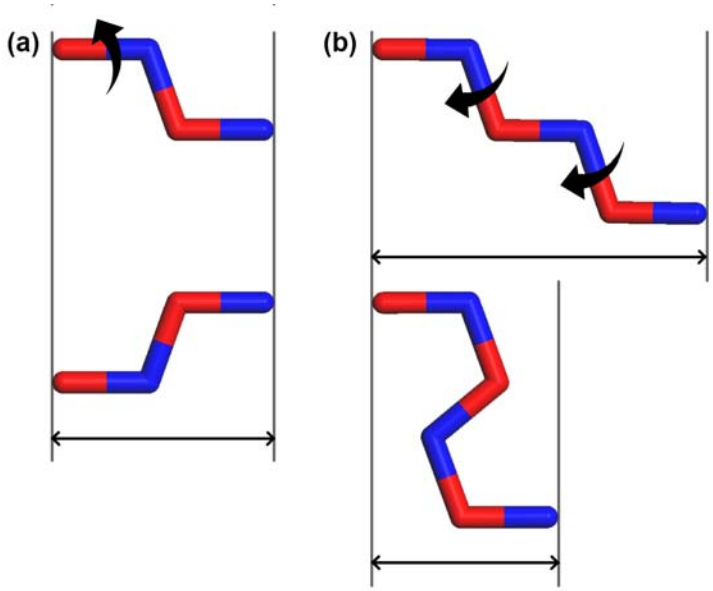

Figure 26 The minimum number of bent parts required for an organic ligand to stretch and to contract by rotational motions is four.

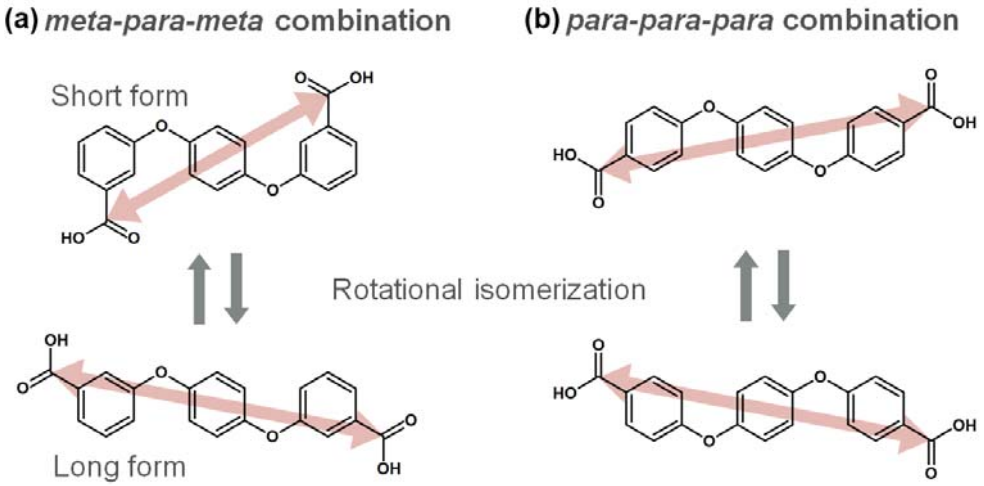

Figure 27 Design of an organic ligand with flexible joints: (a) 3,3'-(1,4-phenylenebis(oxy))dibenzoic acid (H_2*mpm*-PBODB) and (b) 4,4'-(1,4-phenylenebis(oxy))dibenzoic acid (H_2*ppp*-PBODB).

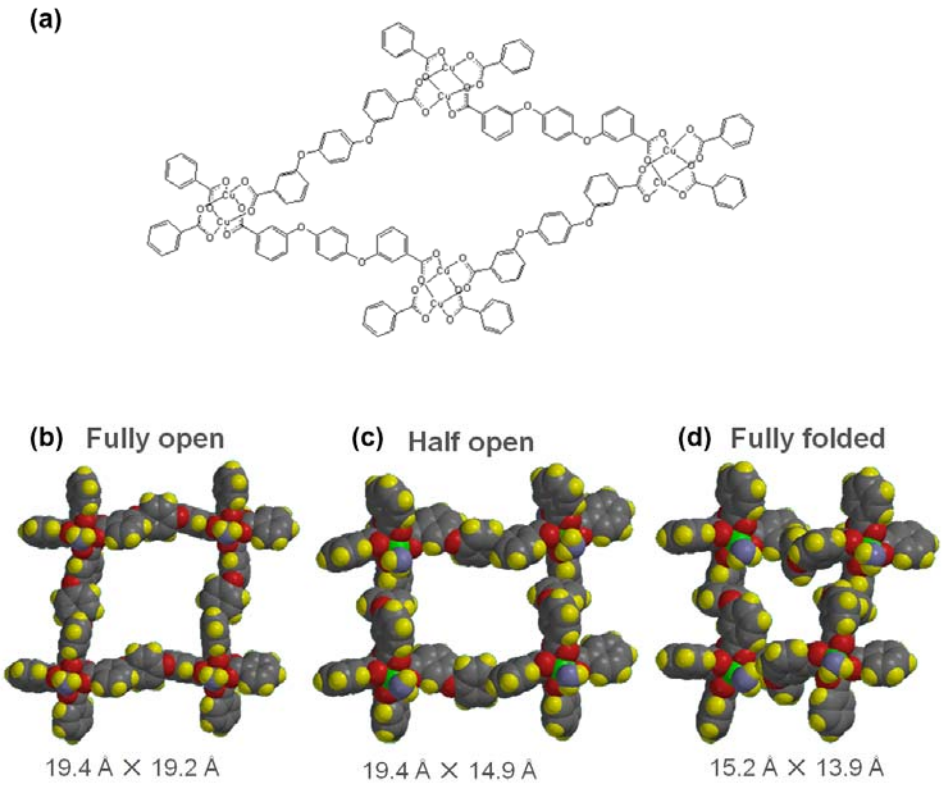

Figure 28 Computational simulation of resulting pores generated from *mpm*-PBODB ligands and Cu-paddlewheel clusters. (a) Schematic illustration. Residual coordination sites of Cu-paddlewheel are capped with benzoate. MM2 energy minimized structures of (b) fully open, (c) half open, and (d) fully folded.

I.3.2. Synthesis and structure analysis of **SNU-110** and **SNU-110'**

SNU-110 was synthesized from solvothermal reaction of 3,3'-(1,4-phenylenebis(oxy))dibenzoic acid (H_2*mpm*-PBODB, Figure 27) with $Zn(NO_3)_2 \cdot 6H_2O$ and 4,4'-bipyridine (bpy) in DMF. It is thermally stable up to 370 °C (Figure 29). In the X-ray crystal structure of **SNU-110**, two Zn^{II} ions form a paddle wheel cluster unit (Zn1 and Zn1a in Figure 30), each of which is connected by four *mpm*-PBODB ligands to construct a corrugated 2D layer extending along the $(10\bar{2})$ plane (Figure 31a). The 2D layers are further connected by bpy ligands along the [101] direction, since the axial sites of the paddle wheel units are coordinated with bpy ligands, which gives rise to a 3D framework generating 1D channels (Figure 31b and Figure 31c). The angle made between the corrugated 2D planes and the bpy pillar is 29.4°, although nearly right angle has been commonly made between the connecting pillar and the 2D layer constructed by the paddle-wheel type Zn_2 cluster units.[29] The 1D channels extending along the [101] direction have the rectangular cavities of effective size 4.4 × 3.7 $Å^2$, and they are filled with guest DMF molecules as characterized by IR, EA, and TGA data. There is a big difference in a pore size between simulated structure and obtained structure, because 1) the 2D plane structure was synthesized with the all ligands folded into a short form, and 2) the 2D planes stacked diagonally to reduce the size of the resulting channels. The solvent accessible volume estimated by PLATON is 30% of the structure (0.248 $cm^3\ g^{-1}$).[123] The crystallographic data for **SNU-110** is summarized in Table 4.

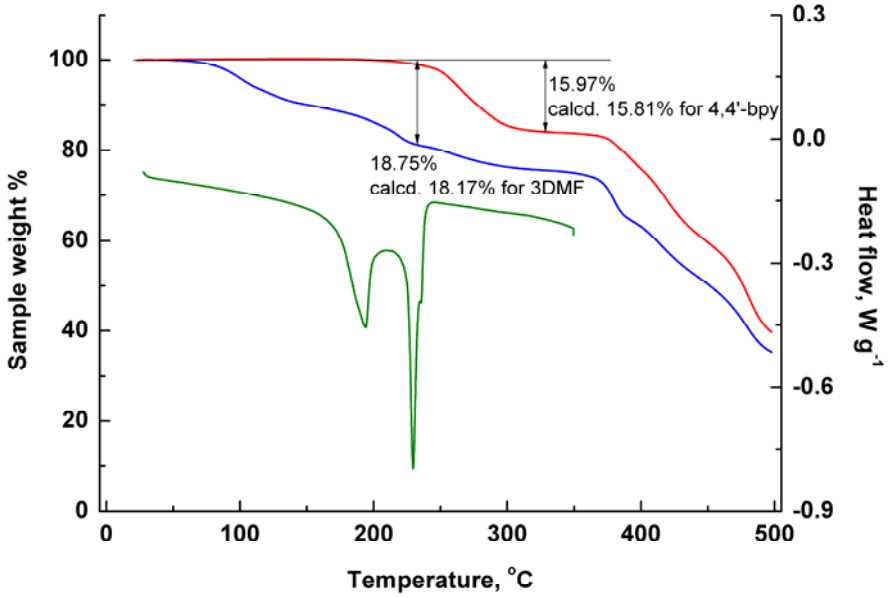

Figure 29 TGA/DSC trace for **SNU-110** (blue and green) and **SNU-110'** (red).

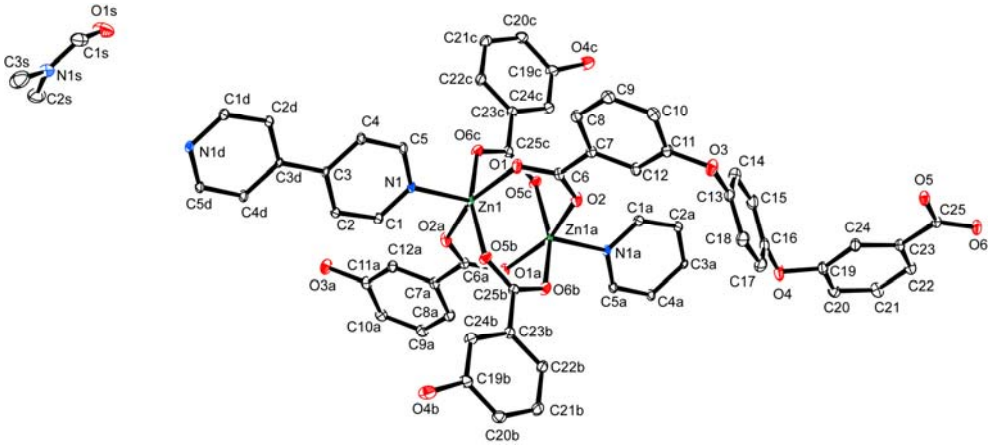

Figure 30 An ORTEP drawing of **SNU-110**, showing the coordination environment of Zn_2 paddle-wheel unit. Thermal ellipsoids are drawn with 30% probability. Symmetry transformations: a, -x+2, -y+1, -z+2; b, x-1, -y+3/2, z-1/2; c, -x+3, y-1/2, -z+5/2; d, -x+1, -y+1, -z+1.

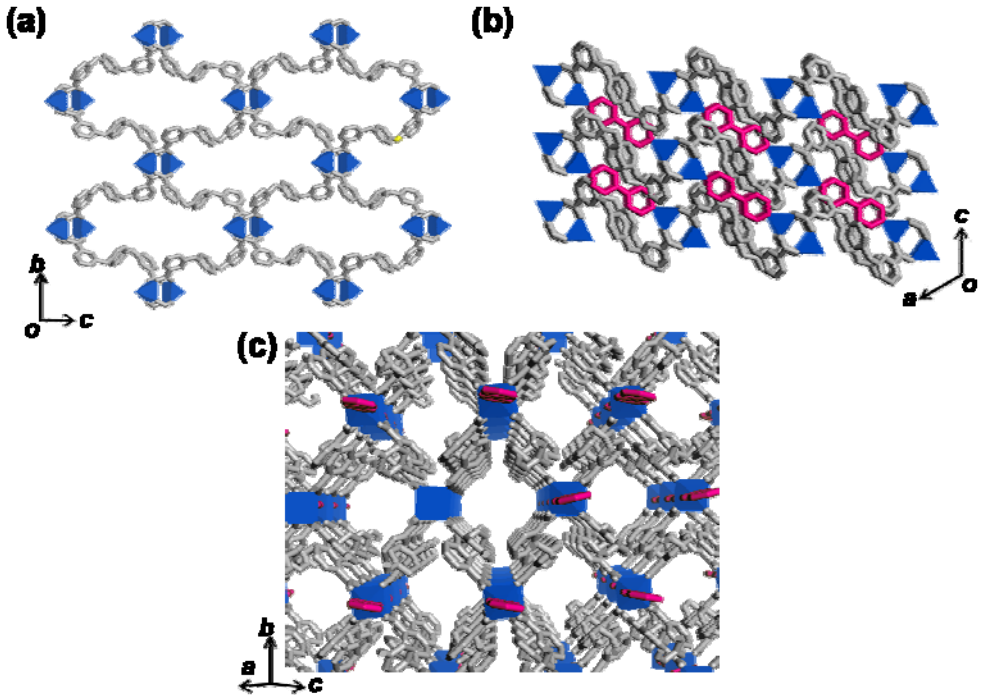

Figure 31 The X-ray structure of **SNU-110**. (a) A corrugated 2D layer formed of [Zn_2(*mpm*-PBODB)$_2$], running on the ($10\bar{2}$ plane). (b) A view seen on the (010) plane showing corrugated 2D layers connected by bpy pillars. (c) A view seen along the [101] direction showing 1D channels. Color scheme: Zinc, blue; *mpm*-PBODB, gray; 4,4'-bpy, red. Hydrogen atoms are omitted for clarity.

Table 4. Crystallographic data for **SNU-110** (Squeezed).

	SNU-110
Formula	$Zn_2\ C_{56}\ H_{46}\ N_4\ O_{14}$
Crystal system	*Monoclinic*
Space group	*P* $2_1/c$
Formula weight	1967.03
a, Å	13.289(3)
b, Å	16.467(3)
c, Å	13.711(3)
β, °	117.02(3)
V, Å^3	2673.0(9)
Z	2
ρ_{calcd}, g cm^{-3}	1.404
T, K	95(2)
λ, Å	0.65000
μ, mm^{-1}	0.967
Goodness-of-fit on F^2	1.065
F(000)	1164
Reflections collected	10576
Independent reflections	9689 [*R*(int) = 0.0459]
Completeness to $\theta = 27.5°$	93.70%
Data / restraints / parameters	9689 / 0 / 343
θ range for data collection, °	1.94 to 33.39
Diffraction limits (*h*, *k*, *l*)	$-22 \le h \le 22$, $-25 \le k \le 25$, $-22 \le l \le 22$
Refinement method	Full-matrix least-squares on F^2
R_1, wR_2 [$I > 2\sigma(I)$]	0.0459,[a] 0.149[b]
R_1, wR_2 (all data)	0.0527,[a] 0.1537[b]
Largest diff. peak and hole, e Å^{-3}	0.993, -2.1

[a] $R = \Sigma||F_0| - |F_c||/\Sigma|F_0|$. [b] $wR(F^2) = [\Sigma w(F_o^2 - F_c^2)^2/\Sigma w(F_o^2)^2]^{1/2}$ where $w = 1/[\ \sigma^2(F_o^2) + (0.0978\ P)^2 + (1.4973)P]$, $P = (F_o^2 + 2F_c^2)/3$

Desolvated sample, $[Zn_2(mpm\text{-}PBODB)_2bpy]_n$ (**SNU-110'**), was prepared by the treatment of **SNU-110** with supercritical CO_2 fluid. Since the single crystallinity was not maintained during this activation process, the desolvated phase was analyzed by powder X-ray diffraction (PXRD) data of **SNU-110'**. The PXRD patterns indicate that **SNU-110'** is different from the structure of as–synthesized sample (Figure 32). The PXRD pattern of **SNU-110'** was indexed by *ab initio* method, using Dicvol04 program,[124] and refined by Pawley method (R_p = 5.24%, R_{wp} = 8.05%, Figure 33), which suggested a triclinic unit cell (P1). Appearance of a peak at $2\theta = 4.56°$ (*hkl* = 010), which is systemically absent in original compound having $P2_1/c$ space group, also supports the triclinic cell that the screw axis along the *b* axis does not exist. According to the refined unit cell, total unit cell volume (2438.59 $Å^3$) of **SNU-110'** is reduced by ca. 8.8% compared with that (2673.0 $Å^3$) of **SNU-110**, suggesting that the desolvated sample has a shrunken structure (Table 5). The pore volume of **SNU-110'** is 0.16 $cm^3\ g^{-1}$ as calculated by subtracting the volume of the skeleton (1909.74 $Å^3$; calculated by PLATON[125]) from its unit cell volume. It is much smaller than that (0.248 $cm^3\ g^{-1}$) of **SNU-110**. Rietveld refinement was also tried, but the reasonable solution or refined structure could not be obtained from the PXRD data due to low resolution of the diffraction data as well as the low symmetry of the unit cell. When **SNU-110'** was immersed in DMF for 10 min, the original structure of **SNU-110** was restored as evidenced by PXRD patterns (Figure 32d).

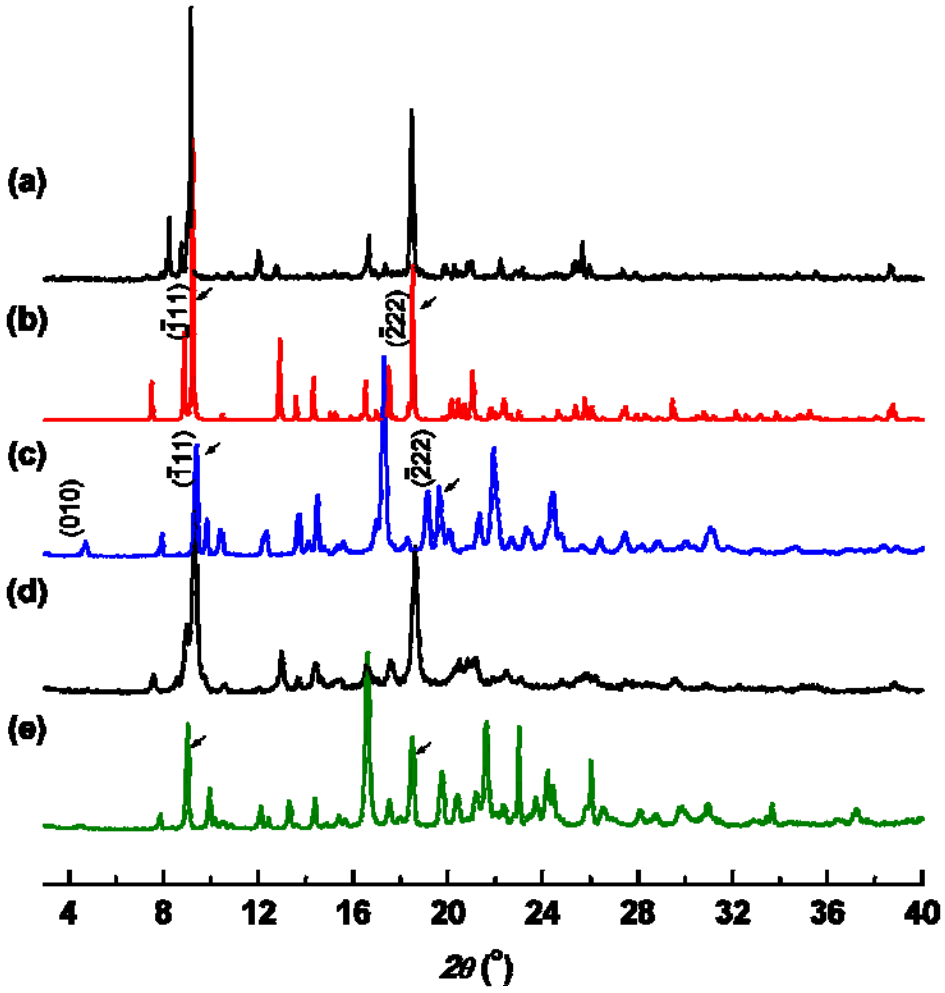

Figure 32 Powder X-ray diffraction patterns of **SNU-110.** (a) As synthesized, (b) simulated from X-ray crystal diffraction data, (c) activated sample, **SNU-110'**: Bragg positions are marked based on cyclically permutated cell parameters for comparison (*abc*→c*ab*), (d) resolvated sample obtained by immersion of **SNU-110'** in DMF for 10 min, and (e) **SNU-110'** under CO_2 stream at 248 K.

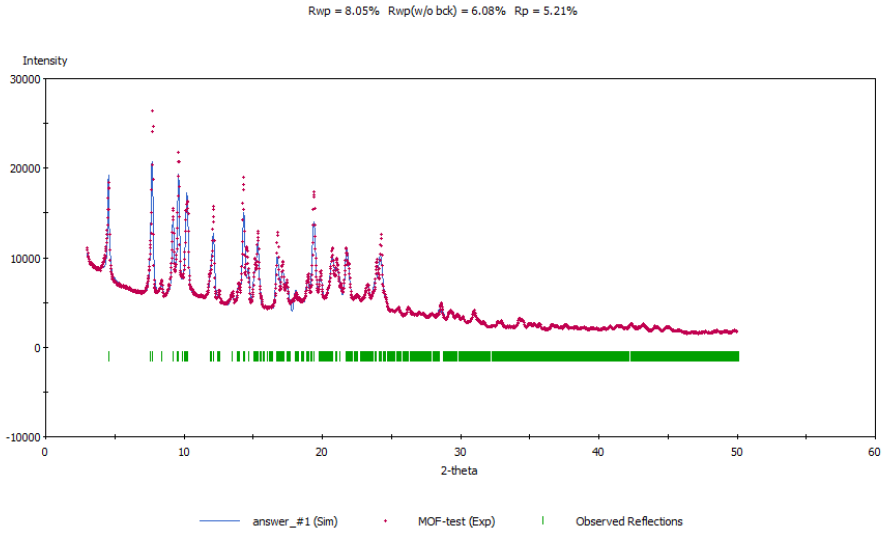

Figure 33 Pawley refinement of the **SNU-110'**. Red crosses: experimental diffraction data, blue line: calculated results, black line: difference plot, green mark: Bragg positions.

Table 5 Cell parameters of **SNU-110** and **SNU-110'** obtained from single crystal X-ray diffraction data and from simulation of PXRD pattern, respectively.

	SNU-110 (Monoclinic, $P2_1/c$)	**SNU-110'** (Triclinic, P1)[a]
a [Å]	13.289	10.7051
b [Å]	16.467	20.1517
c [Å]	13.711	14.4029
α [°]	90	103.808
β [°]	117.02	123.559
γ [°]	90	93.739
V [Å^3]	2673.0	2438.59

[a] The cell parameters are cyclically permutated for comparison. (*abc* → ca*b*)

I.3.3. Gas sorption properties of SNU-110'

The gas adsorption isotherms of **SNU-110'** were measured for N_2, H_2, O_2, CH_4, and CO_2 gases (Figure 34 and Table 6). As seen in Figure 34, **SNU-110'** hardly adsorbs N_2, O_2, and H_2 gases at 77 K as well as CH_4 gas at 195 K, but it adsorbs significant amount of CO_2 at 195 K. Considering the kinetic diameters of CH_4, O_2, N_2, and H_2, which are 3.8, 3.46, 3.64, and 2.89 Å, respectively, the window size of **SNU-110'** must be smaller than 2.89 Å. However, the fact that CO_2 with a kinetic diameter of 3.3 Å is adsorbed in **SNU-110'** suggests that CO_2 interacts with the flexible MOF and opens up the gate due to its large polarizability and quadrupole moment.[103] The facilitated diffusion of CO_2 at 195 K versus H_2 at 77 K must be also a factor in this phenomenon. The adsorption selectivities of **SNU-110** at 195 K and 1 bar for CO_2/N_2 and CO_2/H_2 are 35:1 (v/v) and 61:1 (v/v), respectively, and that for CO_2/CH_4 is 15:1 (v/v).

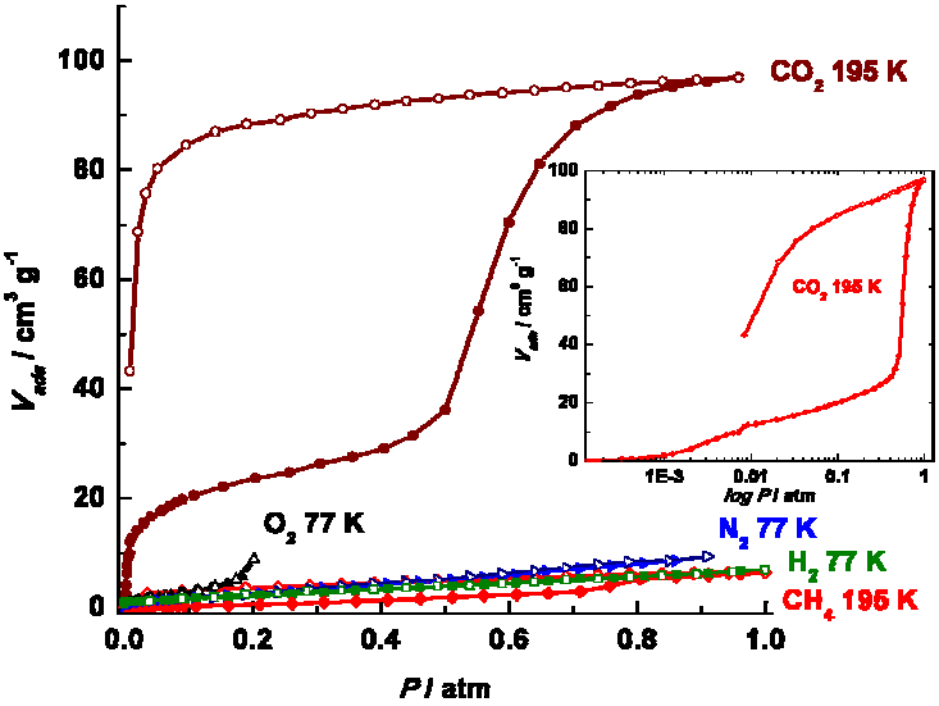

Figure 34 Gas adsorption isotherms of **SNU-110'**. Inset diagram represents CO_2 adsorption at 195 K versus *log P*. Filled shapes: adsorption, open shapes: desorption.

Table 6 gas adsorption data of **SNU-110'**.

compound	Gas	*T* / K	P / atm	Adsorption capacity ($cm^3\ g^{-1}$)	Ref
SNU-110'	CO_2	195	1.0	97.0	This work
		231	1.0	37.0	
		273	1.0	23.6	
		298	1.0	12.9	
	CH_4	195	1.0	6.49	
		298	1.0	0.91	
	N_2	77	0.9	9.39	
		195	1.0	2.79	
		298	1.0	0.22	
	H_2	77	1.0	6.88	
		195	1.0	1.60	
	O_2	77	0.2	8.88	
SNU-31'	CO_2	298	1.0	13.3	45
	N_2	298	1.0	0.56	
PCN-123	CO_2	295	1.0	10.5-26.4	81
	N_2	77	0.9	negligible	

The CO_2 adsorption isotherm at 195 K shows a two-step adsorption curve with a big desorption-hysteresis. The first step shows type-I isotherm and the adsorption saturation occurs at 0.40 atm where uptake amount reaches to 1.3 mmol g^{-1}. The second adsorption step starts at 0.48 atm and uptake amount reaches to 4.3 mmol g^{-1}, i.e. 3 times greater than that of the first step. The step-wise adsorption of CO_2 at 195 K indicates that the framework structure containing flexible organic linker

is altered depending on the CO_2 pressure.[102,116,117] The contracted phase of **SNU-110'** transforms to the open phase when CO_2 pressure exceeds 0.48 atm at 195 K, and then completely opens at 1 atm to get saturated with CO_2. The desorption curve shows a hysteresis with type I isotherm. As the pressure of CO_2 is reduced from 1 atm, the framework maintains the open phase till 3×10^{-2} atm, and then suddenly returns to the contracted phase again. This hysteresis can be reproduced for several cycles in the repeated experiments. The calculated surface areas of **SNU-110',** as estimated from the first step adsorption curve by applying the Dubinin Radushkevich (DR), Brunauer–Emmett–Teller (BET), and Langmuir methods are 409 $m^2 g^{-1}$, 101 $m^2 g^{-1}$, and 111 $m^2 g^{-1}$, respectively. When calculated by using the desorption curve, they are 658 $m^2 g^{-1}$, 411 $m^2 g^{-1}$, and 486 $m^2 g^{-1}$, respectively. The pore volume (0.154 $cm^3 g^{-1}$) estimated from the first step adsorption curve by using the DR equation is similar to the value (0.16 $cm^3 g^{-1}$) calculated by the unit cell volume of **SNU-110'** minus the skeletal volume, while that (0.247 $cm^3 g^{-1}$) obtained from the desorption curve is similar to the free volume (0.248 $cm^3 g^{-1}$) of **SNU-110** estimated by using PLATON[125].

When temperature was elevated to 231, 273, and 298 K, the P/P_0 value for the phase transition of the MOF decreased to 0.021, 0.0044, 0.0036, respectively (Figure 35). This trend can be explained by the increase of thermal energies for both the framework and the CO_2 molecules as the temperature increases.[117]

The PXRD pattern of **SNU-110'** measured under CO_2 pressure (ca. 1 atm) at 248 K indicates that many peaks are shifted to the lower angle regions compared with those of **SNU-110'**, suggesting the expansion of the framework on CO_2 adsorption as well (Figure 32e). The average isosteric heat (Q_{st}) of the CO_2

adsorption in **SNU-110'** is 26.2 kJ mol^{-1}, as calculated from the adsorption data at 195, 231, 273, and 298 K by using Clausius-Clapeyron equation (Figure 36). It is comparable to those (25 - 35 kJ mol^{-1}) of common MOFs.[14]

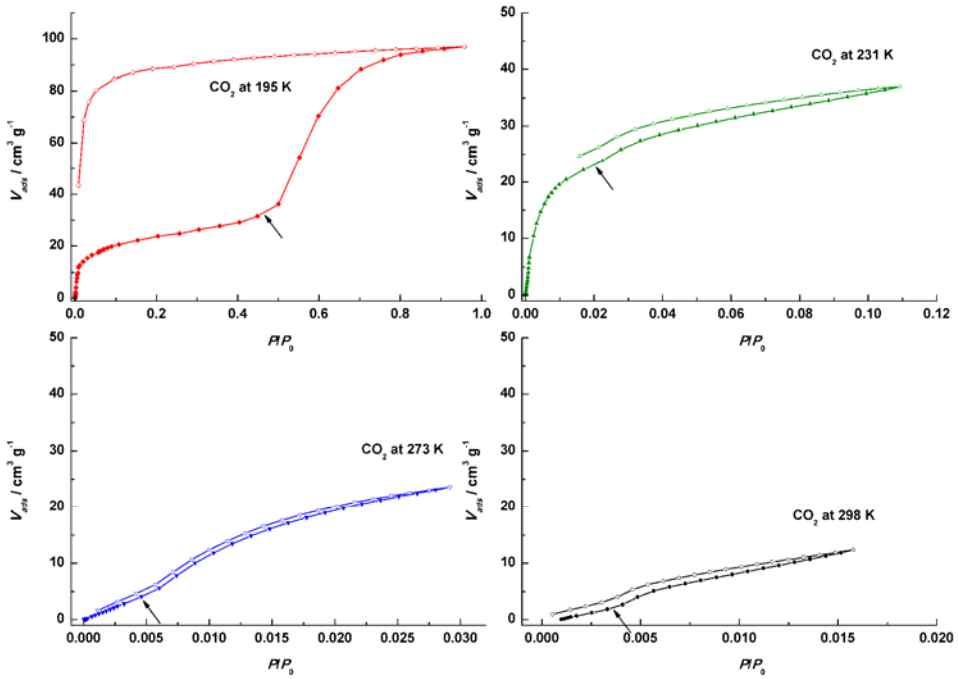

Figure 35 CO_2 adsorption isotherms of **SNU-110'** at various temperatures. The relative pressures (P/P_0) occurring the phase transition are 0.48 at 195 K, 0.021 at 231 K, 0.0044 at 273 K, and 0.0036 at 298 K, as marked by an arrow.

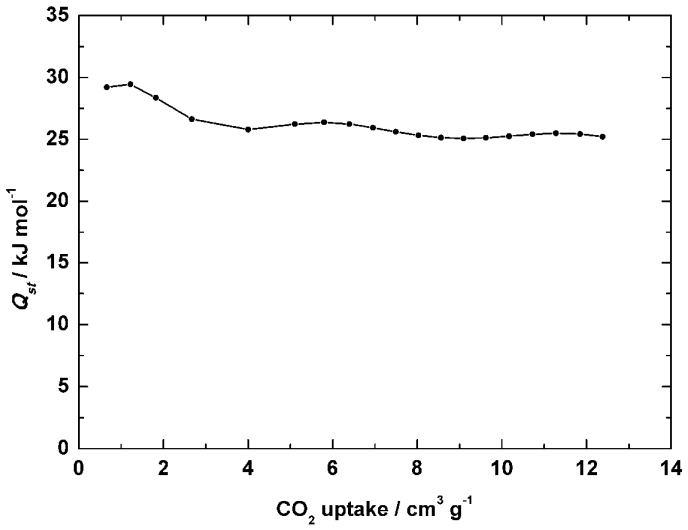

Figure 36 Plot of isosteric heats of adsorption vs CO_2 uptake in **SNU-110'**.

Interestingly, **SNU-110'** in this work hardly adsorbs CH_4 at 195 K**.** In general, at 195 K, MOFs show higher uptake capacity for CO_2 than for CH_4 since CO_2 (T_c = 304.19 K) is subcritical and thus more condensable than CH_4 (T_c = 190.09 K) that is supercritical.[95,126,127] Despite of this, the flexible MOFs selectively adsorbing CO_2 over N_2 and H_2 often cannot efficiently exclude CH_4 that has high polarizability (2.45 Å^3). For example, SNU-M10 adsorbs 123.5 cm^3 g^{-1} of CO_2 and 27.5 cm^3 g^{-1} of CH_4 at 195 K, and SNU-21S adsorbs 257 cm^3 g^{-1} of CO_2 and 124 cm^3 g^{-1} of CH_4 at 195 K.[103,105] Therefore, it is obvious that the flexibility of the present MOF is so well tuned that only CO_2 can open the gate to be adsorbed in the pores.

At 298 K, selective adsorption of CO_2 over CH_4 and N_2 is still observed (Figure 37). Although the uptake capacity is small, the adsorption selectivities of CO_2/N_2 and CO_2/CH_4 are 59 and 14, respectively.

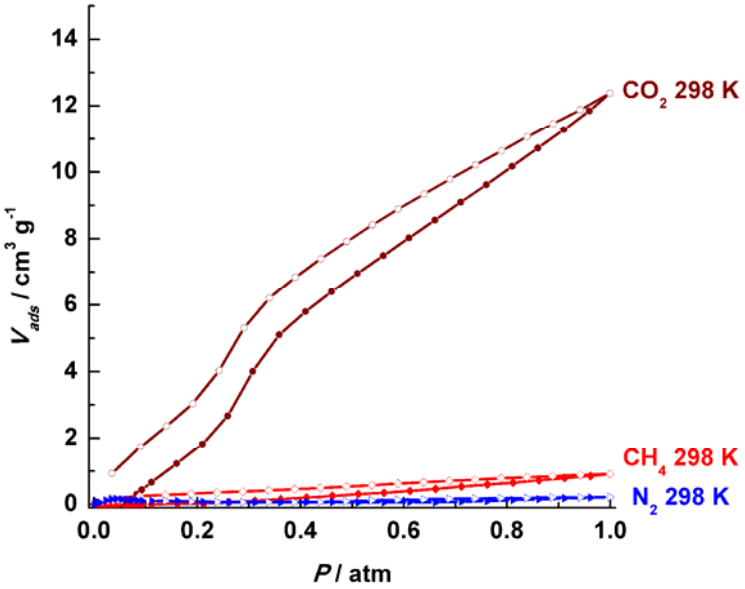

Figure 37 Adsorption isotherms of **SNU-110'** for CO_2 (brown), CH_4 (red), and N_2 (blue) measured at 298 K.

I.4. Conclusions

In conclusion, we have synthesized a porous metal-organic framework, **SNU-110**, by using organic linker having flexible joints. The sample desolvated by using the supercritical CO_2 fluid, **SNU-110'**, has shrunken structure as evidenced by PXRD data. It exhibits a two-step CO_2 adsorption isotherm at 195 K, which is attributed to the structural transformations depending on the amount of CO_2 adsorption. It shows high adsorption selectivity for CO_2 over H_2, N_2, and CH_4 gases at 195 K.

PART II. ENHANCED CARBON DIOXIDE CAPTURE BY POST-SYNTHETIC MODIFICATION OF METAL-ORGAIC FRAMEWORKS WITH FLEXIBLE ALKANEDIOIC ACIDS

II.1. Introduction

II.1.1. Post-synthetic modifications of MOFs

Self-assembled crystalline objects are considered to be constructed by the reversible interaction or reversible bond formation, which corrects the defect formed during the crystallization.[128] The MOF is a material under this category, which creates an infinite network from the reversible metal-ligand coordination bond. It means a building block from a MOF can be substituted.

Metal-organic frameworks have been considered as promising materials for CO_2 separation of landfill gas and flue gas due to their high surface areas and chemical tunability of the pores.[14] However, MOFs commonly have poor stability toward moisture, and their gas-uptake capacities are severely reduced after exposure to moisture.[20] Therefore, water-stable MOFs such as ZIFs[59], MIL-101[57], and UiO-66[33] have attracted great attention and have been employed for post-synthetic modifications (PSMs),[53,54,129] in which some or all building blocks in a synthesized MOF are changed or inserted. PSMs provide alternative routes for functionalizing MOFs, and thus enable to afford the MOFs that cannot be obtained by normal solvothermal synthesis. The methods have been demonstrated to be effective in the introduction of a functional group,[47,130,131] insertion, removal, and exchange of organic linkers[45,53,54,73] as well as exchange of framework metal ions.[129,132] Aniline or bipyridine group in a MOF can be used to introduce additional organic parts or extra metal ion.[131]

II.1.1.1. Coordinated guest exchange grafting

Vacant metal sites in a MOF can be generated when the guest coordinated MOF maintains its structure after guest removal.[44,47,132–137] This site can be used for grafting functional groups such as ethylenediamine,[44,138] *N,N'*-dimethylethylenediamine,[47] and piperazine[139,140] in the pore (Figure 38). Amine grafting is performed by 1) removing coordination guest molecules by heat-evacuation, 2) suspending in non-coordinating solvent such as hexane or toluene, 3) addition of amine, and 4) applying heat occasionally. Amine grafted MOFs can be used for catalytic reaction,[141] metal nanoparticle formation,[141] and increase of low-pressure uptake capacity of CO_2 adsorption with high isosteric heat value.[44,47,138–140] Especially, Mg_2(DOBPDC) grafted with *N,N'*-dimethylethylenediamine can uptake 2 mmol g^{-1} of CO_2 at 380 ppm 25 °C, which means a significant amount of CO_2 can be capture under atmospheric condition.

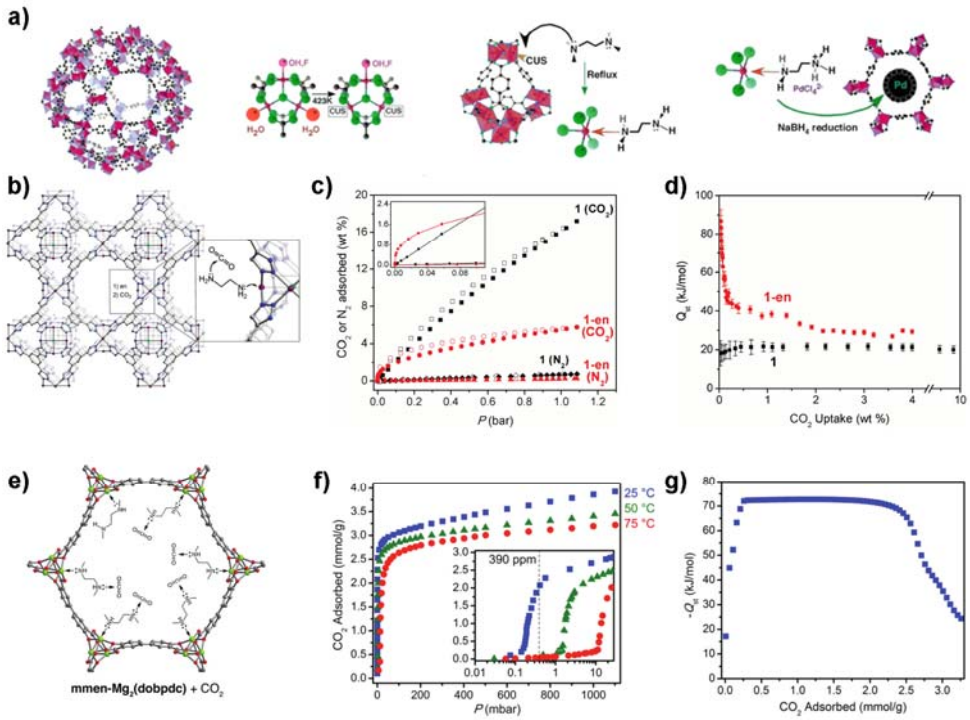

Figure 38 Structure, amine-grafting procedure, and Pd-nanoparticle impregnation of MIL-101 (a). Structure and amine-grafting of Cu-BTTri (b). Gas sorption isotherms (c) and isosteric heat of CO_2 adsorption (d) of Cu-BTTri (**1**) and amine grafted Cu-BTTri (**1-en**). Amine-grafted structure (e), CO_2 sorption isotherms (f) and isosteric heat of CO_2 adsorption (g) of mmem-Mg_2(dobpdc).

II.1.1.2. Ligand insertion/removal/exchange and metal exchange

Not only guest molecules of a MOF, but also a building blocks of the MOF can be exchanged. 3,6-di(4-pyridyl)-1,2,4,5-tetrazine (bpta) ligands in $\{[Zn_2(TCPBDA)(bpta)]\cdot 20DMF\cdot 4H_2O\}_n$ (SNU-31) can be reversibly removed by post-synthetic modification to yield $\{[Zn_2(TCPBDA)(H_2O)_2]\cdot 30DMF\cdot 6H_2O\}_n$ (SNU-

30) (Figure 39).[45] Activated SNU-30' has big pore enough to accommodate CO_2, CH_4, N_2, O_2, and H_2, while SNU-31' adsorbs only CO_2 due to the blockage of bridging ligand (Figure 39b, c).

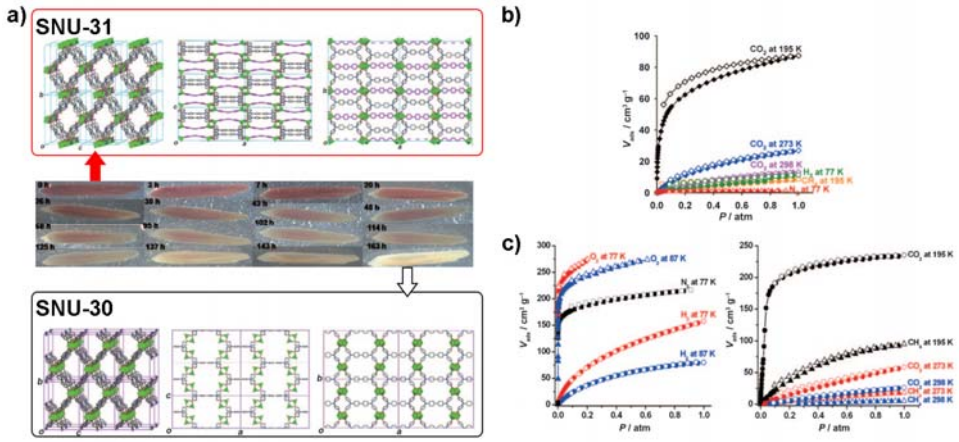

Figure 39 3,6-di(4-pyridyl)-1,2,4,5-tetrazine (bpta) ligands in SNU-31 can be removed via single-crystal-to-single-crystal transformation to yield SNU-30 (a). Adsorption selectivity of CO_2 over other gases can be modulated by post-synthetic insertion/removal of a bridging ligand in SNU-31' (b) and SNU-30' (c).

Post-modification of a MOF with longer ligands than those in the MOF is also available (Figure 40).[73] In bio-MOF-101, 2,6-naphthalenedicarboxylate (NDC) ligands coordinating to zinc-adeninate clusters ($Zn_8Ad_4O_2^{8+}$; Ad = adeninate) have been exchanged with 4,4'-biphenyldicarboxylate (BPDC) ligands to yield bio-MOF-100 in DMF/NMP (1:1) solution at 75 °C. Further exchange with longer ligand has been also available. Stepwise exchange of azobenzene-4,4'-dicarboxylate (ABDC) and 2'-amino-1,1':4',1''-terphenyl-4,4'-dicarboxylate (NH_2-TPDC) into bio-MOF-100 have shown that expansion of porosity by post-synthetic modification is a viable

option. During the exchange procedure, crystallinities of the MOFs have maintained. All the MOFs obtained from the experiment show increasing N_2 sorption properties and pore diameters upon the ligand extension (Figure 40d, e).

The first example of framework cation-exchange in a MOF has been reported by Long group.[142] In the cationic MOF, $Mn_3[(Mn_4Cl)_3(BTT)_8(CH_3OH)_{10}]_2$, free cations have been exchanged by various cations including Li^{I}, Cu^{I}, Fe^{II}, Co^{II}, Ni^{II}, Cu^{II}, and Zn^{II} to increase the isosteric heat of H_2 adsorption. It has been revealed that Cu^{II} and Zn^{II} partially replace framework Mn^{II} ions during the exchange. Framework cation exchange in a MOF is called transmetalation, and various researches have been reported so far (Figure 41).[132,143–146] Those researches can be categorized into complete metal exchange,[132] core-shell transmetallation,[147,148] and metal exchange on struts.[149]

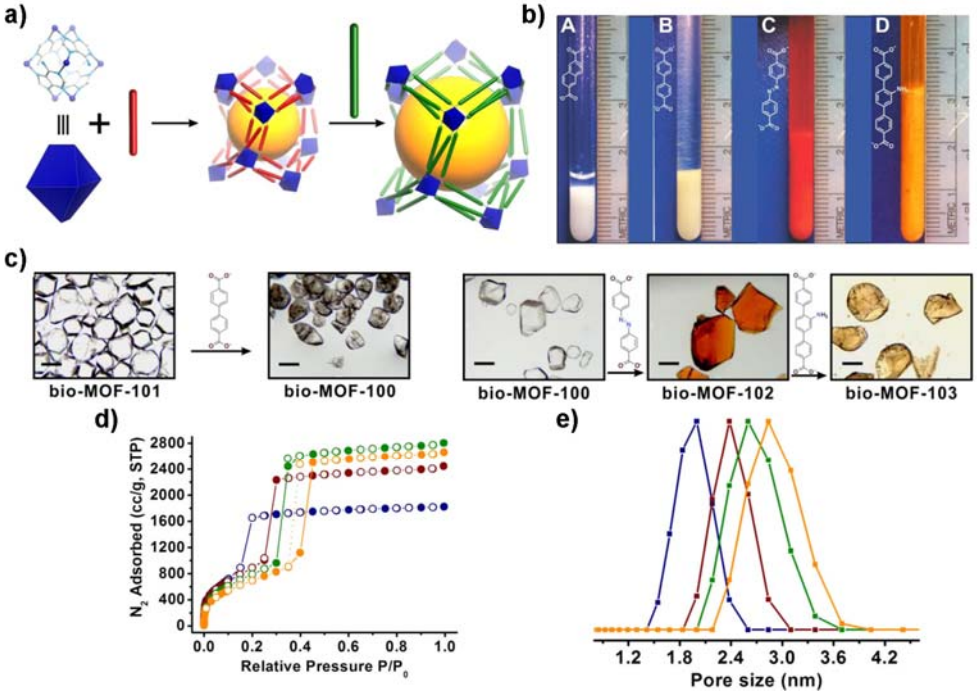

Figure 40 Schematic diagram of synthesis and ligand exchange of bio-MOF-101 (a). Volume expansion of bio-MOF-101(A), 100(B), 102(C), and 103(D), respectively (b). Microscope images of crystalline MOFs before/after ligand exchange(c). N_2 sorption isotherms (d) and pore size distributions (e) of bio-MOF-101 (navy), bio-MOF-100 (red), bio-MOF-102 (green), and bio-MOF-103 (orange),

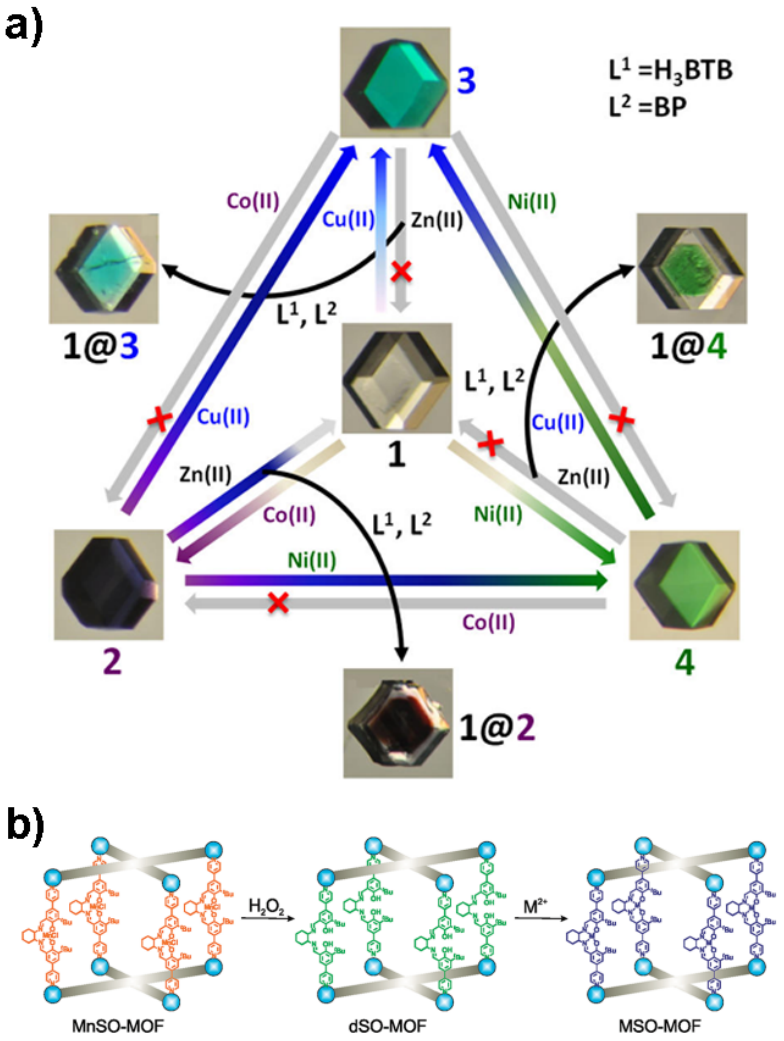

Figure 41 Examples of transmetalation. Complete exchange and total exchange of $M^{II}_6(BTB)_4(BP)_3 \cdot n$Guest (a).[148] Strut metal removal and re-metalation (b).[149]

Cohen group have extensively worked on research about building block exchange.[53,54] They have found that even very stable MOFs such as MIL-53, MIL-68, and UiO-66 can undergo ligand exchange by post-synthetic modifications.[54] MIL-101, however, haven't modified by post-synthetic modification presumably by the non-labile Cr^{III} ion in the structure. Combinations of metal/MOF, ligand/MOF, and MOF-A/MOF-B in solvent condition are all successively experience the exchange of building blocks while MOF-A/MOF-B treated by physical mixing doesn't underwent ligand exchange.[53] Aerosol time-of-flight mass spectrometry (ATOFMS) has been used for analysis of heterogeneity of ligand exchanged MOF particles. During the exchange, effects of solvent polarity and temperature are very important. Various solvent conditions including chloroform, MeOH, DMF, and H_2O with varying temperature at RT, 55 °C, and 85 °C have been tested for ligand exchange between UiO-66-Br and UiO-66-NH_2. It has revealed that conditions of high polarity of solvent and high temperature are favorable for ligand exchange (Table 7).

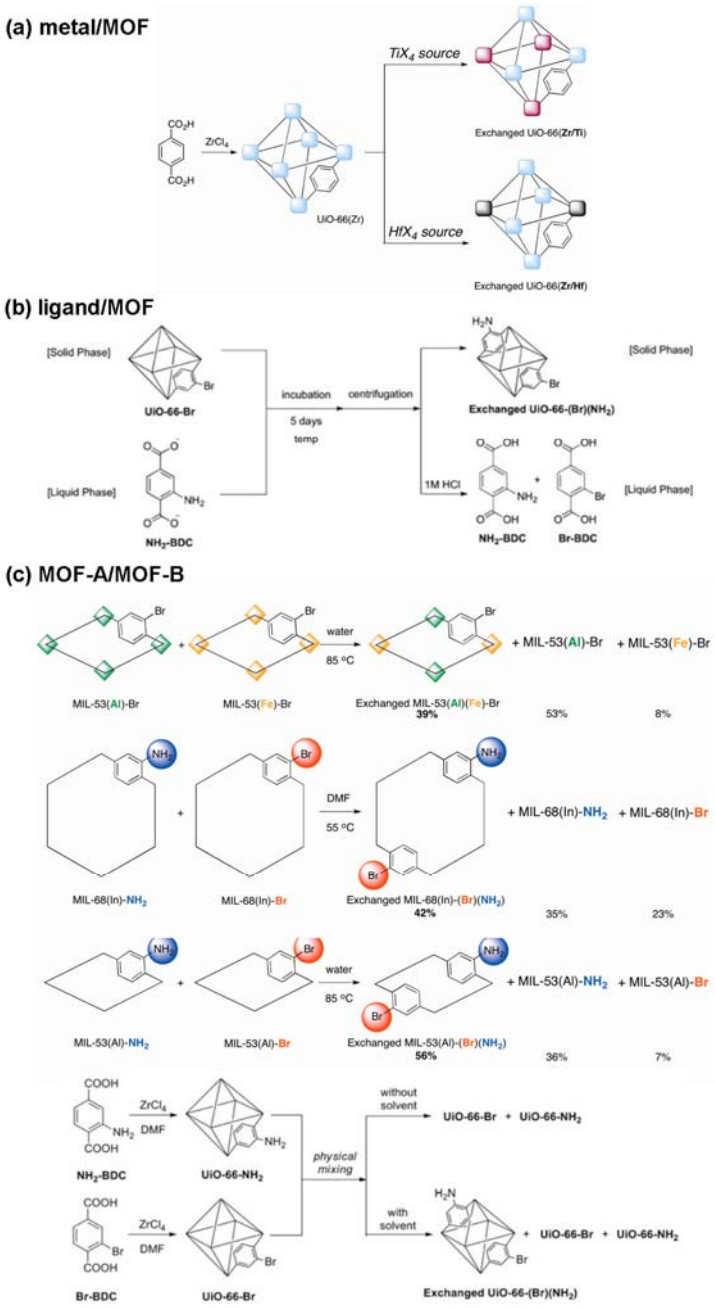

Figure 42 Various methods of post-synthetic modifications. (a) Metal/MOF exchange, (b) ligand/MOF exchange, and (c) MOF-A/MOF-B exchange. In case of MOF-A/MOF-B exchange, ligands or metals of each MOF can be exchanged.[53,54]

Table 7 Solvent and temperature effects in particle-to-particle PSM.[53]

Entry	Conditions[a]	Number of particles Exchanged : UiO-66-Br : UiO-66-NH_2	Percentage of particles exchanged (±2%)[b]
1	$CHCl_3$, RT	387 : 548 : 898	21%
2	$CHCl_3$, 55 °C	785 : 469 : 583	43%
3	MeOH, RT	677 : 644 : 540	36%
4	MeOH, 55 °C	1243 : 250 : 486	63%
5	DMF, RT	1165 : 235 : 606	58%
6	DMF, 55 °C	1344 : 259 : 336	69%
7	DMF, 85 °C	1419 : 187 : 530	66%
8	H_2O, RT	882 : 420 : 332	54%
9	H_2O, 55 °C	1549 : 119 : 276	80%
10	H_2O, 85 °C	1907 : 13 : 56	97%

[a] UiO-66-NH2 (0.1 mmol) and UiO-66-Br (0.1 mmol) have been placed in a vial with 2mL of the solvent indicated for 5 days. [b] (number of particles with both ligands)/(total number of particles)

II.1.2. Energetic aspects of adsorption and desorption functions

It has been reported that the introduction of flexible pendants having hydroxyl, amine, or ether functional groups into MOFs increases CO_2 adsorption selectivity over other gases, since closely located flexible pendants interlock with each other to act as a gate[117] or provide polar adsorption sites for CO_2 gas molecules.[47,114,150] To the best of our knowledge, the entropic effect of a flexible pendant incorporated in a MOF for CO_2 separation has never been previously explored. However, the entropy value must be considered to make a comprehensive assessment of the effect of a flexible pendant on CO_2 adsorption. It has been reported for a zeolite material that separation of alkane isomers is driven by the differences in the reduction of the rotational entropy of each alkane in the pores.[151] Since the adsorption process is governed by the change

in the free energy ($G = H - TS$) and the contribution of the entropy to the free energy increases as the temperature increases, the reduction of the entropy loss for gas adsorption must be advantageous to obtain the improved gas uptake at high temperatures. This view inspired us to introduce the flexible alkyl pendants in a MOF and investigate their entropy effect on the CO_2 gas adsorption.

To apply MOFs as carbon dioxide capture materials, the MOFs should have high CO_2 adsorption capacities and high selectivities of CO_2 adsorption over other gases such as CH_4 and N_2. A high isosteric heat value of the CO_2 adsorption generally leads to a high uptake capacity and increased selectivity of CO_2 adsorption over other gases, but it may require higher energy for regeneration of the adsorbent.[14] Many studies have been performed to increase the isosteric heats of the CO_2 adsorption in MOFs. It is important to note that the isosteric heat is a differential enthalpy of adsorption, which does not include the entropic effect. To fully understand the adsorption phenomenon, free energy (G) or chemical potential (μ) should be taken into consideration. One of the useful thermodynamic tools for analyzing an adsorption isotherm is the desorption functions (G, H, S) suggested by Myers.[152] These functions provide a complete thermodynamic description for an adsorption system with positive quantities, and thus the desorption free energy is the minimum isothermal energy required for regeneration of the adsorbent.

The desorption free energy (G) is the minimum work required for releasing adsorbed gas isothermally at a given temperature and pressure.[152] Under low pressure, the free energy of desorption is calculated by the following equation:

Equation 11 $$G = RT\int_0^P \frac{n}{P}dP = RT\int_0^P nd\ln P$$

For an adsorption isotherm fitted with Langmuir, dual site Langmuir, and Langmuir-Freundlich equations, free energy function (G) can be expressed in analytical form. In this work, we applied Langmuir-Freundlich equation to fit the adsorption isotherms for CO_2, and CH_4 gases and the desorption free energy function was obtained as Equation 13.

Equation 12 $$n = n_m \frac{bP^{(1/t)}}{1 + bP^{(1/t)}}$$

Equation 13 $G = n_m tRT\ln(1 + bP^{(1/t)})$**,** where t is constant.

The enthalpy of desorption (H) was calculated by applying Gibbs-Helmholtz equation to the data obtained from multiple temperatures:

Equation 14 $$H = -T^2\left[\frac{\partial(G/T)}{\partial T}\right]_P = \left[\frac{\partial(G/T)}{\partial(1/T)}\right]_P$$

The entropy of desorption is:

Equation 15 $$S = -\left[\frac{\partial G}{\partial T}\right]_P = \frac{H - G}{T}$$

Calculation of IAST selectivity: The desorption free energies of adsorbed species are all the same under the equilibrium conditions at a fixed temperature. Therefore, selectivity (α) can be calculated by following equations. In a given G value:

Equation 16 $$Py_i = P_i^{\circ}(G)x_i$$

Equation 17 $$\alpha_{i,j} = \frac{x_i / y_i}{x_j / y_j} = \frac{P_j^{\circ}(G)}{P_i^{\circ}(G)}$$

In this study, $P^{\circ}(G)$ was derived from Equation 13.

Equation 18 $$P^{\circ}(G) = \left(\left(\exp\left(\frac{G}{n_m tRT} \right) - 1 \right) / b \right)^t$$

The total pressure (P) and the total loading (n) are:

Equation 19 $$P = \frac{1}{y_i / P_i^{\circ} + y_j / P_j^{\circ}}$$

Equation 20 $$\frac{1}{n} = \sum_i \frac{x_i}{n_i}$$

And individual loadings (n_i) are:

Equation 21 $$n_i = nx_i$$

Nomenclature

α	Selectivity
b	Constant, Equation 12
n	Amount adsorbed (mmol g^{-1})
n_m	Constant, Equation 12 (mmol g^{-1})
G	Gibbs free energy of desorption (kJ kg^{-1})
H	Enthalpy of desorption (kJ kg^{-1})
P	Pressure (atm)
P_i°	Pressure of pure component adsorption (atm)
R	Gas constant, 8.3145 J mol^{-1} K^{-1}
S	Entropy of desorption (kJ kg^{-1} K^{-1})
t	Constant, Equation 12
T	Temperature (K)
x_i	Mole fraction of component *i* in adsorbed phase
y_i	Mole fraction of component *i* in vapor phase

II.2. Experimental Section

General method: All chemicals and solvents used in the synthesis were of reagent grade and used without further purification. Infrared spectra were recorded with a PerkinElmer Spectrum One FT-IR spectrophotometer. NMR spectra were measured on a Bruker Advance DPX-300. Thermogravimetric analyses (TGA) were performed under N_2 (g) at a scan rate of 5 °C min^{-1}, using a TGA Q50 of TA Instruments. Powder X-ray diffraction data were recorded on a Bruker D8 Advance diffractometer at 40 kV and 40 mA for $Cu_{K\alpha}$ (λ = 1.54050 Å), with a scan speed of 0.3 s per step and a step size of 0.02° in 2θ. TEM images were taken by Hitachi H-7600 operating at 100 kV.

Preparation of activated UiO-66: UiO-66 was prepared according to the previously reported method.[33] As-synthesized UiO-66 was sonicated in 1:1 mixture of DMF/MeOH, collected by filtration, and washed with DMF (30 mL × 3) and MeOH (30 mL × 3), successively. The sample was activated by heating at 100 °C under vacuum. UiO-66 immediately adsorbed 16 H_2O molecules on exposure to air. FT-IR (Nujol mull): $\tilde{\nu}$ = 3669, 3639, 3418 (OH^-), 1578 (CO_2^-) cm^{-1}.

Preparation of UiO-66-AD*n* (*n* = 4, 6, 8, and 10) by ligand exchange of UiO-66 with alkanedioic acids followed by activation: Ligand exchange experiments were performed according to the previously reported method.[53] Each of alkanedioic acids ($HO_2C(CH_2)_{n-2}CO_2H$, *n* = 4, 6, 8, and 10; 0.2 mmol) was dissolved in 4% KOH aqueous solution (2 mL). The solution was neutralized to pH 7 with 1 M HCl (total 3 mL). UiO-66 (ca. 57 mg, 0.2 mmol of terephthalate linkers) was immersed in the solution that was kept in pre-heated oven (60 °C) for 1 h, and the mixture was allowed to stand for 5 days. After heating, the mixture was centrifuged

and the aqueous phase was decanted. The solids were immersed in MeOH (10 mL), and the supernatant were exchanged with fresh MeOH (10 mL) every 12 h for 2 days. The solids were collected by filtration and dried under vacuum at 100 °C for 12 h to result in UiO-66-AD*n*s. After gas sorption measurements, IR spectra of the samples were measured. UiO-66-AD*n*s immediately adsorbed water molecules on exposure to air. For UiO-66-AD4, FT-IR (Nujol mull): $\tilde{\nu}$ = 3669, 3638, 3390 (OH^-), 1703 (C=O), 1578 (CO_2^-) cm^{-1}. For UiO-66-AD6, FT-IR (Nujol mull): $\tilde{\nu}$ = 3669, 3639, 3411 (OH^-), 1718 (C=O), 1579 (CO_2^-) cm^{-1}. For UiO-66-AD8, FT-IR (Nujol mull): $\tilde{\nu}$ = 3670, 3640, 3418 (OH^-), 1709 (C=O), 1578 (CO_2^-) cm^{-1}. For UiO-66-AD10, FT-IR (Nujol mull): $\tilde{\nu}$ = 3672, 3641, 3383 (OH^-), 1703 (C=O), 1578 (CO_2^-) cm^{-1}.

^{1}H NMR analysis of UiO-66-AD*n* (*n* = 4, 6, 8, and 10): Each activated UiO-66-AD*n*s (3 mg) was placed in a test tube and digested in d_6-DMSO (580 μL) that contains the aqueous solution of 4.8 wt% HF (20 μL). For accurate integration of NMR spectra, water peak was suppressed.

Preparation of UiO-66-AD6-Sc by using supercritical CO_2 drying method: Prior to activation, the ligand exchanged UiO-66 with adipic acid for 5 days was exchanged with fresh MeOH for 2 days as described previously. The crystals were placed inside the supercritical dryer together with the solvent and the drying chamber was sealed. The temperature and pressure of the chamber were raised to 45 ^oC and 200 bar with CO_2. The chamber was vented at a rate of 10 mL min^{-1} and then filled with CO_2 again. The cycles of refilling with CO_2, pressurizing, and venting were repeated for 5 h. After drying, the closed container having dried sample was transferred to a glove bag filled with argon gas to prevent exposure of the crystals to air. UiO-66-AD6-Sc immediately adsorbed 13 H_2O molecules on exposure to air. FT-

IR (KBr pellet): $\tilde{\nu}$ = 3399 (O-H), 2939 (C-H), 1574 (O-C=O) cm^{-1}.

Partial digestion of UiO-66-AD6-1d and UiO-66-AD6-14d: An aqueous solution of 4.8 wt% HF (11 μL, 0.026 mmol) was diluted with d_6-DMSO (590 μL), and UiO-66-AD6 (7 mg, 14 mg, and 28 mg, respectively), which was dried at 100 °C overnight, was immersed in the solution for 30 min. The molar ratio of HF and the number of carboxylate groups in UiO-66-AD6 were adjusted to 1:2, 1:4, and 1:8 in three runs of digestion, respectively. For accurate integration of NMR spectra, the water peak was suppressed.

Low-pressure gas sorption measurements: The gas adsorption-desorption data were measured by an automated micropore gas analyzer Autosorb-1 or Autosorb-3B (Quantachrome Instruments). All gases used were of 99.9999% purity. Samples were activated at 100 °C under vacuum for 12 h. The N_2 gas isotherms were measured at 77 K. The CO_2 and CH_4 gas isotherms were measured at 273 K, 298 K, and 323 K at each equilibrium pressure by the static volumetric method. After gas sorption measurement, the weight of sample was measured again precisely. Surface area was calculated from the N_2 adsorption data measured at 77 K using Brunauer-Emmett-Teller (BET) and Langmuir methods by using the data points until the value $n_{ads}(1 - P/P°)$ reached the maximum. Pore volume was calculated by applying NLDFT equilibrium model to N_2 adsorption data measured at 77 K.

II.3. Results and Discussion

II.3.1. Preparation of UiO-66-AD*n*s by post synthetic modification of UiO-66

UiO-66 was prepared by heating a DMF solution of $ZrCl_4$ and terephthalic acid (H_2BDC) at 120 °C for 24 h, according to the previously reported method.[33] The framework of UiO-66 consists of a very stable $Zr_6O_4(OH)_4(CO_2)_{12}$ cluster extending to the 12 directions to form a cubic closed packing (ccp) structure, which generates tetrahedral and octahedral cages of size 8 Å and 11 Å, respectively. These cages are connected by a triangular window of size 6 Å (Figure 43).[33]

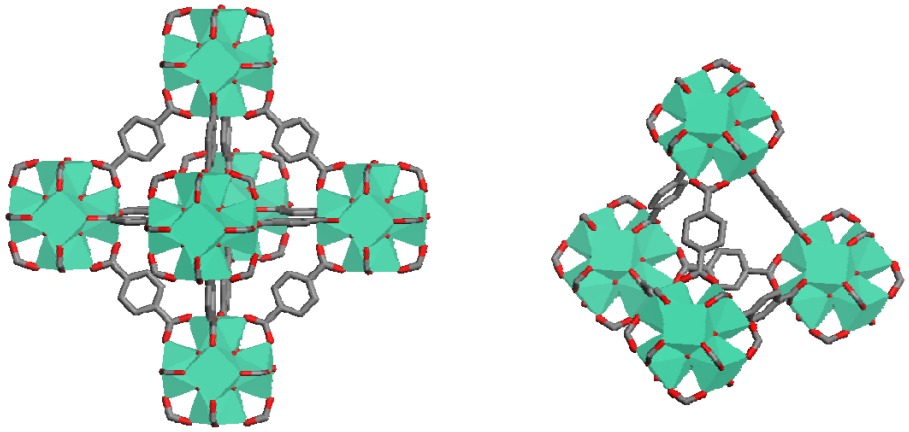

Figure 43 An octahedral cage and a tetrahedral cage in the structure of UiO-66. The pore size is 11 Å for an octahedral cage and 8 Å for a tetrahedral cage. The window size is 6 Å.

For the post-synthetic ligand-exchange of UiO-66, the guest solvent molecules of UiO-66 were removed by the heat-evacuation method at 100 °C. The desolvated sample was then immersed in the aqueous solution of an alkanedioic acid (0.067 M) at 60 °C for 5 days by adjusting the pH to 7 with KOH and HCl (see the Experimental Section).[33,53] As new incoming ligands, succinic acid (n = 4), adipic acid (n = 6), suberic acid (n = 8), and sebacic acid (n = 10) were employed. It should be noted here that adipic acid (n = 6) has a similar length to the terephthalate linker of UiO-66 (Table 8). To remove the possibly pore-included alkanedioic acid, the resulting samples were immersed in MeOH and the solvent was replenished with fresh MeOH every 12 h for 2 days. After activating the samples by heat-evacuation method at 100 °C for 12 h, the dried samples, UiO-66-AD*n*s, were obtained.

Table 8 Crystallographic distance data for dicarboxylic acids from CCDC.

	C-C distance between two carboxylate carbons (Å)	Standard deviations (Å)
Terephthalic acid	5.787	0.059
Succinic acid	3.594	0.326
Adipic acid	5.796	0.516
Suberic acid	7.885	0.898
Sebacic acid	10.091	0.872

As for the introduction of new flexible linkers in UiO-66, there exist three possible different modes (Figure 44): 1) A 1:1 substitution of a terephthalate with an alkanedioate having a similar length as terephthalate; 2) A 1:2 substitution of a terephthalate with two alkanedioates, which leaves free carboxyl pendants in the

structure. 3) Instead of substitution, simple inclusion of alkanedioic acid in the pores of the framework. Various experimental results suggest that a terephthalate in UiO-66 is substituted with two flexible alkanedioates. ^{1}H-NMR spectra of the samples digested in [D_6]DMSO in the presence of HF exhibited that the alkanedioate contents in the digested solutions are 15.9% for UiO-66-AD4, 17.3% for UiO-66-AD6, 23.2% for UiO-66-AD8, and 49.6% for UiO-66-AD10 (Figure 45, and Table 9). An additional experiment that UiO-66 was immersed in the mixture of succinic acid, adipic acid, and suberic acid with the same concentration followed by activation provided a product that contains 3% of succinate, 5% of adipate, and 15% of suberate (Figure 46). The increased introduction of longer alkanedioates may be attributed to the stronger van der Waals interaction between the longer alkane chains in UiO-66-AD*n*. The fact that all alkanedioates could be introduced to UiO-66 independently of their lengths without changing their periodic structures as evidenced by PXRD patterns (Figure 47), and that the IR spectrum of UiO-66-AD*n*s (Figure 48) showed a free carboxylic acid peak in the region of 1703-1718 cm^{-1} suggests that 1:1 substitution model is inappropriate. In the case of UiO-66-AD6, however, a 1:1 substitution mode can be mixed with other substitution mode since an adipic acid has an almost identical length as a terephthalate. It has been reported that an organic ligand in a MOF can be substituted with other ligand having an identical length by 1:1 substitution.[53,54] The following data exclude the possibility that alkanedioic acids are simply included in the pores. 1) A hydrated terephthalate ion ($HBDC \cdot H_2O^-$) was found in the mass spectrum (m/e = 183) of the adipic acid solution, in which UiO-66 sample was immersed for a day (Figure 49). This signal indicates that the terephthalate ligand in the UiO-66 was replaced by adipates, releasing terephthalate.

2) Even after the activation of the sample by using supercritical (Sc) CO_2, which would remove all guest molecules and even weakly bounded solvent molecules at the metal ions,[105] the resulting UiO-66-AD6-Sc still contained 22.4% adipic acid, assigned by the ^{1}H-NMR spectra of the sample digested in [D_6]DMSO in the presence of HF (Table 9). This result reveals that the adipate in the structure is strongly bound to the structure. Therefore, the reasonable mode is 1:2 substitution for all UiO-66-AD*n*s, although 1:1 substitution can be mixed with 1:2 substitution in the case of UiO-66-AD6.

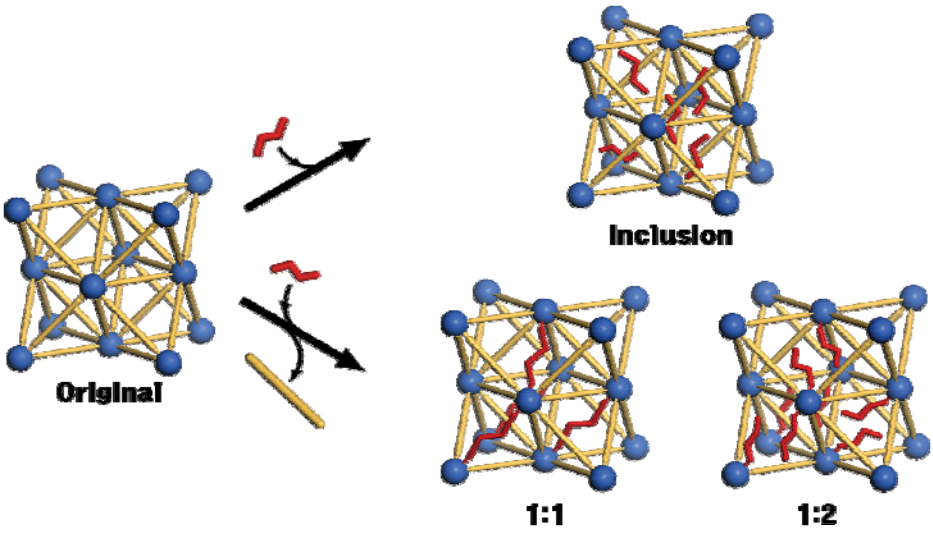

Figure 44 Three possible ways of introducing new flexible functional pendants in UiO-66. The 1:1 model represents that an alkanedioate replaces a terephthalate while 1:2 model represents two alkanedioates substitute a terephthalate leaving uncoordinated carboxylic acid groups. In inclusion model, ligand substitution does not occur. Color scheme: metal cluster, blue; terephthalate, orange; alkanedioate, red.

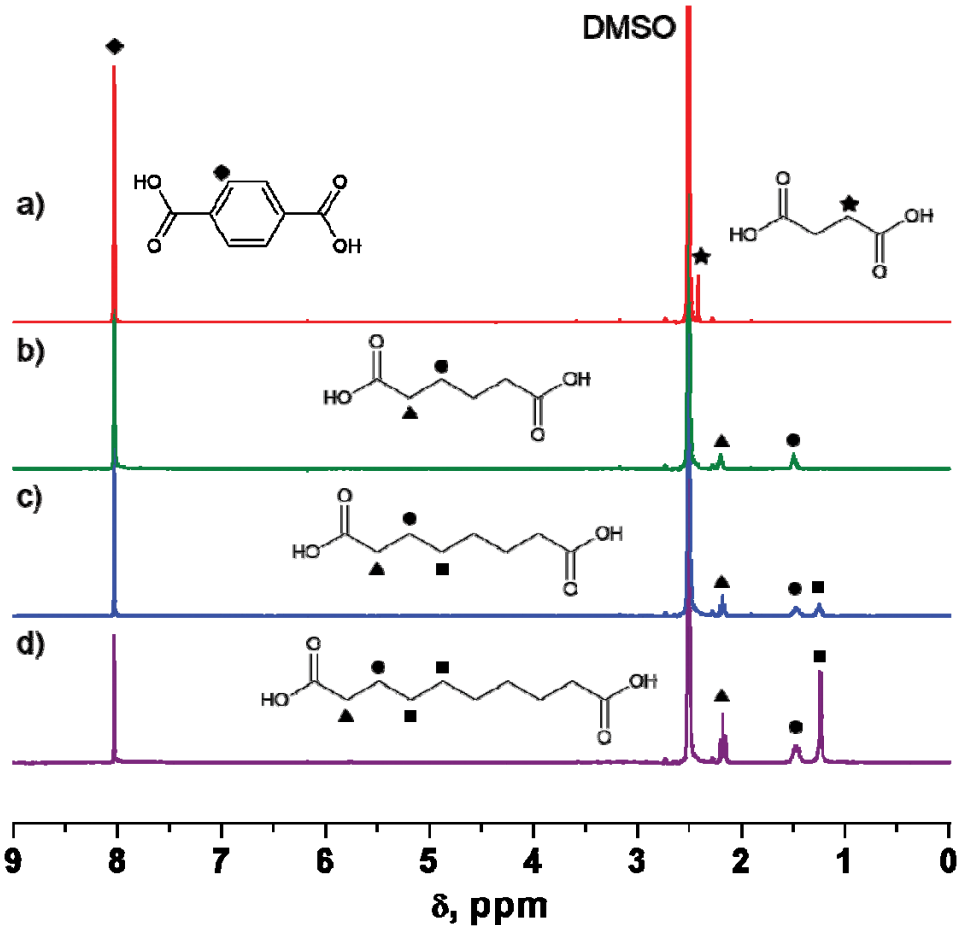

Figure 45 ^{1}H NMR spectra of UiO-66-AD*n*s that were digested in d_6-DMSO by hydrofluoric acid. a) UiO-66-AD4, b) UiO-66-AD6, c) UiO-66-AD8, and d) UiO-66-AD10. Water peaks were suppressed for clarity.

Table 9 ^{1}H NMR data of digested UiO-66-AD*n*s.

	Terephthalic acid		Alkanedioic acid		
	δ	Integration area	δ	Integration area	Ratio %
UiO-66-AD4	8.04 (4H)	100.00	2.42 (4H)	18.84[a]	15.9
UiO-66-AD6	8.04 (4H)	100.00	2.20 (4H), 1.50 (4H)	18.19, 20.87[a]	17.3
UiO-66-AD8	8.04 (4H)	100.00	2.18 (4H), 1.48 (4H), 1.25 (4H)	30.74, 30.60, 30.25[a]	23.2
UiO-66-AD10	8.04 (4H)	100.00	2.18 (4H), 1.47 (4H), 1.24 (8H)	92.84, 95.37, 196.91[a]	49.6
UiO-66-AD6-Sc	8.04 (4H)	100.00	2.20 (4H), 1.50 (4H)	28.08, 28.86[a]	22.4

[a] This value was used to calculate the ratio of terephthalic acid: alkanedioic acid.

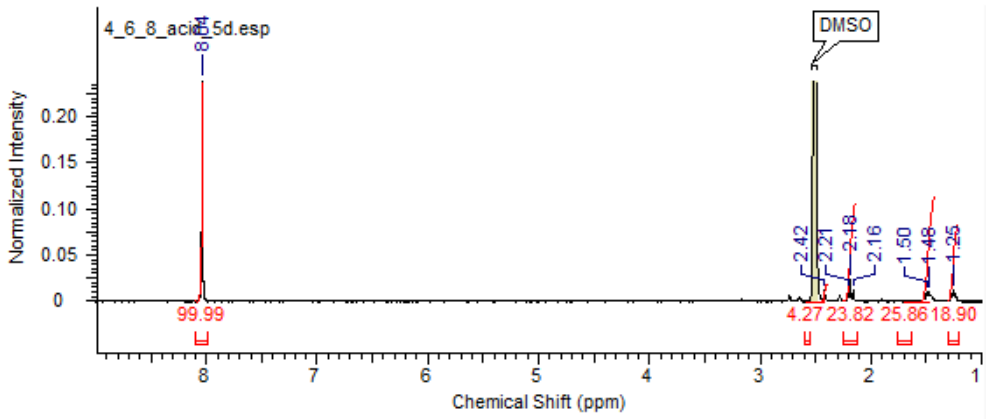

Figure 46 ^{1}H NMR spectrum of post-synthetically modified UiO-66 that was digested in d_6-DMSO by hydrofluoric acid. The sample solid had been immersed in an aqueous solution (3 mL) containing the mixture of 0.067 M succinic acid, 0.067 M adipic acid, and 0.067 M suberic acid for 5 days, washed with MeOH (10 mL × 4) for 2 days, and dried under vacuum for 12 h at 100 °C. The composition of each acid in the solid is 3% for succinic acid, 5% for adipic acid, and 15% for suberic acid.

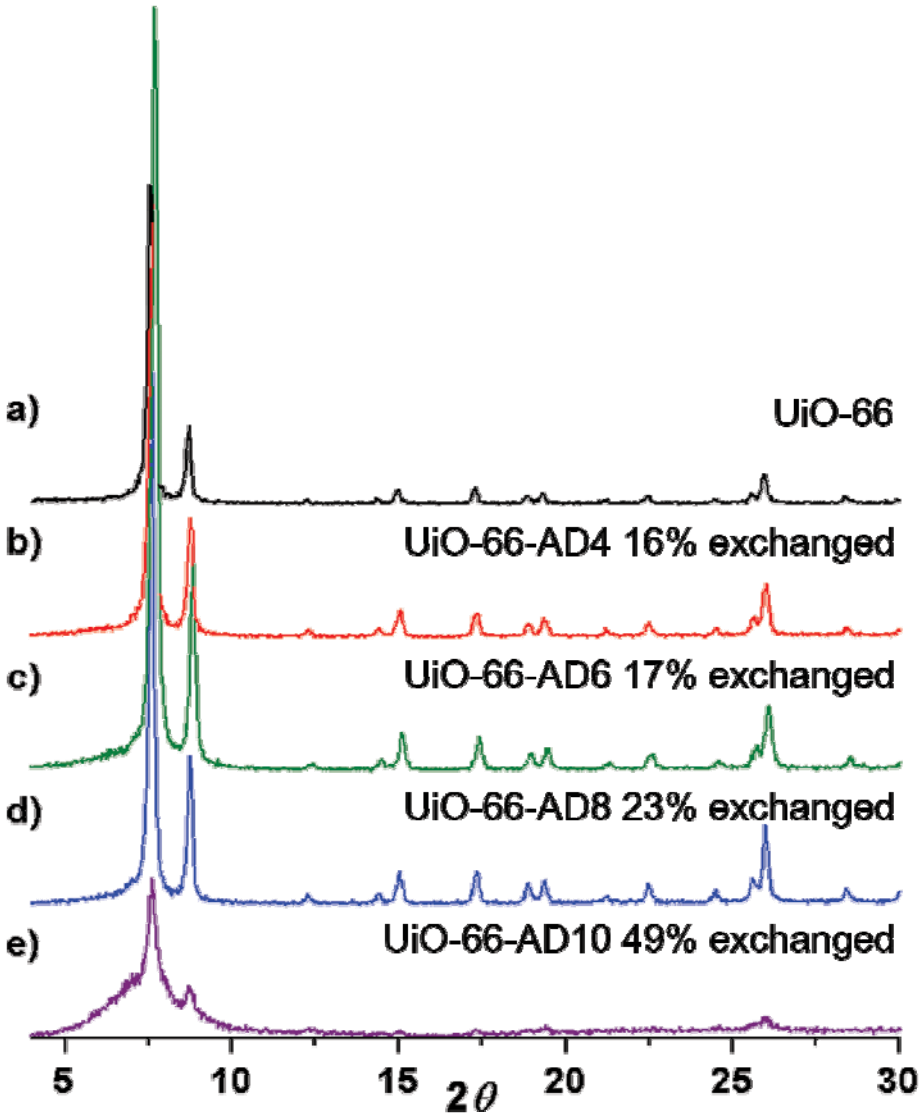

Figure 47 Powder X-ray diffraction patterns for UiO-66-AD*n*s activated by heat-evacuation method at 100 °C. a) UiO-66, b) UiO-66-AD4, c) UiO-66-AD6, d) UiO-66-AD8, and e) UiO-66-AD10

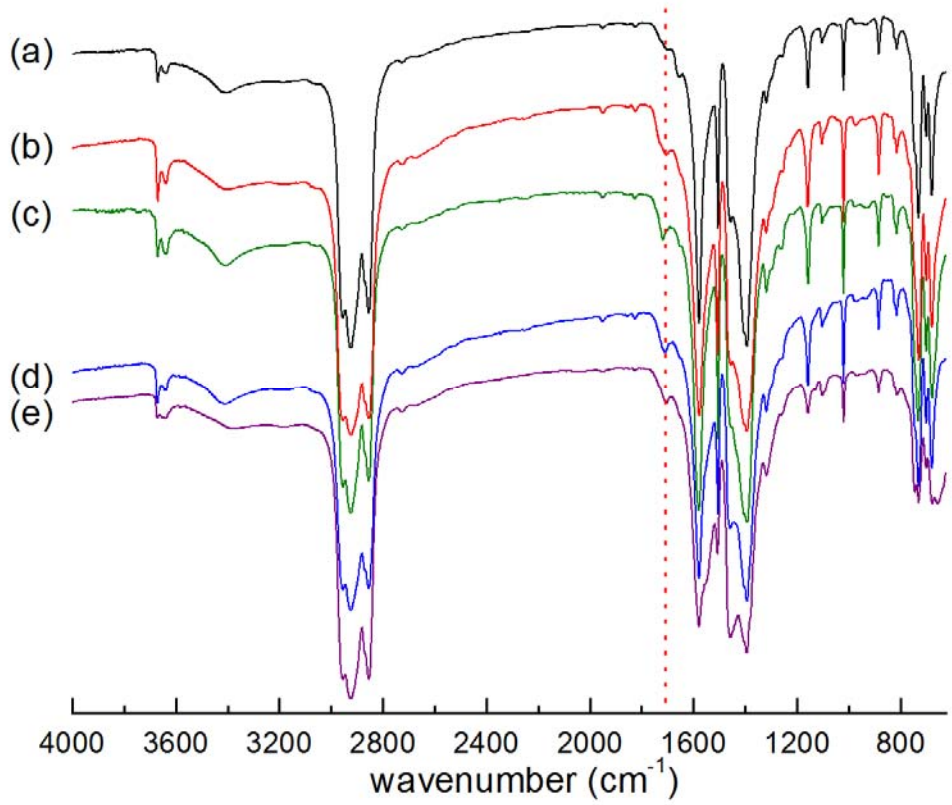

Figure 48 IR spectra (Nujol mull) of (a) activated UiO-66, (b) UiO-66-AD4, (c) UiO-66-AD6, (d) UiO-66-AD8, and (e) UiO-66-AD10. Shoulder peak of free carboxylic acid was denoted as a dotted line.

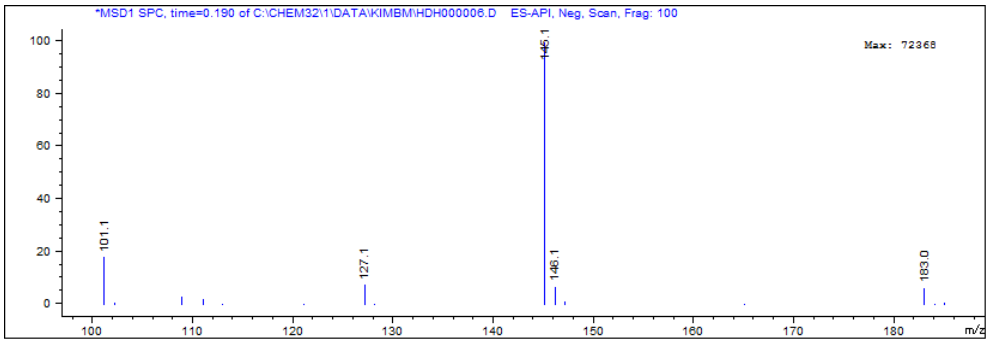

Figure 49 Mass spectrum of an aqueous solution of 0.067 M adipic acid, in which UiO-66 was immersed for 1 day. Adipate (m/e = 145.1) and hydrated terephthalate (m/e = 183.0) were observed. Non-hydrated terephthalate (m/e = 165) was also detected but the signal was very weak.

The PXRD patterns (Figure 47) of UiO-66-AD*n* (*n* = 4, 6, 8, and 10), which were activated by heat-evacuation method at 100 °C, indicate that structural regularities are retained even after the ligand-exchange and activation, although UiO-66-AD10 shows a severe peak broadening. TEM images of the guest removed samples indicate that the sizes and the shapes of UiO-66 are still maintained in UiO-66-AD*n*s (*n* = 4, 6, 8, and 10) (Figure 50). Thermogravimetric analysis data indicate that the desolvated UiO-66, UiO-66-AD4, UiO-66-AD6, and UiO-66-AD8 samples decompose at 510 °C while UiO-66-AD10 decomposes at a much lower temperature, 427 °C (Figure 51).

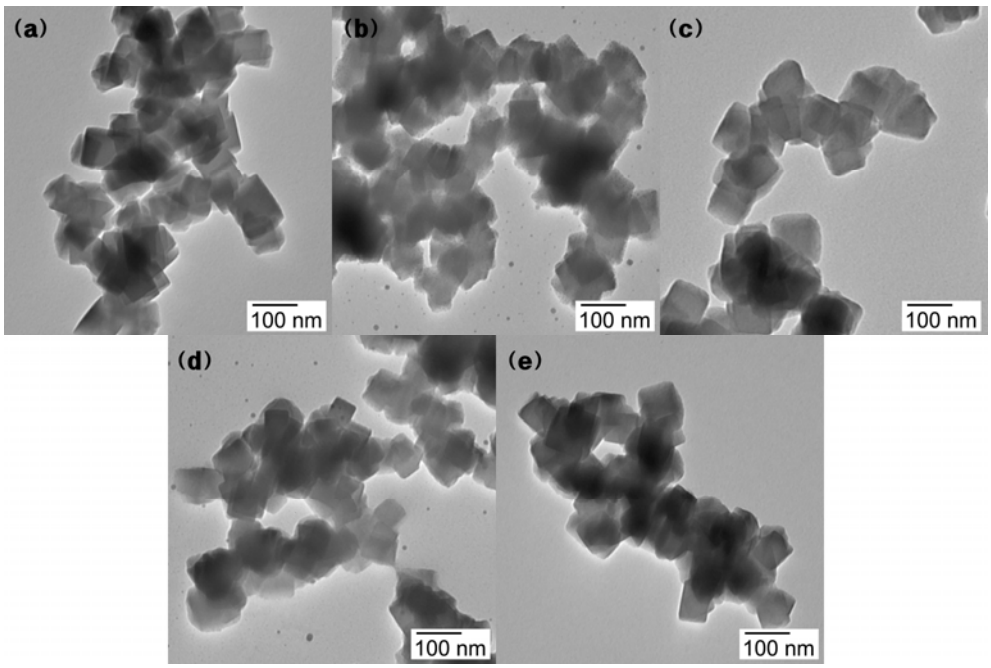

Figure 50 TEM images of activated samples. (a) UiO-66, (b) UiO-66-AD4, (c) UiO-66-AD6, (d) UiO-66-AD8, and (e) UiO-66-AD10 show size and shape of each particle remained intact during the exchange experiment.

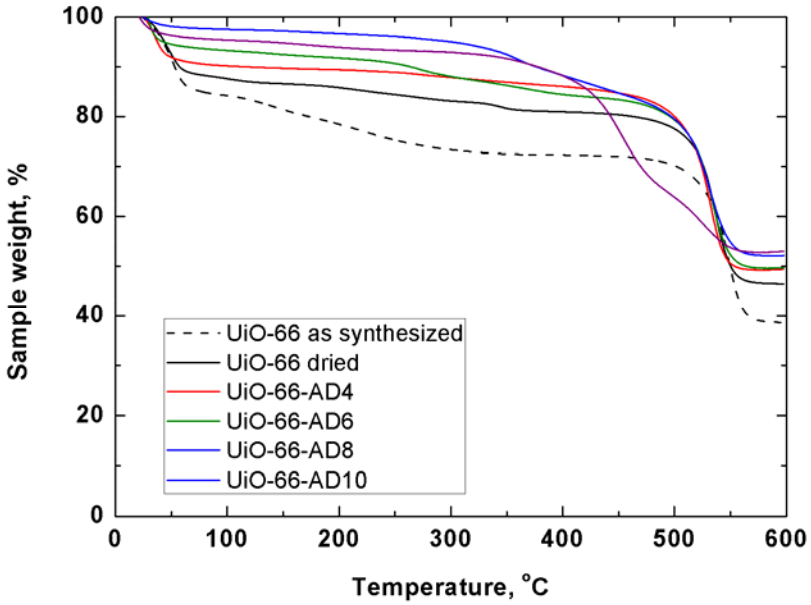

Figure 51 TGA data of as-synthesized UiO-66 (black, dash line), and dried samples of UiO-66 (black, solid line), UiO-66-AD4 (red), UiO-66-AD6 (green), UiO-66-AD8 (blue), and UiO-66-AD10 (violet) by using heat-evacuation method.

II.3.2. Distribution of substituted adipic acid in post-synthetically modified UiO-66

Although there have been several reports on the partial ligand-exchange of a MOF by the post-synthetic modification, the location of exchanged ligand has never been proposed.[53,54] In this study, we investigated the followings after we prepared UiO-66-AD6-1d and UiO-66-AD6-14d according to the same procedure as UiO-66-AD6, with the exception of the immersion time, for 1 day and for 14 days, respectively, in the solution of alkanedioic acids: 1) Distribution of substituted adipic acid in the crystal. 2) Dependence of the degree of ligand substitution on the immersion time of the sample in the adipic acid solution. To do so, a fixed amount of HF in d_6-DMSO

was added to various amounts of UiO-66-AD6-1d or UiO-66-AD6-14d samples, and the ratios of adipic acid/terephthalic acid were determined by ^{1}H NMR spectra (see the Experimental Section). We anticipated that when very small amount of HF was added, only the surface of the MOF crystal could be digested, but as the amount of HF was increased, inner part of the crystal would be also digested (Figure 52).

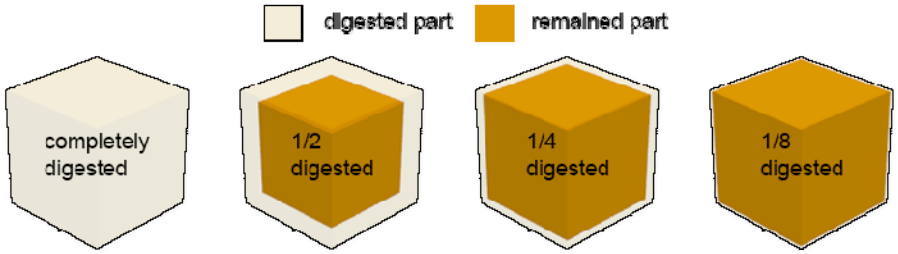

Figure 52 Simplified presentation of partial digestion of a cubic-shaped particle.

In the experiment, minimum amount of HF required for complete digestion of UiO-66-AD6-1d was calculated based on the molar number of carboxylate groups in the sample, and employed in the digestion. The results indicated that one equivalent amount of HF for a carboxyl group was enough for a complete digestion of the sample within 30 min. The fixed amounts of HF that were mixed in d_6-DMSO were added to the 2×, 4×, and 8× excess amounts of UiO-66-AD6-1d, respectively, and the samples were digested for 30 min. After digestion, ^{1}H NMR spectra were measured (see the Experimental Section). The contents of adipic acid were found to be 48%, 41%, and 32% for the 1/8, 1/4 and 1/2 digested samples, respectively, for UiO-66-AD6-1d. A totally digested UiO-66-AD6-1d showed a 20% content of adipic acid (Figure 53). The same digestion method was applied for UiO-66-AD6-14d. The

contents of adipic acid were 48%, 35%, 30%, and 22% for 1/8, 1/4, 1/2 and totally digested samples, respectively. The present results indicate that the lesser digested samples have an increased percentage of adipic acid, demonstrating clearly that the exchanged ligands in the solid are concentrated near the surface of the crystal rather than being homogeneously distributed throughout the crystal. The results also show that the immersion time does not affect the distribution of the substituted adipic acid in the crystal.

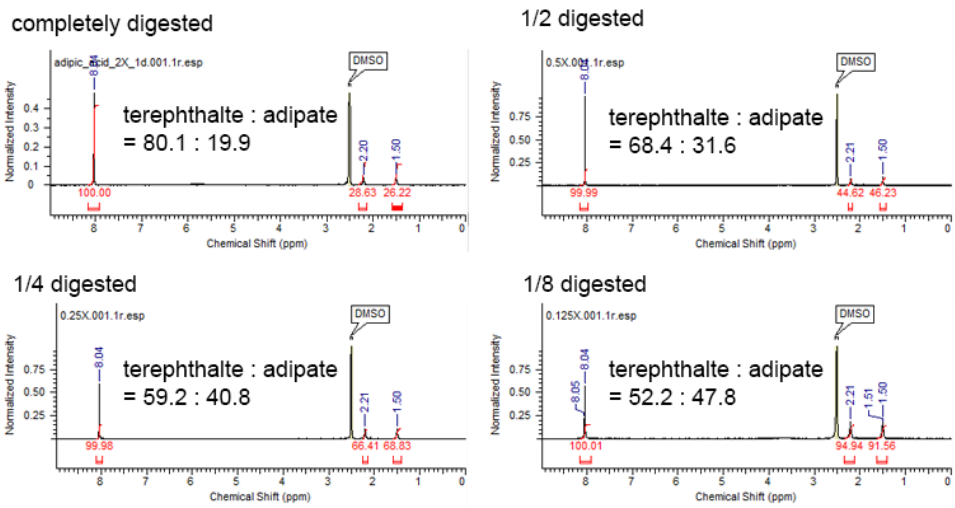

Figure 53 ^{1}H NMR spectra of UiO-66-AD6-1d, which was digested in d_6-DMSO by hydrofluoric acid. For UiO-66-AD6-14d, the ratios between terephthalate and adipate are 78.5:21.5, 69.7:30.3, 64.9:35.1, and 52.3:47.7 for the 100% digested sample, 1/2 digested sample, 1/4 digested sample, and 1/8 digested sample, respectively.

II.3.3. Gas sorption properties and thermodynamic analyses of UiO-66 and UiO-66-AD*n*s

It was previously reported that UiO-66 had a moderate CO_2 uptake capacity, 1.8 mmol g^{-1} at 1 bar and 298 K,[153] and this capacity could be enhanced by the introduction of functional groups such as amino, nitro, methoxy, and naphthyl,[129] or by the post-synthetic modification of framework metal ions.[153] For example, when an amine functional group was introduced, the CO_2 adsorption capacity reached to 3.0 mmol g^{-1} at 1 bar and 298 K.[153] When the framework Zr^{IV} ion was exchanged with a Ti^{IV} ion, the CO_2 uptake was enhanced to 2.2 mmol g^{-1} at 1 bar and 298 K.[129]

The gas sorption isotherms of the present UiO-66-AD*n*s samples were measured for N_2, CO_2, and CH_4 gases (Table 10). From the N_2 adsorption data at 77 K, the BET (Langmuir) surface areas and pore volumes were calculated and they are summarized in Table 10 (see the Experimental Section). UiO-66 has a BET surface area (pore volume) of 1057 m^2 g^{-1} (0.441 cm^3 g^{-1}) while UiO-66-AD4, UiO-66-AD6, UiO-66-AD8, and UiO-66-AD10 have reduced surface areas, 942 m^2 g^{-1} (0.351 cm^3 g^{-1}), 1020 m^2 g^{-1} (0.421 cm^3 g^{-1}), 901 m^2 g^{-1} (0.342 cm^3 g^{-1}), and 213 m^2 g^{-1} (0.100 cm^3 g^{-1}), respectively. Interestingly, UiO-66-AD10 show much more reduced surface area and pore volume than others. This might occur because the long alkanedioate block the pores in UiO-66-AD10 that is highly substituted (50%) with sebacic acid.

Table 10 Gas adsorption data of UiO-66 and UiO-66-AD*n*s

	T/K	*P*/atm	UiO-66/ mmol g^{-1}	UiO-66-AD4/ mmol g^{-1}	UiO-66-AD6/ mmol g^{-1}	UiO-66-AD8/ mmol g^{-1}	UiO-66-AD10/ mmol g^{-1}
N_2	77	0.9	339[a]	247[a]	301[a]	241[a]	75[a]
	298	1.0	0.14	0.14	0.18	0.16	0.04
CO_2	273	1.0	3.14	3.56	3.76	3.31	1.33
	298	1.0	1.96	1.92	2.63	1.83	0.57
	323	1.0	1.07	1.06	1.69	0.97	0.29
CH_4	273	1.0	0.84	0.84	0.89	0.85	0.17
	298	1.0	0.50	0.45	0.48	0.45	0.13
	323	1.0	0.20	0.19	0.27	0.14	0.10
Surface area/m^2 g^{-1}			1057[b] (1098)[c]	942[b] (963)[c]	1020[b] (1038)[c]	901[b] (927)[c]	213[b] (224)[c]
Pore volume/cm^3 g^{-1}			0.441	0.351	0.421	0.342	0.100

[a] in cm^3 g^{-1}, [b] BET surface area, [c] Langmuir surface area.

Contrary to the decreased N_2 uptakes of all UiO-66-AD*n*s at 77 K, the CO_2 adsorption capacities in UiO-66-AD6 at 273, 298, and 323 K are greater than those of UiO-66 (Figure 54). In particular, the decreases in the CO_2 adsorption capacities of UiO-66-AD6 at the elevated temperatures are less significant than that of UiO-66 (Figure 55). As a result, the CO_2 uptake ratio of UiO-66-AD6 over UiO-66 increases from 1.20 at 273 K to 1.34 at 298 K and finally to 1.58 at 323 K. To give insight into

this behavior, the desorption functions (*G*, *H*, *S*) have been calculated from the gas sorption data (see the Experimental Section).[152] These functions give the values in the unit of energy per weight of a sample, and the data are presented in Figure 56 and Figure 57. Since the values of Gibbs free energy, enthalpy, and entropy for the gas adsorption in MOFs are generally negative values, these functions are denoted as "desorption" functions. At 1 atm and 298 K, UiO-66-AD6 has the highest desorption free energy (8.29 kJ kg^{-1}), which is followed by UiO-66-AD4 (6.55 kJ kg^{-1}), UiO-66 (6.38 kJ kg^{-1}), and UiO-66-AD8 (6.30 kJ kg^{-1}). UiO-66-AD10 has the lowest CO_2 uptake and a fairly small desorption free energy (1.84 kJ kg^{-1}). For the desorption enthalpies and entropies, UiO-66-AD4 (69.4 kJ kg^{-1}, 211 J kg^{-1} K^{-1}), UiO-66-AD6 (65.3 kJ kg^{-1}, 191 J kg^{-1} K^{-1}), and UiO-66-AD8 (64.6 kJ kg^{-1}, 195 J kg^{-1} K^{-1}) show ~20% higher values than UiO-66 (56.4 kJ kg^{-1}, 168 J kg^{-1} K^{-1}), while UiO-66-AD10 (25.3 kJ kg^{-1}, 78.8 J kg^{-1} K^{-1}) has lower values than UiO-66 (Figure 56). For these series of compounds, the entropy values have a linear relationship with the enthalpy values (Figure 57). During the adsorption process, the strong interaction between gas molecules and the modified framework results in the increase of entropy loss, counteracting the benefit of the enhanced enthalpy. However, UiO-66-AD6 deviates from this trend, which leads to the highest desorption free energy among the compounds. In contrast to this irregular behavior of UiO-66-AD6 for the CO_2 adsorption, the deviation is not shown in the cases for the CH_4 gas adsorption in UiO-66 and all UiO-66-AD*n*s (Figure 58). The increased CO_2 uptake in UiO-66-AD6 must be attributed to the relatively strong interactions between the CO_2 molecules and the carboxyl pendants with the proper length (Figure 59). We assume that the length of the dangling adipic acids (5.796 Å; distance between two carboxylate

carbons) is optimal to provide multiple interaction modes with the CO_2 molecules in the pores, which increases the enthalpy loss and mitigates the entropy loss on CO_2 adsorption. The diagonal distance of an octahedral cage of UiO-66 is 15.737 Å, which is too long for two succinic acids (3.594 Å × 2) and too short for two suberic acids (7.885 Å × 2).

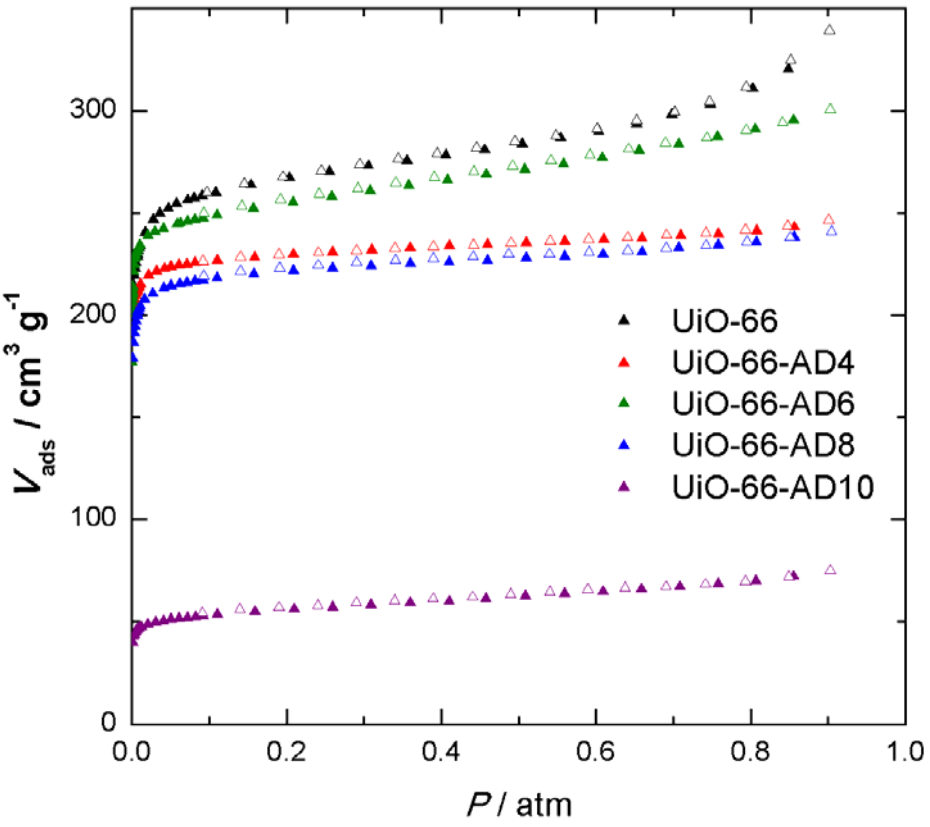

Figure 54 N_2 (triangles) adsorption isotherms of UiO-66 and UiO-66-AD*n*s at 77 K. UiO-66 (black), UiO-66-AD4 (red), UiO-66-AD6 (green), UiO-66-AD8 (blue), and UiO-66-AD10 (violet). Filled shapes: adsorption; open shapes: desorption.

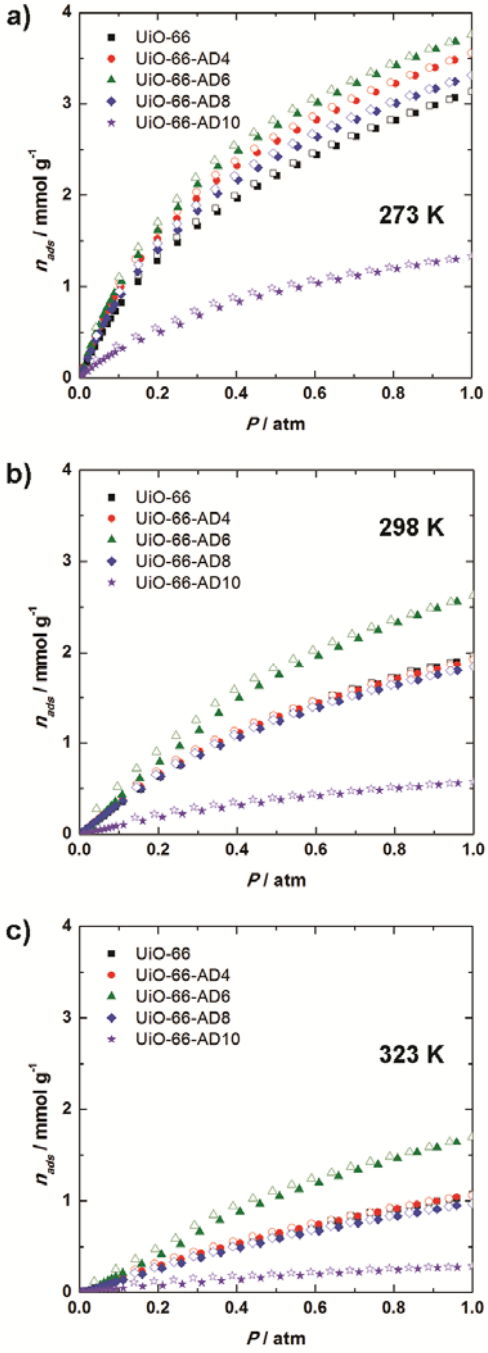

Figure 55 CO_2 adsorption isotherms at a) 273 K, b) 298 K, and c) 323 K for UiO-66 (■), UiO-66-AD4 (●), UiO-66-AD6 (▲), UiO-66-AD8 (◆), and UiO-66-AD10 (★). Filled shapes: adsorption; open shapes: desorption.

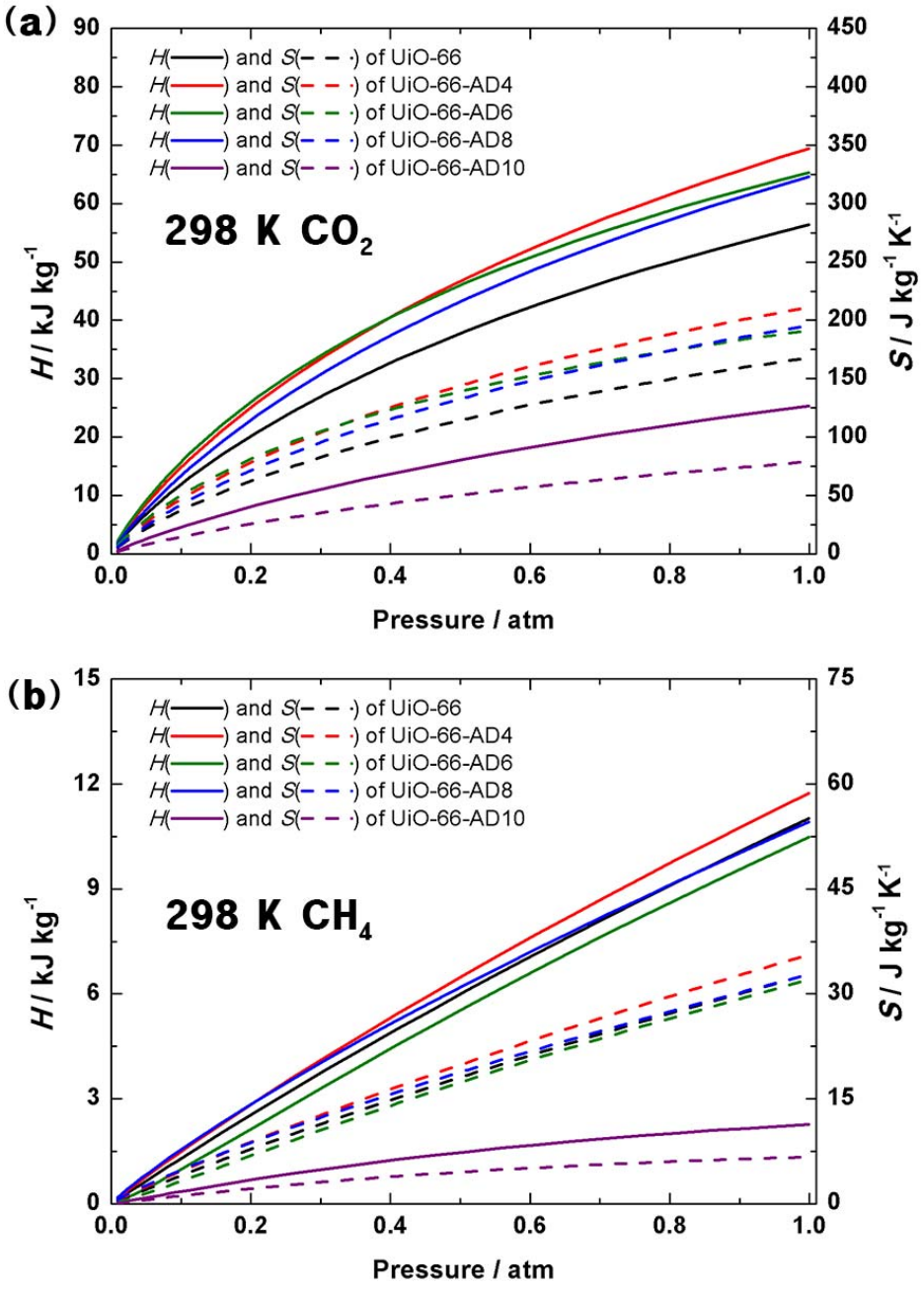

Figure 56 Calculated enthalpy (*H*; solid line) and entropy (*S*; dashed line) of desorption of (a) CO_2 and (b) CH_4 at 298 K. UiO-66 (black), UiO-66-AD4 (red), UiO-66-AD6 (green), UiO-66-AD8 (blue), and UiO-66-AD10 (violet).

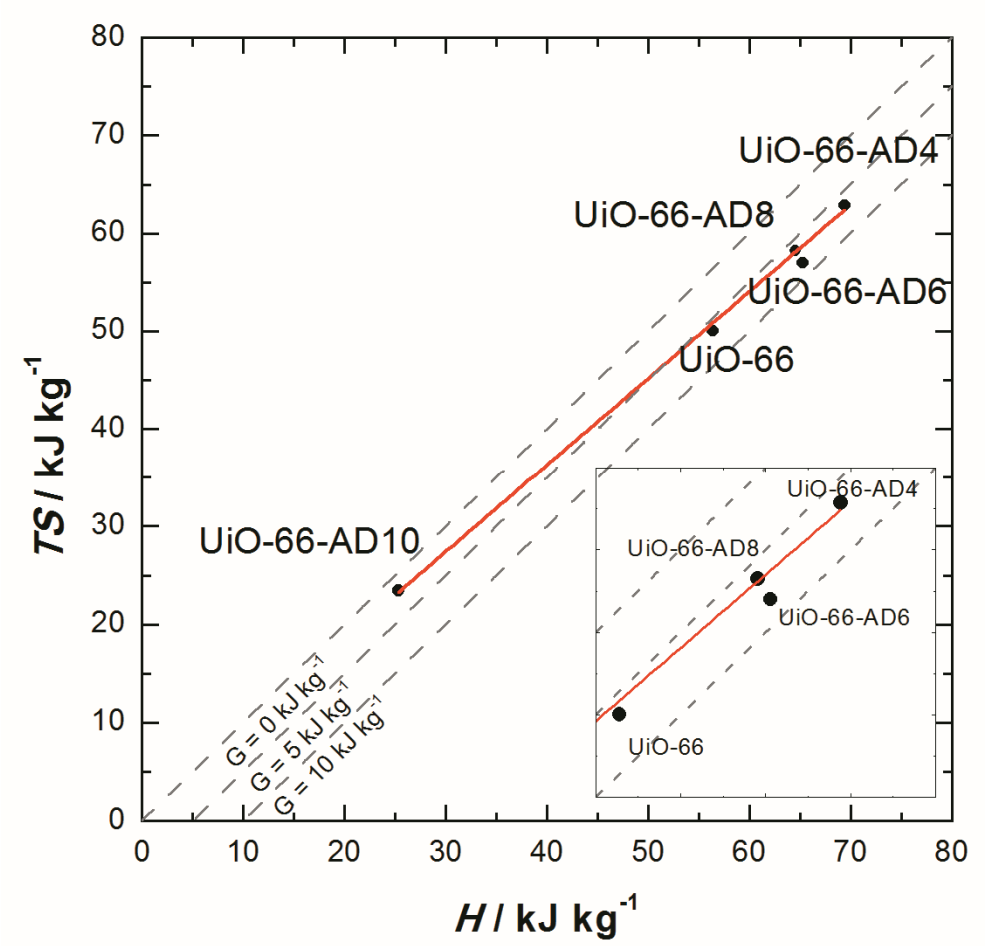

Figure 57 Linear relationship between the enthalpies and the entropies of CO_2 adsorption in UiO-66 and UiO-66-AD*n*s. Iso-value lines of the desorption free energy are drawn as dashed lines. Inset shows that the position of UiO-66-AD6 deviate from the regression line (solid line) by having reduced entropy, resulting in the highest desorption free energy value (8.29 kJ kg^{-1}) increased by 27% compared to that of UiO-66 (6.38 kJ kg^{-1}).

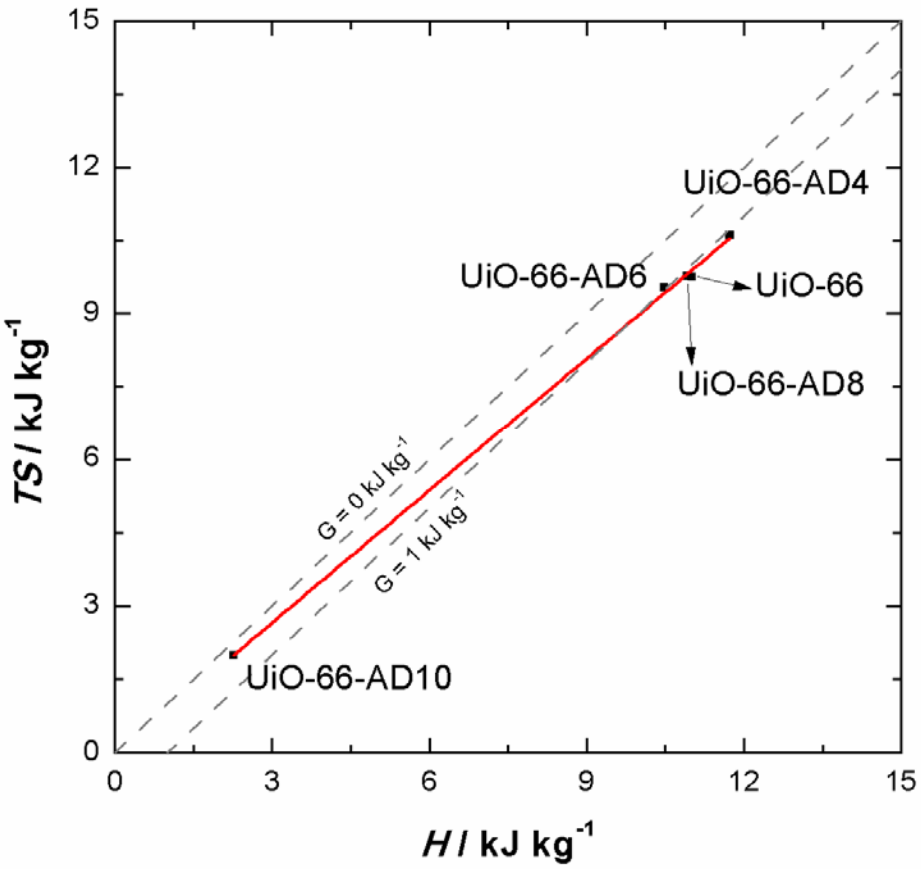

Figure 58 Linear relationship between the enthalpies and the entropies of CH_4 adsorption in UiO-66 and UiO-66-AD*n*s. Iso-value lines of the free energy are drawn as dashed lines.

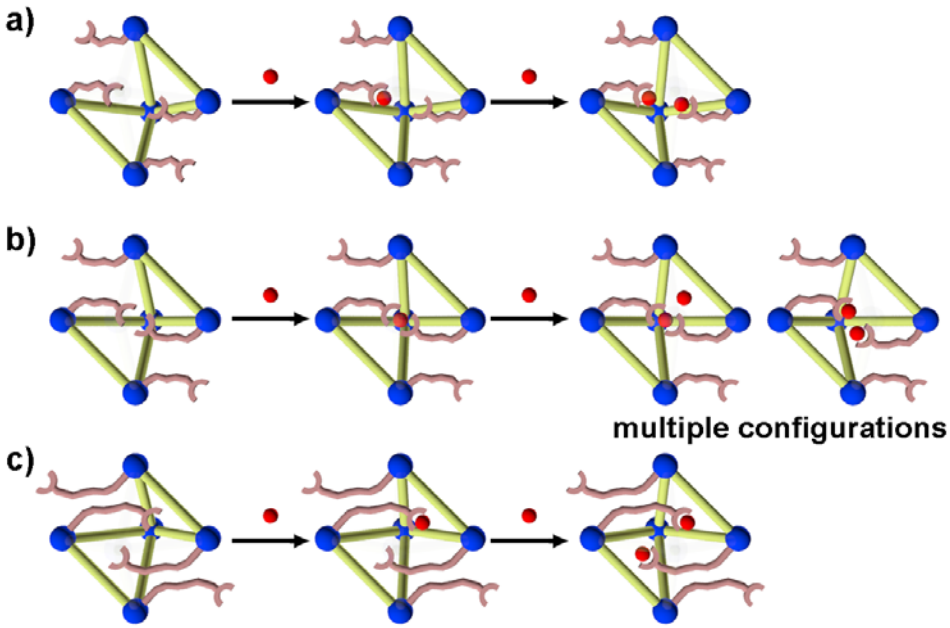

Figure 59 Proposed model for the effect of pendant length in the pores of UiO-66-AD*n*s on the differential enthalpy and differential entropy. a) UiO-66-AD4 (short length), b) UiO-66-AD6 (optimal length), and c) UiO-66-AD8 (long length). In the case of the pendant with an optimal length, multiple configurations are possible. $Zr_6O_4(OH)_4$ cluster, blue; terephthalate, yellow; alkanedioate, tan; CO_2, red.

The isosteric heats (Q_{st}) of the CO_2 and CH_4 adsorption were calculated by using Clausius-Clapeyron (C-C) equation as well as the virial equation (Table 11, and Figure 60 to Figure 64).[14] When the virial equation was used, the Q_{st} values at zero coverage could be calculated. When the Q_{st} values were calculated by the C-C equation, gas adsorption isotherms were fit to the Langmuir-Freundlich equation. In this case, Q_{st} values are diverged at zero coverage, and therefore the values at low coverage instead of zero coverage, are given in Table 11. The Q_{st} values depending on the amount of gas loading obtained from the virial equation fluctuate around the Q_{st}

values obtained from C-C equation since the virial equation contains polynomial terms. Regardless of the calculation methods, the Q_{st} values for the CO_2 adsorption increase in all UiO-66-AD*n*s compared with those in UiO-66, except the Q_{st} value of UiO-66-AD10 calculated by C-C equation. UiO-66-AD6 exhibits the highest Q_{st} values among all samples. Contrary to the CO_2 adsorption, Q_{st} values of CH_4 adsorption are not simply increased by carboxyl pendants. The Q_{st} values of CH_4 adsorption increase in UiO-66-AD6 and decrease in UiO-66-AD8 and UiO-66-AD10, regardless of the calculation methods.

Table 11 Q_{st} values of various samples.

	Q_{st} of CO_2 [kJ mol^{-1}]		Q_{st} of CH_4 [kJ mol^{-1}]	
	Virial[a]	Clausius-Clapeyron[b]	Virial[a]	Clausius-Clapeyron[c]
UiO-66	40.73	34.96	37.17	29.16
UiO-66-AD4	45.72	35.27	34.36	30.43
UiO-66-AD6	49.85	36.65	37.51	31.60
UiO-66-AD8	44.56	35.90	24.69	25.83
UiO-66-AD10	50.77	34.19	19.94	23.58

Calculated when [a] n_{ads} = 0 mmol g^{-1}, [b] n_{ads} = 0.05 mmol g^{-1}, [c] n_{ads} = 0.01 mmol g^{-1}.

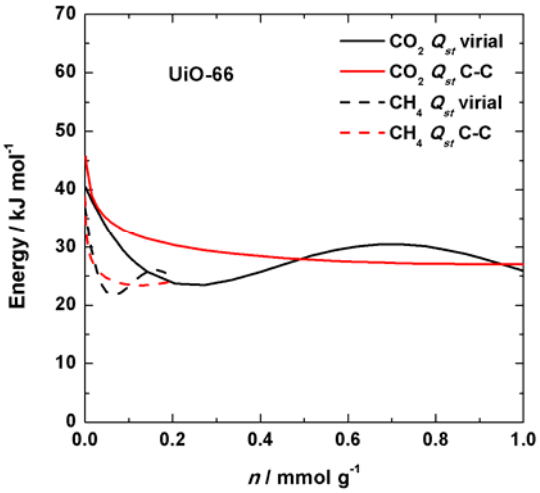

Figure 60 Comparison of isosteric heats of CO_2 (solid line) and CH_4 (dashed line) adsorption in UiO-66 derived by virial equation (black), and Clausius-Clapeyron equation (red).

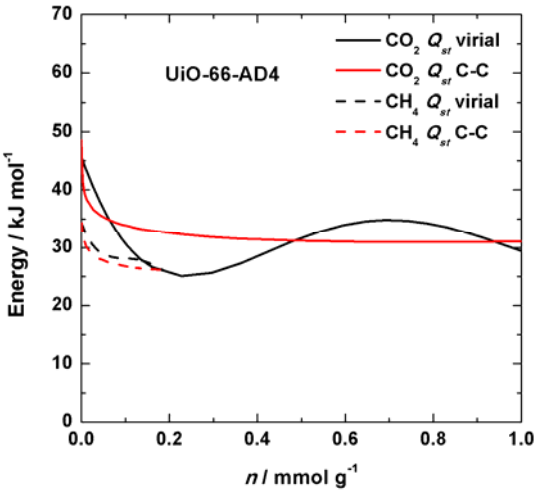

Figure 61 Comparison of isosteric heats of CO_2 (solid line) and CH_4 (dashed line) adsorption in UiO-66-AD4 derived by virial equation (black), and Clausius-Clapeyron equation (red).

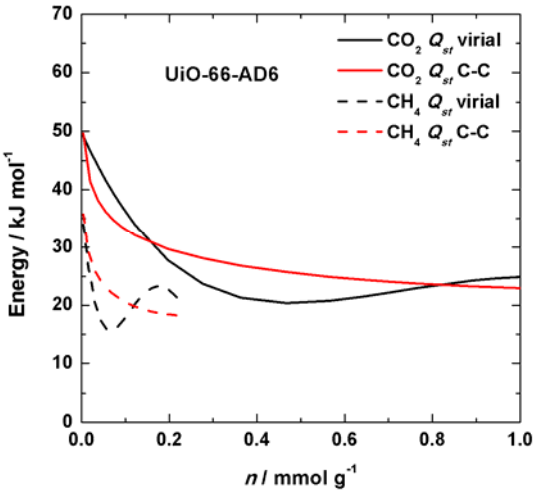

Figure 62 Comparison of isosteric heats of CO_2 (solid line) and CH_4 (dashed line) adsorption in UiO-66-AD6 derived by virial equation (black), and Clausius-Clapeyron equation (red).

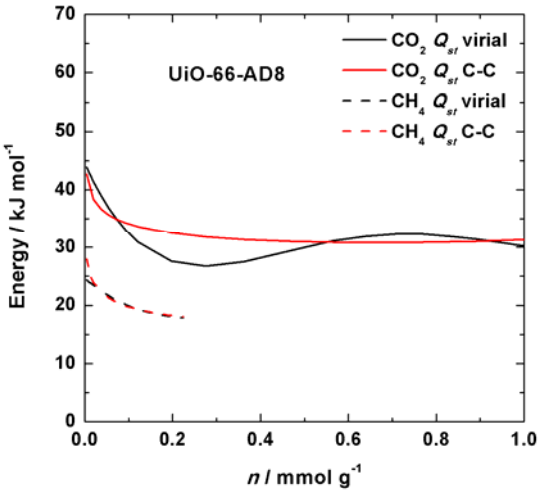

Figure 63 Comparison of isosteric heats of CO_2 (solid line) and CH_4 (dashed line) adsorption in UiO-66-AD8 derived by virial equation (black), and Clausius-Clapeyron equation (red).

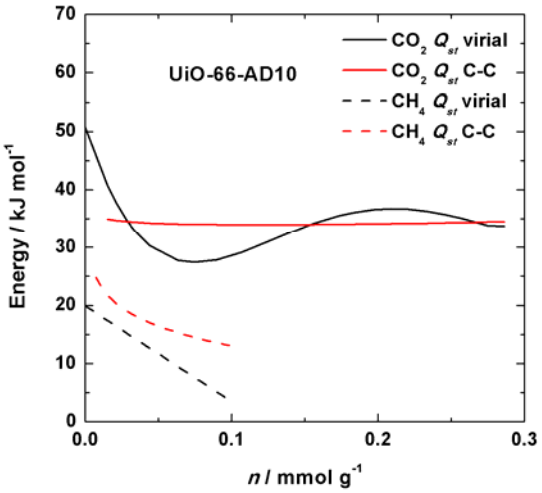

Figure 64 Comparison of isosteric heats of CO_2 (solid line) and CH_4 (dashed line) adsorption in UiO-66-AD10 derived by virial equation (black), and Clausius-Clapeyron equation (red).

II.3.4. Selectivity estimated by ideal adsorption solution theory (IAST)

A selectivity coefficient of ideal adsorption solution is calculated by the assumption that the free energies (G) of each gas adsorbed in a framework are identical at a fixed temperature (see the Experimental Section). The desorption free energy (G) is same as the πA, which is a product of spreading pressure and specific surface area used for describing the thermodynamics of surface adsorption.[152]

The selectivities of CO_2 adsorption over CH_4 at 273 K, 298 K, and 323 K were calculated to determine the applicability of UiO-66-AD*n*s for separations of landfill gas by using the vacuum swing adsorption (VSA) process (Table 12 and Figure 65). In addition to that, the selectivity of CO_2 adsorption over N_2 at 298 K was

also calculated for separations of flue gas using the same materials and the same method. It is assumed that the pressure of adsorption is 1.0 atm and that of desorption is 0.1 atm in VSA.[17] The selectivity values were calculated under the desorption conditions (0.1 atm), because the adsorption data should be extrapolated to P > 1 atm to calculate the free energies of the CH_4 sorption under adsorption conditions. The selectivity values for CO_2/CH_4 adsorption at 273 K calculated under the adsorption conditions did not converge in the cases of UiO-66-AD10.

Four adsorbent evaluation criteria suggested by Snurr group,[17] such as 1) CO_2 uptake under adsorption conditions, 2) working CO_2 capacity, 3) regenerability, and 4) selectivity, have been also calculated and the data are presented in Table 12. For landfill gas separation, all UiO-66-AD*n*s show significantly increased selectivity values of CO_2 adsorption over CH_4, compared to those of UiO-66. In particular, UiO-66-AD6 shows the highest selectivity values as well as the highest CO_2 uptake and the best working CO_2 capacity. In particular, the enhancement factor of the CO_2 uptake and the working CO_2 capacity in UiO-66-AD6 compared to those of UiO-66 increases with the increased temperature, from ca. 20% at 273 K to ca. 70% at 323 K

Table 12 The CO_2/CH_4 and CO_2/N_2 separation parameters of UiO-66 and UiO-66-AD*n*s for landfill gas and flue gas in VSA process.

	T/K	N^{ads}/ mmol g^{-1}	ΔN_{CO_2}/ mmol g^{-1}	Regenerability, R	IAST Selectivity, α [a]
			$CO_2:CH_4 = 50:50$		
UiO-66	273	2.104	1.671	0.794	10.4
	298	1.184	1.017	0.859	6.87
	323	0.568	0.508	0.894	6.87
UiO-66-AD4	273	2.486	1.948	0.784	12.6
	298	1.211	1.031	0.851	8.04
	323	0.620	0.545	0.879	9.05
UiO-66-AD6	273	2.636	2.063	0.783	15.0
	298	1.598	1.415	0.885	10.0
	323	0.945	0.864	0.914	10.1
UiO-66-AD8	273	2.331	1.848	0.793	12.3
	298	1.170	0.998	0.853	7.31
	323	0.536	0.476	0.888	10.9
UiO-66-AD10	273	0.903	0.738	0.817	16.1
	298	0.342	0.295	0.863	9.29
	323	0.162	0.140	0.864	8.25
			$CO_2:N_2 = 15:85$		
UiO-66	298	0.424	0.373	0.880	27.6
UiO-66-AD4	298	0.448	0.391	0.873	31.3
UiO-66-AD6	298	0.524	0.477	0.910	39.0
UiO-66-AD8	298	0.425	0.370	0.870	44.6
UiO-66-AD10	298	0.120	0.106	0.883	35.2

[a] calculated at desorption condition (P = 0.1 atm).

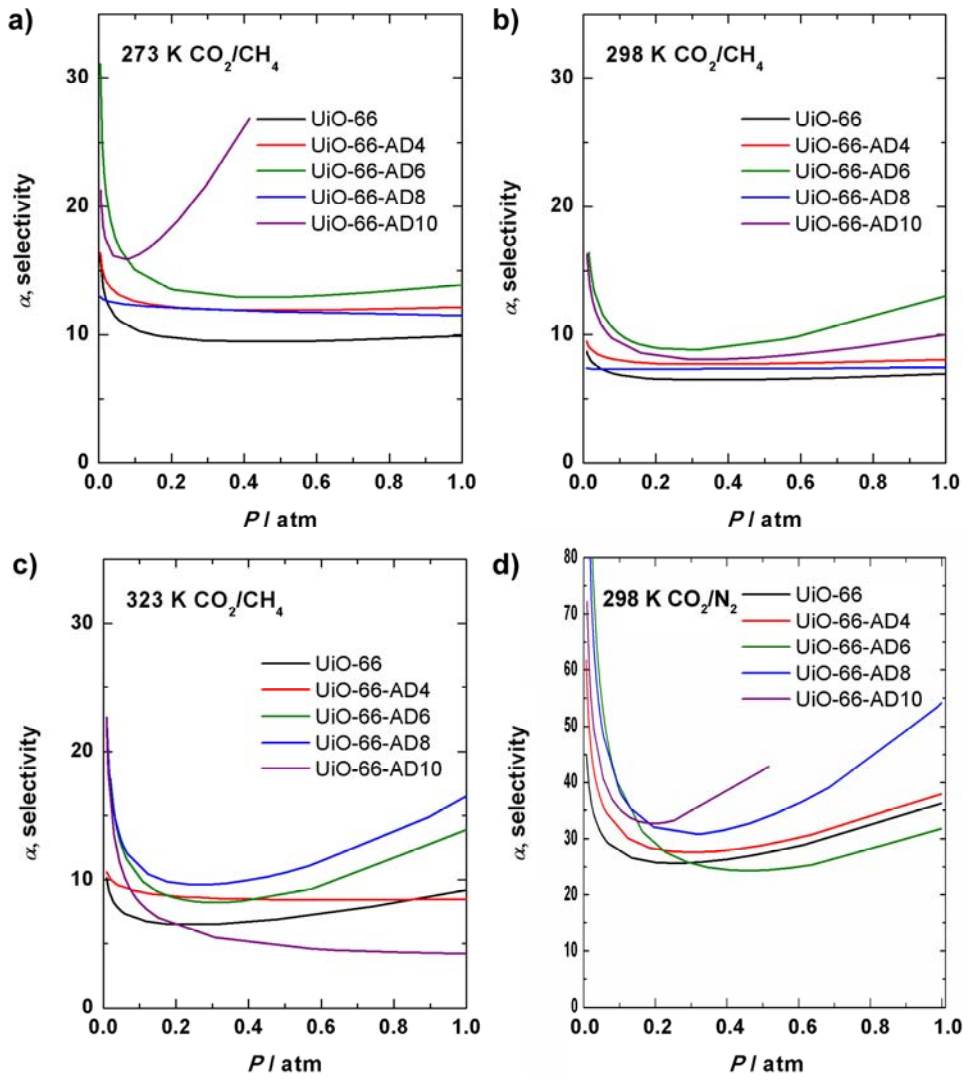

Figure 65 Calculated IAST selectivity of the CO_2 adsorption from the mixture of CO_2:CH_4 = 50:50 at a) 273 K b) 298 K, and c) 323 K; and d) mixture of CO_2:N_2 = 15:85 at 298 K. UiO-66 (black), UiO-66-AD4 (red), UiO-66-AD6 (green), UiO-66-AD8 (blue), and UiO-66-AD10 (violet)..

II.4. Conclusions

We have prepared various UiO-66 derivatives, UiO-66-AD*n*s, which are decorated with a series of flexible carboxylic acid pendants with various lengths by the post synthetic ligand-exchange, and investigated the thermodynamic aspects of the CO_2 adsorption. We found the unprecedented 1:2 ligand substitution of a terephthalate in UiO-66 with two alkanedioates. In particular, UiO-66-AD6 that contains adipic acid pendants exhibits significantly enhanced CO_2 separation abilities for landfill gas, showing the enhanced working capacity and significantly increased selectivity of CO_2 adsorption over CH_4 and N_2, compared to those of UiO-66 and other UiO-66-AD*n*s. By the analysis of enthalpy and entropy, it was revealed that the increased CO_2 capacity of UiO-66-AD6 is attributed to the increased enthalpy loss and the mitigated entropy loss on CO_2 adsorption achieved via the dangling carboxyl pendants with appropriate length. The flexible carboxylic acid pendants with an appropriate length effectively accommodate CO_2, reducing the entropy loss upon CO_2 adsorption. This phenomenon is not manifested in the CH_4 adsorption due to the weak interaction between the CH_4 molecules and the pendant. The present work demonstrates that the introduction of dangling carboxyl pendants with appropriate length in a MOF by the post-synthetic ligand exchange can enhance CO_2 separation performances of the MOF at high temperatures.

References

1. Hassol, S. J. ACIA, 2004. Impacts of a Warming Arctic: Arctic Climate Impact Assessment. ACIA Overview report. Cambridge University Press. *Arct. Clim. Impact Assess.* 140 pp (2004).

2. J., B. T. Recent Greenhouse Gas Concentrations. *Carbon Dioxide Inf. Anal. Cent.* (2013). doi:10.3334/CDIAC/atg.032

3. International Energy Agency. CO2 EMISSIONS FROM FUEL COMBUSTION. (2012).

4. Manua Loa. Recent Monthly Average Mauna Loa CO2. (2013).

5. Stangeland, A. The Bellona Foundation. (2007).

6. CO2CRC. Global emissions. at <http://www.co2crc.com.au/images/imagelibrary/gen_diag/Global-Emissions&World-Population_media.jpg>

7. Rohde, R. A. Atmospheric Transmission. *Glob. Warm. Art* (2007). at <http://www.globalwarmingart.com/wiki/File:Atmospheric_Transmission_png>

8. Stangeland, A. How to Combat Global Warming. (2008).

9. Metz, B., Davidson, O., Coninck, H. de, Loos, M. & Meyer, L. Carbon Dioxide Capture and Storage. *IPCC Spec. Rep.* (2005).

10. CO2CRC. CCS facilities. at <http://www.co2crc.com.au/images/imagelibrary/gen_diag/ccs_facilities_media.jpg>

11. Figueroa, J. D., Fout, T., Plasynski, S., McIlvried, H. & Srivastava, R. D. Advances in CO2 capture technology—The U.S. Department of Energy's Carbon Sequestration Program. *Int. J. Greenh. Gas Control* **2,** 9–20 (2008).

12. Figueroa, J. D., Fout, T., Plasynski, S., McIlvried, H. & Srivastava, R. D. Advances in CO2 capture technology—The U.S. Department of Energy's Carbon Sequestration Program. *Int. J. Greenh. Gas Control* **2,** 9–20 (2008).

13. Lackner, K. S. Climate change. A guide to CO2 sequestration. *Science* **300,** 1677–8 (2003).

14. Sumida, K. *et al.* Carbon dioxide capture in metal-organic frameworks. *Chem. Rev.* **112,** 724–81 (2011).

15. Clarke Energy Co. Syngas Composition. at <http://www.clarke-energy.com/gas-type/synthesis-gas-syngas/>

16. Tchobanoglous, G., Theisen, H. & Vigil, S. A. *Integrated solid waste management: engineering principles and management issues*. 382 (1993).

17. Bae, Y.-S. & Snurr, R. Q. Development and evaluation of porous materials for carbon dioxide separation and capture. *Angew. Chem. Int. Ed. Engl.* **50,** 11586–96 (2011).

18. Wilmer, C. E., Farha, O. K., Bae, Y.-S., Hupp, J. T. & Snurr, R. Q. Structure–property relationships of porous materials for carbon dioxide separation and capture. *Energy Environ. Sci.* **5,** 9849 (2012).

19. Wang, B., Côté, A. P., Furukawa, H., O'Keeffe, M. & Yaghi, O. M. Colossal cages in zeolitic imidazolate frameworks as selective carbon dioxide reservoirs. *Nature* **453,** 207–11 (2008).

20. Low, J. J. *et al.* Virtual high throughput screening confirmed experimentally: porous coordination polymer hydration. *J. Am. Chem. Soc.* **131,** 15834–42 (2009).

21. Sartori, G. & Savage, D. W. Sterically hindered amines for carbon dioxide removal from gases. *Ind. Eng. Chem. Fundam.* **22,** 239–249 (1983).

22. Chue, K. T., Kim, J. N., Yoo, Y. J., Cho, S. H. & Yang, R. T. Comparison of Activated Carbon and Zeolite 13X for CO2 Recovery from Flue Gas by Pressure Swing Adsorption. *Ind. Eng. Chem. Res.* **34,** 591–598 (1995).

23. Batten, S. R. *et al.* Terminology of metal–organic frameworks and coordination polymers (IUPAC Recommendations 2013). *Pure Appl. Chem.* **85,** 1715–1724 (2013).

24. Stock, N. & Biswas, S. Synthesis of metal-organic frameworks (MOFs): routes to various MOF topologies, morphologies, and composites. *Chem. Rev.* **112,** 933–69 (2012).

25. Shah, M., McCarthy, M. C., Sachdeva, S., Lee, A. K. & Jeong, H. Current Status of Metal–Organic Framework Membranes for Gas Separations: Promises and Challenges. *Ind. Eng. Chem. Res.* **51,** 2179–2199 (2012).

26. Suh, M. P., Park, H. J., Prasad, T. K. & Lim, D.-W. Hydrogen storage in metal-organic frameworks. *Chem. Rev.* **112,** 782–835 (2012).

27. Li, J.-R., Kuppler, R. J. & Zhou, H.-C. Selective gas adsorption and separation in metal-organic frameworks. *Chem. Soc. Rev.* **38,** 1477–504 (2009).

28. Kreno, L. E. *et al.* Metal-organic framework materials as chemical sensors. *Chem. Rev.* **112,** 1105–25 (2012).

29. Lee, J. *et al.* Metal-organic framework materials as catalysts. *Chem. Soc. Rev.* **38,** 1450–9 (2009).

30. Hailian, L., Eddaoudi, M., O'Keeffe, M. & Yaghi, O. M. Design and synthesis of an exceptionally stable and highly porous metal-organic framework. *Nature* **402,** 276–279 (1999).

31. Chui, S. S. A Chemically Functionalizable Nanoporous Material [Cu3(TMA)2(H2O)3]n. *Science (80-.).* **283,** 1148–1150 (1999).

32. Férey, G. *et al.* A hybrid solid with giant pores prepared by a combination of targeted chemistry, simulation, and powder diffraction. *Angew. Chem. Int. Ed. Engl.* **43,** 6296–301 (2004).

33. Cavka, J. H. *et al.* A new zirconium inorganic building brick forming metal organic frameworks with exceptional stability. *J. Am. Chem. Soc.* **130,** 13850–1 (2008).

34. Loiseau, T. *et al.* A rationale for the large breathing of the porous aluminum terephthalate (MIL-53) upon hydration. *Chemistry* **10,** 1373–82 (2004).

35. Furukawa, H. *et al.* Ultrahigh porosity in metal-organic frameworks. *Science* **329,** 424–8 (2010).

36. Düren, T., Millange, F., Férey, G., Walton, K. S. & Snurr, R. Q. Calculating Geometric Surface Areas as a Characterization Tool for Metal−Organic Frameworks. *J. Phys. Chem. C* **111,** 15350–15356 (2007).

37. Furukawa, H., Miller, A. & Yaghi, O. M. Independent verification of the saturation hydrogen uptake in MOF-177 and establishment of a benchmark for hydrogen adsorption in metal–organic frameworks. *J. Mater. Chem.* **17,** 3197–3204 (2007).

38. Wang, B., Côté, A. P., Furukawa, H., O'Keeffe, M. & Yaghi, O. M. Colossal cages in zeolitic imidazolate frameworks as selective carbon dioxide reservoirs. *Nature* **453,** 207–11 (2008).

39. Britt, D., Furukawa, H., Wang, B., Glover, T. G. & Yaghi, O. M. Highly efficient separation of carbon dioxide by a metal-organic framework replete with open metal sites. *Proc. Natl. Acad. Sci. U. S. A.* **106,** 20637–40 (2009).

40. Hamon, L. *et al.* Co-adsorption and separation of CO2-CH4 mixtures in the highly flexible MIL-53(Cr) MOF. *J. Am. Chem. Soc.* **131,** 17490–9 (2009).

41. Banerjee, R. *et al.* High-throughput synthesis of zeolitic imidazolate frameworks and application to CO2 capture. *Science* **319,** 939–43 (2008).

42. Bastin, L. *et al.* A Microporous Metal-Organic Framework for Separation of CO2/N2 and CO2/CH4 by Fixed-Bed Adsorption. *J. Phys. Chem. C* **112,** 1575–1581 (2008).

43. Xiang, S. *et al.* Microporous metal-organic framework with potential for carbon dioxide capture at ambient conditions. *Nat. Commun.* **3,** 954 (2012).

44. Demessence, A., D'Alessandro, D. M., Foo, M. L. & Long, J. R. Strong CO2 binding in a water-stable, triazolate-bridged metal-organic framework functionalized with ethylenediamine. *J. Am. Chem. Soc.* **131,** 8784–6 (2009).

45. Park, H. J., Cheon, Y. E. & Suh, M. P. Post-synthetic reversible incorporation of organic linkers into porous metal-organic frameworks through single-crystal-to-single-crystal transformations and modification of gas-sorption properties. *Chemistry* **16,** 11662–9 (2010).

46. Park, H. J. & Suh, M. P. Enhanced isosteric heat, selectivity, and uptake capacity of CO2 adsorption in a metal-organic framework by impregnated metal ions. *Chem. Sci.* **4,** 685 (2013).

47. McDonald, T. M. *et al.* Capture of carbon dioxide from air and flue gas in the alkylamine-appended metal-organic framework mmen-Mg2(dobpdc). *J. Am. Chem. Soc.* **134,** 7056–65 (2012).

48. Banerjee, R. *et al.* High-throughput synthesis of zeolitic imidazolate frameworks and application to CO2 capture. *Science* **319,** 939–43 (2008).

49. Bourrelly, S. *et al.* Different adsorption behaviors of methane and carbon dioxide in the isotypic nanoporous metal terephthalates MIL-53 and MIL-47. *J. Am. Chem. Soc.* **127,** 13519–21 (2005).

50. Wu, D. *et al.* Direct calorimetric measurement of enthalpy of adsorption of carbon dioxide on CD-MOF-2, a green metal-organic framework. *J. Am. Chem. Soc.* **135,** 6790–3 (2013).

51. Dinca, M. & Long, J. R. High-enthalpy hydrogen adsorption in cation-exchanged variants of the microporous metal-organic framework Mn3[(Mn4Cl)3(BTT)8(CH3OH)10]2. *J. Am. Chem. Soc.* **129,** 11172–6 (2007).

52. Deng, H. *et al.* Multiple functional groups of varying ratios in metal-organic frameworks. *Science* **327,** 846–50 (2010).

53. Kim, M., Cahill, J. F., Su, Y., Prather, K. a. & Cohen, S. M. Postsynthetic ligand exchange as a route to functionalization of "inert" metal–organic frameworks. *Chem. Sci.* **3,** 126 (2012).

54. Kim, M., Cahill, J. F., Fei, H., Prather, K. a & Cohen, S. M. Postsynthetic ligand and cation exchange in robust metal-organic frameworks. *J. Am. Chem. Soc.* **134,** 18082–8 (2012).

55. Chui, S. S. A Chemically Functionalizable Nanoporous Material [Cu3(TMA)2(H2O)3]n. *Science (80-.).* **283,** 1148–1150 (1999).

56. Serre, C. *et al.* Very Large Breathing Effect in the First Nanoporous Chromium(III)-Based Solids: MIL-53 or Cr III (OH)·{O 2 C−C 6 H 4 −CO

2 }·{HO 2 C−C 6 H 4 −CO 2 H} x ·H 2 O y. *J. Am. Chem. Soc.* **124,** 13519–13526 (2002).

57. Férey, G. *et al.* A chromium terephthalate-based solid with unusually large pore volumes and surface area. *Science* **309,** 2040–2 (2005).

58. Loiseau, T. *et al.* A rationale for the large breathing of the porous aluminum terephthalate (MIL-53) upon hydration. *Chemistry* **10,** 1373–82 (2004).

59. Park, K. S. *et al.* Exceptional chemical and thermal stability of zeolitic imidazolate frameworks. *Proc. Natl. Acad. Sci. U. S. A.* **103,** 10186–91 (2006).

60. Yuan, D., Zhao, D., Sun, D. & Zhou, H.-C. An isoreticular series of metal-organic frameworks with dendritic hexacarboxylate ligands and exceptionally high gas-uptake capacity. *Angew. Chem. Int. Ed. Engl.* **49,** 5357–61 (2010).

61. Yuan, D., Zhao, D., Sun, D. & Zhou, H.-C. An isoreticular series of metal-organic frameworks with dendritic hexacarboxylate ligands and exceptionally high gas-uptake capacity. *Angew. Chem. Int. Ed. Engl.* **49,** 5357–61 (2010).

62. Farha, O. K. *et al.* De novo synthesis of a metal-organic framework material featuring ultrahigh surface area and gas storage capacities. *Nat. Chem.* **2,** 944–8 (2010).

63. Deng, H. *et al.* Multiple functional groups of varying ratios in metal-organic frameworks. *Science* **327,** 846–50 (2010).

64. Ma, L., Jin, A., Xie, Z. & Lin, W. Freeze drying significantly increases permanent porosity and hydrogen uptake in 4,4-connected metal-organic frameworks. *Angew. Chem. Int. Ed. Engl.* **48,** 9905–8 (2009).

65. Nelson, A. P., Farha, O. K., Mulfort, K. L. & Hupp, J. T. Supercritical processing as a route to high internal surface areas and permanent microporosity in metal-organic framework materials. *J. Am. Chem. Soc.* **131,** 458–60 (2009).

66. Farha, O. K. *et al.* De novo synthesis of a metal-organic framework material featuring ultrahigh surface area and gas storage capacities. *Nat. Chem.* **2,** 944–8 (2010).

67. Suh, M. P., Ko, J. W. & Choi, H. J. A Metal−Organic Bilayer Open Framework with a Dynamic Component: Single-Crystal-to-Single-Crystal Transformations. *J. Am. Chem. Soc.* **124,** 10976–10977 (2002).

68. Serre, C. *et al.* Very Large Breathing Effect in the First Nanoporous Chromium(III)-Based Solids: MIL-53 or Cr III (OH)·{O 2 C−C 6 H 4 −CO 2 }·{HO 2 C−C 6 H 4 −CO 2 H} x ·H 2 O y. *J. Am. Chem. Soc.* **124,** 13519–13526 (2002).

69. Lee, E. Y. & Suh, M. P. A robust porous material constructed of linear coordination polymer chains: reversible single-crystal to single-crystal transformations upon dehydration and rehydration. *Angew. Chem. Int. Ed. Engl.* **43,** 2798–801 (2004).

70. Choi, H. J. & Suh, M. P. Dynamic and redox active pillared bilayer open framework: single-crystal-to-single-crystal transformations upon guest removal, guest exchange, and framework oxidation. *J. Am. Chem. Soc.* **126,** 15844–51 (2004).

71. Park, H. J. & Suh, M. P. Mixed-ligand metal-organic frameworks with large pores: gas sorption properties and single-crystal-to-single-crystal transformation on guest exchange. *Chemistry* **14,** 8812–21 (2008).

72. Suh, M. P., Ko, J. W. & Choi, H. J. A Metal−Organic Bilayer Open Framework with a Dynamic Component: Single-Crystal-to-Single-Crystal Transformations. *J. Am. Chem. Soc.* **124,** 10976–10977 (2002).

73. Li, T., Kozlowski, M. T., Doud, E. A., Blakely, M. N. & Rosi, N. L. Stepwise Ligand Exchange for the Preparation of a Family of Mesoporous MOFs. *J. Am. Chem. Soc.* **100,** 101–104 (2013).

74. Choi, H.-S. & Suh, M. P. Highly selective CO(2) capture in flexible 3D coordination polymer networks. *Angew. Chem. Int. Ed. Engl.* **48,** 6865–9 (2009).

75. Kitaura, R., Seki, K., Akiyama, G. & Kitagawa, S. Porous coordination-polymer crystals with gated channels specific for supercritical gases. *Angew. Chem. Int. Ed. Engl.* **42,** 428–31 (2003).

76. Choi, H. J., Dincă, M. & Long, J. R. Broadly hysteretic H2 adsorption in the microporous metal-organic framework Co(1,4-benzenedipyrazolate). *J. Am. Chem. Soc.* **130,** 7848–50 (2008).

77. Salles, F. *et al.* Multistep N2 breathing in the metal-organic framework co(1,4-benzenedipyrazolate). *J. Am. Chem. Soc.* **132,** 13782–8 (2010).

78. Bourrelly, S. *et al.* Different adsorption behaviors of methane and carbon dioxide in the isotypic nanoporous metal terephthalates MIL-53 and MIL-47. *J. Am. Chem. Soc.* **127,** 13519–21 (2005).

79. Park, J. *et al.* Reversible alteration of CO2 adsorption upon photochemical or thermal treatment in a metal-organic framework. *J. Am. Chem. Soc.* **134,** 99–102 (2012).

80. Lyndon, R. *et al.* Dynamic photo-switching in metal-organic frameworks as a route to low-energy carbon dioxide capture and release. *Angew. Chem. Int. Ed. Engl.* **52,** 3695–8 (2013).

81. Park, J. *et al.* Reversible alteration of CO2 adsorption upon photochemical or thermal treatment in a metal-organic framework. *J. Am. Chem. Soc.* **134,** 99–102 (2012).

82. Serre, C. *et al.* An Explanation for the Very Large Breathing Effect of a Metal–Organic Framework during CO2 Adsorption. *Adv. Mater.* **19,** 2246–2251 (2007).

83. Hamon, L. *et al.* Co-adsorption and separation of CO2-CH4 mixtures in the highly flexible MIL-53(Cr) MOF. *J. Am. Chem. Soc.* **131,** 17490–9 (2009).

84. Serre, C. *et al.* Role of solvent-host interactions that lead to very large swelling of hybrid frameworks. *Science* **315,** 1828–31 (2007).

85. Dybtsev, D. N., Chun, H. & Kim, K. Rigid and flexible: a highly porous metal-organic framework with unusual guest-dependent dynamic behavior. *Angew. Chem. Int. Ed. Engl.* **43,** 5033–6 (2004).

86. Seki, K. & Mori, W. Syntheses and Characterization of Microporous Coordination Polymers with Open Frameworks. *J. Phys. Chem. B* **106,** 1380–1385 (2002).

87. Chun, H., Dybtsev, D. N., Kim, H. & Kim, K. Synthesis, X-ray crystal structures, and gas sorption properties of pillared square grid nets based on paddle-wheel motifs: implications for hydrogen storage in porous materials. *Chemistry* **11,** 3521–9 (2005).

88. Choi, H. J., Dincă, M. & Long, J. R. Broadly hysteretic H2 adsorption in the microporous metal-organic framework Co(1,4-benzenedipyrazolate). *J. Am. Chem. Soc.* **130,** 7848–50 (2008).

89. Salles, F. *et al.* Multistep N2 breathing in the metal-organic framework co(1,4-benzenedipyrazolate). *J. Am. Chem. Soc.* **132,** 13782–8 (2010).

90. Férey, G. & Serre, C. Large breathing effects in three-dimensional porous hybrid matter: facts, analyses, rules and consequences. *Chem. Soc. Rev.* **38,** 1380–99 (2009).

91. Férey, G. & Serre, C. Large breathing effects in three-dimensional porous hybrid matter: facts, analyses, rules and consequences. *Chem. Soc. Rev.* **38,** 1380–99 (2009).

92. Serre, C. *et al.* An Explanation for the Very Large Breathing Effect of a Metal–Organic Framework during CO2 Adsorption. *Adv. Mater.* **19,** 2246–2251 (2007).

93. Couck, S. *et al.* An amine-functionalized MIL-53 metal-organic framework with large separation power for CO2 and CH4. *J. Am. Chem. Soc.* **131,** 6326–7 (2009).

94. Devic, T. *et al.* Effect of the organic functionalization of flexible MOFs on the adsorption of CO2. *J. Mater. Chem.* **22,** 10266 (2012).

95. Couck, S. *et al.* An amine-functionalized MIL-53 metal-organic framework with large separation power for CO2 and CH4. *J. Am. Chem. Soc.* **131,** 6326–7 (2009).

96. Devic, T. *et al.* Effect of the organic functionalization of flexible MOFs on the adsorption of CO2. *J. Mater. Chem.* **22,** 10266 (2012).

97. Chun, H. & Seo, J. Discrimination of small gas molecules through adsorption: reverse selectivity for hydrogen in a flexible metal-organic framework. *Inorg. Chem.* **48,** 9980–2 (2009).

98. Barea, E. *et al.* A flexible pro-porous coordination polymer: non-conventional synthesis and separation properties towards CO(2)/CH(4) mixtures. *Chemistry* **16,** 931–7 (2010).

99. Wu, H., Reali, R. S., Smith, D. A., Trachtenberg, M. C. & Li, J. Highly selective CO2 capture by a flexible microporous metal-organic framework (MMOF) material. *Chemistry* **16,** 13951–4 (2010).

100. Zhang, J., Wu, H., Emge, T. J. & Li, J. A flexible MMOF exhibiting high selectivity for CO(2) over N(2), CH(4) and other small gases. *Chem. Commun. (Camb).* **46,** 9152–4 (2010).

101. Wu, H., Reali, R. S., Smith, D. A., Trachtenberg, M. C. & Li, J. Highly selective CO2 capture by a flexible microporous metal-organic framework (MMOF) material. *Chemistry* **16,** 13951–4 (2010).

102. Zhang, J., Wu, H., Emge, T. J. & Li, J. A flexible MMOF exhibiting high selectivity for CO(2) over N(2), CH(4) and other small gases. *Chem. Commun. (Camb).* **46,** 9152–4 (2010).

103. Choi, H.-S. & Suh, M. P. Highly selective CO(2) capture in flexible 3D coordination polymer networks. *Angew. Chem. Int. Ed. Engl.* **48,** 6865–9 (2009).

104. Lu, Z. *et al.* Water Stable Metal–Organic Framework Evolutionally Formed from a Flexible Multidentate Ligand with Acylamide Groups for Selective CO 2 Adsorption. *Cryst. Growth Des.* **12,** 1081–1084 (2012).

105. Kim, T. K. & Suh, M. P. Selective CO2 adsorption in a flexible non-interpenetrated metal-organic framework. *Chem. Commun. (Camb).* **47,** 4258–60 (2011).

106. Zheng, B., Bai, J., Duan, J., Wojtas, L. & Zaworotko, M. J. Enhanced CO2 binding affinity of a high-uptake rht-type metal-organic framework decorated with acylamide groups. *J. Am. Chem. Soc.* **133,** 748–51 (2011).

107. Zheng, B., Yang, Z., Bai, J., Li, Y. & Li, S. High and selective CO2 capture by two mesoporous acylamide-functionalized rht-type metal-organic frameworks. *Chem. Commun. (Camb).* **48,** 7025–7 (2012).

108. Tan, Y.-X., Wang, F., Kang, Y. & Zhang, J. Dynamic microporous indium(III)-4,4'-oxybis(benzoate) framework with high selectivity for the adsorption of CO2 over N2. *Chem. Commun. (Camb).* **47,** 770–2 (2011).

109. Hong, D. H. & Suh, M. P. Selective CO2 adsorption in a metal-organic framework constructed from an organic ligand with flexible joints. *Chem. Commun. (Camb).* **48,** 9168–70 (2012).

110. Kitaura, R., Seki, K., Akiyama, G. & Kitagawa, S. Porous coordination-polymer crystals with gated channels specific for supercritical gases. *Angew. Chem. Int. Ed. Engl.* **42,** 428–31 (2003).

111. Maji, T. K., Matsuda, R. & Kitagawa, S. A flexible interpenetrating coordination framework with a bimodal porous functionality. *Nat. Mater.* **6,** 142–8 (2007).

112. Maji, T. K., Matsuda, R. & Kitagawa, S. A flexible interpenetrating coordination framework with a bimodal porous functionality. *Nat. Mater.* **6,** 142–8 (2007).

113. Henke, S., Schmid, R., Grunwaldt, J.-D. & Fischer, R. A. Flexibility and sorption selectivity in rigid metal-organic frameworks: the impact of ether-functionalised linkers. *Chemistry* **16,** 14296–306 (2010).

114. Henke, S. & Fischer, R. A. Gated channels in a honeycomb-like zinc-dicarboxylate-bipyridine framework with flexible alkyl ether side chains. *J. Am. Chem. Soc.* **133,** 2064–7 (2011).

115. Henke, S., Schneemann, A., Wütscher, A. & Fischer, R. A. Directing the breathing behavior of pillared-layered metal-organic frameworks via a systematic library of functionalized linkers bearing flexible substituents. *J. Am. Chem. Soc.* **134,** 9464–74 (2012).

116. Henke, S., Schneemann, A., Wütscher, A. & Fischer, R. A. Directing the breathing behavior of pillared-layered metal-organic frameworks via a systematic library of functionalized linkers bearing flexible substituents. *J. Am. Chem. Soc.* **134,** 9464–74 (2012).

117. Seo, J., Matsuda, R., Sakamoto, H., Bonneau, C. & Kitagawa, S. A pillared-layer coordination polymer with a rotatable pillar acting as a molecular gate for guest molecules. *J. Am. Chem. Soc.* **131,** 12792–800 (2009).

118. Ullmann, F. & Sponagel, P. Ueber die Phenylirung von Phenolen. *Berichte der Dtsch. Chem. Gesellschaft* **38,** 2211–2212 (1905).

119. Arvai, A. J. & Nielsen, C. ADSC Quantum-210 ADX Program. (1983).

120. Otwinowski, Z. & Minor, W. *Methods in Enzymology, vol. 276*. 307 (Academic Press, 1997).

121. Sheldrick, G. M. A short history of SHELX. *Acta Crystallogr. A.* **64,** 112–22 (2008).

122. Sheldrick, G. M. SHELEX97, Program for the crystal structure refinement. (1997).

123. Spek, A. L. PLATON99, A Multipurpose Crystallographic Tool. (1999).

124. Boultif, A. & Louër, D. Powder pattern indexing with the dichotomy method. *J. Appl. Crystallogr.* **37,** 724–731 (2004).

125. Spek, A. L. PLATON99, A Multipurpose Crystallographic Tool. (1999).

126. Horike, S., Inubushi, Y., Hori, T., Fukushima, T. & Kitagawa, S. A solid solution approach to 2D coordination polymers for CH4/CO2 and CH4/C2H6 gas separation: equilibrium and kinetic studies. *Chem. Sci.* **3,** 116 (2012).

127. Britt, D., Furukawa, H., Wang, B., Glover, T. G. & Yaghi, O. M. Highly efficient separation of carbon dioxide by a metal-organic framework replete with open metal sites. *Proc. Natl. Acad. Sci. U. S. A.* **106,** 20637–40 (2009).

128. Côté, A. P. *et al.* Porous, crystalline, covalent organic frameworks. *Science* **310,** 1166–70 (2005).

129. Lau, C. H., Babarao, R. & Hill, M. R. A route to drastic increase of CO2 uptake in Zr metal organic framework UiO-66. *Chem. Commun. (Camb).* **49,** 3634–6 (2013).

130. Kim, M. & Cohen, S. M. Discovery, development, and functionalization of Zr(iv)-based metal–organic frameworks. *CrystEngComm* **14,** 4096 (2012).

131. Tanabe, K. K. & Cohen, S. M. Postsynthetic modification of metal-organic frameworks--a progress report. *Chem. Soc. Rev.* **40,** 498–519 (2011).

132. Prasad, T. K., Hong, D. H. & Suh, M. P. High gas sorption and metal-ion exchange of microporous metal-organic frameworks with incorporated imide groups. *Chemistry* **16,** 14043–14050 (2010).

133. Hwang, Y. K. *et al.* Amine grafting on coordinatively unsaturated metal centers of MOFs: consequences for catalysis and metal encapsulation. *Angew. Chem. Int. Ed. Engl.* **47,** 4144–8 (2008).

134. Das, A. *et al.* Application of the piperazine-grafted CuBTTri metal-organic framework in postcombustion carbon dioxide capture. *Microporous Mesoporous Mater.* **174,** 74–80 (2013).

135. Das, A. *et al.* Carbon dioxide adsorption by physisorption and chemisorption interactions in piperazine-grafted Ni2(dobdc) (dobdc = 1,4-dioxido-2,5-benzenedicarboxylate). *Dalton Trans.* **41,** 11739–44 (2012).

136. Choi, S., Watanabe, T., Bae, T.-H., Sholl, D. S. & Jones, C. W. Modification of the Mg/DOBDC MOF with Amines to Enhance CO 2 Adsorption from Ultradilute Gases. *J. Phys. Chem. Lett.* **3,** 1136–1141 (2012).

137. Lee, Y.-G., Moon, H. R., Cheon, Y. E. & Suh, M. P. A comparison of the H2 sorption capacities of isostructural metal-organic frameworks with and without accessible metal sites: [{Zn2(abtc)(dmf)2}3] and [{Cu2(abtc)(dmf)2}3] versus [{Cu2(abtc)}3]. *Angew. Chem. Int. Ed. Engl.* **47,** 7741–5 (2008).

138. Choi, S., Watanabe, T., Bae, T.-H., Sholl, D. S. & Jones, C. W. Modification of the Mg/DOBDC MOF with Amines to Enhance CO 2 Adsorption from Ultradilute Gases. *J. Phys. Chem. Lett.* **3,** 1136–1141 (2012).

139. Das, A. *et al.* Carbon dioxide adsorption by physisorption and chemisorption interactions in piperazine-grafted Ni2(dobdc) (dobdc = 1,4-dioxido-2,5-benzenedicarboxylate). *Dalton Trans.* **41,** 11739–44 (2012).

140. Das, A. *et al.* Application of the piperazine-grafted CuBTTri metal-organic framework in postcombustion carbon dioxide capture. *Microporous Mesoporous Mater.* **174,** 74–80 (2013).

141. Hwang, Y. K. *et al.* Amine grafting on coordinatively unsaturated metal centers of MOFs: consequences for catalysis and metal encapsulation. *Angew. Chem. Int. Ed. Engl.* **47,** 4144–8 (2008).

142. Dinca, M. & Long, J. R. High-enthalpy hydrogen adsorption in cation-exchanged variants of the microporous metal-organic framework Mn3[(Mn4Cl)3(BTT)8(CH3OH)10]2. *J. Am. Chem. Soc.* **129,** 11172–6 (2007).

143. Lalonde, M. *et al.* Transmetalation: routes to metal exchange within metal–organic frameworks. *J. Mater. Chem. A* **1,** 5453 (2013).

144. Song, X., Jeong, S., Kim, D. & Lah, M. S. Transmetalations in two metal–organic frameworks with different framework flexibilities: Kinetics and core–shell heterostructure. *CrystEngComm* **14,** 5753 (2012).

145. Song, X. *et al.* Post-Synthetic Modifications of Framework Metal Ions in Isostructural Metal–Organic Frameworks: Core–Shell Heterostructures via Selective Transmetalations. *Chem. Mater.* **24,** 3065–3073 (2012).

146. Shultz, A. M., Sarjeant, A. A., Farha, O. K., Hupp, J. T. & Nguyen, S. T. Post-synthesis modification of a metal-organic framework to form metallosalen-containing MOF materials. *J. Am. Chem. Soc.* **133,** 13252–5 (2011).

147. Song, X., Jeong, S., Kim, D. & Lah, M. S. Transmetalations in two metal–organic frameworks with different framework flexibilities: Kinetics and core–shell heterostructure. *CrystEngComm* **14,** 5753 (2012).

148. Song, X. *et al.* Post-Synthetic Modifications of Framework Metal Ions in Isostructural Metal–Organic Frameworks: Core–Shell Heterostructures via Selective Transmetalations. *Chem. Mater.* **24,** 3065–3073 (2012).

149. Shultz, A. M., Sarjeant, A. A., Farha, O. K., Hupp, J. T. & Nguyen, S. T. Post-synthesis modification of a metal-organic framework to form metallosalen-containing MOF materials. *J. Am. Chem. Soc.* **133,** 13252–5 (2011).

150. Planas, N. *et al.* The mechanism of carbon dioxide adsorption in an alkylamine-functionalized metal-organic framework. *J. Am. Chem. Soc.* **135,** 7402–5 (2013).

151. Denayer, J. F. M. *et al.* Rotational entropy driven separation of alkane/isoalkane mixtures in zeolite cages. *Angew. Chem. Int. Ed. Engl.* **44,** 400–3 (2005).

152. Myers, A. Equation of state for adsorption of gases and their mixtures in porous materials. *Adsorption* **9,** 9–16 (2003).

153. Cmarik, G. E., Kim, M., Cohen, S. M. & Walton, K. S. Tuning the adsorption properties of UiO-66 via ligand functionalization. *Langmuir* **28,** 15606–13 (2012).

FULL PAPER

DOI: 10.1002/chem.201002135

High Gas Sorption and Metal-Ion Exchange of Microporous Metal–Organic Frameworks with Incorporated Imide Groups

Thazhe Kootteri Prasad, Dae Ho Hong, and Myunghyun Paik Suh*[a]

Abstract: Metal–organic frameworks (MOFs), $[[Cu_2(bdcppi)(dmf)_2]\cdot 10DMF\cdot 2H_2O]_n$ (SNU-50) and $[[Zn_2(bdcppi)(dmf)_3]\cdot 6DMF\cdot 4H_2O]_n$ (SNU-51), have been prepared by the solvothermal reactions of *N,N'*-bis(3,5-dicarboxyphenyl)pyromellitic diimide (H_4BDCPPI) with $Cu(NO_3)_2$ and $Zn(NO_3)_2$, respectively. Framework SNU-50 has an NbO-type net structure, whereas SNU-51 has a PtS-type net structure. Desolvated solid $[Cu_2(bdcppi)]_n$ (SNU-50′), which was prepared by guest exchange of SNU-50 with acetone followed by evacuation at 170 °C, adsorbs high amounts of N_2, H_2, O_2, CO_2, and CH_4 gases due to the presence of a vacant coordination site at every metal ion, and to the presence of imide groups in the ligand. The Langmuir surface area is 2450 $m^2 g^{-1}$. It adsorbs H_2 gas up to 2.10 wt% at 1 atm and 77 K, with zero coverage isosteric heat of 7.1 kJ mol^{-1}, up to a total of 7.85 wt% at 77 K and 60 bar. Its CO_2 and CH_4 adsorption capacities at 298 K are 77 wt% at 55 bar and 17 wt% at 60 bar, respectively. Of particular note is the O_2 adsorption capacity of SNU-50′ (118 wt% at 77 K and 0.2 atm), which is the highest reported so far for any MOF. By metal-ion exchange of SNU-51 with Cu^{II}, $[[Cu_2(bdcppi)(dmf)_3]\cdot 7DMF\cdot 5H_2O]_n$ (SNU-51-Cu_{DMF}) with a PtS-type net was prepared, which could not be synthesized by a direct solvothermal reaction.

Keywords: gas adsorption · hydrogen storage · metal–organic frameworks · microporous materials · oxygen

Introduction

Metal–organic frameworks (MOFs) with pores and channels have attracted great attention because of their potential applications in gas storage, gas separation, catalysis, and fabrication of nanoparticles.[1-4] The storage of H_2 and CH_4 gases and the capture of CO_2 have become particularly important issues in MOF chemistry, because of the potential utility of H_2 and CH_4 as energy carriers, and the implications of CO_2 in global warming. There are a number of MOFs that adsorb high levels of CO_2[4] and CH_4[5-7] at room temperature, but their H_2 storage capacities[1,3,8-10] are generally very low at room temperature because of the low isosteric heat of H_2 adsorption. The isosteric heat of H_2 adsorption can be increased by the creation of open metal sites, through synthesis of catenated frameworks, and by imbedding metal nanoparticles in the MOF.[1,2f,3] Gas sorption properties also depend on pore volume and ligand structures. It has been reported that curved ligands incorporated into a MOF can increase H_2 adsorption because they provide a pocket for adsorption.[11]

Various MOFs have been constructed from Cu^{II} and tetracarboxylic acids,[3,5,6,8,11,12] some of which are reported to show high H_2 adsorption capacities,[3,8,11,12a] but sorption properties for other gases have been less well explored.[6] In addition, the tetracarboxylate ligands used in the previous studies did not contain extra functional groups. This has prompted us to synthesize MOFs in which the organic ligand incorporates imide groups, and to explore their effects on gas sorption. In addition, several recent reports show that the properties of MOFs can be altered by using postsynthetic modifications, such as covalent transformations, tandem modifications, protonation, and doping with metals.[13] It has been also reported that the coordinated metal ions in the MOF can be reversibly exchanged while maintaining structural integrity.[14]

In this work, we have prepared a new ligand *N,N'*-bis(3,5-dicarboxyphenyl)pyromellitic diimide (H_4BDCPPI). We ex-

[a] Dr. T. K. Prasad, D. H. Hong, Prof. M. P. Suh
Department of Chemistry, Seoul National University
Seoul 151-747 (Republic of Korea)
Fax: (+82) 28868516
E-mail: mpsuh@snu.ac.kr

Supporting information for this article is available on the WWW under http://dx.doi.org/10.1002/chem.201002135 or from the author. It includes general methods, additional views of the crystal structures, TGA, PXRD patterns, and technical details of adsorption measurements.

pected that the imide groups might influence the gas sorption properties. By employing this long tetracarboxylate ligand, we synthesized $\{[Cu_2(bdcppi)(dmf)_2]\cdot 10DMF\cdot 2H_2O\}_n$ (SNU-50) and $\{[Zn_2(bdcppi)(dmf)_3]\cdot 6DMF\cdot 4H_2O\}_n$ (SNU-51), which have entirely different structures; namely, NbO-type and PtS-type net structures, respectively (see Scheme 1). The desolvated solid $[Cu_2(bdcppi)]_n$ (SNU-50′)

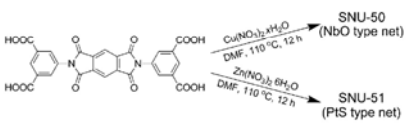

Scheme 1. Construction of porous networks by using *N,N′*-bis(3,5-dicarboxyphenyl)pyromellitic diimide (H_4BDCPPI).

exhibits high adsorption capacities for N_2, H_2, O_2, CO_2, and CH_4 gases, which must be attributed to the presence of the vacant coordination site at every metal ion and the presence of imide groups in the ligand. The Zn^{II} ions in SNU-51 were exchanged with Cu^{II} ions with retention of the PtS-type net—a structure that was impossible to prepare through solvothermal reaction.

Results and Discussion

Synthesis and X-ray structure of SNU-50: Bluish green crystals of SNU-50 were prepared by heating an acidified mixture of $Cu(NO_3)_2$ and H_4BDCPPI in DMF at 110 °C for 12 h. The X-ray crystal structure of SNU-50 indicates that the Cu^{II} ions form a paddlewheel-type $[Cu_2(OOC)_4]$ cluster as a square-planar secondary building unit (SBU) that is linked with the rectangular organic building block $BDCPPI^{4-}$ to give rise to a NbO-type 3D network (see Figure 1). Each Cu^{II} ion shows square pyramidal geometry, with the coordination of four oxygen atoms from four different $BDCPPI^{4-}$ units and a DMF molecule coordinated at the axial position of the paddlewheel unit.

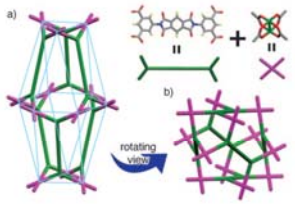

Figure 1. X-ray crystal structure of SNU-50. a) View showing a barrel-like cage that consists of $Cu_{24}(BDCPPI)_{48}$. Color scheme: $[Cu_2(OOC)_4]$ paddlewheel units = purple, BDCPPI ligand = green. b) Simplified view showing the NbO-type net.

The framework creates barrel-like cages, each of which is composed of 12 nodes occupied by $[Cu_2(OOC)_4]$ cluster units (see Figure 1a). The edge length of the external triangular ring of the cage is about 10 Å, as estimated from the centers of the paddlewheel units, while the diagonal distance for the internal hexagonal ring is about 28 Å. Because of the long organic linker, a huge void space is created in the lattice. The void volume of SNU-50 calculated by PLATON is 63% of the unit-cell volume without any guest molecules, and it increases to 74% upon removal of the coordinated DMF molecules. The framework contains three types of channels, two of which are similar. The cylindrical channel with an aperture diameter of 3 Å passes along the *c* axis of the unit cell. The two similar channels, with maximum in-circle diameters of 2.0 Å, pass along the *a* and *b* axes of the unit cell (see Figure S2 in the Supporting Information). The channels are filled with DMF and H_2O guest molecules. Because the guest solvent molecules could not be located from the difference map due to their high thermal disorder in the large unit cells, the identity and numbers of guest molecules were determined from elemental analysis (EA) and thermogravimetric analysis (TGA) data. The channel size increases upon removal of the coordinated DMF molecules; the channel along the *c* axis increases to 4 Å, while the channels along the *a* and *b* axes change to triangular type with maximum in-circle diameters of 4.5 Å (see Figure S2 in the Supporting Information). TGA of SNU-50 indicates that the coordinated DMF molecules can be removed at 220 °C, and the framework is stable up to 290 °C (see Figure S5 in the Supporting Information).

When SNU-50 was immersed in anhydrous acetone, the coordinated DMF molecules and the guest solvent molecules were exchanged with acetone to produce $\{[Cu_2(bdcppi)(CH_3COCH_3)_2]\cdot 5CH_3COCH_3\cdot 2H_2O\}_n$ ($SNU\text{-}50_{Ac}$). $SNU\text{-}50_{Ac}$ was characterized by IR, EA, and TGA. The coordinated acetone at the Cu^{II} ion could be clearly seen at 1689 cm^{-1} in the IR spectra. A few X-ray structures have been reported for acetone-coordinated complexes.[15] Although the single-crystal X-ray structure of $SNU\text{-}50_{Ac}$ could not be determined because of the poor diffraction profile, the powder XRD (PXRD) pattern indicated that the framework structure changed very little with guest exchange (see Figure S7 in the Supporting Information).

Gas sorption of SNU-50′: The preparation of SNU-50′ was achieved by heating $SNU\text{-}50_{Ac}$ at 60 °C for 24 h and then at 170 °C for 4 h. The structure of SNU-50′ contains a vacant coordination site at every Cu^{II} ion, and is extremely moisture sensitive; its dark blue color changes instantly to pale green on exposure to air, and its PXRD pattern becomes broadened, although the peak positions are similar to those of SNU-50 and $SNU\text{-}50_{Ac}$ (see Figure S7 in the Supporting Information). Once SNU-50′ is exposed to air, it does not adsorb any gases even after it is reactivated.

The permanent porosity of SNU-50′ was confirmed by the adsorption isotherms of N_2, H_2, O_2, CO_2, and CH_4 gases (see Figure 2 and Table 1). The N_2 adsorption isotherm at 77 K

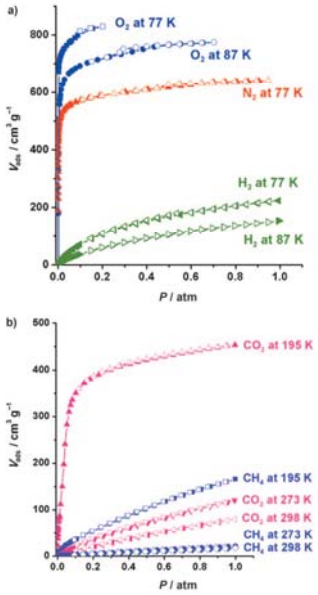

Figure 2. Gas adsorption isotherms of SNU-50′ for a) H_2, N_2, and O_2 at 77 K and 87 K, and b) CO_2 and CH_4 at 195 K, 273 K, and 298 K. Filled shapes = adsorption, open shapes = desorption.

Table 1. Gas adsorption data for SNU-50′.

Gas	T [K]	P [bar]	V_{ads} [cm^{3}g^{-1}]	Amount [mmol g^{-1}]	Amount [wt%]
N_2	77	0.9	641	28.6	80.1
H_2	77	1.0	233	10.4	2.10
	87	1.0	154	6.88	1.39
	77	60	614,[a] 913[b]	27.4,[a] 39.0[b]	5.53,[a] 7.86[b]
	298	61	44.4,[a] 119[b]	1.98,[a] 4.86[b]	0.399,[a] 0.980[b]
O_2	77	0.20	829	37.0	118
	87	0.70	774	34.6	110
CO_2	195	1.0	454	20.3	89.3
	273	1.0	120	5.36	23.6
	298	1.0	80	3.6	16
	298	46	383	17.1	75.2
CH_4	195	1.0	166	7.41	11.9
	273	1.0	21	0.94	1.5
	298	1.0	17	0.76	1.2
	298	61	237	10.6	17.0

[a] Excess adsorption capacity. [b] Total adsorption capacity.

shows Type-I sorption behavior, which is characteristic of microporosity. SNU-50′ adsorbs 641 cm^{3}g^{-1} of N_2 at 77 K and 0.89 atm. The Brunauer–Emmett–Teller (BET) and Langmuir surface areas are 2300 and 2450 m^{2}g^{-1}, respectively, which are smaller than the accessible surface area (3455 m^{2}g^{-1}) calculated for SNU-50 by simple Monte Carlo simulation with N_2 as a probe molecule (probe diameter = 3.681 Å).[16] The pore volume calculated by using the Dubinin–Radushkevich method was 1.08 cm^{3}g^{-1}, which is slightly smaller than the value (1.11 cm^{3}g^{-1}) calculated from the X-ray crystal structure of SNU-50 by using PLATON.[17] The reduced surface area and pore volume, compared with those of the theoretical values, indicate that the framework shrinks on removal of the coordinated solvent molecules as well as the guest molecules. The pore diameter calculated with the Saito–Foley model[18] was 11.0 Å (see the Supporting Information). The density of N_2 adsorbed in SNU-50′, as calculated by using the pore volume (1.08 cm^{3}g^{-1}) estimated from the N_2 adsorption data, is 743 kg m^{-3}, which is close to the liquid N_2 density of 807 kg m^{-3} at 77 K and 1 atm.

The H_2 adsorption isotherms measured at 77 and 87 K show the high H_2 uptake capability of SNU-50′. It adsorbs up to 2.10 wt% of H_2 (233 cm^{3}g^{-1} at standard temperature and pressure (STP), 6.9 H_2 molecules per formula unit) at 77 K and 1 atm, and up to 1.39 wt% (154 cm^{3}g^{-1} at STP, 4.5 H_2 molecules per formula unit) at 87 K and 1 atm. The isosteric heat of H_2 adsorption calculated by using the virial equation[10b,19] is 7.1–4.7 kJ mol^{-1}, depending on the amount of H_2 uptake (see Figure S12 in the Supporting Information). The values are comparable with those of previously reported Cu^{II} MOFs that contain the accessible metal sites on Cu^{II} and the long tetracarboxylate ligand.[3,8,11] The density of adsorbed H_2 in SNU-50′ at 77 K and 1 atm, as calculated by using the pore volume (1.08 cm^{3}g^{-1}) estimated from the N_2 adsorption data, is 19 kg m^{-3}, which is much lower than that of liquid H_2 (71 kg m^{-3} at 1 atm and 20 K).

The O_2 gas adsorption isotherm of SNU-50′ was measured up to 0.20 atm because the saturation pressure of O_2 at 77 K is 147.8 Torr. SNU-50′ adsorbs 829 cm^{3}g^{-1} (118 wt%) of O_2 at 77 K and 0.20 atm, and 774 cm^{3}g^{-1} (110 wt%) at 87 K and 0.7 atm. These values are the highest yet observed for any MOF. Previously, the highest adsorption data reported for O_2 was 618 cm^{3}g^{-1} (88 wt%) at 77 K and 0.19 atm for Co(BDP).[20] In addition, SNU-50′ adsorbs much higher amounts (1.5×) of O_2 than N_2 at 77 K and 0.2 atm. This may be attributed to the fact that the vacant coordination sites on the Cu^{II} centers of the framework interact with O_2 more strongly than with N_2.[21] In addition, O_2 is more accessible to the channels with smaller apertures because of its smaller kinetic diameter (3.47 Å) than that of N_2 (3.64 Å). The density of adsorbed O_2 in the framework, as calculated by using the pore volume (1.08 cm^{3}g^{-1}) estimated from the N_2 adsorption isotherm, is 1098 kg m^{-3} at 77 K and 0.20 atm, which is close to the liquid O_2 density (1204 kg m^{-3}) at 77 K and 0.20 atm.

The CO_2 adsorption isotherms of SNU-50′ show CO_2 uptake capacities of 454 cm^{3}g^{-1} (81 wt%) at 195 K, 120 cm^{3}g^{-1} (21 wt%) at 273 K, and 80 cm^{3}g^{-1} (15.7 wt%) at 298 K under 1 atm of CO_2 pressure. The highest CO_2 uptake capacities reported so far for MOFs under similar conditions is 114 wt% in SNU-6 at 195 K and 1 atm.[4a] The isosteric heat of CO_2 adsorption calculated by using the Clausius–

Clapeyron equation is 25.8 kJ mol^{-1} at low coverage range (see Figure S13 in the Supporting Information). The value is higher than that (15.8–16.5 kJ mol^{-1}) for MOF-5,[22] but similar to that of Prussian blue analogues.[23] Interestingly, the isosteric heat of adsorption only changes from 25 to 23 kJ mol^{-1} as CO_2 loading increases from 5 to 16 wt%, which indicates the strong interaction between SNU-50′ and CO_2 even at high loading.

The CH_4 uptake capacities of SNU-50′ at 1 atm are 166 cm^3 g^{-1} (12 wt%) at 195 K, 21 cm^3 g^{-1} (1.5 wt.%) at 273 K, and 17 cm^3 g^{-1} (1.2 wt%) at 298 K. The heat of CH_4 adsorption calculated by using the Clausius–Clapeyron equation is 26.8 kJ mol^{-1} at low coverage of CH_4, which indicates the strong interaction between the host framework and CH_4 gas at low coverage (see Figure S14 in the Supporting Information). The highest heat of CH_4 adsorption reported so far is 30 kJ mol^{-1} for PCN-14.[6] Contrary to CO_2 adsorption, the isosteric heat of CH_4 adsorption changes drastically from 25 to 17 kJ mol^{-1} as the loading increases from 0.5 to 1.2 wt%. The higher adsorption capacities of CO_2 relative to CH_4, and the higher isosteric heat of CO_2 adsorption (slightly depending on the amount of CO_2 loading) must be attributed to the quadrupole moment of CO_2 (1.34×10^{-39} Cm^2).

High-pressure gas-sorption properties of SNU-50′: The high-pressure gas-sorption isotherms were measured for H_2 at 77 K, and for H_2, CO_2, and CH_4 gases at 298 K (see Figure 3). SNU-50′ adsorbs an excess of 5.53 wt% H_2 at 77 K and 60 bar with no hysteresis. The total H_2 adsorption, which is the sum of the adsorbed amount on the pore surface and the amount of pressurized gas in the pore, is 7.85 wt% at 60 bar. To the best of our knowledge, only four MOFs have higher H_2 uptake capacities than this; MOF-5 (11.5 wt%, 170 bar, 77 K), MOF-177 (11.0 wt%, 70 bar, 77 K), SNU-6 (10 wt%, 50 bar, 77 K),[1] and NOTT-112 (10 wt%, 77 bar, 77 K).[24] At 298 K, the H_2 uptake capacities are reduced significantly to the excess adsorption of 0.40 wt% and the total uptake of 0.97 wt% at 60 bar.[10] NOTT-103, constructed from Cu^{II} and a long tetracarboxylate, showed a BET surface area of 2930 m^2 g^{-1} and a pore volume of 1.14 cm^3 g^{-1}.[8] It exhibited a total H_2 uptake capacity of 7.22 wt% at 77 K and 60 bar. Despite the lower BET surface area (2300 m^2 g^{-1}) and lower pore volume estimated by N_2 sorption data (1.08 cm^3 g^{-1}), SNU-50′ shows higher H_2 uptake capacity (7.85 wt%) than NOTT-103 under similar conditions, which indicates that a MOF with imide groups is better for H_2 uptake than a MOF containing simple benzene rings.

The CO_2 adsorption isotherm at 298 K also shows relatively high uptake. SNU-50′ adsorbs CO_2 with an excess adsorption of 64 wt% and a total uptake of 77 wt% at 298 K and 55 bar. The CO_2 uptake decreases slightly as the pressure increases above 45 bar, due to saturation, and the sorption isotherm shows no hysteresis. The highest CO_2 uptake capacity reported so far is 176 wt% at 304 K and 50 bar for MIL-101c(Cr).[4b]

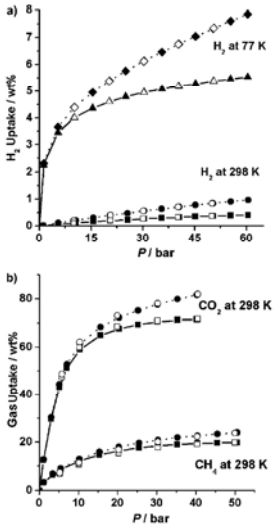

Figure 3. High-pressure gas-adsorption isotherms of SNU-50′. a) H_2 at 77 K and 298 K, b) CO_2 and CH_4 at 298 K. Solid line = excess uptake; dashed line = total uptake. Filled shape = adsorption; open shape = desorption.

SNU-50′ adsorbs CH_4 with an excess adsorption of 12 wt% and a total uptake of 17 wt% CH_4 at 298 K and 60 bar. The highest CH_4 uptake capacity reported so far is an excess adsorption of 18.1 wt% (220 v/v) with a total uptake of 18.9 wt% (230 v/v) at 35 bar and 290 K in PCN-14.[6] The high adsorption capacities for H_2 and CH_4 gases at high pressures may be attributed to the large pore volume, exposed metal sites, and the incorporation of imide groups in SNU-50′.[1,6,8]

Synthesis and X-ray crystal structure of SNU-51: Framework SNU-51 was synthesized by heating $Zn(NO_3)_2$ and H_4BDCPPI in DMF at 110 °C for 12 h, similarly to SNU-50. The X-ray crystal structure indicates that the framework structure of SNU-51 is entirely different from that of SNU-50. Instead of the paddlewheel-type SBUs in SNU-50, distorted tetrahedral $[Zn_2(OOC)_4(dmf)_3]$ SBUs are formed, and they are linked with the square-planar tetracarboxylate, which gives rise to a PtS-type network (see Figure 4). In SNU-51 there are two crystallographically independent Zn atoms, Zn1 and Zn2. They both have distorted octahedral geometry; one through coordination of six oxygen atoms of four $BDCPPI^{4-}$ units, and the other through coordination of three carboxylate oxygen atoms and three DMF oxygen atoms. The network contains two types of rectangular chan-

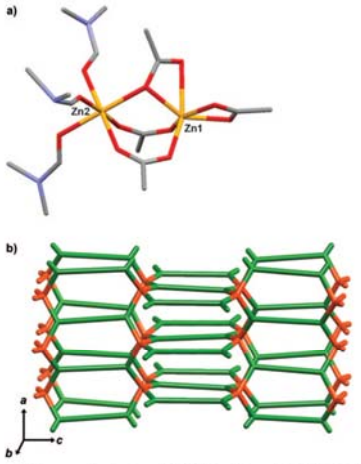

Figure 4. X-ray crystal structure of SNU-51. a) View of the $[Zn_2(OOC)_4(dmf)_3]$ SBU. b) Schematic representation of the framework: $[Zn_2(OOC)_4(dmf)_3]$ unit = orange, BDCPPI ligand = green.

nels with effective aperture sizes of 3×10 and 2×8 Å^2 along the *a* axis of the unit cell (see Figure S4 in the Supporting Information). Along the *b* axis, there are also two types of channels with effective aperture sizes of 3×13 and 2×10 Å^2. The channels running parallel to the *c* axis are completely blocked by the coordinated DMF molecules, but channels of 3 Å in diameter are generated on removal of the DMF (see Figure S4 in the Supporting Information). The guest molecules in the framework could not be determined from the difference map due to their severe thermal disorder in the large unit cell, and thus they were characterized by EA and TGA. The void volume of the framework without any guest solvent molecules is 50% of the cell volume, while the void volume increases to 69% on removal of the coordinated DMF molecules, as estimated by PLATON.[17] The measured PXRD pattern of SNU-51 is not coincident with the simulated pattern derived from the single-crystal X-ray data due to changes in the framework structure on release of the guest molecules during powder sample preparation. TGA shows that all guest molecules can be removed below 120°C, while the coordinated DMF molecules are removed slowly at 120–430°C (see Figure S6 in the Supporting Information). The desolvated framework collapses according to the PXRD pattern. The activated solid does not absorb any gas independent of the activation temperature (between 25 and 150°C under vacuum), which confirms the collapse of the framework.

Metal-ion exchange of SNU-51: The structure of SNU-51 is composed of relatively uncommon SBUs[25] and has a large crystallographic free volume. Therefore, we explored the possibility of replacing the Zn^{II} ions in SNU-51 with other metal ions, such as Cu^{II}, by a postsynthetic method; whereby crystals of SNU-51 were immersed in a 0.1 M solution of $Cu(NO_3)_2\cdot2.5H_2O$ in MeOH. The color of the crystals changed from pale yellow to green–blue in a few minutes, and then to a more intense blue over four days, as observed under an optical microscope (see Figure 5). During this process, the

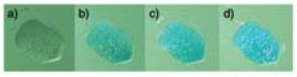

Figure 5. Photos of crystal SNU-51 taken during the exchange of Zn^{II} with Cu^{II} by immersion in a MeOH solution of $Cu(NO_3)_2$ (0.1 M) for four days. a) 0 h, b) 2 h, c) 24 h, and d) 96 h.

thin platelike crystals developed cracks and, although their transparency was retained, a single-crystal X-ray structure could not be determined for the Cu^{II} structure. Inductively coupled plasma–atomic emission spectroscopy (ICP-AES) for the resulting crystals indicated that 97% of the Zn^{II} ions had been exchanged with Cu^{II} over the four days. Interestingly, in the MeOH solution that contained the mixture of Co^{II}, Ni^{II}, Cu^{II}, and Cd^{II} ions, the Zn^{II} ions in SNU-51 were exchanged only with Cu^{II} ions. In particular, the metal exchange was very sensitive to the solvent used. For example, when DMF or 1-pentanol was used instead of MeOH, the Zn^{II} ions in SNU-51 were not exchanged with Cu^{II}, and color of the crystals did not change. In acetone, the exchange was extremely slow. This indicates that the diffusion of metal ions into the channels is sensitive to the size of the solvated metal ion and counteranion.

To prepare the metal-ion-exchanged sample on a bulk scale, SNU-51 was pulverized and stirred in a solution of 0.1 M $Cu(NO_3)_2\cdot2.5H_2O$ in MeOH for two days. The isolated powder was suspended in fresh MeOH for a further three days to remove any extra $Cu(NO_3)_2$ inclusions from the pores. The process yielded $\{[Cu_2(bdcppi)(MeOH)_3]\cdot6MeOH\cdot7H_2O\}_n$ (SNU-51-Cu_{MeOH}) as confirmed by IR, TG, and EA. The counteranion (NO_3^-) of the substituting metal ion was not detected in the IR spectra for any samples taken during the ion-exchange process. The PXRD pattern of SNU-51-Cu_{MeOH} was significantly broadened. However, when SNU-51-Cu_{MeOH} was immersed in DMF for 24–48 h, the PXRD pattern became similar to that of SNU-51 (see Figure 6). In addition, the color of SNU-51-Cu_{MeOH} changed from blue to green after immersion in DMF for a few minutes, which indicated that DMF molecules had become coordinated at the Cu^{II} ions. IR, EA, and TGA confirmed that $\{[Cu_2(bdcppi)(dmf)_3]\cdot7DMF\cdot5H_2O\}_n$ (SNU-51-Cu_{DMF}) had formed. The PXRD pattern of SNU-51-Cu_{DMF} was similar to that of SNU-51, which indicated that the framework structure was maintained during the metal ex-

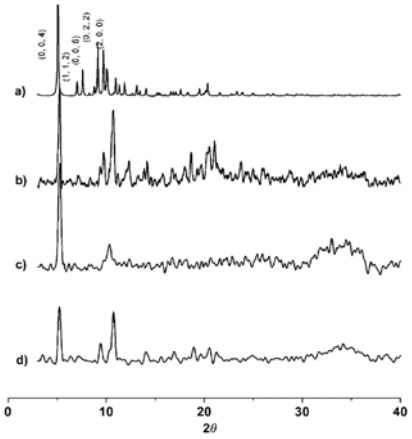

Figure 6. The PXRD patterns. a) Simulated pattern from the single crystal X-ray data of SNU-51, b) as synthesized SNU-51, c) the metal-exchanged sample, SNU-51-Cu_{MeOH}, and d) SNU-51-Cu_{DMF}.

change (see Figure 6). The Cu^{II}-exchanged sample, SNU-51-Cu_{DMF}, did not undergo ion exchange with Zn^{II} even in a concentrated solution of $Zn(NO_3)_2$ (ca. 0.1 M) in MeOH.

The kinetics of metal-ion exchange were followed by measuring the relative amount of Zn^{II} to Cu^{II} in the solid at specific time intervals. During the reaction, a small portion of the solid sample was removed and converted to SNU-51-Cu_{DMF}, and the ratio of Zn^{II} to Cu^{II} was determined by ICP-AES. The exchange of Zn^{II} with Cu^{II} was very fast during the initial stage; 27% conversion took place within 10 min, 44% within 30 min, and 75% within 2 h. Within 6 h, 97% of Zn^{II} in SNU-51 had been replaced with Cu^{II} (see Figure 7). This fast exchange process excludes the possibility of dissolution followed by recrystallization; rather, it indicates direct metal-ion exchange.

This type of metal-ion exchange is important for the preparation of new MOFs that cannot be synthesized by direct solvothermal reactions, although the mechanism is unclear at this point. The exchange described herein between Zn^{II} and Cu^{II} in a 3D MOF is unprecedented. It had been reported previously that a Cd MOF could be converted to a Pb MOF, which could then be transformed back to the Cd MOF by metal-ion exchange.[14] In that case, the Cd and Pb MOFs had the same structures and could also be synthesized by direct solvothermal reactions. In the present work, a direct solvothermal reaction of Cu^{II} with the BDCPPI ligand yielded a NbO-type net structure, whereas the reaction of Zn^{II} with the same ligand yielded a PtS-type net structure. The Cu^{II} MOF with the PtS-type net topology could be prepared only by using the postsynthetic metal-ion exchange strategy.

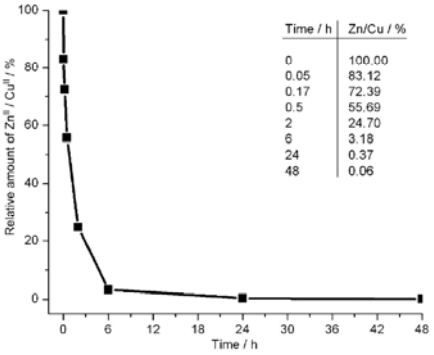

Time / h	Zn/Cu / %
0	100.00
0.05	83.12
0.17	72.39
0.5	55.69
2	24.70
6	3.18
24	0.37
48	0.06

Figure 7. Metal-ion exchange of SNU-51 with Cu^{II}. The change in the relative amount of Zn^{II} over Cu^{II} with immersion time of SNU-51 in the Cu^{II} solution. Raw data are presented in the inset table.

Conclusion

We have synthesized new porous MOFs, SNU-50 and SNU-51 by utilizing a long tetracarboxylate with imide groups, H_4BDCPPI. The desolvated solid (SNU-50′) adsorbs high levels of N_2, H_2, O_2, CO_2, and CH_4 gases due to the presence of vacant coordination sites at the metal ions, and to the presence of imide groups in the ligands. The framework adsorbs 2.10 wt% of H_2 at 1 atm and 77 K with an isosteric heat of H_2 adsorption of 7.1 kJ mol^{-1}, and a total 7.85 wt% of H_2 at 77 K and 60 bar. Of particular note is the O_2 adsorption capacity (829 cm^3 g^{-1} at 77 K and 0.20 atm), which is the highest yet reported for any MOF. The solvothermal reaction of Zn^{II} with the same ligand under similar conditions gives rise to SNU-51, with a PtS-type net that is entirely different from the NbO-type net of Cu^{II} MOF (SNU-50). Interestingly, the Zn^{II} ions in SNU-51 could be exchanged with Cu^{II} ions to afford the Cu^{II} MOF with a PtS-type net, which could not be produced from direct solvothermal synthesis. This result suggests that the metal-ion-exchange strategy can be utilized for the synthesis of new MOFs that cannot otherwise be obtained by direct solvothermal reactions.

Experimental Section

Ligand synthesis: The synthesis of *N,N′*-bis(3,5-dicarboxyphenyl)pyromellitic diimide (H_4BDCPPI) was achieved by using a modified version of a previously reported procedure:[26] 1,2,4,5-benzene tetracarboxylate dianhydride (2.18 g, 10 mmol) and 5-aminoisophthalic acid (3.62 g, 20 mmol) were dissolved in DMF (40 mL). The solution was heated at reflux for 8 h, and then allowed to cool to room temperature. A pale yellow crystalline precipitate (2.80 g, 51%) was formed, which was filtered, washed with MeOH, and dried under vacuum. ^{1}H NMR (300 MHz, [D_6]DMSO, 25 °C): δ = 8.36 (s; 4H), 8.43 (s; 2H), 8.55 ppm (s; 2H); IR (KBr): $\tilde{\nu}$ =

1777, 1732 (C=O(pyromellitic diimide)), 1660, 1601 cm^{-1} (C=O(carboxylic acid)); elemental analysis calcd (%) for $C_{56}H_{32}N_2O_{12}{\cdot}0.5C_3H_7NO$: C 56.85, H 2.69, N 6.02; found: C 55.78, H 2.83, N 5.93.

Preparation of {[Cu_2(bdcppi)(dmf)$_2$]-10DMF-2H_2O}$_n$ (SNU-50): Cu-$(NO_3)_2{\cdot}2.5H_2O$ (0.024 g, 0.103 mmol), H_4BDCPPI (0.030 g, 0.051 mmol), and DMF (5 mL) were placed in a glass bottle, and acidified with HNO_3 (13 N, 3 drops). The bottle was sealed and heated at 110°C for 12 h. Blue–green prismatic crystals (0.045 g, 60%) formed, which were filtered and washed with DMF. IR (KBr): $\tilde{\nu}$ = 1780, 1728 (C=O(pyromellitic diimide)), 1667 (C=O(coordinated DMF)), 1640 (sh), 1590 cm^{-1} (carboxylate); UV/Vis (diffuse reflectance): λ_{max} = 760, 715 nm; elemental analysis calcd (%) for $C_{62}H_{86}Cu_2N_{14}O_{26}$: C 47.11, H 6.12, N 12.41; found: C 46.92, H 6.35, N 12.79.

Preparation of {[Cu_2(bdcppi)((CH_3COCH_3)$_2$]-5CH_3COCH_3-2H_2O}$_n$ (SNU-50$_{Ac}$): Crystals of SNU-50 were immersed in dried acetone for 5–7 days. The acetone was removed by decanting, and was replaced with fresh acetone at least twice a day. The color of the crystals changed from blue–green to gray–blue. IR (nujol): $\tilde{\nu}$ = 1781, 1729 (C=O(pyromellitic diimide)), 1703 (C=O(guest acetone)), 1689 (m, C=O(coordinated acetone)), 1637, 1591 cm^{-1} (carboxylate); UV/Vis (diffuse reflectance): λ_{max} = 690 nm; elemental analysis calcd (%) for $C_{47}H_{54}Cu_2N_2O_{21}$: C 50.85, H 4.90, N 2.52; found: C 50.66, H 4.65, N 2.66.

Preparation of [Cu_2(bdcppi)]$_n$ (SNU-50′): Crystals of SNU-50$_{Ac}$ (≈0.2 g) were transferred to a gas adsorption cell and the cell was kept under N_2 flow at room temperature for 30 min to remove loosely bound solvent molecules. The sample was activated on the gas sorption instrument at 60°C for 24 h and then at 170°C for 4 h under vacuum. The color of the crystals changed from gray–blue to dark purple–blue (the color of the activated compound instantly changes to pale green upon exposure to air). IR (nujol; prepared under Ar in glove bag): $\tilde{\nu}$ = 1782, 1735 (C=O(pyromellitic diimide)), 1630, 1588 cm^{-1} (carboxylate); elemental analysis calcd (%) for $C_{28}H_8Cu_2N_2O_{12}$: C 46.79, H 1.21, N 4.20; found: C 46.86, H 1.23, N 4.46.

Preparation of {[Zn_2(bdcppi)(dmf)$_2$]-6DMF-4H_2O}$_n$ (SNU-51): Zn-$(NO_3)_2{\cdot}6H_2O$ (0.029 g, 0.100 mmol), H_4BDCPPI (0.030 g, 0.051 mmol), and DMF (5 mL) were placed in a glass bottle, which was sealed with rubber and aluminum caps and heated at 110°C for 12 h. On cooling to room temperature, yellow platelike crystals formed (0.040 g, 57%), which were filtered and washed with DMF. IR (KBr): $\tilde{\nu}$ = 1779, 1727 (C=O(pyromellitic diimide)), 1668 (C=O(coordinated DMF)), 1632 (sh), 1587 cm^{-1} (carboxylate); elemental analysis calcd (%) for $C_{53}H_{59}Zn_2N_{11}O_{25}$: C 45.43, H 5.68, N 11.00; found: C 44.24, H 5.25, N 11.07.

Preparation of {[Cu_2(bdcppi)($MeOH$)$_2$]-6MeOH-7H_2O}$_n$ (SNU-51-Cu$_{MeOH}$): Crystals of SNU-51 (≈0.75 g) were pulverized and added to a solution of $Cu(NO_3)_2{\cdot}2.5H_2O$ (0.1 M, 100 mL) in methanol, which was then stirred for 48 h. The color of the solid changed from pale yellow to blue. After 6 h and then 24 h of immersion, the $Cu(NO_3)_2$ solution was removed by decanting, and replenished with fresh $Cu(NO_3)_2$ solution in methanol. The compound was isolated and suspended in fresh MeOH for three days at 50°C to remove any Cu or Zn salt present in the pores of the framework. During this process, the MeOH was removed by decanting, and was replaced with fresh MeOH at least twice. IR (KBr): $\tilde{\nu}$ = 1782, 1727 (C=O(pyromellitic diimide)), 1652, 1630 (sh), 1563 cm^{-1} (carboxylate); elemental analysis calcd (%) for $Cu_2C_{35}H_{46}N_2O_{26}$: C 38.85, H 5.40, N 2.59; found: C 38.58, H 5.13, N 2.61.

Preparation of {[Cu_2(bdcppi)(dmf)$_3$]-7DMF-5H_2O}$_n$ (SNU-51-Cu$_{DMF}$): A suspension of SNU-51-Cu$_{MeOH}$ in methanol was decanted to remove the methanol, and DMF was added, during which time the color of the solid changed to blue–green. The solid was kept in DMF for three days, which afforded SNU-51-Cu$_{DMF}$. IR (KBr): $\tilde{\nu}$ = 1782, 1728 (C=O(pyromellitic diimide)), 1663 (C=O(coordinated DMF)), 1630 (sh), 1591 (m), 1560 cm^{-1} (m; carboxylate); UV/Vis (diffuse reflectance): λ_{max} = 810, 770, 670 nm; elemental analysis calcd (%) for $Cu_2C_{56}H_{88}N_{12}O_{27}$: C 45.19, H 5.96, N 11.29; found: C 45.30, H 6.02, N 11.29.

Kinetics of metal-ion exchange: The pulverized crystals of SNU-51 were immersed in a solution of $Cu(NO_3)_2{\cdot}2.5H_2O$ in MeOH. A small amount of solid sample was removed at specific time intervals and suspended in DMF. The SNU-51-Cu$_{DMF}$ was decomposed with concentrated HNO_3, and the ratio of Zn/Cu was determined by ICP-AES.

Selective metal-ion exchange experiment: Crystals of SNU-51 were immersed in a mixture of $Co(NO_3)_2{\cdot}6H_2O$, $Ni(NO_3)_2{\cdot}6H_2O$, $Cu(NO_3)_2{\cdot}2.5H_2O$, and $Cd(NO_3)_2{\cdot}6H_2O$ (0.1 M, 15 mL). The crystals were isolated from the solution after 24 h, and suspended in fresh MeOH for three days. The crystals were filtered and decomposed with concentrated HNO_3. ICP-AES analysis gave the following composition: 77.4% Cu, 18.3% Zn, 1.2% Co, 1.3% Ni, and 1.9% Cd, which indicated that metal exchange was selective.

X-ray crystallography: Data were collected on an Enraf Nonius Kappa CCD diffractometer by using graphite-monochromated $Mo_{K\alpha}$ radiation (λ = 0.71073 Å) at 298 K. Each crystal was sealed in a glass capillary together with the mother liquor. Preliminary orientation matrices and unit cell parameters were obtained from the peaks of the first ten frames and then refined with the whole data set. Frames were integrated and corrected for Lorentz and polarization effects by using DENZO.[27] Scaling and global refinement of crystal parameters were performed by using SCALEPACK.[27] The structure was solved by using SHELXS-97.[28] All hydrogen atoms were assigned on the basis of geometrical considerations and allowed to ride on the respective carbon atoms. The solvent molecules could not be located from the difference maps, and the residual electron density corresponding to the solvent molecules were ignored by using the SQUEEZE[29] option of PLATON.[17] Because of the disorder in the benzene rings, all atoms except Cu and O in SNU-50 were refined isotropically. CCDC-760674 and 760675 contain the supplementary crystallographic data for this paper. These data can be obtained free of charge from The Cambridge Crystallographic Data Centre via www.ccdc.cam.ac.uk/data_request/cif. Crystallographic data for SNU-50 and SNU-51 are summarized in Table 2.

Table 2. Crystallographic data for SNU-50 and SNU-51 (squeezed data).

	SNU-50	SNU-51
formula	$C_{12}H_{22}Cu_2N_4O_{14}$	$C_{35}H_{28}N_4O_{12}Zn_2$
space group	$R\bar{3}m$	*Icab*
M_r	813.64	890.41
a [Å]	18.794(7)	18.119(3)
b [Å]	18.794(7)	20.125(4)
c [Å]	50.17(2)	69.8204(14)
α [°]	90	90
β [°]	90	90
γ [°]	120	90
V [Å^3]	15347(10)	25572(7)
Z	9	16
ρ_{calcd} [g cm^{-3}]	0.792	0.925
T [K]	298	298
μ [mm^{-1}]	0.661	0.796
GOF (F^2)	0.846	1.040
R_1,wR_2 [$I > 2\sigma(I)$]	0.1049,[a] 0.2698[b]	0.0817,[b] 0.2293[c]
R_1,wR_2 (all data)	0.2099,[a] 0.3113[b]	0.1277,[b] 0.2419[c]

[a] $R = \Sigma||F_o| - |F_c||/\Sigma|F_o|$. [b] $wR(F^2) = [\Sigma w(F_o^2 - F_c^2)^2/\Sigma w(F_o^2)^2]^{1/2}$ in which $w = 1/[\sigma^2(F_o^2) + (0.1582P)^2 + (0.0000)P]$, $P = (F_o^2 + 2F_c^2)/3$ for SNU-50. [c] $wR(F^2) = [\Sigma w(F_o^2 - F_c^2)^2/\Sigma w(F_o^2)^2]^{1/2}$ in which $w = 1/[\sigma^2(F_o^2) + (0.1146P)^2 + (0.0000)P]$, $P = (F_o^2 + 2F_c^2)/3$ for SNU-51.

Gas sorption measurements: Low-pressure gas adsorption–desorption measurements were performed by using Autosorb-1 or Autosorb-3B (Quantachrome Instruments). All gases used were of 99.999% purity. After gas sorption measurements, the sample was precisely weighed again. The surface area and total pore volume were determined from the N_2 gas isotherm at 77 K. For multipoint BET and Langmuir surface area estimations, the data were taken in the range of P/P_0 = 0.001–0.08 and P/P_0 = 0.0001–0.016, respectively. High-pressure gas sorption isotherms of SNU-50′ were measured for H_2 (77 K), CO_2 (298 K), and CH_4 (298 K) in the range 1–60 bar by the gravimetric method with a Rubotherm magnetic suspension balance (MSB). Crystals of SNU-50$_{Ac}$ were heated at 60°C

for 3 h and 170 °C for 20 h with gas sorption apparatus under vacuum. All data were corrected for buoyancy of the system and sample. The sample density used in the buoyancy correction was determined from He displacement isotherms measured at 298 K.

Acknowledgements

This work was supported by National Research Foundation of Korea (NRF) Grant funded by the Korean Government (MEST) (no. 2009-0093842 and no. 2010-0001485).

[1] L. J. Murray, M. Dinca, J. R. Long, *Chem. Soc. Rev.* **2009**, *38*, 1294–1314.
[2] a) J.-R. Li, R. J. Kuppler, H.-C. Zhou, *Chem. Soc. Rev.* **2009**, *38*, 1477–1504; b) M. P. Suh, Y. E. Cheon, E. Y. Lee, *Coord. Chem. Rev.* **2008**, *252*, 1007–1026; c) J. Lee, O. K. Farha, J. Roberts, K. A. Scheidt, S. T. Nguyen, J. T. Hupp, *Chem. Soc. Rev.* **2009**, *38*, 1450–1459; d) L. Q. Ma, C. Abney, W. B. Lin, *Chem. Soc. Rev.* **2009**, *38*, 1248–1256; e) M. P. Suh, H. R. Moon, E. Y. Lee, S. Y. Jang, *J. Am. Chem. Soc.* **2006**, *128*, 4710–4718; f) Y. E. Cheon, M. P. Suh, *Angew. Chem.* **2009**, *121*, 2943–2947; *Angew. Chem. Int. Ed.* **2009**, *48*, 2899–2903.
[3] Y. G. Lee, H. R. Moon, Y. E. Cheon, M. P. Suh, *Angew. Chem.* **2008**, *120*, 7855–7859; *Angew. Chem. Int. Ed.* **2008**, *47*, 7741–7745.
[4] a) H. J. Park, M. P. Suh, *Chem. Eur. J.* **2008**, *14*, 8812–8821; b) P. L. Llewellyn, S. Bourrelly, C. Serre, A. Vimont, M. Daturi, L. Hamon, G. De Weireld, J.-S. Chang, D.-Y. Hong, Y. K. Hwang, S. H. Jhung, G. Ferey, *Langmuir* **2008**, *24*, 7245–7250; c) A. R. Millward, O. M. Yaghi, *J. Am. Chem. Soc.* **2005**, *127*, 17998–17999; d) H.-S. Choi, M. P. Suh, *Angew. Chem.* **2009**, *121*, 6997–7001; *Angew. Chem. Int. Ed.* **2009**, *48*, 6865–6869.
[5] X.-S. Wang, S. Q. Ma, K. Rauch, J. M. Simmons, D. Q. Yuan, X. P. Wang, T. Yildirim, W. C. Cole, J. J. Lopez, A. de Meijere, H.-C. Zhou, *Chem. Mater.* **2008**, *20*, 3145–3152.
[6] S. Q. Ma, D. F. Sun, J. M. Simmons, C. D. Collier, D. Q. Yuan, H.-C. Zhou, *J. Am. Chem. Soc.* **2008**, *130*, 1012–1016.
[7] H. Wu, W. Zhou, T. Yildirim, *J. Am. Chem. Soc.* **2009**, *131*, 4995–5000.
[8] X. Lin, I. Telepeni, A. J. Blake, A. Dailly, C. M. Brown, J. M. Simmons, M. Zoppi, G. S. Walker, K. M. Thomas, T. J. Mays, P. Hubberstey, N. R. Champness, M. Schroder, *J. Am. Chem. Soc.* **2009**, *131*, 2159–2171.
[9] a) H. Furukawa, M. A. Miller, O. M. Yaghi, *J. Mater. Chem.* **2007**, *17*, 3197–3204; b) A. G. Wong-Foy, A. J. Matzger, O. M. Yaghi, *J. Am. Chem. Soc.* **2006**, *128*, 3494–3495; c) A. G. Wong-Foy, O. Lebel, A. J. Matzger, *J. Am. Chem. Soc.* **2007**, *129*, 15740–15741.
[10] a) S. S. Kaye, A. Dailly, O. M. Yaghi, J. R. Long, *J. Am. Chem. Soc.* **2007**, *129*, 14176–14177; b) M. Dinca, A. Dailly, Y. Liu, C. M. Brown, D. A. Neumann, J. R. Long, *J. Am. Chem. Soc.* **2006**, *128*, 16876–16883.
[11] S. H. Yang, X. Lin, A. Dailly, A. J. Blake, P. Hubberstey, N. R. Champness, M. Schroder, *Chem. Eur. J.* **2009**, *15*, 4829–4835.
[12] a) X. Lin, J. H. Jia, X. B. Zhao, K. M. Thomas, A. J. Blake, G. S. Walker, N. R. Champness, P. Hubberstey, M. Schroder, *Angew. Chem.* **2006**, *118*, 7518–7524; *Angew. Chem. Int. Ed.* **2006**, *45*, 7358–7364; b) X.-S. Wang, S. Q. Ma, P. M. Forster, D. Q. Yuan, J. Eckert, J. J. Lopez, B. J. Murphy, J. B. Parise, H.-C. Zhou, *Angew. Chem.* **2008**, *120*, 7373–7376; *Angew. Chem. Int. Ed.* **2008**, *47*, 7263–7266; c) M. Xue, G. S. Zhu, Y. X. Li, X. J. Zhao, Z. Jin, E. Kang, S. L. Qiu, *Cryst. Growth Des.* **2008**, *8*, 2478–2483; d) A. J. Cairns, J. A. Perman, L. Wojtas, V. C. Kravtsov, M. H. Alkordi, M. Eddaoudi, M. J. Zaworotko, *J. Am. Chem. Soc.* **2008**, *130*, 1560–1561.
[13] a) Z. Q. Wang, S. M. Cohen, *Chem. Soc. Rev.* **2009**, *38*, 1315–1329; b) T. Uemura, N. Yanai, S. Kitagawa, *Chem. Soc. Rev.* **2009**, *38*, 1228–1236.
[14] S. Das, H. Kim, K. Kim, *J. Am. Chem. Soc.* **2009**, *131*, 3814–3815.
[15] a) T. Akitsu, Y. Einaga, *Acta Crystallogr. Sect. C* **2004**, *60*, m162–m164; b) D. A. Grossie, W. A. Feld, L. Scanlon, G. Sandi, Z. Wawrzak, *Acta Crystallogr. Sect. E* **2006**, *62*, m827–m829.
[16] T. Duren, F. Millange, G. Férey, K. S. Walton, R. Q. Snurr, *J. Phys. Chem. C* **2007**, *111*, 15350–15356.
[17] a) A. L. Spek, *Acta Crystallogr. Sect. A* **1990**, *46*, C34; b) A. L. Spek, PLATON, A Multipurpose Crystallographic Tool, Utrecht University, Utrecht, **1998**.
[18] A. Saito, H. C. Foley, *AIChE J.* **1991**, *37*, 429–436.
[19] a) L. Czepirski, J. Jagiello, *Chem. Eng. Sci.* **1989**, *44*, 797–801; b) J. L. C. Rowsell, O. M. Yaghi, *J. Am. Chem. Soc.* **2006**, *128*, 1304–1315.
[20] H. J. Choi, M. Dinca, J. R. Long, *J. Am. Chem. Soc.* **2008**, *130*, 7848–7850.
[21] Y. Li, R. T. Yang, *Langmuir* **2007**, *23*, 12937–12944.
[22] J.-S. Choi, W.-J. Son, J. Kim, W.-S. Ahn, *Microporous Mesoporous Mater.* **2008**, *116*, 727–731.
[23] S. Natesakhawat, J. T. Culp, C. Matranga, B. Bockrath, *J. Phys. Chem. C* **2007**, *111*, 1055–1060.
[24] Y. Yan, X. Lin, S. H. Yang, A. J. Blake, A. Dailly, N. R. Champness, P. Hubberstey, M. Schroder, *Chem. Commun.* **2009**, 1025–1027.
[25] B. L. Chen, N. W. Ockwig, F. R. Fronczek, D. S. Contreras, O. M. Yaghi, *Inorg. Chem.* **2005**, *44*, 181–183.
[26] C. Degenhardt III, D. B. Shortell, R. D. Adams, K. D. Shimizu, *Chem. Commun.* **2000**, 929–930.
[27] DENZO-SCALEPACK: Z. Otwinowski, W. Minor, *Processing of X-ray Diffraction Data Collected in Oscillation Mode, Methods in Enzymology, Vol. 276: Macromolecular Crystallography, Part A* (Eds.: C. W. Carter, Jr., R. M. Sweet), Academic Press, New York, **1997**, pp. 307–326.
[28] G. M. Sheldrick, SHELXS-97: Programs for crystal structure analysis, University of Göttingen, Göttingen (Germany), **1997**.
[29] P. van der Sluis, A. L. Spek, *Acta Crystallogr. Sect. A* **1990**, *46*, 194–201.

Received: July 26, 2010
Published online: October 22, 2010

View Online / Journal Homepage / Table of Contents for this issue
Dynamic Article Links

ChemComm

Cite this: *Chem. Commun.*, 2012, **48**, 9168–9170

www.rsc.org/chemcomm

COMMUNICATION

Selective CO_2 adsorption in a metal–organic framework constructed from an organic ligand with flexible joints†

Dae Ho Hong and Myunghyun Paik Suh*

Received 22nd June 2012, Accepted 24th July 2012
DOI: 10.1039/c2cc34482c

A metal–organic framework (SNU-110) constructed from an organic ligand with flexible joints exhibits selective CO_2 adsorption over N_2, O_2, H_2 and CH_4 gases.

Metal–organic frameworks (MOFs) have great potential to be applied in gas storage,[1–9] gas separation,[10–26] and fabrication of metal nanoparticles.[3,27,28] In particular, they can be applied as capture materials for CO_2 from the industry flue gas that is implicated in the global warming.[2,10,13] The industry flue gas contains not only CO_2 but also other gases such as N_2, H_2, H_2O, and O_2 depending on the combustion methods. Therefore, selective adsorption properties of MOFs for CO_2–N_2 and CO_2–H_2 are important for post-combustion and pre-combustion CO_2 capture, respectively. In addition, the MOFs with selective adsorption property for CO_2–CH_4 can be applied in purification of low quality natural gas.[24–26]

To be a CO_2 capture material, the MOFs should have high CO_2 adsorption capacity at ambient temperature,[8,9] high adsorption selectivity of CO_2 over other gases,[10–12] and high thermal stability. To increase the CO_2 capture ability of MOFs, various strategies have been employed such as making the network inherently flexible,[10] functionalizing the pore-surface with amines,[11,12] creating accessible metal sites,[13] attaching flexible arms,[14,15] exposing Lewis base sites,[18] and exchanging counter ions included in the charged framework.[19] It has been reported that MOFs constructed from flexible organic components, even if they do not adsorb N_2 and H_2 gases due to the smaller pores of the activated samples than the kinetic diameters of these gases, often selectively adsorb CO_2 since they open the gates for CO_2 that has much higher polarizability (2.51 $Å^3$) and quadrupole moment (1.4×10^{-39} C m^2) than other gases.[10,15–17,20] However, some of those MOFs still adsorb considerable amounts of CH_4 at 195 K because they are flexible enough to open the gates for CH_4 having high polarizability (2.45 $Å^3$), and cannot be applied in purification of natural gas.

Department of Chemistry, Seoul National University, Seoul 151-747, Republic of Korea. E-mail: mpsuh@snu.ac.kr; Fax: +82 2-886-8516; Tel: +82 2-880-7760

† Electronic supplementary information (ESI) available: Detailed experimental procedures, ORTEP drawings, ^{1}H-NMR spectra, TGA/DSC traces, PXRD patterns, table of X-ray data for **SNU-110**, tables of gas adsorption data for **SNU-110′**. CCDC 885397. For ESI and crystallographic data in CIF or other electronic format see DOI: 10.1039/c2cc34482c

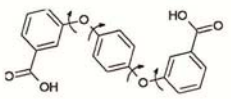

Scheme 1 Design of an organic ligand with flexible joints: 3,3′-(1,4-phenylenebis(oxy))dibenzoic acid (H_2*mpm*-PBODB).

Here we report on {[Zn_2(*mpm*-PBODB)$_2$bpy]·3DMF}$_n$ (**SNU-110**) synthesized from the organic linker having flexible joints (Scheme 1). The MOF shows a selective CO_2 adsorption property over CH_4 as well as N_2 and H_2 gases at 195 K.

SNU-110 was synthesized from solvothermal reaction of 3,3′-(1,4-phenylenebis(oxy))dibenzoic acid (H_2*mpm*-PBODB) with $Zn(NO_3)_2 \cdot 6H_2O$ and 4,4′-bipyridine (bpy) in DMF. It is thermally stable up to 370 °C (see ESI†). In the X-ray crystal structure of **SNU-110**, two Zn^{II} ions form a paddle wheel cluster unit, each of which is connected by four *mpm*-PBODB ligands to construct a corrugated 2D layer extending along the $(10\bar{2})$ plane (Fig. 1a). The 2D layers are further connected by bpy ligands along the [101] direction, since the axial sites of the paddle wheel units are coordinated with bpy ligands, which gives rise to a 3D framework generating 1D channels (Fig. 1b and c). The angle made between the corrugated 2D planes and the bpy pillar is 29.4°,

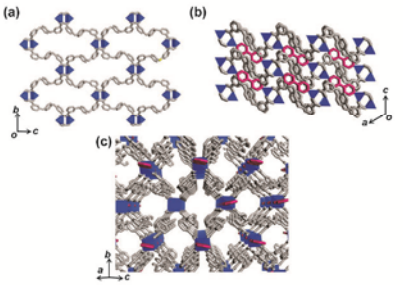

Fig. 1 The X-ray structure of **SNU-110**. (a) A corrugated 2D layer formed of [Zn_2(*mpm*-PBODB)$_2$], running on the $(10\bar{2}$ plane). (b) A view seen on the (010) plane showing corrugated 2D layers connected by bpy pillars. (c) A view seen along the [101] direction showing 1D channels. Color scheme: Zinc, blue; *mpm*-PBODB, gray; 4,4′-bpy, red. Hydrogen atoms are omitted for clarity.

although nearly right angle has been commonly made between the connecting pillar and the 2D layer constructed by the paddle-wheel type Zn_2 cluster units.[29] The 1D channels extending along the [101] direction have the rectangular cavities of effective size 4.4 × 3.7 Å^2, and they are filled with guest DMF molecules as characterized by IR, EA, and TGA data. The solvent accessible volume estimated by PLATON is 30% of the structure (0.248 cm^3 g^{-1}).[30]

The desolvated sample, $[Zn_2(mpm\text{-}PBODB)_2bpy]_n$ (**SNU-110′**), was prepared by the treatment of **SNU-110** with supercritical CO_2 fluid. Since the single crystallinity was not maintained during this activation process, the desolvated phase was analysed by powder X-ray diffraction (PXRD) data of **SNU-110′**. The PXRD patterns indicate that **SNU-110′** is different from the structure of the as-synthesized sample (Fig. 2). The PXRD pattern of **SNU-110′** was indexed by an *ab initio* method, using Dicvol04 program,[31] and refined by the Pawley method (R_p = 5.24%, R_{wp} = 8.05%, see ESI†), which suggested a triclinic unit cell ($P1$). Appearance of a peak at 2θ = 4.56° (hkl = 010), which is systemically absent in the original compound having the $P2_1/c$ space group, also supports the triclinic cell that the screw axis along the b axis does not exist. According to the refined unit cell, the total unit cell volume (2438.59 Å^3) of **SNU-110′** is reduced by *ca.* 8.8% compared with that (2673.0 Å^3) of **SNU-110**, suggesting that the desolvated sample has a shrunken structure. The pore volume of **SNU-110′** is 0.16 cm^3 g^{-1} as calculated by subtracting the volume of the skeleton (1909.74 Å^3; calculated by PLATON[30]) from its unit cell volume. It is much smaller than that (0.248 cm^3 g^{-1}) of **SNU-110**. Rietveld refinement was also tried, but the reasonable solution or refined structure could not be obtained from the PXRD data due to low resolution of the diffraction data as well as the low symmetry of the unit cell. When **SNU-110′** was immersed in DMF for 10 min, the original structure of **SNU-110** was restored as evidenced by PXRD patterns (Fig. 2d).

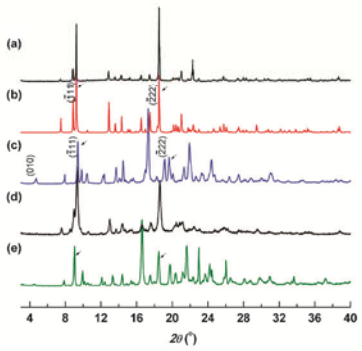

Fig. 2 Powder X-ray diffraction patterns of **SNU-110**. (a) As synthesized, (b) simulated from X-ray crystal diffraction data, (c) activated sample, **SNU-110′**: Bragg positions are marked based on cyclically permutated cell parameters for comparison (*abc* → *cab*), (d) resolvated sample obtained by immersion of **SNU-110′** in DMF for 10 min, and (e) **SNU-110′** under CO_2 stream at 248 K.

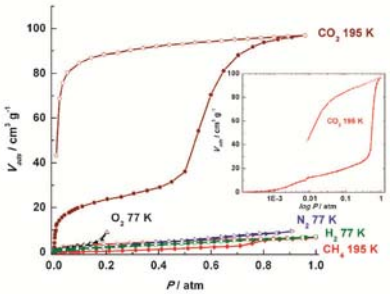

Fig. 3 Gas adsorption isotherms of **SNU-110′**. Inset diagram represents CO_2 adsorption at 195 K *versus* log *P*. Filled shapes: adsorption, open shapes: desorption.

The gas adsorption isotherms of **SNU-110′** were measured for N_2, H_2, O_2, CH_4, and CO_2 gases (Fig. 3 and Table 1). As seen in Fig. 3, **SNU-110′** hardly adsorbs N_2, O_2, and H_2 gases at 77 K as well as CH_4 gas at 195 K, but it adsorbs a significant amount of CO_2 at 195 K. Considering the kinetic diameters of CH_4, O_2, N_2, and H_2, which are 3.8, 3.46, 3.64, and 2.89 Å, respectively, the window size of **SNU-110′** must be smaller than 2.89 Å. However, the fact that CO_2 with a kinetic diameter of 3.3 Å is adsorbed in **SNU-110′** suggests that CO_2 interacts with the flexible MOF and opens up the gate due to its large polarizability and quadrupole moment.[10] The facilitated diffusion of CO_2 at 195 K *versus* H_2 at 77 K must be also a factor in this phenomenon. The adsorption selectivities of **SNU-110′** at 195 K and 1 bar for CO_2–N_2 and CO_2–H_2 are 35 : 1 (v/v) and 61 : 1 (v/v), respectively, and that for CO_2–CH_4 is 15 : 1 (v/v).

The CO_2 adsorption isotherm at 195 K shows a two-step adsorption curve with a big desorption-hysteresis. The first step shows a type-I isotherm and the adsorption saturation occurs at 0.40 atm where the uptake amount reaches 1.3 mmol g^{-1}. The second adsorption step starts at 0.48 atm and the uptake amount reaches 4.3 mmol g^{-1}, *i.e.* 3 times greater than that of the first step. The step-wise adsorption of CO_2 at 195 K indicates that the framework structure containing the flexible

Table 1 Gas adsorption data of **SNU-110′**

Compound	Gas	T/K	P/atm	Adsorption capacity (cm^3 g^{-1})	Ref.
SNU-110′	CO_2	195	1.0	97.0	This work
		231	1.0	37.0	
		273	1.0	23.6	
		298	1.0	12.9	
	CH_4	195	1.0	6.49	
		298	1.0	0.91	
	N_2	77	0.9	9.39	
		195	1.0	2.79	
		298	1.0	0.22	
	H_2	77	1.0	6.88	
		195	1.0	1.60	
	O_2	77	0.2	8.88	
SNU-31′	CO_2	298	1.0	13.3	22
	N_2	298	1.0	0.56	
PCN-123	CO_2	295	1.0	10.5–26.4	32
	N_2	77	0.9	Negligible	

organic linker is altered depending on the CO_2 pressure.[15–17] The contracted phase of **SNU-110′** transforms to the open phase when CO_2 pressure exceeds 0.48 atm at 195 K, and then completely opens at 1 atm to get saturated with CO_2. The desorption curve shows a hysteresis with type I isotherm. As the pressure of CO_2 is reduced from 1 atm, the framework maintains the open phase till 3×10^{-2} atm, and then suddenly returns to the contracted phase again. This hysteresis can be reproduced for several cycles in the repeated experiments. The calculated surface areas of **SNU-110′**, as estimated from the first step adsorption curve by applying the Dubinin Radushkevich (DR), Brunauer–Emmett–Teller (BET), and Langmuir methods, are 409 $m^2\ g^{-1}$, 101 $m^2\ g^{-1}$, and 111 $m^2\ g^{-1}$, respectively. When calculated by using the desorption curve, they are 658 $m^2\ g^{-1}$, 411 $m^2\ g^{-1}$, and 486 $m^2\ g^{-1}$, respectively. The pore volume (0.154 $cm^3\ g^{-1}$) estimated from the first step adsorption curve by using the DR equation is similar to the value (0.16 $cm^3\ g^{-1}$) calculated by the unit cell volume of **SNU-110′** minus the skeletal volume, while that (0.247 $cm^3\ g^{-1}$) obtained from the desorption curve is similar to the free volume (0.248 $cm^3\ g^{-1}$) of **SNU-110** estimated by using PLATON.[30]

When temperature was elevated to 231, 273, and 298 K, the P/P_0 value for the phase transition of the MOF decreased to 0.021, 0.0044, 0.0036, respectively (see ESI†). This trend can be explained by the increase of thermal energies for both the framework and the CO_2 molecules as the temperature increases.[16]

The PXRD pattern of **SNU-110′** measured under CO_2 pressure (*ca.* 1 atm) at 248 K indicates that many peaks are shifted to the lower angle regions compared with those of **SNU-110′**, suggesting the expansion of the framework on CO_2 adsorption as well (Fig. 2e). The average isosteric heat (Q_{st}) of the CO_2 adsorption in **SNU-110′** is 26.2 kJ mol^{-1}, as calculated from the adsorption data at 195, 231, 273, and 298 K by using the Clausius–Clapeyron equation (see ESI†). It is comparable to those (25–35 kJ mol^{-1}) of common MOFs.[2]

Interestingly, **SNU-110′** in this work hardly adsorbs CH_4 at 195 K. In general, at 195 K, MOFs show higher uptake capacity for CO_2 than for CH_4 since CO_2 (T_c = 304.19 K) is subcritical and thus more condensable than CH_4 (T_c = 190.09 K) that is supercritical.[24–26] Despite this, the flexible MOFs selectively adsorbing CO_2 over N_2 and H_2 often cannot efficiently exclude CH_4 that has high polarizability (2.45 $Å^3$). For example, SNU-M10 adsorbs 123.5 $cm^3\ g^{-1}$ of CO_2 and 27.5 $cm^3\ g^{-1}$ of CH_4 at 195 K, and SNU-21S adsorbs 257 $cm^3\ g^{-1}$ of CO_2 and 124 $cm^3\ g^{-1}$ of CH_4 at 195 K.[10,20] Therefore, it is obvious that the flexibility of the present MOF is so well tuned that only CO_2 can open the gate to be adsorbed in the pores.

In conclusion, we have synthesized a porous metal–organic framework, **SNU-110**, by using an organic linker having flexible joints. The sample desolvated by using the supercritical CO_2 fluid, **SNU-110′**, has shrunken structure as evidenced by PXRD data. It exhibits a two-step CO_2 adsorption isotherm at 195 K, which is attributed to the structural transformations depending on the amount of CO_2 adsorption. It shows high adsorption selectivity for CO_2 over H_2, N_2, and CH_4 gases at 195 K.

This work was supported by National Research Foundation of Korea (NRF) Grant funded by the Korean Government (MEST) (No. 2011-0031432 and No. 2011-0001341). We thank Korean Student Aids for a graduate fellowship to D. H. Hong, and we thank Dr Hyun-Sook Lee of Korea Institute of Science and Technology for measurement of PXRD on Bruker D8.

Notes and references

1 M. P. Suh, H. J. Park, T. K. Prasad and D. W. Lim, *Chem. Rev.*, 2012, **112**, 782–835.
2 K. Sumida, D. L. Rogow, J. A. Mason, T. M. McDonald, E. D. Bloch, Z. R. Herm, T. H. Bae and J. R. Long, *Chem. Rev.*, 2012, **112**, 724–781.
3 Y. E. Cheon and M. P. Suh, *Angew. Chem., Int. Ed.*, 2009, **48**, 2899–2903.
4 H. J. Park, D. W. Lim, W. S. Yang, T. R. Oh and M. P. Suh, *Chem.–Eur. J.*, 2011, **17**, 7251–7260.
5 H. J. Park and M. P. Suh, *Chem. Commun.*, 2010, **46**, 610–612.
6 H. J. Park and M. P. Suh, *Chem. Commun.*, 2012, **48**, 3400–3402.
7 T. K. Prasad, D. H. Hong and M. P. Suh, *Chem.–Eur. J.*, 2010, **16**, 14043–14050.
8 O. K. Farha, A. O. Yazaydin, I. Eryazici, C. D. Malliakas, B. G. Hauser, M. G. Kanatzidis, S. T. Nguyen, R. Q. Snurr and J. T. Hupp, *Nat. Chem.*, 2010, **2**, 944–948.
9 H. Furukawa, N. Ko, Y. B. Go, N. Aratani, S. B. Choi, E. Choi, A. O. Yazaydin, R. Q. Snurr, M. O'Keeffe, J. Kim and O. M. Yaghi, *Science*, 2010, **329**, 424–428.
10 H. S. Choi and M. P. Suh, *Angew. Chem., Int. Ed.*, 2009, **48**, 6865–6869.
11 J. Rabone, Y. F. Yue, S. Y. Chong, K. C. Stylianou, J. Bacsa, D. Bradshaw, G. R. Darling, N. G. Berry, Y. Z. Khimyak, A. Y. Ganin, P. Wiper, J. B. Claridge and M. J. Rosseinsky, *Science*, 2010, **329**, 1053–1057.
12 T. M. McDonald, D. M. D'Alessandro, R. Krishna and J. R. Long, *Chem. Sci.*, 2011, **2**, 2022–2028.
13 S. R. Caskey, A. G. Wong-Foy and A. J. Matzger, *J. Am. Chem. Soc.*, 2008, **130**, 10870–10871.
14 S. Henke and R. A. Fischer, *J. Am. Chem. Soc.*, 2011, **133**, 2064–2067.
15 S. Henke, A. Schneemann, A. Wutscher and R. A. Fischer, *J. Am. Chem. Soc.*, 2012, **134**, 9464–9474.
16 J. Seo, R. Matsuda, H. Sakamoto, C. Bonneau and S. Kitagawa, *J. Am. Chem. Soc.*, 2009, **131**, 12792–12800.
17 J. Zhang, H. Wu, T. J. Emge and J. Li, *Chem. Commun.*, 2010, **46**, 9152–9154.
18 J. An, S. J. Geib and N. L. Rosi, *J. Am. Chem. Soc.*, 2010, **132**, 38–39.
19 J. An and N. L. Rosi, *J. Am. Chem. Soc.*, 2010, **132**, 5578–5579.
20 T. K. Kim and M. P. Suh, *Chem. Commun.*, 2011, **47**, 4258–4260.
21 L. H. Xie and M. P. Suh, *Chem.–Eur. J.*, 2011, **17**, 13653–13656.
22 H. J. Park, Y. E. Cheon and M. P. Suh, *Chem.–Eur. J.*, 2010, **16**, 11662–11669.
23 J. R. Li, R. J. Kuppler and H.-C. Zhou, *Chem. Soc. Rev.*, 2009, **38**, 1477–1504.
24 S. Horike, Y. Inubushi, T. Hori, T. Fukushima and S. Kitagawa, *Chem. Sci.*, 2012, **3**, 116–120.
25 S. Couck, J. F. M. Denayer, G. V. Baron, T. Remy, J. Gascon and F. Kapteijn, *J. Am. Chem. Soc.*, 2009, **131**, 6326–6327.
26 D. Britt, H. Furukawa, B. Wang, T. G. Glover and O. M. Yaghi, *Proc. Natl. Acad. Sci. U. S. A.*, 2009, **106**, 20637–20640.
27 H. R. Moon, J. H. Kim and M. P. Suh, *Angew. Chem., Int. Ed.*, 2005, **44**, 1261–1265.
28 M. P. Suh, H. R. Moon, E. Y. Lee and S. Y. Jang, *J. Am. Chem. Soc.*, 2006, **128**, 4710–4718.
29 H. Chun, D. N. Dybtsev, H. Kim and K. Kim, *Chem.–Eur. J.*, 2005, **11**, 3521–3529.
30 A. L. Spek, *PLATON99, A Multipurpose Crystallographic Tool*, Utrecht University, Utrecht, The Netherlands, 1999.
31 A. Boultif and D. Louer, *J. Appl. Crystallogr.*, 2004, **37**, 724–731.
32 J. Park, D. Q. Yuan, K. T. Pham, J. R. Li, A. Yakovenko and H.-C. Zhou, *J. Am. Chem. Soc.*, 2012, **134**, 99–102.

CHEMISTRY
A EUROPEAN JOURNAL

ChemPubSoc Europe

DOI: 10.1002/chem.201303086

Comparison of Gas Sorption Properties of Neutral and Anionic Metal–Organic Frameworks Prepared from the Same Building Blocks but in Different Solvent Systems

Myung-Ho Choi, Hye Jeong Park, Dae Ho Hong, and Myunghyun Paik Suh*[a]

Abstract: Two different 3D porous metal–organic frameworks, $[Zn_4O(NTN)_2]\cdot 10DMA\cdot 7H_2O$ (**SNU-150**) and $[Zn_5(NTN)_4(DEF)_2][NH_2(C_2H_5)_2]_2\cdot 8DEF\cdot 6H_2O$ (**SNU-151**), are synthesized from the same metal and organic building blocks but in different solvent systems, specifically, in the absence and the presence of a small amount of acid. **SNU-150** is a doubly interpenetrated neutral framework, whereas **SNU-151** is a non-interpenetrated anionic framework containing diethylammonium cations in the pores. Comparisons of the N_2, H_2, CO_2, and CH_4 gas adsorption capacities as well as the CO_2 adsorption selectivity over N_2 and CH_4 in desolvated **SNU-150′** (BET: 1852 $m^2 g^{-1}$) and **SNU-151′** (BET: 1563 $m^2 g^{-1}$) samples demonstrate that the charged framework is superior to the neutral framework for gas storage and gas separation, despite its smaller surface area and different framework structure.

Keywords: adsorption · carbon dioxide · cationic guests · gas separation · metal–organic frameworks

Introduction

Metal–organic frameworks (MOFs) have attracted great attention because of their potential applications in gas storage[1–6] and separation.[7–14] The gas adsorption capacities of MOFs are enhanced by the increase in surface areas, presence of accessible metal sites,[6,15] and functional groups.[16] The gas separation capabilities of MOFs, in particular for CO_2 separation from flue gas and landfill gas, are affected by the flexibility of the frameworks[7,17] and the ions or molecules contained in the pores of the MOFs,[18–20] because CO_2 molecules can interact with the MOF much more strongly than other gases because of the high quadrupole moment (14.3×10^{-40} C m^2) and polarizability (26.3×10^{-25} cm^3). Recently, it has been reported that anionic MOFs containing metal cations in their pores show higher gas sorption capacities and significantly enhanced CO_2 adsorption selectivities over other gases than common neutral MOFs.[18] However, the synthetic method for obtaining charged MOFs exclusively from neutral MOFs has not yet been well established. Moreover, simple comparison of the gas sorption properties between charged MOFs and neutral MOFs encounters difficulties owing to the large differences in their framework structures and surface areas, because they are constructed from different metal ions and organic building blocks.

Here, we report two porous MOFs, $[Zn_4O(NTN)_2]\cdot 10DMA\cdot 7H_2O$ (**SNU-150**) and $[Zn_5(NTN)_4(DEF)_2][NH_2(C_2H_5)_2]_2\cdot 8DEF\cdot 6H_2O$ (**SNU-151**) (H_3NTN = 6,6′,6″-nitrilotri-2-naphthoic acid, DMA = *N*,*N*-dimethylacetamide, DEF = *N*,*N*-diethylformamide), which are synthesized by using the same metal and organic building blocks but different solvent systems, in particular, in the absence and presence of a small amount of acetic acid (Scheme 1). **SNU-150** is a neutral framework, whereas **SNU-151** is an anionic framework containing diethylammonium cations as guests. Desolvated solid **SNU-151′** ($[Zn_5(NTN)_4][NH_2(C_2H_5)_2]_2$), obtained by supercritical CO_2 treatment, exhibits higher adsorption capacities and higher isosteric heats of H_2, CO_2, and CH_4 gas adsorption, as well as higher CO_2 adsorption selectivities over N_2 and CH_4 gases, than **SNU-150′** ($[Zn_4O(NTN)_2]$), because of the stronger interaction of the gas molecules with the anionic framework and the ammonium cations included in the channels.

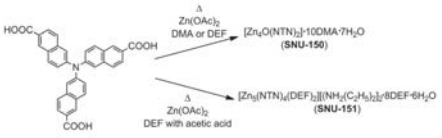

Scheme 1. Preparation of **SNU-150** and **SNU-151**.

Results and Discussion

Synthesis and X-ray crystal structures of neutral (SNU-150) and charged (SNU-151) frameworks: Greenish truncated-oc-

[a] M.-H. Choi, H. J. Park, D. H. Hong, Prof. M. P. Suh
Department of Chemistry, Seoul National University
Seoul 151-747 (Republic of Korea)
Fax: (+82) 2-886-8516
E-mail: mpsuh@snu.ac.kr

Supporting information for this article is available on the WWW under http://dx.doi.org/10.1002/chem.201303086.

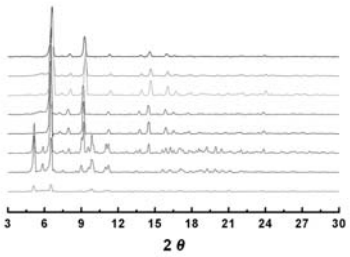

Figure 1. PXRD patterns of the products formed from the solvothermal reaction of $Zn(OAc)_2 \cdot 2H_2O$ (67.3 mg, 0.3 mmol) and H_3NTN (26.3 mg, 0.05 mmol) in DEF (1.5 mL) in the presence of various amount of acetic acid: **SNU-150** is formed in the presence of less than 75 μL (1.3 mmol) of acetic acid, whereas **SNU-151** is formed in the presence of 75 μL (1.3 mmol) to 300 μL (5.2 mmol) of acetic acid. Reaction conditions (from top to bottom): 90 °C, no acid; 90 °C, acetic acid (20 μL); 90 °C, acetic acid (30 μL); 90 °C, acetic acid (50 μL); 90 °C, acetic acid (60 μL); 90 °C, acetic acid (75 μL); 90 °C, acetic acid (250 μL); 90 °C, acetic acid (300 μL).

tahedral crystals of **SNU-150** were prepared by heating a DMA solution of $Zn(OAc)_2 \cdot 2H_2O$ and H_3NTN at 90 °C for 24 h. Brown rhombus-shaped crystals of **SNU-151** were synthesized by heating a DEF solution of $Zn(OAc)_2 \cdot 2H_2O$ and H_3NTN in the presence of acetic acid (DEF/acetic acid = 100:3–100:12, v/v) at 90 °C for 24 h. When the volume ratio of acetic acid/DEF was less than 2.4 %, **SNU-150** was formed instead of **SNU-151**, as shown by the powder X-ray diffraction (PXRD) data (Figure 1). That is, the addition of a small amount of acetic acid to the reaction mixture leads to a totally different MOF. **SNU-150** and **SNU-151** are insoluble in common organic solvents.

In the single-crystal X-ray structure of **SNU-150** (Figure 2a), the $Zn_4O(CO_2)_6$ cluster acts as an octahedral secondary building unit (SBU), and NTN^{3-} acts as a triangular organic building block, which results in a (6,3)-connected net with a PdF_2-type net topology, similarly to those reported previously.[21–23] **SNU-150** is doubly interpenetrated, and generates 3D channels that extend along the three orthogonal directions. The effective window size of the channels is 4.5 × 1.7 Å^2. The void volume of **SNU-150** is 49.5 %, as calculated by PLATON (Table 1).[24]

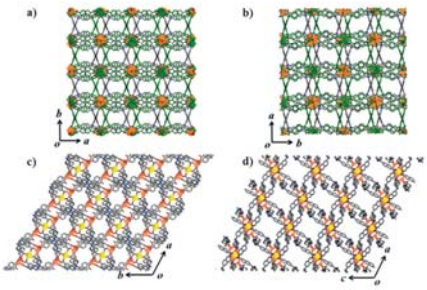

Figure 2. X-ray crystal structures of **SNU-150**, **SNU-150′**, and **SNU-151**. a) View of **SNU-150** on the *ab* plane. b) View of **SNU-150′** on the *ab* plane. c) View of **SNU-151** on the *ab* plane. d) View of **SNU-151** on the *ac* plane. Tetrahedral Zn, orange; octahedral Zn, yellow.

When single crystals of **SNU-150** were activated by using supercritical CO_2 fluid, a desolvated sample of **SNU-150′** was obtained, as shown by IR data, elemental analysis (EA), and thermogravimetric analysis (TGA). Interestingly, **SNU-150** undergoes single-crystal-to-single-crystal transformation during the activation process (Figure 2b). The single-crystal X-ray structure of activated **SNU-150′** exhibits a fine structure that differs from that of **SNU-150**. Many of the key dihedral angles of **SNU-150′** become different from those of **SNU-150**, and the pore size is enlarged to approximately 5.9 × 2.7 Å (compared to 4.5 × 1.7 Å for as-synthesized **SNU-150**) (see Table S1 and Figure S6 in the Support-

Table 1. Crystallographic data of **SNU-150**, **SNU-150′**, and **SNU-151** (squeezed).

	SNU-150	**SNU-150′**	**SNU-151**
formula	$Zn_4C_{90}H_{30}N_2O_{13}$	$Zn_4C_{66}H_{36}N_2O_{13}$	$Zn_5C_{142}H_{84}N_8O_{26}$
crystal system	cubic	cubic	triclinic
space group	$Ia\bar{3}$	$Pa\bar{3}$	$P\bar{1}$
M_r	1326.45	1326.45	2627.08
a [Å]	27.143(3)	27.3095(6)	16.158(3)
b [Å]	27.143(3)	27.3095(6)	18.171(4)
c [Å]	27.143(3)	27.3095(6)	18.955(4)
α [°]	90	90	99.19(3)
β [°]	90	90	106.28(3)
γ [°]	90	90	116.34(3)
V [Å^3]	19997(4)	20367.7(8)	4518.8(27)
Z	8	8	1
ρ_{calcd} [g cm^{-3}]	0.881	0.865	0.965
T [K]	100(2)	120(2)	100(2)
λ [Å]	0.80003	0.71073	0.69999
μ [mm^{-1}]	1.316	0.970	0.646
GOF (F^2)	1.271	0.999	1.539
$F(000)$	5360	5360	1346
reflections collected	3912	11598	16832
R_1, wR_2 [$I > 2\sigma(I)$]	0.1107,[a] 0.3329[b]	0.0771,[a] 0.2090[c]	0.1059,[a] 0.3253[b]
R_1, wR_2 (all data)	0.1328,[a] 0.3499[b]	0.0970,[a] 0.2187[c]	0.1120,[a] 0.3371[b]
largest diff. peak/hole [e Å^{-3}]	0.289/−0.350	4.170/−1.125	1.559/−3.119

[a] $R = \Sigma||F_o| - |F_c||/\Sigma|F_o|$. [b] $wR(F^2) = [\Sigma w(F_o^2 - F_c^2)^2/\Sigma w(F_o^2)^2]^{1/2}$ where $w = 1/[\sigma^2(F_o^2) + (0.2000P)^2 + (0.0000)P]$, $P = (F_o^2 + 2F_c^2)/3$ for **SNU-150** and **SNU-151**. [c] $wR(F^2) = [\Sigma w(F_o^2 - F_c^2)^2/\Sigma w(F_o^2)^2]^{1/2}$ where $w = 1/[\sigma^2(F_o^2) + (0.1469P)^2 + (0.0000)P]$, $P = (F_o^2 + 2F_c^2)/3$ for **SNU-150′**.

ing Information), similarly to the case of **SNU-77S**.[21] The powder X-ray diffraction patterns indicate that the framework structure of **SNU-150′** is similar to that of **SNU-150** (Figure 3).

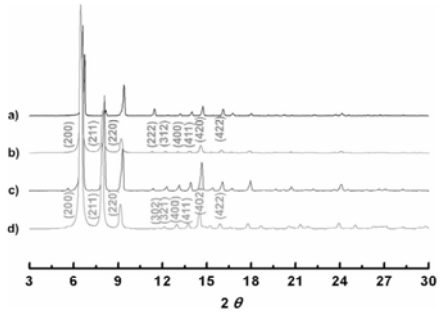

Figure 3. PXRD patterns of a) as-synthesized **SNU-150**, b) simulated powder pattern of **SNU-150** based on its single-crystal X-ray data, c) **SNU-150′** obtained by treatment of **SNU-150** with supercritical CO_2 fluid, and d) simulated powder pattern of **SNU-150′** based on its single-crystal X-ray data.

In the X-ray structure of **SNU-151**, there are three crystallographically independent Zn^{II} centers (Zn1, Zn2, and Zn3), which are linked in the sequence Zn1–Zn2–Zn3–Zn2–Zn1 to form a Zn_5 cluster unit. Zn1 and Zn2 show tetrahedral (td) coordination geometry, being coordinated with four carboxylate oxygen atoms of four different NTN^{3-} ligands. Zn3 shows octahedral coordination geometry, being coordinated with four carboxylate oxygen atoms of four different NTN^{3-} ligands and two oxygen atoms of DEF solvent molecules (see Figure S7 in the Supporting Information). The Zn_5 cluster units are connected by carboxylate groups to form a non-interpenetrated anionic 3D framework generating 2D channels. The effective window sizes of the square channels extending along the *ab* plane and of the cylindrical channels extending along the *ac* plane are 5.2×2.5 and 7.7×6.5 Å^2, respectively (Figure 2c and 2d). Because the Zn_5 metal cluster consists of five Zn^{II} ions and twelve carboxylate groups, two diethylammonium species should be included per formula unit of the host as the counter cationic guests. The chemical formula of **SNU-151** was determined from the EA data as well as the IR spectrum showing ammonium peaks at 2875 cm^{-1}, because the diethylammonium cations could not be refined through single-crystal X-ray diffraction owing to the severe disorder. The void volume of **SNU-151** is 51.5% without taking the diethylammonium guests into consideration. When **SNU-151** was activated by using supercritical CO_2 fluid, two DEF molecules coordinated at the Zn3 atom were removed together with the DEF and water guest solvent molecules included in the channels. The PXRD patterns indicate that the framework structure of **SNU-151′** differs significantly from that of the as-synthesized **SNU-151** (Figure 4).

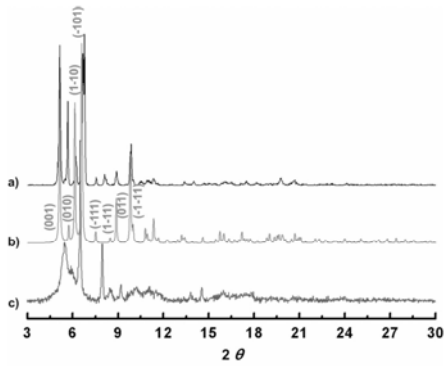

Figure 4. PXRD patterns of a) as-synthesized **SNU-151**, b) simulated powder pattern of **SNU-151** based on its single-crystal data, c) **SNU-151′** obtained from the treatment of **SNU-151** with supercritical CO_2 fluid.

Gas sorption properties: The gas adsorption isotherms of **SNU-150′** and **SNU-151′** were measured for N_2, H_2, CO_2, and CH_4 gases, and the data are summarized and compared with those of the previously reported **SNU-77S**[21] and **SNU-100′**,[18] which have similar structures to **SNU-150′** and **SNU-151′**, respectively (Table 2).

The N_2 sorption isotherms of **SNU-150′** and **SNU-151′** show type-I curves, which are characteristic of microporous materials (Figure 5a). **SNU-150′** shows a small hysteresis of type H-4 in the N_2 desorption curve, which may be associated with the narrow slit-like pores.[25] The BET (Langmuir) surface areas of **SNU-150′** and **SNU-151′** are 1852 (1945) and 1563 (1674) m^2 g^{-1}, respectively. The pore volumes esti-

Table 2. Gas adsorption data of **SNU-150′** and **SNU-151′** together with the comparison with **SNU-77S** and **SNU-100′**.

	T [K]	*P* [atm]	Adsorption capacity [wt%] **SNU-150′**	**SNU-77S**[21]	**SNU-151′**	**SNU-100′**[18]
N_2	77	0.95	71.1	131	55.3	26.2
	298	1	0.546	0.40	0.519	0.624
H_2	77	1	1.54	1.79	2.00	1.81
	87	1	1.00	1.01	1.24	1.30
Q_{st} of H_2 adsorption [kJ mol^{-1}]			5.04–4.65	7.05	6.27–5.82	8.14–7.08
CO_2	195	1	78.6	169	67.8	45.2
	231	1	40.5	130	56.0	37.2
	273	1	12.0	8.21	22.2	19.9
	298	1	6.09	3.94	14.1	14.1
Q_{st} of CO_2 adsorption [kJ mol^{-1}]			17.1–16.5	19.9–19.4	27.1–21.0	29.3–27.7
CH_4	195	1	11.1	8.70	11.3	10.4
	231	1	3.15	4.12	7.30	7.57
	273	1	1.29	1.20	2.00	2.56
	298	1	0.859	0.62	1.24	1.41
Q_{st} of CH_4 adsorption [kJ mol^{-1}]			12.8–12.3	14.3–14.2	18.2–16.6	26.5–22.4

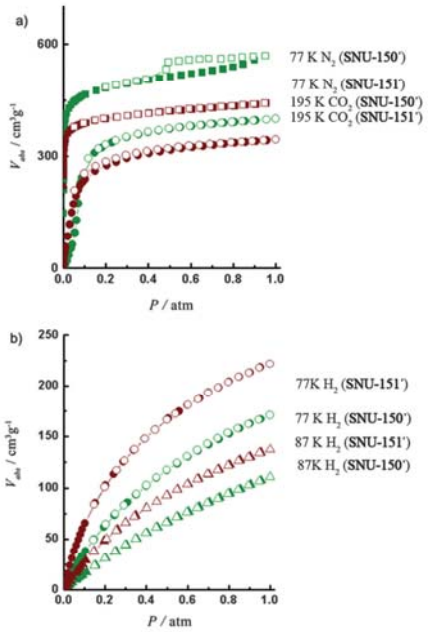

Figure 5. Gas sorption isotherms for **SNU-150′** (green) and **SNU-151′** (burgundy). a) N_2 at 77 K (squares) and CO_2 at 195 K (circles). b) H_2 at 77 K (circles) and 87 K (triangles). Filled shapes, adsorption; open shapes, desorption.

mated by applying the Dubinin–Radushkevich (DR) equation are 0.717 cm^{3}g^{-1} for **SNU-150′** and 0.614 cm^{3}g^{-1} for **SNU-151′**. The pore-size distributions obtained through the Horvath–Kawazoe (HK) method suggest that **SNU-150′** and **SNU-151′** have pore sizes of 6.18 and 6.08 Å, respectively (Figure 6).[26]

The H_2 adsorption capacities of **SNU-150′** and **SNU-151′** are 1.54 and 2.00 wt%, respectively, at 77 K and 1 atm (Figure 5b). The isosteric heats (Q_{st}) of the H_2 adsorption estimated from the isotherms measured at 77 and 87 K by using a virial equation[27] are 5.04–4.65 kJ mol^{-1} for **SNU-150′** and 6.27–5.82 kJ mol^{-1} for **SNU-151′**, depending on the degree of H_2 loading.

The CO_2 and CH_4 gas adsorption capacities of **SNU-151′** at 1 atm at T = 231 and 273 K are higher than those of **SNU-150′**, as shown in Table 2 and Figure 7. At 298 K and 1 atm, **SNU-151′** adsorbs 14.1 wt% of CO_2, which is approximately 2.3 times higher than the CO_2 uptake capacity (6.09 wt%) of **SNU-150′**. The Q_{st} values of the CO_2 and CH_4 adsorptions were calculated by using the Clausius–Clapeyron equation, applying the polynomial equation and Langmuir–Freundlich equation, respectively, to the adsorption isotherms measured at 195, 231, 273, and 298 K. The Q_{st} values of the CO_2 and CH_4 adsorptions in **SNU-151′** are 27.1–21.0 kJ mol^{-1} and 18.2–16.6 kJ mol^{-1}, respectively, which are also higher than those (17.1–16.5 and 12.8–12.3 kJ mol^{-1}, respectively) in **SNU-150′** (see Figure S11 in the Supporting Information).

The higher uptake capacities and higher Q_{st} values for the H_2, CO_2, and CH_4 adsorptions in **SNU-151′** than in **SNU-150′** must be attributed to the stronger interactions of those gas molecules with the anionic framework and diethylammonium cationic guests included in **SNU-151′**, compared to their interactions with the neutral framework of **SNU-150′**.

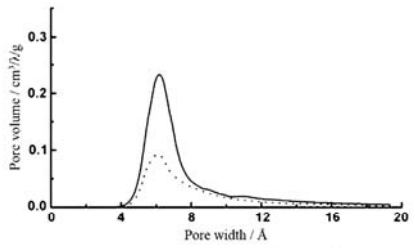

Figure 6. Pore-size distributions of **SNU-150′** (solid line) and **SNU-151′** (dotted line), estimated by using the Horvath–Kawazoe (HK) method using the N_2 sorption data measured at 77 K.

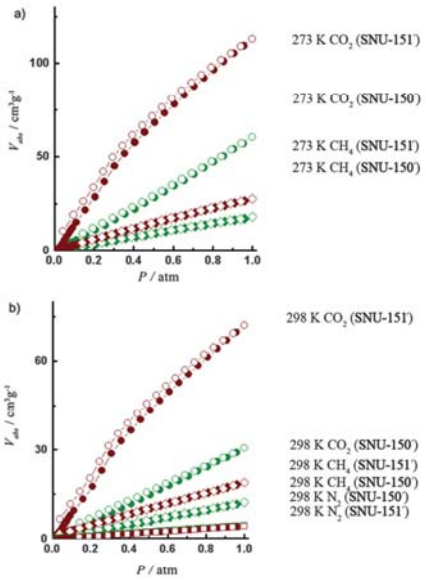

Figure 7. Gas sorption isotherms for **SNU-150′** (green) and **SNU-151′** (burgundy). a) CO_2 (circles) and CH_4 (diamonds) at 273 K. b) CO_2 (circles), CH_4 (diamonds), and N_2 (squares) at 298 K. Filled shapes, adsorption; open shapes, desorption.

In addition, the pore size (6.08 Å) of **SNU-151′** is slightly smaller than that (6.18 Å) of **SNU-150′** as estimated from the N_2 adsorption data (Figure 6), which is also responsible for the higher Q_{st} values of the gas adsorption in **SNU-151′**, even though its activated framework structure is different from that of **SNU-150′**. It is quite well recognized that charged frameworks show superior gas sorption properties to neutral ones.[18,28–30]

When the gas adsorption properties of **SNU-150′** are compared with those of **SNU-77S**,[21] which also has PdF_2 topology, it is found that **SNU-150′** adsorbs much smaller amounts of N_2 and H_2 gases at 77 K and 1 atm, as well as a smaller amount of CO_2 gas at 195 K and 1 atm. This must be attributed to the significantly smaller surface area (1852 m^2g^{-1}) of **SNU-150′** than that (3670 m^2g^{-1}) of **SNU-77S**. When the gas adsorption properties of **SNU-151′** are compared with those of **SNU-100′**, which has an anionic framework with diethylammonium cations, it is observed that **SNU-151′** is superior to **SNU-100′**.[18] This is also attributed to the higher surface area (1563 m^2g^{-1}) of **SNU-151′** than that (814 m^2g^{-1}) of **SNU-100′**. However, at 298 K and 1 atm, the CO_2 and CH_4 gas uptake capacities of **SNU-150′** and **SNU-151′** become comparable to those of **SNU-77S** and **SNU-100′**, respectively.

SNU-150′ and **SNU-151′** adsorb CO_2 gas selectively at 298 K, with hardly any adsorption of N_2 and CH_4 gases (Figure 7b) (see Figure S10 in the Supporting Information). According to the calculation using the ideal adsorbed solution theory (IAST) with the assumption that the flue gas has a CO_2/N_2 volume ratio of 15:85, the selectivity values of the CO_2/N_2 adsorption at 298 K are 30.0 for **SNU-151′** and 5.44–6.42 for **SNU-150′** depending on the pressure (up to 1 atm) (Figure 8). The present result is consistent with our previous report that an anionic framework (**SNU-100′**) with cationic guests showed very high CO_2 uptake selectivity over N_2.[18] The CO_2/N_2 adsorption selectivity of **SNU-151′** is higher than those of **SNU-100′** (26.5)[18] and $H_3[(Cu_4Cl)_3(BTTri)_8]$ (21.0).[31] The selectivity values of the CO_2 adsorption over CH_4 were also calculated by using IAST with the assumption that the landfill gas has a CO_2/CH_4 volume ratio of 50:50 at 298 K. The values are 7.20 for **SNU-151′** and 2.26–2.35 for **SNU-150′** depending on the pressure (up to 1 atm) at 298 K. **SNU-151′** shows a higher selectivity for CO_2 adsorption over CH_4 than $[Cu(bpy\text{-}2)_2(SiF_6)]$[32] (bpy-2 = 1,2-bis(4-pyridyl)ethene) and the $[Zn_2(BDC)_2(DABCO)]$ (DMOF) series.[33]

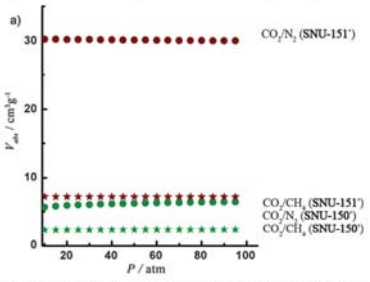

Figure 8. Selectivities of **SNU-150′** (green) and **SNU-151′** (burgundy) for CO_2/N_2 (circles) and CO_2/CH_4 (stars) adsorption depending on the pressure, calculated by using ideal adsorbed solution theory (IAST) with the assumption that the flue gas has a CO_2/N_2 volume ratio of 15:85 and landfill gas has a CO_2/CH_4 volume ratio of 50:50.

Conclusion

We have prepared two different porous MOFs, **SNU-150** and **SNU-151**, from the same metal and organic building blocks but in the presence and absence of acetic acid. **SNU-150** is a neutral framework, whereas **SNU-151** is an anionic framework containing diethylammonium guests. **SNU-150** undergoes a single-crystal-to-single-crystal transformation upon guest removal, which affords **SNU-150′** with a slightly altered structure. **SNU-151′**, which is formed upon the removal of guest solvent as well as coordinated solvent molecules from **SNU-151**, has a different structure from **SNU-151.** **SNU-151′** shows higher uptake capacities for H_2, CO_2, and CH_4 gases as well as higher isosteric heats of those gas adsorptions than **SNU-150′**, despite the smaller surface area of **SNU-151′** (BET: 1563 m^2g^{-1}) than that of **SNU-150′** (BET: 1852 m^2g^{-1}). These properties are attributed to the charged framework and smaller pore size of **SNU-151′**. Furthermore, **SNU-151′** shows a significantly higher CO_2/N_2 adsorption selectivity at 298 K than **SNU-150′**. The present results suggest that for gas storage and gas separation applications, the synthesis of charged frameworks rather than neutral ones should be recommended, regardless of the framework structures.

Experimental Section

General methods: Anhydrous 1,4-dioxane was purchased from Sigma Aldrich, and used without further purification. Other chemicals and solvents used in the syntheses were of reagent grade and were used without further purification. Infrared spectra were recorded with a Perkin–Elmer 2000 FTIR spectrophotometer. Elemental analyses were recorded with a Perkin–Elmer 2400 Series II CHNS/O Analyzer. ^1H NMR spectra were measured on Bruker Advance DPX-300 spectrometer (300 MHz) at room temperature. Thermogravimetric analysis (TGA) and differential scanning calorimetry (DSC) were performed under N_2 (g) at a scan rate of 5 °C with a TGA Q50 and DSC Q10, respectively (TA instruments). Powder X-ray diffraction (PXRD) data were recorded on a Bruker D5005 diffractometer at 40 kV and 40 mA (CuK_α, $\lambda = 1.54050$ Å) with a scan speed of 0.5 °min^{-1} and a step size of 0.02° (2θ).

Synthesis of H_3NTN: H_3NTN (6,6′,6″-nitrilotri-2-naphthoic acid) was prepared as follows through modification of the previously reported methods.[34]

Synthesis of trimethyl 6,6′,6″-nitrilotri-2-naphthoate: Under a N_2 atmosphere, $Pd(OAc)_2$ (129 mg, 0.575 mmol) and *rac*-2,2′-bis(diphenylphosphino)-1,1′-binaphthyl) (*rac*-BINAP) (716 mg, 1.15 mmol) were dissolved in anhydrous 1,4-dioxane (100 mL). After stirring for 15 min, methyl 6-bromo-2-naphthoate (8.16 g, 30.8 mmol, 2.8 equiv), methyl 6-amino-2-naphthoate (2.32 g, 11.5 mmol, 1 equiv), and Cs_2CO_3 (5.63 g, 29.2 mmol, 2.5 equiv) were added. The solution was heated at reflux for five days,

cooled to room temperature, and diluted with CH_2Cl_2 (200 mL). The crude mixture was filtered through celite, concentrated through evaporation of the solvent, and then purified by silica gel column chromatography with *n*-hexane/CH_2Cl_2 (2:1, v/v) and then CH_2Cl_2 as eluents. The product was obtained as a light yellow powder. ^{1}H NMR ($CDCl_3$): δ = 3.99 (s, 9H), 7.44 (d, J = 8.8 Hz, 3H), 7.60–7.62 (m, 6H), 7.90 (d, J = 8.9 Hz, 3H), 8.03 (d, J = 8.6 Hz, 3H), 8.60 ppm (s, 3H).

Synthesis of 6,6′,6″-nitrilotri-2-naphthoic acid (H_3NTN): Trimethyl 6,6′,6″-nitrilotri-2-naphthalate was dissolved in MeOH, and then a saturated aqueous solution of NaOH was added until the solution reached pH 8. The solution was heated at reflux for one day, and then the solvent was removed by evaporation. The crude product was dissolved with distilled water, and HCl was added until the solution reached pH 2. The solution was cooled to room temperature, and the solid formed was filtered off, washed with water, and dried in vacuo. ^{1}H NMR ([D$_6$]DMSO): δ = 7.40 (d, J = 8.4 Hz, 3H), 7.64 (s, J = 35.7 Hz, 3H), 7.76 –7.90 (m, 6H), 8.00 (d, J = 9 Hz, 3H), 8.03 (d, J = 9 Hz, 3H), 8.46 ppm (s, J = 25.8 Hz, 3H); elemental analysis calcd (%) for $C_{33}H_{21}NO_6$: C 75.13, H 4.01, N 2.66; found: C 73.01, H 4.06, N 2.56.

Synthesis of $[Zn_4O(NTN)_2]$·10 DMA·7 H_2O (SNU-150): The DMA solution (1.5 mL) of $Zn(OAc)_2$·2 H_2O (67.3 mg, 0.3 mmol) and the DMA solution (1 mL) of H_3NTN (26.3 mg, 0.05 mmol) were added in a serum glass bottle. The bottle was sealed and heated in an oven at 90 °C for 24 h, and truncated octahedral green crystals of $[Zn_4O(NTN)_2]$·10 DMA·7 H_2O were obtained. When DEF was used as the solvent instead of DMA with the same reaction mixture, the product was formed as a polycrystalline powder, the PXRD data of which indicated that it had the same framework structure as **SNU-150**. Yield: 42.5 mg (73.2 % based on H_3NTN); FTIR for **SNU-150** (KBr): $\tilde{\nu}$ = 3401 (O–H), 3053 (C–$H_{(NTN)}$), 2931 (C–$H_{(DMA)}$), 1626, 1587 cm^{-1} (O=C–O); elemental analysis calcd (%) for $Zn_4C_{106}H_{140}N_{12}O_{30}$: C 54.78, H 6.07, N 7.23; found: C 54.46, H 5.90, N 7.33.

Preparation of $[Zn_4O(NTN)_2]$ (SNU-150′): Before being dried, crystals of as-synthesized **SNU-150** were transferred into a vial (20 mL) together with the mother liquor. The mother liquor was decanted and the crystals were washed briefly with pure DMA (2 × 15 mL). The sample was desolvated by using supercritical CO_2 fluid. FTIR for **SNU-150′** (KBr): $\tilde{\nu}$ = 3052 (C–$H_{(NTN)}$), 1623, 1589 cm^{-1} (O=C–O); elemental analysis calcd (%) for $Zn_4C_{66}H_{36}O_{13}N_2$: C 57.67, H 2.64, N 2.04; found: C 57.36, H 2.66, N 2.24.

Synthesis of $[Zn_5(NTN)_4(DEF)_2][NH_2(C_2H_5)_2]_2$·8 DEF·6 H_2O (SNU-151): The DEF solution (1.5 mL) of $Zn(OAc)_2$·2 H_2O (67.3 mg, 0.3 mmol) was mixed with the DEF solution (1 mL) of H_3NTN (26.3 mg, 0.05 mmol) in a serum glass bottle, and then acetic acid (0.1 mL) was added. The reaction bottle was sealed and heated in an oven at 90 °C for 24 h, and rhombus-shaped brown crystals of $[Zn_5(NTN)_4(DEF)_2][NH_2(C_2H_5)_2]_2$·8 DEF·6 H_2O were formed. Yield: 0.0306 mg (67.1 % based on H_3NTN); FTIR for **SNU-151** (KBr pellet): $\tilde{\nu}$ = 3429 (O–H), 3054 (C–$H_{(NTN)}$), 2975, 2935 (C–$H_{(NTN)}$), 2875 (N–$H_{(diethylammonium)}$), 1659 (C=$O_{(DEF)}$), 1625, 1594 cm^{-1} (O=C–O); elemental analysis calcd (%) for $Zn_5C_{190}H_{208}N_{16}O_{35}$: C 61.80, H 5.95, N 6.07; found: C 61.39, H 5.77, N 5.95.

Preparation of $[Zn_5(NTN)_4][NH_2(C_2H_5)_2]_2$ (SNU-151′): Prior to activation, crystals of as-synthesized $[Zn_5(NTN)_4(DEF)_2][NH_2(C_2H_5)_2]_2$·8 DEF·6 H_2O were transferred to a vial (20 mL) together with the mother liquor. The mother liquor was decanted and the crystals were washed briefly with pure DEF (2 × 15 mL). The sample was desolvated by using supercritical CO_2 fluid. FTIR for **SNU-151′** (KBr pellet): $\tilde{\nu}$ = 3050 (C–$H_{(NTN)}$), 2853 (N–$H_{(diethylammonium)}$), 1690 (C=$O_{(NTN)}$), 1624, 1590 cm^{-1} (O=C–O); elemental analysis calcd (%) for $Zn_5C_{146}H_{86}O_{24}N_6$: C 65.34, H 3.76, N 3.27; found: C 65.81, H 3.80, N 3.39.

X-ray crystallography: Crystals of $[Zn_4O(NTN)_2]$·10 DMA·2 H_2O (**SNU-150**) and $[Zn_5(NTN)_4(DEF)_2][NH_2(C_2H_5)_2]_2$·8 DEF·6 H_2O (**SNU-151**) were coated with Paratone-N oil, and the diffraction data were measured at 100 K with synchrotron radiation (λ = 0.80003 Å for **SNU-150** and λ = 0.69999 Å for **SNU-151**) on an ADSC Quantum-210 detector at 2D SMC with a silicon (111) double crystal monochromator (DCM) at the Pohang Accelerator Laboratory, Korea. The ADSC Q210 ADX program[35] was used for data collection (**SNU-150**: detector distance, 62 mm; omega scan, $\Delta\omega$ = 1°; exposure time, 10 s/frame; **SNU-151**: detector distance, 70 mm; omega scan, $\Delta\omega$ = 1°; exposure time, 10 s/frame), and HKL3000 sm (Ver. 703r)[36] was used for cell refinement, reduction, and absorption corrections. The diffraction data of the activated sample $[Zn_4O(NTN)_2]$ (**SNU-150′**) were collected at 100 K with an Enraf–Nonius Kappa CCD diffractometer (MoK_α, λ = 0.71073 Å, graphite monochromator) by coating the crystal with Paratone-N oil. Preliminary orientation matrices and unit-cell parameters were obtained from the peaks of the first ten frames, and then refined by using the whole data set. Frames were integrated and corrected for Lorentz and polarization effects by using DENZO.[36] The scaling and global refinement of crystal parameters were performed by using SCALEPACK.[36] No adsorption correction was made. The crystal structures of **SNU-150**, **SNU-151**, and **SNU-150′** were solved by direct methods[37] and refined through full-matrix least-squares refinement using the SHELXL-97 program.[38] The hydrogen atoms were positioned geometrically by using a riding model. The electron densities of the disordered guest molecules were flattened by using the SQUEEZE option of PLATON.[39] In **SNU-150**, the overall framework was statistically disordered over two sites with 1:1 occupancies. Consequently, all the atoms were given by 0.5 occupancy, except Zn(1), O(1), O(1)′, N(1), and N(1)′, which sit on threefold crystallographic axes, and were given by the occupancy of 1/6. In **SNU-150′**, the site occupancy factors were given as 0.33333 for the Zn(1), O(1), N(1), and N(2) atoms, which sit on threefold crystallographic axes. CCDC-917750 (**SNU-150**), 917751 (**SNU-150′**), and 917752 (**SNU-151**) contain the supplementary crystallographic data for this paper. These data can be obtained free of charge from The Cambridge Crystallographic Data Centre via www.ccdc.cam.ac.uk/data_request/cif.

Supercritical CO_2 activation method: Before being dried, as-synthesized crystals, which were still in the mother liquor, were transferred to a vial (20 mL). The mother liquor was decanted and the crystals were washed briefly with pure solvent (2 × 15 mL). The crystals were placed inside the supercritical dryer together with the solvent, and the drying chamber was sealed. The temperature and pressure of the chamber were raised to 45 °C and 200 bar with CO_2, above the critical point (31.8 °C, 73 atm) of CO_2. The chamber was vented at a rate of 10 mL min^{-1} and then filled with CO_2 again. The cycles of refilling with CO_2, pressurizing, and venting were repeated for 6 h. After drying, the closed container with the dried crystals was transferred to a glove bag to avoid exposure of the crystals to air. The gas sorption isotherms of the samples were measured without further activation.

Gas sorption measurements: The gas adsorption/desorption experiments were performed with an automated micropore gas analyzer, Autosorb-3B (Quantachrome Instruments). All the gases used were of 99.999 % purity. **SNU-150′** and **SNU-151′** were pre-desolvated by using supercritical CO_2 fluid at 45 °C for 8 h. The predried solid was introduced to a gas sorption cell, the weight of which was measured exactly, and then the gas sorption isotherms were measured. The sample weight was measured precisely after the measurement of gas sorption. Between the experiments with various gases, the out-gassing procedure was repeated for approximately 1 h. The N_2 gas sorption isotherms were monitored at 77 K by using liquid nitrogen, and the H_2 gas sorption isotherms were monitored at 77 and 87 K, at each equilibrium pressure, by the static volumetric method. The adsorption isotherms for CO_2 and CH_4 gases were measured at 195, 231, 273, and 298 K. The sorption properties, including pore volume, pore size, and surface area were analyzed by using Autosorb 1 for Windows 1.24 software.

Estimation of isosteric heats of H_2 adsorption: The isosteric heats (Q_{st}) of H_2 adsorption in **SNU-150′** and **SNU-151′** were estimated from the H_2 sorption data measured at 77 and 87 K. A virial-type expression was used [Eq. (1)], which is composed of parameters a_i and b_i, which are independent of temperature. In Equation (1), P is the pressure (atm), N is the amount of adsorbed H_2 gas (mg g^{-1}), T is the temperature (K), a_i and b_i are the virial coefficients, and m and n represent the number of coefficients required to describe the isotherms adequately. An equation was fit using the R statistical software package.[40]

$$\ln P = \ln N + \frac{1}{T}\sum_{i=0}^{m} a_i N^i + \sum_{i=0}^{n} b_i N^i \quad (1)$$

The values of the virial coefficients, a_0 through a_m, were used to calculate the isosteric heat of adsorption by using Equation (2), in which Q_{st} is the coverage-dependent isosteric heat of adsorption and R is the universal gas constant.

$$Q_{st} = +R\sum_{i=0}^{m} a_i N^i \quad (2)$$

Estimation of isosteric heats of CO_2 and CH_4 adsorptions: The CO_2 adsorption data of **SNU-150′** and **SNU-151′** at 195, 231, 273, and 298 K were fit to a polynomial equation by using the *Origin 8* program, and the CH_4 adsorption data of **SNU-150′** and **SNU-151′** at 195, 231, 273, and 298 K were fit to the Langmuir–Freundlich equation, in which N is the amount of absorbed gas, N_{sat} is the amount of adsorbed gas at saturation, P is the pressure, and b and t are constants [Eq. (3)]. The heat of the gas adsorption was calculated by using the Clausius–Clapeyron equation [Eq. (4)] at each gas loading point.

$$\frac{N}{N_{sat}} = \frac{bP^t}{1+bP^t} \quad (3)$$

$$\frac{\partial(\ln P)}{\partial(1/T)} = -\frac{Q_{st}}{R} \quad (4)$$

Calculation of selectivity of CO_2 adsorption: The selectivities of CO_2 adsorption over N_2 and CH_4 were calculated by using the ideal adsorbed solution theory (IAST),[41] which enables the prediction of adsorption equilibriums of binary gas mixtures from the related single-component isotherms. The CO_2, N_2, and CH_4 adsorption isotherms of **SNU-150′** and **SNU-151′** measured at 298 K were fit to the Allometric1 equation ($y = ax^b$) and polynomial equation, respectively, on a logarithmic scale, and the IAST parameters used in the selectivity calculations were obtained (see Figures S8, S17, and S18 and Tables S2 and S3 in the Supporting Information).

Acknowledgements

This work was supported by a National Research Foundation of Korea (NRF) grant funded by the Korean Government (MSIP) (no. 2012–055324 and no. 2005–0049412). The authors acknowledge the Pohang Accelerator Laboratory (PAL) for the use of the synchrotron beamline.

[1] H. Furukawa, N. Ko, Y. B. Go, N. Aratani, S. B. Choi, E. Choi, A. O. Yazaydin, R. Q. Snurr, M. O'Keeffe, J. Kim, O. M. Yaghi, *Science* **2010**, *329*, 424–428.
[2] M. P. Suh, H. J. Park, T. K. Prasad, D.-W. Lim, *Chem. Rev.* **2012**, *112*, 782–835.
[3] J.-R. Li, R. J. Kuppler, H.-C. Zhou, *Chem. Soc. Rev.* **2009**, *38*, 1477–1504.
[4] K. Sumida, D. L. Rogow, J. A. Mason, T. M. McDonald, E. D. Bloch, Z. R. Herm, T.-H. Bae, J. R. Long, *Chem. Rev.* **2012**, *112*, 724–781.
[5] Y. E. Cheon, M. P. Suh, *Angew. Chem.* **2009**, *121*, 2943–2947; *Angew. Chem. Int. Ed.* **2009**, *48*, 2899–2903.
[6] Y.-G. Lee, H. R. Moon, Y. E. Cheon, M. P. Suh, *Angew. Chem.* **2008**, *120*, 7855–7859; *Angew. Chem. Int. Ed.* **2008**, *47*, 7741–7745.
[7] H.-S. Choi, M. P. Suh, *Angew. Chem.* **2009**, *121*, 6997–7001; *Angew. Chem. Int. Ed.* **2009**, *48*, 6865–6869.
[8] J. Rabone, Y. F. Yue, S. Y. Chong, K. C. Stylianou, J. Bacsa, D. Bradshaw, G. R. Darling, N. G. Berry, Y. Z. Khimyak, A. Y. Ganin, P. Wiper, J. B. Claridge, M. J. Rosseinsky, *Science* **2010**, *329*, 1053–1057.
[9] T. M. McDonald, D. M. D'Alessandro, R. Krishna, J. R. Long, *Chem. Sci.* **2011**, *2*, 2022–2028.
[10] S. R. Caskey, A. G. Wong-Foy, A. J. Matzger, *J. Am. Chem. Soc.* **2008**, *130*, 10870–10871.
[11] S. Henke, R. A. Fischer, *J. Am. Chem. Soc.* **2011**, *133*, 2064–2067.
[12] M. Higuchi, D. Tanaka, S. Horike, H. Sakamoto, K. Nakamura, Y. Takashima, Y. Hijikata, N. Yanai, J. Kim, K. Kato, Y. Kubota, M. Takata, S. Kitagawa, *J. Am. Chem. Soc.* **2009**, *131*, 10336–10337.
[13] L.-H. Xie, M. P. Suh, *Chem. Eur. J.* **2011**, *17*, 13653–13656.
[14] H. J. Park, Y. E. Cheon, M. P. Suh, *Chem. Eur. J.* **2010**, *16*, 11662–11669.
[15] X. Kong, E. Scott, W. Ding, J. A. Mason, J. R. Long, J. A. Reimer, *J. Am. Chem. Soc.* **2012**, *134*, 14341–14344.
[16] T. M. McDonald, W. R. Lee, J. A. Mason, B. M. Wiers, C. S. Hong, J. R. Long, *J. Am. Chem. Soc.* **2012**, *134*, 7056–7065.
[17] D. H. Hong, M. P. Suh, *Chem. Commun.* **2012**, *48*, 9168–9170.
[18] H. J. Park, M. P. Suh, *Chem. Sci.* **2013**, *4*, 685–690.
[19] H. J. Park, M. P. Suh, *Chem. Commun.* **2012**, *48*, 3400–3402.
[20] J. J. Ravichandar Babarao, *J. Am. Chem. Soc.* **2009**, *131*, 11417–11425.
[21] H. J. Park, D.-W. Lim, W. S. Yang, T.-R. Oh, M. P. Suh, *Chem. Eur. J.* **2011**, *17*, 7251–7260.
[22] E. Y. Lee, S. Y. Jang, M. P. Suh, *J. Am. Chem. Soc.* **2005**, *127*, 6374–6381.
[23] H. K. Chae, J. Kim, O. D. Friedrichs, M. O'Keefe, O. M. Yaghi, *Angew. Chem.* **2003**, *115*, 4037–4039; *Angew. Chem. Int. Ed.* **2003**, *42*, 3907–3909.
[24] A. L. Spek, PLATON99, Utrecht University, Utrecht (The Netherlands), **1999**.
[25] F. Rouquerol, J. Rouquerol, K. Sing, *Adsorption by Powders, Porous Solids Principles, Methodology and Applications*, Academic Press, San Diego, CA, **1999**.
[26] G. Horváth, K. Kawazoe, *J. Chem. Eng. Jpn.* **1983**, *16*, 470–475.
[27] L. Czepirski, J. Jagiello, *Chem. Eng. Sci.* **1989**, *44*, 797–801.
[28] E. Haldoupis, S. Nair, D. S. Sholl, *J. Am. Chem. Soc.* **2012**, *134*, 4313–4323.
[29] S. Yang, X. Lin, A. J. Blake, K. M. Thomas, P. Hubberstey, N. R. Champness, M. Schröder, *Chem. Commun.* **2008**, 6108–6110.
[30] "Zeolitelike Metal–Organic Frameworks (ZMOFs): Design, Structure, and Properties": M. H. Alkordi, M. Eddaoudi, in *Supramolecular Chemistry: From Molecules to Nanomaterials*, Wiley, **2012**.
[31] A. Demessence, D. M. D'Alessandro, M. L. Foo, J. R. Long, *J. Am. Chem. Soc.* **2009**, *131*, 8784–8786.
[32] S. D. Burd, S. Ma, J. A. Perman, B. J. Sikora, R. Q. Snurr, P. K. Thallapally, J. Tian, L. Wojtas, M. J. Zaworotko, *J. Am. Chem. Soc.* **2012**, *134*, 3663–3666.
[33] N. C. Burtch, H. Jasuja, D. Dubbeldam, K. S. Walton, *J. Am. Chem. Soc.* **2013**, *135*, 7172–7180.
[34] G. Bordeau, R. Lartia, G. Metge, C. Fiorini-Debuisschert, F. Charra, M.-P. Teulate-Fichou, *J. Am. Chem. Soc.* **2008**, *130*, 16836–16837.
[35] A. J. Arvai, C. Nielsen, ADSC Quantum-210 *ADX Program*, Area Detector System Corporation; Poway, CA, USA, **1983**.
[36] Z. Otwinowski, W. Minor, in *Methods in Enzymology, Vol. 276, Part A* (Eds.: C. W. Carter, Jr., R. M. Sweet, Academic Press, New York, **1997**, p. 307.
[37] G. M. Sheldrick, *Acta Crystallogr. Sect A* **2008**, *64*, 112–122.
[38] G. M. Sheldrick, SHELEX97, Program for the crystal structure refinement, University of Göttingen: Göttingen (Germany), **1997**.
[39] G. M. Sheldrick, *Acta Crystallogr. A* **1990**, *46*, 467–473.
[40] The software package is available online at http://www.r-project.org.
[41] A. L. Myers, J. M. Prausnitz, *AIChE J.* **1965**, *11*, 121_127.

Received: August 5, 2013
Published online: November 8, 2013

ChemPubSoc Europe
DOI: 10.1002/chem.201303801
CHEMISTRY A European Journal Full Paper

Metal–Organic Frameworks

Enhancing CO_2 Separation Ability of a Metal–Organic Framework by Post-Synthetic Ligand Exchange with Flexible Aliphatic Carboxylates

Dae Ho Hong and Myunghyun Paik Suh*[a]

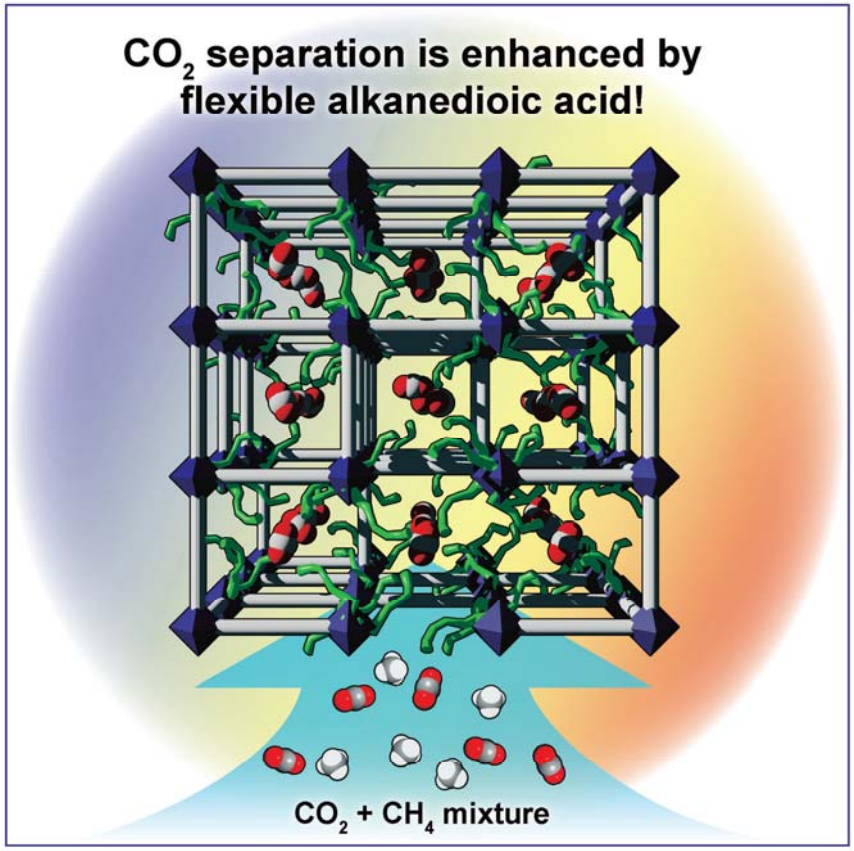

Abstract: A series of porous metal–organic frameworks having flexible carboxylic acid pendants in their pores (UiO-66-AD*n*: $n=4$, 6, 8, and 10, where *n* denotes the number of carbons in a pendant) has been synthesized by post-synthetic ligand exchange of terephthalate in UiO-66 with a series of alkanedioic acids ($HO_2C(CH_2)_{n-2}CO_2H$). NMR, IR, PXRD, TEM, and mass spectral data have suggested that a terephthalate linker in UiO-66 was substituted by two alkanedioate moieties, resulting in free carboxyl pendants in the pores. When post-synthetically modified UiO-66 was partially digested by adjusting the amount of added HF/sample, NMR spectra indicated that the ratio of alkanedioic acid/terephthalic acid was increased with smaller amounts of acid, implying that the ligand substitution proceeded from the outer layer of the particles. Gas sorption studies indicated that the surface areas and the pore volumes of all UiO-66-AD*n*s were decreased compared to those of UiO-66, and that the CO_2 adsorption capacities of UiO-66-AD*n* ($n=4$, 8) were similar to that of UiO-66. In the case of UiO-66-AD6, the CO_2 uptake capacity was 34% higher at 298 K and 58% higher at 323 K compared to those of UiO-66. It was elucidated by thermodynamic calculations that the introduction of flexible carboxyl pendants of appropriate length has two effects: 1) it increases the interaction enthalpy between the host framework and CO_2 molecules, and 2) it mitigates the entropy loss upon CO_2 adsorption due to the formation of multiple configurations for the interactions between carboxyl groups and CO_2 molecules. The ideal adsorption solution theory (IAST) selectivity for CO_2 adsorption over that of CH_4 was enhanced for all of the UiO-66-AD*n*s compared to that of UiO-66 at 298 K. In particular, UiO-66-AD6 showed the most strongly enhanced CO_2 uptake capacity and significantly increased selectivity for CO_2 adsorption over that of CH_4 at ambient temperature, suggesting that it is a promising material for sequestering CO_2 from landfill gas.

Introduction

Metal–organic frameworks have been considered as promising materials for separating CO_2 from landfill gas and industrial flue gas due to their high surface areas and the chemical tunability of their pores.[1,2] However, MOFs commonly show poor stability toward moisture, and when hydrated their gas-uptake capacities are severely reduced.[3] Therefore, water-stable MOFs such as ZIFs,[4] MIL-101,[5] and UiO-66[6] have attracted great attention and have been employed for post-synthetic modifications (PSMs),[7–9] in which some or all of the building blocks in a synthesized MOF are changed. PSMs provide alternative routes for functionalizing MOFs, and thus enable the creation of MOFs that cannot be obtained by normal solvothermal synthesis. Such methods have been demonstrated to be effective in the introduction of functional groups,[10] the insertion, removal, or exchange of organic linkers,[7,8,11,12] as well as the exchange of framework metal ions.[9,13]

To apply MOFs as carbon dioxide capture materials, they should have high CO_2 adsorption capacities and high selectivities for CO_2 adsorption over that of other gases such as CH_4 or N_2. A high isosteric heat value for CO_2 adsorption generally leads to a high uptake capacity and increased selectivity for CO_2 adsorption over that of other gases, but a higher energy may be required for regeneration of the adsorbent.[1] Many studies have been performed with the aim of increasing the isosteric heats of CO_2 adsorption in MOFs. It is important to note that the isosteric heat is a differential enthalpy of adsorption, which does not include the entropic effect. To fully understand the adsorption phenomenon, free energy (*G*) or chemical potential (μ) should be taken into consideration. One of the useful thermodynamic tools for analyzing an adsorption isotherm is consideration of the desorption functions (*G*, *H*, *S*) suggested by Myers.[14] These functions provide a complete thermodynamic description for an adsorption system with positive quantities, and the desorption free energy is the minimum isothermal energy required for regeneration of the adsorbent.

It has been reported that the introduction of flexible pendants bearing hydroxyl, amine, or ether functional groups into MOFs increases the selectivity for CO_2 adsorption over that of other gases, since closely located flexible pendants interlock with each other to act as a gate[15] or provide polar adsorption sites for CO_2 molecules.[10,16,17] To the best of our knowledge, the entropic effect of a flexible pendant incorporated into an MOF for CO_2 separation has not hitherto been explored. However, the entropy value must be considered in order to make a comprehensive assessment of the effect of a flexible pendant on CO_2 adsorption. It has been reported that separation of alkane isomers by a zeolite material is driven by differences in the degree of reduction of the rotational entropy of each alkane in the pores.[18] Since the adsorption process is governed by the change in the free energy ($\Delta G=\Delta H-T\Delta S$) and the contribution of the entropy to the free energy increases with increasing temperature, a reduction of the entropy loss associated with gas adsorption must be advantageous for obtaining improved gas uptake at high temperatures. This view inspired us to introduce flexible alkyl pendants into an MOF and to investigate their entropy effect on the adsorption of CO_2.

Herein, we report post-synthetic ligand exchange of UiO-66, a water-stable MOF, with various flexible alkanedioic acids ($HO_2C(CH_2)_{n-2}CO_2H$), which afforded a series of modified UiO-

[a] D. H. Hong, Prof. M. P. Suh
Department of Chemistry, Seoul National University
Seoul 151-747 (South Korea)
Fax: (+82) 2-886-8516
E-mail: mpsuh@snu.ac.kr

Supporting information for this article is available on the WWW under http://dx.doi.org/10.1002/chem.201303801.

66-AD*n* ($n=4$, 6, 8, and 10). During the post-synthetic ligand exchange, a single terephthalate ligand was substituted by two flexible alkanedioate ligands. This unique 1:2 ligand substitution has not previously been achieved by post-synthetic modification of MOFs.[7,8,12] For various alkanedioic acids, the degree of ligand substitution increased as the length of the acid increased. By partial digestion of the solid samples, it has also been revealed for the first time that post-synthetic ligand substitution proceeds from the outer layer of the solid instead of homogeneously in the whole crystal. Interestingly, gas adsorption studies showed that UiO-66-AD6 led to a smaller decrease in CO_2 uptake at elevated temperatures than did UiO-66. According to thermodynamic calculations based on Myers' desorption functions, the high CO_2 uptake capacities of UiO-66-AD6 at 298 K and 323 K are related to an increase in the free energy loss upon CO_2 adsorption, which is caused by the mitigated entropy loss. This entropy effect suggests that an appropriately adjusted length of flexible pendant would allow for various interaction modes between carboxyl groups and CO_2 molecules. The introduction of carboxyl pendants increased the low-coverage isosteric heats of CO_2 adsorption in all of the UiO-66-AD*n*s compared to UiO-66, with the maximum effect being observed for UiO-66-AD6. IAST selectivities for CO_2 adsorption over CH_4 adsorption increased for all of the UiO-66-AD*n*s due to stronger interactions between the carboxylic acid groups and CO_2 molecules.[19] In particular, UiO-66-AD6 proved to be the most promising for CO_2 sequestration from landfill gas at ambient temperature, since it showed the highest uptake capacity and significantly increased selectivity for CO_2 adsorption over that of CH_4.

Results and Discussion

Post-synthetic modification of UiO-66

UiO-66 was prepared by heating a solution of $ZrCl_4$ and terephthalic acid (H_2BDC) in DMF at 120 °C for 24 h, according to the previously reported method.[6] The framework of UiO-66 consists of a very stable $Zr_6O_4(OH)_4(CO_2)_{12}$ cluster extending in twelve directions to form a cubic closed packed (ccp) structure, which generates tetrahedral and octahedral cages of sizes 8 Å and 11 Å, respectively. These cages are connected by a triangular window of size 6 Å (Figure S1 in the Supporting Information).[6]

For the post-synthetic ligand exchange of UiO-66, its guest solvent molecules were removed by the heat-evacuation method at 100 °C. The desolvated sample was then immersed in an aqueous solution of the requisite alkanedioic acid (0.067 M) at 60 °C for five days, adjusting the pH to 7 with KOH and HCl (see the Experimental Section).[6,8] As new incoming ligands, succinic acid ($n=4$), adipic acid ($n=6$), suberic acid ($n=8$), and sebacic acid ($n=10$) were employed. It should be noted here that adipic acid ($n=6$) is similar in length to the terephthalate linker of UiO-66 (see Table S1 in the Supporting Information). To remove any alkanedioic acid residing in the pores, the resulting samples were immersed in MeOH and the supernatant was replenished with fresh MeOH every 12 h for two days. After activating the samples by heat treatment at 100 °C for 12 h, the dried samples, UiO-66-AD*n*s, were obtained.

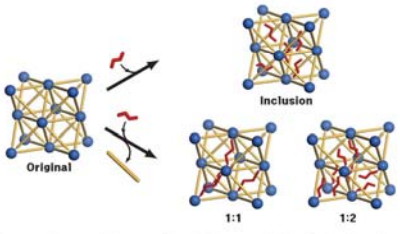

Figure 1. Three possible ways of introducing new flexible functional pendants into UiO-66. The 1:1 model represents a situation whereby an alkanedioate ligand replaces a terephthalate ligand, whereas in the 1:2 model two alkanedioate ligands substitute terephthalate leaving uncoordinated carboxylic acid groups. In the inclusion model, ligand substitution does not occur. Color scheme: metal cluster, blue; terephthalate, orange; alkanedioate, red.

For the introduction of new flexible linkers in UiO-66, three distinct modes are possible (Figure 1): 1) 1:1 substitution of a terephthalate ligand with an alkanedioate ligand of similar length; 2) 1:2 substitution of a terephthalate ligand with two alkanedioate ligands, which leaves free carboxyl pendants in the structure; and 3) simple inclusion of the alkanedioic acid in the pores of the framework, without substitution. Various experimental results suggest that each terephthalate ligand in UiO-66 is substituted by two flexible alkanedioate ligands. ^{1}H NMR spectra of samples digested in [D$_6$]DMSO containing HF revealed that the alkanedioate contents of the resulting solutions were 15.9% for UiO-66-AD4, 17.3% for UiO-66-AD6, 23.2% for UiO-66-AD8, and 49.6% for UiO-66-AD10 (Figure 2 and Table S2). In an additional experiment, UiO-66 was immersed in a mixture of succinic acid, adipic acid, and suberic acid at the same concentrations. Subsequent activation gave a product that contained 3% succinate, 5% adipate, and 15% suberate (Figure S2). The greater incorporation of longer alkanedioate ligands may be attributed to the stronger van der Waals interaction between the longer alkane chains in UiO-66-AD*n*. The fact that all of the alkanedioate ligands could be incorporated into UiO-66 irrespective of their lengths, without changing the periodic structure, as evidenced by PXRD patterns (Figure 3), coupled with the observation of free carboxylic acid peaks in the region $\tilde{\nu}=1703$–1718 cm^{-1} in the IR spectra of UiO-66-AD*n*s (Figure S3), strongly disfavored the 1:1 substitution model. In the case of UiO-66-AD6, however, a 1:1 substitution mode may be mixed with another substitution mode since the length of an adipic acid ligand is almost identical to that of terephthalate. It has been reported that an organic ligand in an MOF can be substituted in a 1:1 fashion by another ligand of identical length.[7,8] The following data exclude the possibility that alkanedioic acids are simply included in the pores. 1) A peak attributable to a hydrated terephthalate ion (HBDC-H$_2$O$^-$) was found in the mass spectrum ($m/z=183$) of

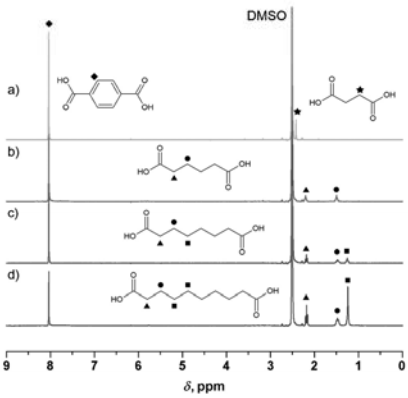

Figure 2. ^{1}H NMR spectra of UiO-66-AD*n*s after digestion with hydrofluoric acid in [D_6]DMSO solution: a) UiO-66-AD4, b) UiO-66-AD6, c) UiO-66-AD8, and d) UiO-66-AD10. Water peaks have been suppressed for clarity.

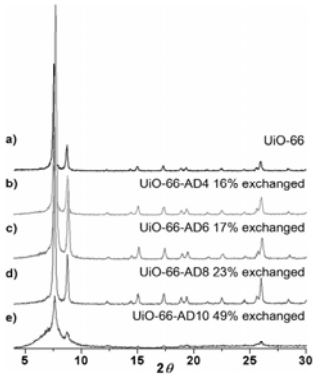

Figure 3. Powder X-ray diffraction patterns for UiO-66-AD*n*s activated by the heat-evacuation method at 100 °C: a) UiO-66, b) UiO-66-AD4, c) UiO-66-AD6, d) UiO-66-AD8, and e) UiO-66-AD10.

an adipic acid solution in which UiO-66 had been immersed for a day (Figure S4). This signal indicated that the terephthalate ligand in the UiO-66 had been displaced by adipate. 2) Even after activation of the sample using supercritical (Sc) CO_2, which would remove all guest molecules and even weakly bound solvent molecules at the metal ions,[20] the resulting UiO-66-AD6-Sc still contained 22.4% adipic acid, as estimated from the ^{1}H NMR spectrum of a sample digested in [D_6]DMSO containing HF (Table S2). This result revealed that the adipate in the structure was strongly bound. Therefore, the most likely mode is 1:2 substitution for all of the UiO-66-AD*n*s, although 1:1 substitution may be mixed with 1:2 substitution in the case of UiO-66-AD6.

The PXRD patterns (Figure 3) of UiO-66-AD*n*s (n = 4, 6, 8, and 10), obtained after activation by heat treatment at 100 °C, indicated that the structural regularities were retained even after ligand exchange and activation, although UiO-66-AD10 showed severe peak broadening. TEM images of the samples after removal of the guests indicated that the size and shape of UiO-66 were still maintained in the UiO-66-AD*n*s (n = 4, 6, 8, and 10) (Figure S5). Thermogravimetric analysis data indicated that the desolvated UiO-66, UiO-66-AD4, UiO-66-AD6, and UiO-66-AD8 samples decomposed at 510 °C, whereas UiO-66-AD10 decomposed at a much lower temperature of 427 °C (Figure S6).

Distribution of substituted adipic acid in post-synthetically modified UiO-66

Although there have been several reports on partial ligand exchange of MOFs by post-synthetic modification, the location of the exchanged ligand has never been specified.[7,8] In this study, we investigated this issue after preparing UiO-66-AD6-1d and UiO-66-AD6-14d according to the same procedure as for UiO-66-AD6, but with immersion times of 1 day and 14 days, respectively, in the solution of the alkanedioic acid. We then assessed the distribution of the adipic acid incorporated in the crystal, and the dependence of the degree of ligand substitution on the immersion time of the sample in the adipic acid solution. To this end, a fixed amount of HF in [D_6]DMSO was added to various amounts of UiO-66-AD6-1d or UiO-66-AD6-14d samples, and the ratios of adipic acid/terephthalic acid were determined from the ^{1}H NMR spectra (see the Experimental Section). We anticipated that when only a very small amount of HF was added, only the surface of the MOF crystal would be digested, but as the amount of HF was increased, the inner part of the crystal would also be digested.

In the experiment, the minimum amount of HF required for complete digestion of UiO-66-AD6-1d was calculated based on the number of moles of carboxylate groups in the sample, and this was employed in the digestion. The results indicated that one equivalent of HF per carboxyl group was sufficient for complete digestion of the sample within 30 min. This fixed amount of HF diluted with [D_6]DMSO was then added to 2×, 4×, and 8× excesses of UiO-66-AD6-1d, respectively, and the samples were digested for 30 min. After digestion, ^{1}H NMR spectra were measured (see the Experimental Section). The contents of adipic acid were found to be 48%, 41%, and 32% for the 1/8, 1/4, and 1/2 digested samples, respectively, for UiO-66-AD6-1d. A totally digested UiO-66-AD6-1d sample showed a 20% content of adipic acid (Figure S7). The same digestion method was applied to UiO-66-AD6-14d. The contents of adipic acid were found to be 48%, 35%, 30%, and 22% for the 1/8, 1/4, 1/2, and totally digested samples, respectively.

These results indicated that the less digested samples had increased percentages of adipic acid, clearly demonstrating that the exchanged ligands in the solid were concentrated near the surface of the crystal rather than being homogeneously distributed throughout its interior. The results also showed that the immersion time did not affect the distribution of the adipic acid incorporated into the crystal.

Gas sorption properties and thermodynamic analyses of UiO-66 and UiO-66-AD*n*s

It has previously been reported that UiO-66 has a moderate CO_2 uptake capacity of 1.8 mmol g^{-1} at 1 bar and 298 K,[21] and that this capacity may be enhanced by the introduction of functional groups such as amino, nitro, methoxy, or naphthyl,[9] or by post-synthetic modification of the framework metal ions.[21] For example, when an amine functional group was introduced, the CO_2 adsorption capacity reached 3.0 mmol g^{-1} at 1 bar and 298 K.[21] When framework Zr^{IV} ions were replaced by Ti^{IV} ions, the CO_2 uptake was enhanced to 2.2 mmol g^{-1} at 1 bar and 298 K.[9]

Gas sorption isotherms of the present UiO-66-AD*n* samples were measured for N_2, CO_2, and CH_4 (Table 1). From the N_2 adsorption data at 77 K, the BET (Langmuir) surface areas and pore volumes were calculated and they are summarized in Table 1 (see the Experimental Section). UiO-66 has a BET surface area (pore volume) of 1057 m^2 g^{-1} (0.441 cm^3 g^{-1}) whereas UiO-66-AD4, UiO-66-AD6, UiO-66-AD8, and UiO-66-AD10 have reduced surface areas of 942 m^2 g^{-1} (0.351 cm^3 g^{-1}), 1020 m^2 g^{-1} (0.421 cm^3 g^{-1}), 901 m^2 g^{-1} (0.342 cm^3 g^{-1}), and 213 m^2 g^{-1} (0.100 cm^3 g^{-1}), respectively. Interestingly, the surface area and pore volume of UiO-66-AD10 were much lower than those of the other samples. This might have been because the high loading of sebacic acid (50%) partially blocked the pores.

In contrast to the decreased N_2 uptakes of all of the UiO-66-AD*n*s at 77 K, the CO_2 adsorption capacities of UiO-66-AD6 at 273, 298, and 323 K were found to be greater than those of UiO-66. In particular, the decreases in the CO_2 adsorption capacities of UiO-66-AD6 at elevated temperatures are less significant than those of UiO-66 (Figure 4). As a result, the ratios of the CO_2 uptake of UiO-66-AD6 compared to that of UiO-66 increase from 1.20 at 273 K, to 1.34 at 298 K, and finally to 1.58 at 323 K. To gain insight into this behavior, the desorption functions (*G*, *H*, *S*) were calculated from the gas sorption data (see the Experimental Section).[14] These functions give values in units of energy per weight of a sample, and the data are presented in Figure 5. Since the values of Gibbs free energy, enthalpy, and entropy for gas adsorption in MOFs are generally negative, these functions are denoted as "desorption" functions. At 1 atm and 298 K, UiO-66-AD6 had the highest desorption free energy (8.29 kJ kg^{-1}), followed by UiO-66-AD4 (6.55 kJ kg^{-1}), UiO-66 (6.38 kJ kg^{-1}), and UiO-66-AD8 (6.30 kJ kg^{-1}). UiO-66-AD10 had the lowest CO_2 uptake and a fairly small desorption free energy (1.84 kJ kg^{-1}). In terms of desorption enthalpies and entropies, UiO-66-AD4 (69.4 kJ kg^{-1}, 211 J kg^{-1} K^{-1}), UiO-66-AD6 (65.3 kJ kg^{-1}, 191 J kg^{-1} K^{-1}), and UiO-66-AD8 (64.6 kJ kg^{-1}, 195 J kg^{-1} K^{-1}) showed around 20% higher values than UiO-66 (56.4 kJ kg^{-1}, 168 J kg^{-1} K^{-1}), whereas UiO-66-AD10 (25.3 kJ kg^{-1}, 78.8 J kg^{-1} K^{-1}) showed lower values than UiO-66 (Figure S8). For this series of compounds, the entropy values had a linear relationship with the enthalpy values (Figure 5). During the adsorption process, strong interactions between the gas molecules and the modified framework result in an increased entropy loss, counteracting the benefit of the enhanced enthalpy. However, UiO-66-AD6 deviated from this trend, leading to the highest desorption free energy among the compounds. In contrast to this irregular behavior of UiO-66-AD6 for CO_2 adsorption, no such deviation was seen for CH_4 adsorption in UiO-66 and the respective UiO-66-AD*n*s (Figure S9). The increased CO_2 uptake in UiO-66-AD6 must be attributed to relatively strong interactions between the CO_2 molecules and the carboxyl pendants of appropriate length. We assume that the length of the dangling adipic acid groups (5.796 Å; distance between the two carboxylate carbon atoms) is optimal to allow for multiple interaction modes with the CO_2 molecules in the pores, which increases the enthalpy loss and mitigates the entropy loss on CO_2 adsorption. The diagonal distance of an octahedral cage of UiO-66 is 15.737 Å, which is too long for two succinic acid ligands (3.594 Å × 2) and too short for two suberic acid ligands (7.885 Å × 2).

The isosteric heats (Q_{st}) of CO_2 and CH_4 adsorption were calculated by using the Clausius–Clapeyron (C–C) equation as well as the virial equation (Table 2 and Figures S10–S14).[15] When the virial equation was used, the Q_{st} values at zero coverage could be calculated. When the Q_{st} values were calculated with the C–C equation, the gas adsorption isotherms could be fitted to the Langmuir–Freundlich equation. In this case, the Q_{st} values diverged at zero coverage, and therefore the values at low coverage rather than zero coverage are given in Table 2. Depending on the amount of gas loading, the Q_{st} values obtained from the virial equation

Table 1. Gas adsorption data of UiO-66 and UiO-66-AD*n*s.

	T [K]	*P* [atm]	UiO-66 [mmol g^{-1}]	UiO-66-AD4 [mmol g^{-1}]	UiO-66-AD6 [mmol g^{-1}]	UiO-66-AD8 [mmol g^{-1}]	UiO-66-AD10 [mmol g^{-1}]
N_2	77	0.9	339[a]	247[a]	301[a]	241[a]	75[a]
CO_2	273	1.0	3.14	3.56	3.76	3.31	1.33
	298	1.0	1.96	1.92	2.63	1.83	0.57
	323	1.0	1.07	1.06	1.69	0.97	0.29
CH_4	273	1.0	0.84	0.84	0.89	0.85	0.17
	298	1.0	0.50	0.45	0.48	0.45	0.13
	323	1.0	0.20	0.19	0.27	0.14	0.10
Surface area [m^2 g^{-1}]			1057[b] (1098)[c]	942[b] (963)[c]	1020[b] (1038)[c]	901[b] (927)[c]	213[b] (224)[c]
Pore volume [cm^3 g^{-1}]			0.441	0.351	0.421	0.342	0.100

[a] In cm^3 g^{-1}. [b] BET surface area. [c] Langmuir surface area.

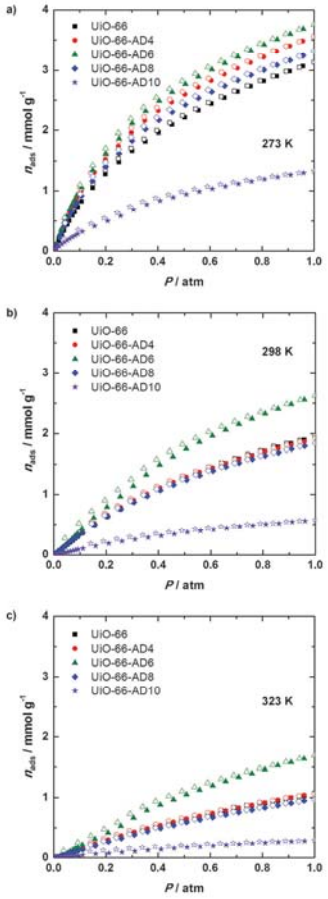

Figure 4. CO_2 adsorption isotherms at a) 273 K, b) 298 K, and c) 323 K for UiO-66 (■), UiO-66-AD4 (●), UiO-66-AD6 (▲), UiO-66-AD8 (◆), and UiO-66-AD10 (★). Filled shapes: adsorption; open shapes: desorption.

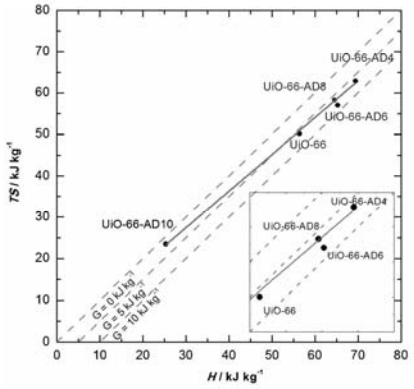

Figure 5. Linear relationship between the enthalpies and the entropies of CO_2 adsorption in UiO-66 and UiO-66-AD*n*s. Iso-value lines of the desorption free energy are drawn as dashed lines. The inset shows that the position of UiO-66-AD6 deviates from the regression line (solid line) by having reduced entropy, resulting in the highest desorption free energy value (8.29 kJ kg^{-1}), increased by 27% compared to that of UiO-66 (6.38 kJ kg^{-1}).

Table 2. Q_{st} values of various samples.

	Q_{st} of CO_2 [kJ mol^{-1}]		Q_{st} of CH_4 [kJ mol^{-1}]	
	Virial[a]	Clausius–Clapeyron[b]	Virial[a]	Clausius–Clapeyron[c]
UiO-66	40.73	34.96	37.17	29.16
UiO-66-AD4	45.72	35.27	34.36	30.43
UiO-66-AD6	49.85	36.65	37.51	31.60
UiO-66-AD8	44.56	35.90	24.69	25.83
UiO-66-AD10	50.77	34.19	19.94	23.58

[a] $n_{ads} = 0$ mmol g^{-1}. [b] $n_{ads} = 0.05$ mmol g^{-1}. [c] $n_{ads} = 0.01$ mmol g^{-1}.

fluctuate around the Q_{st} values obtained from the C–C equation, since the virial equation contains polynomial terms. Regardless of the calculation method, the Q_{st} values for CO_2 adsorption increased for all of the UiO-66-AD*n*s compared with those for UiO-66, except for the Q_{st} value of UiO-66-AD10 calculated with the C–C equation. UiO-66-AD6 exhibited the highest Q_{st} values among all of the samples. In contrast to the CO_2 adsorption, the Q_{st} values for CH_4 adsorption were not simply increased by the carboxyl pendants. The Q_{st} values for CH_4 adsorption increased in UiO-66-AD6 and decreased in UiO-66-AD8 and UiO-66-AD10, regardless of the calculation method.

Selectivity estimated by ideal adsorption solution theory (IAST)

A selectivity coefficient of ideal adsorption solution is calculated by assuming that the free energies (G) of each gas adsorbed in a framework are identical at a fixed temperature (see the Experimental Section). The desorption free energy (G) is the same as πA, which is a product of spreading pressure and specific surface area used for describing the thermodynamics of surface adsorption.[14]

The selectivities for CO_2 adsorption over that of CH_4 at 273 K, 298 K, and 323 K were calculated to determine the ap-

Table 3. The CO_2/CH_4 separation parameters of UiO-66 and UiO-66-AD*n*s for landfill gas in the VSA process. The composition of landfill gas was assumed to be 50% CO_2 and 50% CH_4.

	T [K]	n_{CO_2} [mmol g^{-1}]	Δn_{CO_2} [mmol g^{-1}]	R[a]	α[b]
UiO-66	273	2.104	1.671	0.794	10.4
	298	1.184	1.017	0.859	6.87
	323	0.568	0.508	0.894	6.87
UiO-66-AD4	273	2.486	1.948	0.784	12.6
	298	1.211	1.031	0.851	8.04
	323	0.620	0.545	0.879	9.05
UiO-66-AD6	273	2.636	2.063	0.783	15.0
	298	1.598	1.415	0.885	10.0
	323	0.945	0.864	0.914	10.1
UiO-66-AD8	273	2.331	1.848	0.793	12.3
	298	1.170	0.998	0.853	7.31
	323	0.536	0.476	0.888	10.9
UiO-66-AD10	273	0.903	0.738	0.817	16.1
	298	0.342	0.295	0.863	9.29
	323	0.162	0.140	0.864	8.25

[a] R = regenerability. [b] α = IAST selectivity, calculated under desorption conditions (P = 0.1 atm).

plicability of UiO-66-AD*n*s for the separation of landfill gas by using the vacuum swing adsorption (VSA) process (Table 3 and Figure S15). The pressure of adsorption was taken as 1.0 atm and that of desorption as 0.1 atm in VSA.[22] The selectivity values were calculated under the desorption conditions (0.1 atm), because the adsorption data should be extrapolated to $P > 1$ atm to calculate the free energies of the CH_4 sorption under the adsorption conditions. For instance, single-component CH_4 gas adsorption data up to 4.0 atm at 298 K was required to calculate the IAST selectivity for the 1:1 mixture of CO_2 and CH_4 gases adsorbed on UiO-66 at 1 atm 298 K. The selectivity values for CO_2/CH_4 adsorption at 273 K calculated under the adsorption conditions did not converge in the case of UiO-66-AD10.

Four adsorbent evaluation criteria suggested by Snurr's group,[22] namely CO_2 uptake under adsorption conditions, working CO_2 capacity, regenerability (R), and selectivity (α), were also calculated and the data are presented in Table 3. For landfill gas separation, all of the UiO-66-AD*n*s showed significantly increased selectivity values for CO_2 adsorption over that of CH_4 compared to those of UiO-66. In particular, UiO-66-AD6 showed the highest selectivity values as well as the highest CO_2 uptake and the best working CO_2 capacity. Notably, the enhancement factors of the CO_2 uptake and the working CO_2 capacity in UiO-66-AD6 compared to those of UiO-66 increased with increasing temperature, from about 20% at 273 K to about 70% at 323 K.

Conclusion

We have prepared various UiO-66 derivatives, designated as UiO-66-AD*n*s, in which a series of flexible carboxylic acid pendants of various lengths has been incorporated by post-synthetic ligand exchange. We then proceeded to investigate the thermodynamic aspects of CO_2 adsorption in these systems. An unprecedented 1:2 ligand substitution of terephthalate in UiO-66 by two alkanedioate ligands has been identified. In particular, UiO-66-AD6, containing adipic acid pendants, has been found to exhibit a significantly enhanced CO_2 separation ability for landfill gas, showing enhanced working capacity and significantly increased selectivity for CO_2 adsorption over that of CH_4, compared to those of UiO-66 and the other UiO-66-AD*n*s. From an analysis of enthalpy and entropy, it was revealed that the increased CO_2 capacity of UiO-66-AD6 can be attributed to an increased enthalpy loss and a mitigated entropy loss upon CO_2 adsorption as a result of interaction with the dangling carboxyl pendants of appropriate length. These flexible carboxylic acid pendants effectively accommodate CO_2, reducing the entropy loss upon CO_2 adsorption. No such phenomenon is manifested in CH_4 adsorption due to weak interaction between the CH_4 molecules and the pendants. The present work has demonstrated that the introduction of dangling carboxyl pendants of appropriate length in an MOF by post-synthetic ligand exchange can enhance the CO_2 separation performance of the MOF at high temperatures.

Experimental Section

General methods

All chemicals and solvents used in the synthesis were of reagent grade and were used without further purification. Infrared spectra were recorded with a Perkin-Elmer Spectrum One FTIR spectrophotometer. NMR spectra were measured on a Bruker Advance DPX-300 spectrometer. Thermogravimetric analyses (TGA) were performed under N_2 (g) at a scan rate of 5 °C min^{-1}, using a TGA Q50 from TA Instruments. Powder X-ray diffraction data were recorded on a Bruker D8 Advance diffractometer operating at 40 kV and 40 mA and employing $Cu_{K\alpha}$ radiation (λ = 1.54050 Å), with a scan speed of 0.3 s per step and a step size of 0.02° in 2θ. TEM images were acquired with a Hitachi H-7600 operating at 100 kV.

Preparation of activated UiO-66

UiO-66 was prepared according to the previously reported method.[6] The as-synthesized UiO-66 was then sonicated in DMF/MeOH (1:1), collected by filtration, and washed successively with DMF (3 × 30 mL) and MeOH (3 × 30 mL). The sample was activated by heating at 100 °C under vacuum. UiO-66 immediately adsorbed 16 equivalents of H_2O molecules on exposure to air. FTIR (Nujol mull): $\tilde{\nu}$ = 3669, 3639, 3418 (OH^-), 1578 cm^{-1} (CO_2^-).

Preparation of UiO-66-AD*n* (*n* = 4, 6, 8, and 10) by ligand exchange of UiO-66 with alkanedioic acids followed by activation

Ligand-exchange experiments were performed according to the previously reported method.[8] Each alkanedioic acid (HO_2C-$(CH_2)_{n-2}CO_2H$, n = 4, 6, 8, and 10; 0.2 mmol) was dissolved in 4% aqueous KOH solution (2 mL). The solution was neutralized to pH 7 with 1 M HCl (total 3 mL). UiO-66 (ca. 57 mg, 0.2 mmol of terephthalate linkers) was immersed in the solution, which had been kept in a pre-heated oven (60 °C) for 1 h, and the mixture was allowed to stand for 5 days. After immersion, the mixture was centrifuged and the aqueous phase was decanted off. The solid was immersed in MeOH (10 mL), and the supernatant was exchanged with fresh

MeOH (10 mL) every 12 h for 2 days. The solid was collected by filtration and dried under vacuum at 100 °C for 12 h to afford the respective UiO-66-AD*n*. After gas sorption measurements, IR spectra of the samples were measured. Each UiO-66-AD*n* immediately adsorbed water molecules on exposure to air. For UiO-66-AD4, FTIR (Nujol mull): $\tilde{\nu}$ = 3669, 3638, 3390 (OH^-), 1703 (C=O), 1578 cm^{-1} (CO_2^-). For UiO-66-AD6, FTIR (Nujol mull): $\tilde{\nu}$ = 3669, 3639, 3411 (OH^-), 1718 (C=O), 1579 cm^{-1} (CO_2^-). For UiO-66-AD8, FTIR (Nujol mull): $\tilde{\nu}$ = 3670, 3640, 3418 (OH^-), 1709 (C=O), 1578 cm^{-1} (CO_2^-). For UiO-66-AD10, FTIR (Nujol mull): $\tilde{\nu}$ = 3672, 3641, 3383 (OH^-), 1703 (C=O), 1578 cm^{-1} (CO_2^-).

^{1}H NMR analysis of UiO-66-AD*n* (*n* = 4, 6, 8, and 10)

Each activated UiO-66-AD*n* (3 mg) was placed in a test tube and digested in [D_6]DMSO (580 μL) containing an aqueous solution of 4.8 wt% HF (20 μL). For accurate integration of NMR spectra, the water peak was suppressed.

Preparation of UiO-66-AD6-Sc by a supercritical CO_2 drying method

Prior to activation, a sample of UiO-66 that had been ligand exchanged with adipic acid for 5 days was exchanged with fresh MeOH for 2 days as described previously. The crystals were placed inside a supercritical dryer together with the solvent, and the drying chamber was sealed. The temperature was set at 45 °C and the pressure of the chamber was raised to 200 bar with CO_2. The chamber was vented at a rate of 10 mL min^{-1} and then refilled with CO_2. Cycles of refilling with CO_2, pressurizing, and venting were repeated for 5 h. After drying, the closed vessel containing the dried sample was transferred to a glove bag filled with argon to prevent exposure of the crystals to air. UiO-66-AD6-Sc immediately adsorbed 13 equivalents of H_2O molecules on exposure to air. FTIR (KBr pellet): $\tilde{\nu}$ = 3399 (OH^-), 2939 (C-H), 1574 cm^{-1} (CO_2^-).

Partial digestion of UiO-66-AD6–1d and UiO-66-AD6–14d

An aqueous solution of 4.8 wt% HF (11 μL, 0.026 mmol) was diluted with [D_6]DMSO (590 μL). UiO-66-AD6 (7 mg, 14 mg, or 28 mg, respectively), which had been dried at 100 °C overnight, was then immersed in the solution for 30 min. The molar ratio of HF to the number of carboxylate groups in UiO-66-AD6 was adjusted to 1:2, 1:4, and 1:8 in three digestion runs, respectively. For accurate integration of NMR spectra, the water peak was suppressed.

Low-pressure gas sorption measurements

Gas adsorption–desorption data were measured by means of an automated micropore gas analyzer (Autosorb-1 or Autosorb-3B; Quantachrome Instruments). All gases used were of 99.9999% purity. Samples were activated at 100 °C under vacuum for 12 h. The N_2 gas isotherms were measured at 77 K. The CO_2 and CH_4 gas isotherms were measured at 273 K, 298 K, and 323 K at each equilibrium pressure by the static volumetric method. After gas sorption measurement, the weight of the sample was precisely measured once more. Surface area was calculated from the N_2 adsorption data measured at 77 K using the Brunauer–Emmett–Teller (BET) and Langmuir methods by plotting the data points until the value of $n_{ads}(1-P/P^\circ)$ reached the maximum. Pore volume was calculated by applying the NLDFT (non-local density functional theory) equilibrium model to N_2 adsorption data measured at 77 K.

Calculation of thermodynamic functions (*G*, *H*, *S*) from gas adsorption isotherms

The desorption free energy (*G*) is the minimum work required for the isothermal release of adsorbed gas at a given temperature and pressure.[14] Under low pressure, the free energy of desorption can be calculated by Equation (1):

$$G = RT\int_0^P \frac{n}{P}\,dP = RT\int_0^P n\,d\ln P \tag{1}$$

For an adsorption isotherm fitted with Langmuir, dual-site Langmuir, and Langmuir–Freundlich equations, the free energy function (*G*) can be expressed in analytical form [Eq. (2)]. In this work, we applied the Langmuir–Freundlich equation to fit the adsorption isotherms for CO_2 and CH_4, and the desorption free energy function was obtained as Equation (3):

$$n = n_m \frac{bP^{(1/t)}}{1 + bP^{(1/t)}} \tag{2}$$

$$G = n_m tRT \ln\left(1 + bP^{(1/t)}\right) \tag{3}$$

The enthalpy of desorption (*H*) was calculated by applying the Gibbs–Helmholtz equation to the data obtained at multiple temperatures [Eq. (4)]:

$$H = -T^2\left[\frac{\partial(G/T)}{\partial T}\right]_P = \left[\frac{\partial(G/T)}{\partial(1/T)}\right]_P \tag{4}$$

The entropy of desorption was obtained as follows [Eq. (5)]:

$$S = -\left[\frac{\partial G}{\partial T}\right]_P = \frac{H-G}{T} \tag{5}$$

Calculation of IAST selectivity

The desorption free energies of adsorbed species are all the same under the equilibrium conditions at a fixed temperature. Therefore, selectivity (α) can be calculated by the following equations [Eqs. (6) and (7)]. For a given *G* value:

$$Py_i = P_i^\circ(G)x_i \tag{6}$$

$$\alpha_{i,j} = \frac{x_i/y_i}{x_j/y_j} = \frac{P_j^\circ(G)}{P_i^\circ(G)} \tag{7}$$

In this study, $P^\circ(G)$ was derived from Equation (3) [Eq. (8)]:

$$P^\circ(G) = \left(\left(\exp\left(\frac{G}{n_m tRT}\right) - 1\right)/b\right)^t \tag{8}$$

The total pressure (*P*) and the total loading (*n*) are given by the following expressions [Eqs. (9) and (10)]:

$$P = \frac{1}{y_i/P_i^\circ + y_j/P_j^\circ} \tag{9}$$

$$\frac{1}{n} = \sum_i \frac{x_i}{n_i} \quad (10)$$

The individual loadings (n_i) are given as follows [Eq. (11)]:

$$n_i = n x_i \quad (11)$$

Abbreviations

α: Selectivity; b: Constant in Equation (2); n: amount adsorbed (mmol g^{-1}); n_m: Constant in Equation (2) (mmol g^{-1}); G: Gibbs free energy of desorption (kJ kg^{-1}); H: enthalpy of desorption (kJ kg^{-1}); P: Pressure (atm); P_i^o: pressure of pure component adsorption (atm): R: gas constant, 8.3145 J mol^{-1} K^{-1}; S: entropy of desorption (kJ kg^{-1} K^{-1}); t: constant in Equation (2); T: temperature (K); x_i: mole fraction of component i in adsorbed phase; y_i: mole fraction of component i in vapor phase.

Acknowledgements

This work was supported by a National Research Foundation (NRF) grant funded by the Korean Government (MSIP) (NRF-2012-055324 and NRF-2005-0049412). D.H.H. acknowledges support by Global Ph.D. Fellowship (GPF) programs of the NRF. We thank Sung-Soo Kim for obtaining the TEM images.

Keywords: carbon dioxide separation · carboxyl pendants · ligand substitution · metal–organic frameworks · post-synthetic modification · thermodynamics

[1] K. Sumida, D. L. Rogow, J. A. Mason, T. M. McDonald, E. D. Bloch, Z. R. Herm, T.-H. Bae, J. R. Long, *Chem. Rev.* **2012**, *112*, 724–781.
[2] S. Xiang, Y. He, Z. Zhang, H. Wu, W. Zhou, R. Krishna, B. Chen, *Nat. Commun.* **2012**, *3*, 954.
[3] J. J. Low, A. I. Benin, P. Jakubczak, J. F. Abrahamian, S. A. Faheem, R. R. Willis, *J. Am. Chem. Soc.* **2009**, *131*, 15834–15842.
[4] K. S. Park, Z. Ni, A. P. Côté, J. Y. Choi, R. Huang, F. J. Uribe-Romo, H. K. Chae, M. O'Keeffe, O. M. Yaghi, *Proc. Natl. Acad. Sci. USA* **2006**, *103*, 10186–10191.
[5] G. Férey, C. Mellot-Draznieks, C. Serre, F. Millange, J. Dutour, S. Surblé, I. Margiolaki, *Science* **2005**, *309*, 2040–2042.
[6] J. H. Cavka, S. Jakobsen, U. Olsbye, N. Guillou, C. Lamberti, S. Bordiga, K. P. Lillerud, *J. Am. Chem. Soc.* **2008**, *130*, 13850–13851.
[7] M. Kim, J. F. Cahill, H. Fei, K. A. Prather, S. M. Cohen, *J. Am. Chem. Soc.* **2012**, *134*, 18082–18088.
[8] M. Kim, J. F. Cahill, Y. Su, K. A. Prather, S. M. Cohen, *Chem. Sci.* **2012**, *3*, 126.
[9] C. H. Lau, R. Babarao, M. R. Hill, *Chem. Commun.* **2013**, *49*, 3634–3636.
[10] T. M. McDonald, W. R. Lee, J. A. Mason, B. M. Wiers, C. S. Hong, J. R. Long, *J. Am. Chem. Soc.* **2012**, *134*, 7056–7065.
[11] H. J. Park, Y. E. Cheon, M. P. Suh, *Chem. Eur. J.* **2010**, *16*, 11662–11669.
[12] T. Li, M. T. Kozlowski, E. A. Doud, M. N. Blakely, N. L. Rosi, *J. Am. Chem. Soc.* **2013**, *135*, 11688–11691.
[13] T. K. Prasad, D. H. Hong, M. P. Suh, *Chem. Eur. J.* **2010**, *16*, 14043–14050.
[14] A. Myers, *Adsorption* **2003**, *9*, 9–16.
[15] J. Seo, R. Matsuda, H. Sakamoto, C. Bonneau, S. Kitagawa, *J. Am. Chem. Soc.* **2009**, *131*, 12792–12800.
[16] N. Planas, A. L. Dzubak, R. Poloni, L.-C. Lin, A. McManus, T. M. McDonald, J. B. Neaton, J. R. Long, B. Smit, L. Gagliardi, *J. Am. Chem. Soc.* **2013**, *135*, 7402–7405.
[17] S. Henke, R. A. Fischer, *J. Am. Chem. Soc.* **2011**, *133*, 2064–2067.
[18] J. F. M. Denayer, R. A. Ocakoglu, I. C. Arik, C. E. A. Kirschhock, J. A. Martens, G. V. Baron, *Angew. Chem.* **2005**, *117*, 404–407; *Angew. Chem. Int. Ed.* **2005**, *44*, 400–403.
[19] Q. Yang, A. D. Wiersum, P. L. Llewellyn, V. Guillerm, C. Serre, G. Maurin, *Chem. Commun.* **2011**, *47*, 9603–9605.
[20] T. K. Kim, M. P. Suh, *Chem. Commun.* **2011**, *47*, 4258–4260.
[21] G. E. Cmarik, M. Kim, S. M. Cohen, K. S. Walton, *Langmuir* **2012**, *28*, 15606–15613.
[22] Y.-S. Bae, R. Q. Snurr, *Angew. Chem.* **2011**, *123*, 11790–11801; *Angew. Chem. Int. Ed.* **2011**, *50*, 11586–11596.

Received: September 28, 2013
Published online on December 20, 2013

국문 초록

Part I. 유연한 선형 리간드를 이용하여 조립된 다공성의 금속-유기 골격체와 이를 이용한 선택적인 이산화탄소 포집 연구

유연한 에테르 연결단위가 포함된 리간드인 H_2*mpm*-PBODB와 bipyridyl 리간드, 그리고 아연이온을 80 °C DMF 에서 자가조립을 하여 새로운 금속-유기 골격체 {[Zn_2(*mpm*-PBODB)$_2$bpy]·3DMF}$_n$ (**SNU-110**)를 합성하였다. 합성된 구조는 X-선 단결정 구조분석을 통해 4.4 × 3.7 Å^2 크기의 1차원 동공을 갖고 단위격자 부피의 30%는 손님분자로 채워진 구조인 것을 확인하였다. 초임계 상태의 이산화탄소로 시료를 활성화시킨 결과 손님분자가 제거된 [Zn_2(*mpm*-PBODB)$_2$bpy]$_n$ (**SNU-110'**)을 얻어낼 수 있었다. **SNU-110'**은 단결정이 유지가 되지 않았기 때문에 분말 X-선 회절 실험을 통해 구조의 변화를 조사해 보았는데, 단위격자의 부피가 8.8% 줄어들었음을 알 수 있었다. 가스포집실험을 해본 결과 **SNU-110'**은 77 K에서 질소와 수소, 195 K에서 메탄가스를 포집 하지 않았지만, 수소기체(2.89 Å)보다 크기가 큰 이산화탄소 분자(3.3 Å)를 195 K에서 두 단계의 포집과정을 거쳐 97 cm^3 g^{-1}까지 흡착하고 탈착시에는 큰 이력성을 보였다. 이렇게 독특한 흡착양상은 이산화탄소 포집과정에서 발생하는 금속-유기 골격체의 상전이에 의한 것이다. 이산화탄소로 포화된 **SNU-110'**은 그 구조가 손님분자를 포함한 초기구조인 **SNU-100**과 동등함을 표면적과 동공 크기 분석, 그리고 이산화탄소 조건 하의

분말 엑스선 회절실험을 통해 확인하였다. 195 K에서 질소, 수소와 메탄가스 대비 이산화탄소의 흡착선택성은 각각 35:1, 61:1과 15:1였다. 이러한 선택성은 이산화탄소가 다른 가스들에 비해 큰 사중극자모멘트와 편극성을 가지기 때문이다. 이러한 선택성은 298 K까지 유지되었으며 질소와 메탄가스 대비 이산화탄소의 선택성이 각각 59:1과 14:1였다.

주 요 어: 금속-유기 골격체 • 이산화탄소 포집 • 다단계 흡착 • 유연한 골격체 • 이력성

Part II. 유연한 양방향 지방산을 이용한 금속-유기 골격체의 합성 후 변환과 향상된 이산화탄소 포집능 연구

물에 안정한 지르코늄과 카복시산의 연결로 이루어진 UiO-66를 합성하고, 합성 후 변환과정을 통해 양방향의 지방족 카복시산이 동공 내부에 포함된 UiO-66-AD*n* (*n*은 지방족 탄소의 길이이며, 4, 6, 8 그리고 10이다.) 구조들을 합성하였다. UiO-66 구조에 존재하는 일부의 테레프탈산이 1:2 치환을 통해 지방족 카복시산으로 바뀌며 배위하지 않은 카복시산을 이 존재한다는 증거를 핵자기공명 분석, 적외선 분광법, 분말 X선 산란, 전자현미경 이미지, 질량 스펙트럼을 통해 제시하였다. 합성 후 변환을 거친 UiO-66를 가해주는 불소산의 양을 조절해가면서 입자들을 부분적으로 녹인 이후에 핵자기공명 분석실험을 수행한 결과 녹여낸 양을 줄일수록 양방향의 지방족산과 테레프탈산의 비율이 증가함을 알 수 있었는데, 이는 리간드 교환반응이 입자의 표면으로부터 진행되었음을 의미한다. 가스포집실험을 수행한 결과 UiO-66-AD*n*의 표면적과 동공 부피가 원래의 UiO-66보다 조금 줄어들었지만 UiO-66-AD4와 UiO-66-AD8의 경우 이산화탄소 포집능력이 UiO-66와 유사함을 알 수 있었다. UiO-66-AD6의 경우 오히려 이산화탄소 포집능력이 UiO-66에 비해 298 K에서 34% 323 K에서 58% 증가하였다. 열역학 계산을 통해 분석해 본 결과 이러한 현상은 적절한 길이의 유연한 카복시산 펜던트에 의해 1) 이산화탄소와 골격구조간의 상호작용 엔탈피가 증가하고, 2) 여러 카복시산 펜던트와 이산화탄소가 다양한 양상으로 상호작용하면서

흡착과정에서 감소하는 엔트로피가 줄어든 것을 알 수 있었다. 이상적 흡착용액 이론을 이용하여 계산한 298 K에서의 메탄가스대비 이산화탄소의 흡착선택성은 모든 UiO-66-AD*n*이 UiO-66에 비해서 증가한 값을 가졌다. 특히 UiO-66-AD6는 상온에서 가장 높은 이산화탄소 포집량과 증가한 메탄가스 대비 이산화탄소 포집선택성을 보이기 때문에 매립가스의 이산화탄소 포집 물질로 적합하리라 예상된다.

주 요 어: 금속-유기 골격체 • 이산화탄소 구분 • 카복시산 펜던트 • 합성 후 변환 • 리간드 교환 • 열역학

감사의 말

박사과정이 끝났습니다. 이 논문이 완성될 때까지 아낌 없이 지도와 편달을 해주시며 한 사람의 과학자로서 길러주신 백명현 선생님께 감사의 말씀 드립니다. 제가 국내대학원에 진학할 수 있도록 신념을 심어주시고 위원장으로서 저의 학위 논문 심사를 맡아 주신 정두수 교수님, 바쁘신 와중에도 멀리서 몸소 찾아오셔서 심사를 맡아 주신 KAIST 유룡 교수님과 숭실대학교 김자헌 교수님, 그리고 논문심사를 해 주시고 앞으로 저를 거두어 함께 연구를 이끌어주실 이동환 교수님께 귀중한 시간을 내어주신 점에 깊은 감사를 드립니다. 그리고 학부 과정을 지도해 주셨던 이성훈 교수님과 박승범 교수님께도 감사의 말씀 올립니다.

5년이라는 시간 동안 많은 것을 느끼고 배웠습니다. 인생은 자기자신과의 싸움이라 하는데, 이 5년간은 지난 30년 가까이 살아온 인생 중 가장 치열하게 나 자신과 겨루어 왔던 시간이었습니다. 방종하며 살아왔던 제 자신을 다잡아 두고 이해해가는 과정에서, 제 자신이 가지고 있던 목표는 흔들림 없이 잘 움켜쥔 채 자신을 과신하지 않도록 많이 노력해왔습니다. 막바지 일년 반을 남긴 시점에서는 시간의 소중함을 절실하게 느끼면서 내가 하루에 시간을 어떻게 쓰는지 타이머를 돌려가며 초 단위로 분석을 한 적도 있었습니다. 마지막 순간까지도 졸업을 위협할만한 위기의 순간이 닥치기도 했지만 저를 믿고 이해하는 마음과 저의 버팀목이 되어준 많은 사람들- 가족들을 비롯하여 선생님과 실험실 가족들, 그리고 친구들- 의 도움이

있었기에 끝까지 잘 완수해낼 수 있었습니다. 함께해준 인연들에게 감사하다는 말을 하고 싶습니다.

자가조립의 간결한 아름다움을 통해 무기화학으로 이끌어 주신 백명현 선생님께 다시금 감사의 말씀 드립니다. 창의적인 인재로 길러주시고자 꾸지람과 조언을 아끼지 않고 베풀어주셨으며, 훌륭한 선배님들의 이야기를 많이 해 주셨습니다. 선생님 덕분에 화학이 무엇인가에 대해서도 많이 생각해볼 기회를 가질 수 있었고 앞으로 나아갈 길에 방향을 잡는 데에도 큰 도움을 받았습니다.

실험실에서도 여러 사람들의 도움을 받았습니다. 회리누나, 영은누나,우승이형, 태록이형, 혜정누나, 태경누나, 정은누나, 혜선누나 해서 총 8명의 선배님들에게 여러 가지 실험도구 및 기기들을 다루는 법을 배우고, 실험이 잘 안 풀리거나 할 때는 조언도 받고 격려도 받았습니다. 특히 혜정누나는 4년 이상의 세월 동안 같이 실험실생활을 하면서 헌신적이고 카리스마 있는 리더십으로 화목한 실험실 분위기를 이끌어 주고, 제가 심각하게 부족했던 정리벽을 많이 고쳐주어서 마지막 졸업하는 순간까지 큰 도움이 되었습니다. 세용이, 승안이형, 명호형, 시영이 해서 총 4명의 후배들은 내 일에 치이느라 많이 도와주지 못했지만 각자 본인의 일을 잘 해내어 졸업 해냈고 여러 실험실 유지관리 일을 도맡아 도와 주었습니다. 그리고 동기로 같이 들어온 대운이형은 기민하고 일 처리속도가 빨라서 많은 일을 해 내고, 졸업 요건 맞추느라 급할 시기에 방장을 맡아 여러모로 신경

쓰이는 일들을 처리해주었습니다. 명성이 높으신 선생님 덕분에 세계 각지에서 모였던 Prasad, Xie, 그리고 Prem 박사님들과 연구에 관해 이야기하고 실험을 배우기도 했습니다. 실험실 생활 같이한 모든 이에게 많이 배웠으며 특별히 감사하다고 말하고 싶습니다.

힘들 때 같이 모여 이야기를 나눌 수 있었던 사람들에게도 감사합니다. 항상 내 개똥철학을 귀담아 들어주고 좋은 토론을 이끌어주는 내 화학의 지음인 욱래. 어릴 때부터 항상 함께 놀며 노는 취향도 비슷한 붕우지성이. 무리수계를 함께 한 멤버들인 선우, 상헌, 성현이. 동내 친구 규민이, 재환이, 승주. 같은 장학금 동지에서 말벗이 된 혜진이. 멘토링으로 시작해서 놂으로 연이 이어지는 자영이, 내 인생에 화학을 소개해준 동국이형, 그리고 절친한 동창 동기들인 현수, 호영이, 정호, 상준이, 윤재, 성수, 준환, 준우, 준홍이 모두에게 감사합니다.

어린 시절부터 저에게 큰 방향을 세워주시고 학업에 정진할 수 있도록 헌신하시며 가정을 이끌어오신 나의 아버지, 항상 한결 같이 막대한 사랑으로 제 심신의 안정감을 형성해주신 나의 어머니, 그리고 일상의 말상대와 놀이상대를 해주며 즐거움을 함께 한 큰 기둥같이 든든한 나의 형. 사랑하고 존경하는 저의 가족들이 항상 묵묵하고 성실하게 자신의 자리를 지켜주었기에 저도 흔들림 없이 잘 해낼 수 있었습니다. 그리고 박사가 되기 전부터 홍박사라 불러주시며 힘과 기대를 실어주신 친지어르신들과 사촌형제들, 특히 멋진 기업가로서 열정적인 삶을 몸소 보여주시는 이모부와

항상 잘 반겨주시던 이모, 그리고 친동생보다 아끼는 이종사촌동생 주현이, 지영이, 지환이 모두들 감사합니다.

마지막으로, 욱래가 알려준 마하트마 간디의 “A man is but the product of his thoughts. What he thinks he becomes” 라는 말이 생각납니다. 사람은 자신이 생각한 대로 이끌리고, 그렇게 된다는 말로 이해하고 있습니다. 기억도 잘 나지 않는 어린 시절부터 만드는 것을 좋아하던 저는 초등학교 때부터 과학자가 하고 싶었고, 지금도 차분히 그 길을 따라 정진하고 있습니다. 앞으로 졸업하면서 받게 되는 박사 학위는 스스로 연구할 역량이 있고, 그 결과를 세상과 공유할 자질을 가진 자라고 선생님께서 인정해주시는 자격증이라 생각하고 있습니다. 이 자격증을 쥐고서, 앞으로도 좋은 사람들과 함께 새로운 것을 만들어내며 행복하게 살고자 합니다. 감사합니다.

2014년 2월 3일 홍대호